Dissertation

SUBMITTED TO THE

Combined Faculties of the Natural Sciences and Mathematics
of the Ruperto-Carola-University of Heidelberg, Germany

FOR THE DEGREE OF

Doctor of Natural Sciences

Put forward by

Lida Zhang (张理达)

Born in: Tongcheng, Hubei/ People's Republic of China (PRC)

(出生地:中华人民共和国湖北省通城县龙潭村石板桥)

Oral examination: 15.04.2015

Coherent control and manipulation of classical or quantum light via nonlocal effects

Referees: **Priv. Doz. Dr. Jörg Evers**
Prof. Dr. Jürgen Berges

Zusammenfassung

Gegenstand dieser Arbeit ist die theoretische Untersuchung von kohärenter Kontrolle und Manipulation von klassischem oder quantenmechanischem Licht mittels nichtlokaler Effekte. Im klassischen Fall wird die Propagationsdynamik von Licht in paraxialer Näherung betrachtet. In thermischen atomaren Gasen wird dabei der spezifische Einfluss von nichtlokalen linearen Effekten analysiert und für Laserstrahlen mit beliebigem räumlichen Profil wird beugungs- und verlustfreie Propagation, gleichförmige Phasenmodulation und Frequenzumwandlung mit Erhaltung der Bildinformation gezeigt. Weiterhin wird untersucht, wie die Propagationsdynamik wechselwirkender thermischer Rydbergatome durch nichtlokale und nichtlineare Effekte beeinflusst wird. Es zeigt sich, dass dabei für jede Wellenkomponente die nichtlokale nichtlineare Absorption mit der Modulationsinstabilität konkurriert. Ferner wird die PT-symmetrische Dynamik in kalten Rydbergatomen ausgenutzt und es wird gezeigt, dass durch nichtlokale nichtlineare Effekte ein Phasenübergang von erhaltener zu gebrochener PT Symmetrie erreicht werden kann. Auf der Quantenebene wird außerdem ein Test zum Nachweis quantenmechanischer Nichtlokalität einzelner Röntgenphotonen, die mit ^{57}Fe Kernen in dünnen Kavitäten wechselwirken, vorgeschlagen, indem eine Version der Bellschen Ungleichung für einzelne Photonen verletzt wird. Die experimentelle Realisierung aller diskutierten Phänomene ist mit bestehenden Mitteln möglich.

Abstract

The thesis is devoted to the theoretical studies of coherent control and manipulation of classical or quantum light via nonlocal effects. At the classical level, controllable light propagation dynamics in the paraxial regime is investigated. The specific type of nonlocal linear effects induced in thermal atomic vapor is explored to achieve diffractionless and lossless propagation, uniform phase modulation, and frequency conversion with diffractionless image duplication for laser beams with arbitrarily encoded spatial profiles. Next, the study is extended to investigate propagation dynamics in the presence of nonlocal nonlinear effects generated in thermal interacting Rydberg atoms, which mainly reveals simultaneous competition between the nonlocal nonlinear absorption and the modulational instability for each wave component. Moreover, parity-time (PT) symmetric dynamics in cold Rydberg atoms are exploited, and it is shown that a phase transition from unbroken to broken PT symmetry can be induced by nonlocal nonlinear effects. At the quantum level, it is further proposed to test the quantum nonlocality of single x-ray photons in a system where very weak x-ray pulses interact with ^{57}Fe nuclei in a thin cavity, such that a Bell-like inequality in the single-photon version is violated. All these proposals are feasible in current experimental settings.

Within the framework of this thesis, the following articles were published in refereed journals:

- ***Control of beam propagation in optically written waveguides beyond the paraxial approximation***
  Lida Zhang (张理达), Tarak N. Dey, and Jörg Evers,
  Phys. Rev. A **87**, 043842 (2013).

- ***Optical cloning of arbitrary images beyond the diffraction limits***,
  Onkar N. Verma, Lida Zhang (张理达), Jörg Evers, and Tarak N. Dey
  Phys. Rev. A **88**, 013810 (2013).

- ***Diffractionless image propagation and frequency conversion via four-wave mixing exploiting the thermal motion of atoms***
  Lida Zhang (张理达) and Jörg Evers
  Phys. Rev. A **89**, 013817 (2014).

- ***Uniform phase modulation via control of refractive index in a thermal atom vapor with vanishing diffraction or absorption***
  Lida Zhang (张理达) and Jörg Evers
  Phys. Rev. A **90**, 023826 (2014).

Articles in preparation:

- ***Testing nonlocality of a single photon in the X-ray regime***
  Lida Zhang (张理达) and Jörg Evers

- ***Nonlocal nonlinear response of thermal Rydberg atoms***
  Lida Zhang (张理达) and Jörg Evers

- ***PT-symmetric dynamics in the presence of nonlocal nonlinearity induced in cold interacting Rydberg atoms***
  Lida Zhang (张理达) and Jörg Evers

Contents

1 Introduction **1**

2 Theoretical Background **7**
2.1 Wave equation in the paraxial regime 7
2.1.1 Maxwell's equations 7
2.1.2 Paraxial wave equation 8
2.1.3 Paraxial optics and the Schrödinger equation 11
2.2 Introduction to classical and quantum nonlocality 12
2.2.1 Classical nonlocal linear effects in paraxial optics 12
2.2.2 Classical nonlocal nonlinear effects and modulational instability . . 13
2.2.3 Quantum nonlocality 19
2.3 Optical Schrödinger equation in periodic system 24
2.3.1 Bloch theorem 24
2.3.2 Band structure in periodic system 26
2.3.3 Band structure in periodic system with nonlocal nonlinear effects . 28

3 Validity of the paraxial approximation **31**
3.1 Theoretical model 31
3.1.1 Equations of motion 31
3.1.2 Steady-state solution for the linear susceptibility 33
3.1.3 Realization of spatial waveguide-like structures 34
3.1.4 Incoherent pumping 35
3.2 Propagation dynamics within and beyond the paraxial approximation . . 36
3.2.1 Beam propagation in a single optically induced waveguide 36
3.2.2 Beam propagation in a branched waveguide structure 38
3.3 Conclusion 42

4 Control of light propagation via nonlocal linear effects **43**
4.1 Diffractionless and lossless light propagation in thermal atomic vapor . . . 43
4.1.1 Motivation 43
4.1.2 Theoretical description of thermal atoms 45
4.1.3 Laser beam propagation with arbitrary spatial profiles 50
4.1.4 Discussions 55
4.2 Uniform phase modulation with vanishing diffraction or absorption 57
4.2.1 Motivation 57
4.2.2 Phase modulation for laser beams with arbitrary spatial profiles . 58
4.2.3 Spatial uniformity of the phase modulation 62
4.2.4 Discussions 63
4.3 Diffractionless image reproduction and frequency conversion 64
4.3.1 Motivation 64
4.3.2 The four-wave mixing process in thermal atoms 65
4.3.3 Image reproduction and frequency conversion 70

4.3.4 Discussions . . . 78
4.4 Conclusions . . . 80

5 Propagation dynamics in the presence of nonlocal nonlinear effects 81
5.1 Nonlocal nonlinear effects in thermal interacting Rydberg atoms . . . 81
5.1.1 Introduction to Rydberg atoms . . . 81
5.1.2 Theoretical model for thermal Rydberg atoms . . . 83
5.1.3 Propagation dynamics in thermal interacting Rydberg atoms . . . 90
5.1.4 Discussions . . . 99
5.2 Parity-time symmetric dynamics in cold interacting Rydberg atoms . . . 100
5.2.1 Introduction to Parity-time symmetry . . . 100
5.2.2 Optical periodic potential respecting parity-time symmetry . . . 102
5.2.3 Band structure of the optical system . . . 107
5.2.4 Phase transition from unbroken to broken PT-symmetry . . . 109
5.2.5 Broken or unbroken PT-symmetric propagation dynamics . . . 110
5.2.6 Discussions . . . 113
5.3 Conclusions . . . 114

6 Quantum nonlocality of a single photon in the x-ray regime 115
6.1 Introduction to quantum nonlocality of a single photon . . . 115
6.2 Modeling weak x-ray pulses interacting with the thin cavity . . . 116
6.2.1 The weak x-ray source . . . 118
6.2.2 The mode-entangled state of the x-ray photon . . . 118
6.3 Derivation of the locality criterion in a Mach-Zehnder interferometer . . . 118
6.4 Quantum nonlocality of a single x-ray photon . . . 122
6.4.1 Theoretical demonstration . . . 122
6.4.2 Experimental implementations . . . 122
6.5 Conclusions . . . 124

7 Summary and outlook 125

Bibliography 129

Chapter 1

Introduction

Where there is a wish, there is a way. Where there is a way, there is always light shining to the future. In every aspect of life, light has been a silent but bright and colorful companion guiding us to warmness and hope. From ancient uncivilized age to high technology-armed modern times, light has been one of the most common and significant ways to deliver information and communicate with each other for human beings. It is thus not surprising that people have been trying for centuries to pursuit a fundamental understanding of the physical nature of light. In the long history of study of light, there were two outstanding views representing the great power of our perception of nature in the poor background of empirical knowledge gained from light phenomena in the seventeenth century. One of these is the corpuscular theory of light proposed by Issac Newton [1] based on his unprecedented discovery of the three universal laws of motion which form the backbone of classical mechanics. In this model, light was described to be a series of corpuscular particles that have well-defined masses and positions in space and obey the laws of motion that he discovered. However, in a second theory of light developed by Christiaan Huygens [1], it was argued that light behaves as waves having specific frequencies, amplitudes and phases, which are capable of explaining interference and polarization of light. Instead of giving a comprehensive overview of these two theories and their further developments in the following time which has already well-known to everyone in the physical community, we emphasize here their physical consequences and connections to modern physics, in which the new physical pictures of light are deeply bonded to its two classical views developed at the seventeenth century.

Following the wave nature of light, it is eventually revealed by Maxwell's equations [1] that light is nothing but a peculiar type of electromagnetic wave phenomena in the late nineteenth century. From Maxwell's equations, there is no theoretical constraint for the energy contained in the light which is defined by its evolving electric and magnetic fields. In fact, any amount of energy is possible and can be infinitely small from the wave view of light. On the other side, at the beginning of the twentieth century, Max Planck has made the assumption that the energy of light has a minimal bound and is discretized, in order to correctly interpret the spectrum of blackbody radiation. The light with this minimal amount of energy is termed as a "quanta", and any other possible energy of light can only be multiples of this quanta. Here, a light quanta, which is called "photon" in modern times, differs from the classical particle view of light in the sense that a quanta of light is defined by its energy scale while a particle is defined by its mass and position. Apparently, the two basic modern views of light, which is now called "wave-particle duality", essentially repels each other and cannot be combined into a unified picture in the classical fashion. The relations between these two mutually exclusive properties of light, which has been generalized as "complementarity" by Nils Bohr [2], lies in the heart of quantum mechanics. Based on the particle-like nature of light, Albert Einstein [2] conceived the idea of stimulated emission of light quanta in quantum radiation processes which finally gives birth to the great invention of light amplification

by stimulated emission of radiation, i.e., the laser, after a series of elegant theoretical and experimental works. Amazingly, the laser light consisting of a bunch of highly correlated light quanta in a quantum point of view behaves as a coherent electromagnetic wave and is well described by Maxwell's equations.

The wave-particle duality, which is closely related to the uncertainty principle [3], has been one of the backbones of quantum mechanics. As somehow conflicting with the wave-particle duality, there are two other equally important and fundamental concepts derived from classical mechanics, i.e., "locality" and "reality". In retrospect, inspired by the famous gedankenexperiment that a propagating light wave will not stand still even when being observed in a moving frame of reference with the speed of light, Albert Einstein [4] noticed a direct contradiction between Maxwell's equations and the Galilean transformation which defines the space-time transform in different inertial reference frames based on the reasoning that the physical laws should have the identical mathematical forms in any inertial frames. This leads to his special relativity in which light is assumed to have a unique property of maximal speed that is constant in any possible inertial frame. Surprisingly, this bold assumption has been favored by all performed experiments at various situations, and there is no evidence against this assumption until now. Extended from the special relativity, it is certain that any interacting process should not be faster than the speed of light, alternatively, an event cannot be simultaneously influenced by another remote event, i.e., "*no action at a distance*", it nowadays refers to the concept of locality. A few examples exhibiting nonlocal effects include Aharonov-Bohm effect [5, 6], quantum entanglement [7], measurement processes [7], etc.. Another belief conceived from classical mechanics and pointed out by Einstein, Podolsky, and Rosen (EPR) is the concept of reality in the famous paper [8] in 1935. It is argued that a physical reality should be related to a physical quantity, and a correct and complete theory should be able to predict deterministically the value of the physical quantity without performing any kind of experiential measurements. In common sense, reality means that every physical object's properties must have precise pre-existing values, which can be certainly derived from the correct theory and does not depend on being measured. The combination of locality and reality refers to "*local realism*" which is obeyed by classical mechanics, but conflicts with quantum theory.

Since the invention of laser, great effects have been devoted to the studies in the realm of light-matter interaction, in particular, laser-atom interaction. The evident reason appears to be that the absence of phonon coupling such as rotations, thermal or lattice vibrations in laser-atom interaction processes remarkably simplifies both the theoretical considerations and experimental implementations but remains the essential physical dynamics. The presence of laser has flourished a variety of fields ranging from nonlinear to quantum optics, with exciting discoveries of new phenomena including sum- and difference frequency generation [9–11], four-wave mixing [9–11], femtosecond optical frequency comb [12], attosecond physics [13], electromagnetically induced transparency [7, 14], Bose-Einstein condensates and matter waves [15, 16], quantum entanglement [17, 18], and cavity optomechanics [19], to mention a few. In return, it has enhanced considerably the ability to control light at either the classical or the quantum level at man's will, and has promoted great progresses in a variety of fields including not only physics, but also chemistry, biology and information technologies. Especially, in our current information age, it is hard to imagine what our lives would be without optical communication. Ultrafast and large-capacity optical data transmission via laser pulses propagating in optical fibers has been one of the indispensable components of the infrastructure for the current world-wide networking. The even more ambitious dream is to promote ourselves

to the quantum information world, where information processing is dramatically faster and more reliable.

It is fair to say that entering into the next-generation all-optical quantum information world does not only rely on fresh applications on control and manipulation of light waves, but also prompt for a broader and deeper understanding of the properties of a single photon at a fundamental level. In these directions, a particularly interesting and important topic is the nonlocal effects on the propagation dynamics of either classical or quantum light [8, 20–34]. The intent of this thesis responds closely to these two aspects with new insights in the regime beyond locality. The first and main part of the thesis is devoted to the studies of coherent control of classical laser light propagation via nonlocal linear or nonlinear effects induced by laser-atom interactions. Here, the nonlocal effects mean that the laser field propagating in the atomic ensemble at one point can be simultaneously affected by itself at other points owing to the interaction with atoms. The second part addresses the intrinsic nature of a single photon, where the quantum nonlocality of a single x-ray photon is examined. The quantum nonlocality here refers to the violation of local realism in entangled quantum parties, which will be elaborated later.

We start with presenting the necessary theoretical background for the whole thesis in **Chapter 2**. Since on the one hand, light propagation in the paraxial regime has already been able to describe a great deal of striking optical phenomena, for example, optical spatial solitons [10, 35], modulational instability [10, 36–39], etc.; On the other hand, owing to the mathematical equivalence between the paraxial wave equation and the Schrödinger equation, paraxial optics has served as a playground for testing physical mechanisms developed in quantum mechanics such as transverse Anderson localization of light [40–45], photonic Floquet topological insulator [46–50], superfluid motion of light [51, 52], and parity-time reflection symmetry [53–64]. We therefore limit ourselves to focus on the classical light propagation in the paraxial regime. The deduction of the paraxial wave equation from Maxwell's equations is firstly given in Sec. 2.1, under the paraxial approximation which states that the laser field varies much slower in the propagation direction than in the transverse plane. We then introduce the physical meaning of nonlocal effects and its possible consequences for both classical and quantum settings in Sec. 2.2. Sec. 2.3 shows the general procedures to calculate the band structure for the optical Schrödinger equation when an optical periodic potential is introduced.

Before we further investigate the paraxial propagation dynamics in various systems exhibiting nonlocal linear or nonlinear effects, in the following **Chapter 3**, we examine the validity of the paraxial approximation by studying beam propagation in an optically written waveguide structure. The waveguide structure, which is in terms of spatial-varied reflective index and leads to diffractionless light propagation, is imprinted on a five-level atomic medium driven by spatially dependent laser fields. We then first study the probe beam propagation in a single optically written waveguide, and already find that the paraxial approximation does not provide an accurate description of the probe propagation, given that the beam size is not large enough compared to its wavelength. Furthermore, beam propagation dynamics is carefully investigated beyond paraxial propagation through an induced branched-waveguide structure which allows selective steering of the probe beam into different branches.

After the careful check of validity of the paraxial approximation, we focus on the coherent control and manipulation of classical light propagation by nonlocal linear effects in thermal atomic vapor in **Chapter 4**. It has been theoretically proposed and experientially verified by Firstenberg *et al.* [20–24] that thermal motion and collisions in

a three-level lambda atomic vapor under the electromagnetically induced transparency configuration can give rise to a specific type of nonlocal linear effects in the regime of Dicke narrowing. This nonlocal linear effects are found to be able to exactly eliminate the paraxial diffraction of laser beams with arbitrary spatial profiles under the specific condition of negative two-photon detuning. However, strong inevitable absorption involved in this initially proposed mechanism owing to the required two-photon detuning leads to severe attenuation of the input probe beam, rendering it useless for practical application. In the first section of this chapter, we first propose an enhanced scheme in which arbitrary images encoded onto a probe field can propagate without either diffraction or absorption. This is done by simply applying an additional two-way incoherent pump field to couple another transition in a four-level double-lambda atomic system. The absorption can be compensated by the atomic coherences generated by the incoherent pump together with the coherent laser fields, meanwhile, the dispersion still behaves to cancel the paraxial diffraction except for a different constant offset. Consequently, the probe field can propagate in the prepared thermal medium with neither diffraction nor absorption.

Next, in the second section of **Chapter 4**, we then find that the constant offset in the linear dispersion can be utilized to apply an uniform π phase modulation to the probe beam while its other physical properties are fairly preserved. This uniform π phase modulation can be accomplished at a quite low atomic density and over a rather short distance which is much less than one Rayleigh length, and is independent of the probe field intensity. Again, it is suitable for the probe fields with arbitrary spatial profiles.

In the last section of **Chapter 4**, based on the knowledge gained from the previous proposals to realize diffractionless and lossless light propagation and uniform phase modulation, we extend our study to diffractionless image reproduction and frequency conversion based on four-wave mixing (FWM) in a thermal five-level triple-lambda atomic vapor driven by laser fields. The generated FWM signal field has a different frequency but the same spatial distribution as compared to the probe field. This method is capable of transmitting and frequency-converting arbitrary two-dimensional images without either diffraction or absorption, requiring only short propagation distance of less than one Rayleigh length. These proposals are feasible to be implemented in current experimental setups. And it also sheds light on all-optical processing in which diffraction lies in the way as one of the major obstacles.

We then turn to the investigation of light propagation dynamics in the presence of nonlocal nonlinear effects introduced by dipole-dipole interactions in Rydberg atoms. The availability of strong long-range interactions in cold Rydberg atoms has shown the powerful capabilities in illustrating local or nonlocal nonlinear effects [25, 26, 65–69], Rydberg blockade [70–72], and has enabled promising applications in quantum information processing [73, 74]. Theoretical models to describe the cold interacting Rydberg atoms have also been developed, such as the mean-field theory [75–78], cluster expansion [25, 79, 80], and the rate equation model [69, 81–84].

At the same time when exceptional advances have been made in ultracold Rydberg atoms, there have been experiments conducted in the thermal Rydberg atoms [85–92], showing evidences for coherent long-range dipole-dipole interactions. However, the theoretical models mentioned above seem to fail in describing the involved dynamics. With the input from the theoretical modeling of the thermal atoms in **Chapter 4**, we develop a novel approach in the first section of **Chapter 5** to describe the thermal Rydberg atoms interacting with external laser fields. Under the crucial approximation that the time variation in the dipole-dipole interactions due to atomic motion can be neglected,

an analytical form can be obtained for the nonlocal nonlinear atomic response of the thermal Rydberg atoms. Based on this analytical result, we find the propagation dynamics in the near-resonant regime differs qualitatively from that in far-detuned regime. In the near-resonant regime, the nonlinear absorption plays the dominant role in the probe propagation and is weakened as the temperature increases. However, when the laser fields are far-off resonant, the propagation dynamics is governed by both the nonlocal nonlinear dispersion and absorption. Furthermore, the nonlocal nonlinear dispersion remains almost unchanged while the nonlocal nonlinear absorption is firstly enhanced and then weakened as the temperature grows. Consequently, modulational instability (MI) is initially suppressed and then strengthened with increasing temperature. In sharp contrast to a nonlinear medium which is purely dispersive, counterintuitively, we find that in absorptive nonlinear medium each wave component will exhibit the MI effect, which, however, simultaneously competes with the nonlocal nonlinear absorption, and eventually is suppressed.

In the second section of **Chapter 5**, stimulated by the mathematical equivalence between the paraxial wave equation and the Schödinger equation, we explore in the cold interacting Rydberg atoms the concept of parity-time (PT) reflection symmetry developed in quantum mechanics which can lead to real eigenvalues despite of its non-Hermitian nature. By employing two different physical mechanisms, i.e., active Raman gain and electromagnetically induced transparency in two different atomic species interacting with standing-wave laser fields, a linear optical periodic potential is formed to respect PT symmetry. When the amplitude of the imaginary part of the linear optical potential is small, it is found that the resulting band structure can be completely real, referring to an unbroken PT symmetry. As this amplitude exceeds a certain value, a phase transition occurs, and complex conjugate eigenvalue pairs appear in the band structure, corresponding to a broken PT symmetry. The presence of nonlinear nonlocal effects due to the Rydberg-Rydberg interaction can break not only the PT symmetry of the system but also the symmetry of the band structure. The phase transition from unbroken to broken PT symmetry is put forward further by studying the corresponding propagation dynamics.

In the end, we study in **Chapter 6** the quantum nonlocality of a single photon. In particular, we focus on the nonlocal nature of a single photon in the x-ray regime. Quantum nonlocality originates from the famous argument by Einstein, Podolsky, and Rosen in 1935 that non-commutable quantities (e.g., position and momentum) can have simultaneous values in a quantum correlated system, under the assumption of local realism [8]. Almost thirty years later, Bell provided a theoretical proof [28] in 1964 that a direct contradiction raises between quantum physics and the EPR assumptions of local realism in an entangled bipartite system, and it has been respected by all reliable experiments done so far. Until now, there is little doubt about the quantum nonlocality between entangled bipartite systems [29–34], and further researches have also been stimulated to study nonlocality beyond quantum theory [93–96] and to search certain fundamental physical principles to re-construct the quantum theory [97–99]. However, unlike the nonlocality of correlated bipartite system that have been widely accepted, the nonlocality of a single party has lead to intensive debates [100–106]. In this chapter, we start with first presenting a general historic overview of quantum nonlocality of a single photon. Based on the recently developed theory [107] and followed experiments [108, 109] where the weak x-ray pulses with energy centered at 14.4 keV interact with ^{57}Fe nuclei embedded in a thin cavity, we theoretically propose a scheme to test the nonlocality of a single photon in the x-ray regime. The x-ray pulses emitted from a synchrotron radiation source are

so weak that they can only excite one of the nuclei at a time and can thus be considered as single resonant photons. We find that the x-ray pulses interacting with the cavity and the embedded ^{57}Fe nuclei can be treated as a Mach-Zehnder interferometer, in which one mode of path is the empty cavity and the other one is the combination of the nuclei and the cavity, leading to the entangled states between the two modes for the single x-ray photons. Analogous to a Mach-Zehnder interferometer with phase shifters inserted in the two arms, we then deduce the locality criterion for the x-ray photons in the system. In the end, we find that this locality criterion can be violated at specific incident angles and detunings of the x-ray pulses impinging on the cavity, indicating the nonlocality of x-ray photons. We have also discussed the possible experimental procedures to test the proposal in current experiments.

In the final **Chapter 7**, the thesis is ended by a brief summary, and an outlook on possible further directions is also given based on the results presented in the thesis.

In a nutshell, we study nonlocal effects on both classical and quantum light. At the classical level, it is found that diffrectionless and lossless light propagation, uniform phase modulation, and frequency conversion with preserved image duplication for laser beams with arbitrary spatial profiles can be achieved by utilizing nonlocal linear effects induced in thermal atomic vapor. This may lead to promising applications for all-optical processing. Furthermore, we study light propagation dynamics in the presence of nonlocal nonlinear effects in interacting Rydberg atoms. Specifically, we propose a model to describe thermal Rydberg atoms interacting with laser fields and find counterintuitive behaviors for the probe propagation with respect to that in ultracold Rydberg atoms. We then explore to investigate PT-symmetric dynamics in cold Rydberg atoms, and it is shown that phase transition from unbroken to broken PT-symmetry can be induced by nonlocal nonlinear effects. At the quantum level, we propose a scheme to test the quantum nonlocality of a single x-ray photon in the system of very weak x-ray pulses interacting with ^{57}Fe nuclei embedding thin cavity. This may deepen our understanding of the fundamental nature of a single photon.

Chapter 2

Theoretical Background

In this chapter, we briefly introduce the theoretical background to which the whole thesis is rooted. Throughout the whole thesis, we concentrate on the coherent control and manipulation of classical or quantum light via nonlocal effects. Classical light, as an electromagnetic field, is governed by Maxwell's equations. Since in the thesis we are mostly dealing with light propagation in the paraxial regime, the paraxial wave equation is firstly derived from Maxwell's equations in Sec. 2.1.2. Owing to the mathematical isomorphism between the paraxial wave and Schrödinger equation, a further general comparison between them is presented in Sec. 2.1.3 to show the power of paraxial optics. Next, we introduce the concept of nonlocality and its physical consequences for both classical and quantum light in Sec. 2.2. Based on the close connection between paraxial optics and the Schrödinger equation, procedures to calculate the band structure in an optical periodic system with or without nonlocal effects are given in Sec. 2.3 by exploiting the Bloch theorem.

2.1 Wave equation in the paraxial regime

2.1.1 Maxwell's equations

The laws for electromagnetic phenomena are described by Maxwell's equations in the form[1],

$$\nabla \cdot \mathbf{D} = \rho \,, \tag{2.1a}$$

$$\nabla \times \mathbf{E} = -\frac{\partial \mathbf{B}}{\partial t} \,, \tag{2.1b}$$

$$\nabla \cdot \mathbf{B} = 0 \,, \tag{2.1c}$$

$$\nabla \times \mathbf{H} = \mathbf{J} + \frac{\partial \mathbf{D}}{\partial t} \,, \tag{2.1d}$$

where $\mathbf{D}, \rho, \mathbf{E}, \mathbf{B}, \mathbf{H}$, and $\mathbf{J}$ stand for displacement current, total charge density, electric field, magnetic field, magnetic field strength and current density respectively. Those quantities are related by the material equations

$$\mathbf{D} = \varepsilon_0 \mathbf{E} + \mathbf{P} \,, \tag{2.2a}$$

$$\mathbf{B} = \mu_0 \mathbf{H} + \mathbf{M} \,, \tag{2.2b}$$

$$\mathbf{J} = \sigma \mathbf{E} \,, \tag{2.2c}$$

with ε_0, μ_0 being the permittivity and permeability of free space, and $\mathbf{P}, \mathbf{M}$ and σ being the macroscopic polarization and magnetization, and conductivity of the medium

[1] The International System of Units (SI) is used for all equations, physical quantities, functions, and parameters throughout this thesis.

respectively. We are interested in the medium that contains no free charges, so that

$$\rho = 0\,, \tag{2.3}$$

and that contains no free current, i.e.,

$$\mathbf{J} = 0\,, \tag{2.4}$$

we also assume that the medium is nonmagnetic such that

$$\mathbf{M} = 0\,. \tag{2.5}$$

We can then derive the equation of motion for the electric field from Eq. (2.1) and (2.2), which yields

$$\nabla \times \nabla \times \mathbf{E} + \frac{1}{c^2}\frac{\partial^2 \mathbf{E}}{\partial t^2} = -\mu_0 \frac{\partial^2 \mathbf{P}}{\partial t^2}\,, \tag{2.6}$$

where we have applied the relation $\varepsilon_0\mu_0 = 1/c^2$ with c being the speed of light in vacuum. Eq. (2.6) is one of the most general forms of wave equation to characterize its propagation in diverse media. Owing to the second-order curl and time derivative involved in Eq. (2.6), an analytical solution is usually unachievable. An alternative direction is to make use of numerical calculations by taking advantage of present high-performance computing technology, which has already become to be difficult and time-consuming for large-dimension systems. Fortunately, the wave equation can be further simplified by a series of approximations in most cases of interest. Before doing this, we first take the vector calculus in Eq. (2.6)

$$\nabla \times \nabla \times \mathbf{E} = \nabla(\nabla \cdot \mathbf{E}) - \nabla^2 \mathbf{E}\,. \tag{2.7}$$

In the linear optics of isotropic media with $\rho = 0$, the term containing $\nabla \cdot \mathbf{E}$ vanishes because of $\nabla \cdot \mathbf{D} = 0$ in Eq. (2.1a). In anisotropic media where $\mathbf{D} = \varepsilon_0 \varepsilon(\mathbf{r})\mathbf{E}$, $\nabla \cdot \mathbf{E}$ needs to be further identified. Furthermore, this term is generally nonzero in nonlinear optics even for isotropic materials, as a result of the relation (2.2a). Fortunately, this term can often be shown to be too small to be taken into account, especially in the case that the slowly varying envelope approximation (SVEA) is valid [10], which is also the regime considered in this thesis. We shall then assume that the contribution of $\nabla(\nabla \cdot \mathbf{E})$ is negligible and can be reasonably dropped, eventually the wave equation simplifies to

$$\nabla^2 \mathbf{E} - \frac{1}{c^2}\frac{\partial^2 \mathbf{E}}{\partial t^2} = \mu_0 \frac{\partial^2 \mathbf{P}}{\partial t^2}\,. \tag{2.8}$$

2.1.2 Paraxial wave equation

Usually, it remains still quite challenging to solve Eq. (2.8) either analytically or numerically, in order to obtain the complete knowledge of classical light propagation. Furthermore, it is not necessary to directly solve Eq. (2.8) in most cases, further simplifications of Eq. (2.8) are possible and reasonable under certain approximations, among which one of the most known examples is the paraxial approximation. Before diving into studying the paraxial approximation and understanding its physical consequence, we shall first suppose that the electric field $\mathbf{E}$ and the macroscopic polarization $\mathbf{P}$ are given by

$$\mathbf{E} = \frac{1}{2}E(\mathbf{r},t)e^{-i(\omega_0 t-\mathbf{k}_0\cdot\mathbf{r})}\hat{\mathbf{e}}_E + c.c.\,, \tag{2.9a}$$

$$\mathbf{P} = \frac{1}{2}P(\mathbf{r},t)e^{-i(\omega_0 t-\mathbf{k}_0\cdot\mathbf{r})}\hat{\mathbf{e}}_P + c.c.\,, \tag{2.9b}$$

where $E(\mathbf{r},t)$ and $P(\mathbf{r},t)$ are slowly-varying amplitudes of the positive-frequency part of the electric field and polarization, respectively, with $\hat{\mathbf{e}}_E$ and $\hat{\mathbf{e}}_P$ being the corresponding unit polarization vectors, and ω_0 and $\mathbf{k}_0$ are the carrier frequency and wavevector, respectively. "*c.c.*" is the abbreviation for "complex conjugate" which denotes the negative-frequency part. Then the second-order derivatives in Eq.(2.8) can be calculated

$$\frac{\partial^2\mathbf{E}}{\partial t^2} = \frac{1}{2}\left[\frac{\partial^2 E(\mathbf{r},t)}{\partial t^2} - 2i\omega_0\frac{\partial E(\mathbf{r},t)}{\partial t} - \omega_0^2 E(\mathbf{r},t)\right]e^{-i(\omega_0 t-\mathbf{k}_0\cdot\mathbf{r})}\hat{\mathbf{e}}_E + c.c.\,, \tag{2.10a}$$

$$\nabla^2\mathbf{E} = \frac{1}{2}\left[\nabla^2 E(\mathbf{r},t) + 2i\mathbf{k}_0\cdot\frac{\partial E(\mathbf{r},t)}{\partial\mathbf{r}} - \mathrm{k}_0^2 E(\mathbf{r},t)\right]e^{-i(\omega_0 t-\mathbf{k}_0\cdot\mathbf{r})}\hat{\mathbf{e}}_E + c.c.\,, \tag{2.10b}$$

$$\frac{\partial^2\mathbf{P}}{\partial t^2} = \frac{1}{2}\left[\frac{\partial^2 P(\mathbf{r},t)}{\partial t^2} - 2i\omega_0\frac{\partial P(\mathbf{r},t)}{\partial t} - \omega_0^2 P(\mathbf{r},t)\right]e^{-i(\omega_0 t-\mathbf{k}_0\cdot\mathbf{r})}\hat{\mathbf{e}}_P + c.c.\,. \tag{2.10c}$$

Substituting Eq. (2.10) back into Eq. (2.8) and then considering the equation of motion for the positive-frequency part leads to

$$\begin{aligned}&\nabla^2 E(\mathbf{r},t) + 2i\mathbf{k}_0\cdot\frac{\partial E(\mathbf{r},t)}{\partial\mathbf{r}} - \frac{1}{c^2}\left[\frac{\partial^2 E(\mathbf{r},t)}{\partial t^2} - 2i\omega_0\frac{\partial E(\mathbf{r},t)}{\partial t}\right]\\ &= \mu_0\left[\frac{\partial^2 P(\mathbf{r},t)}{\partial t^2} - 2i\omega_0\frac{\partial P(\mathbf{r},t)}{\partial t} - \omega_0^2 P(\mathbf{r},t)\right]\hat{\mathbf{e}}_E\cdot\hat{\mathbf{e}}_P\,,\end{aligned} \tag{2.11}$$

where we have applied the relation $\omega_0^2 = c^2\mathrm{k}_0^2$. The equation of motion for the negative-frequency part can be found by simply taking the complex conjugate of Eq. (2.11). In the slowly varying envelope approximation, the changes in the amplitude $E(\mathbf{r},t)$ of the electric field $\mathbf{E}$ is much slower than its frequency

$$\left|\frac{\partial E}{\partial t}\right| \ll \left|i\omega_0 E\right|. \tag{2.12}$$

Then, Eq. (2.11) can be simplified to

$$\left[\hat{\mathbf{e}}_{\mathrm{k}_0}\cdot\frac{\partial}{\partial\mathbf{r}} + \frac{1}{c}\frac{\partial}{\partial t} - \frac{i}{2\mathrm{k}_0}\frac{\partial^2}{\partial\mathbf{r}^2}\right]E(\mathbf{r},t) = i\frac{\mathrm{k}_0}{2\varepsilon_0}P(\mathbf{r},t)\hat{\mathbf{e}}_E\cdot\hat{\mathbf{e}}_P\,, \tag{2.13}$$

where we have set $\mathbf{k}_0 = \mathrm{k}_0\hat{\mathbf{e}}_{\mathrm{k}_0}$. Normally, Eq. (2.13) is already enough to describe the wave propagation in various situations. In the case that the medium is an ensemble of atoms, the macroscopic polarization can be written as a summation over contributions of all individual atoms

$$\mathbf{P} = \frac{\sum_i\langle\hat{\mathbf{d}}_i\rangle}{V}\,, \tag{2.14}$$

where $\hat{\mathbf{d}}_i$ is the dipole moment operator of atom i and V is the volume of the ensemble, and "$\langle\cdots\rangle$" denotes the expectation value. It can be further rewritten in terms of density

matrix elements

$$\mathbf{P} = n_0 \mathrm{Tr}(\hat{\mathbf{d}}\rho)\,, \tag{2.15}$$

where n_0 is the atomic density, ρ is the density matrix of an individual atom which obeys the master equation

$$\frac{d\rho}{dt} = -\frac{i}{\hbar}[H,\rho] - L\rho\,. \tag{2.16}$$

Here H is the Hamiltonian of the system and $L\rho$ stands for the incoherent contributions including, for instance, spontaneous decay, dephasing and other dissipative processes. Then by solving the coupled master and wave equations, the propagation dynamics can be obtained. In general, the macroscopic polarization can be written in the form

$$\mathbf{P} = n_0 \mathbf{d}\rho_{ab} e^{-i(\omega_0 t - \mathbf{k}_0\cdot\mathbf{r})} + c.c.\,, \tag{2.17}$$

with $\mathbf{d}$ being the dipole moment and ρ_{ab} representing the slowly varying amplitude of the density matrix element related to $\mathbf{P}$. a and b denote the upper and lower states for the transition coupled by the electric field $\mathbf{E}$, respectively. By comparing Eq. (2.9b) and (2.17), we find that

$$P(\mathbf{r},t) = 2n_0\rho_{ab}\mathbf{d}\cdot\hat{\mathbf{e}}_P\,. \tag{2.18}$$

Substituting Eq. (2.18) back into Eq. (2.13) results in

$$\left[\hat{\mathbf{e}}_{\mathrm{k}_0}\cdot\frac{\partial}{\partial\mathbf{r}} + \frac{1}{c}\frac{\partial}{\partial t} - \frac{i}{2\mathrm{k}_0}\frac{\partial^2}{\partial\mathbf{r}^2}\right]E(\mathbf{r},t) = i\frac{\mathrm{k}_0}{\varepsilon_0}n_0\rho_{ab}\mathbf{d}\cdot\hat{\mathbf{e}}_E\,. \tag{2.19}$$

In quantum optics, we concern more about the Rabi frequency of the electric field which is defined here by

$$\Omega(\mathbf{r},t) = \frac{E(\mathbf{r},t)\mathbf{d}\cdot\hat{\mathbf{e}}_E}{2\hbar}\,, \tag{2.20}$$

Note that there is also another definition widely used in literatures which is $\Omega'(\mathbf{r},t) = 2\Omega(\mathbf{r},t)$, here we stick to the definition given in Eq. (2.20) throughout the thesis. Then the wave equation for the Rabi frequency yields

$$\left[\hat{\mathbf{e}}_{\mathrm{k}_0}\cdot\frac{\partial}{\partial\mathbf{r}} + \frac{1}{c}\frac{\partial}{\partial t} - \frac{i}{2\mathrm{k}_0}\frac{\partial^2}{\partial\mathbf{r}^2}\right]\Omega(\mathbf{r},t) = i\frac{n_0|\mathrm{d}|^2\mathrm{k}_0}{2\varepsilon_0\hbar}\rho_{ab}\,. \tag{2.21}$$

From the Weisskopf-Wigner theory of spontaneous emission for a two-level atom in free space [7], we find that

$$|\mathrm{d}|^2 = \frac{3\varepsilon_0\hbar\lambda^3\Gamma_{ab}}{8\pi^2}\,, \tag{2.22}$$

where $\lambda = 2\pi/\mathrm{k}_0$ and Γ_{ab} is the corresponding spontaneous decay rate. With the help of Eq. (2.22), the wave equation is reduced to

$$\left[\hat{\mathbf{e}}_{\mathrm{k}_0}\cdot\frac{\partial}{\partial\mathbf{r}} + \frac{1}{c}\frac{\partial}{\partial t} - \frac{i}{2\mathrm{k}_0}\frac{\partial^2}{\partial\mathbf{r}^2}\right]\Omega(\mathbf{r},t) = i\frac{3n_0\lambda^2\Gamma_{ab}}{8\pi}\rho_{ab}\,. \tag{2.23}$$

When the involved electric field is a continuous wave, i.e., $E(\mathbf{r},t) = E(\mathbf{r})$, the time derivative in Eq. (2.23) can be removed, yielding

$$\left[\frac{\partial}{\partial z} - \frac{i}{2\mathrm{k}_0}\frac{\partial^2}{\partial \mathbf{r}^2}\right]\Omega(\mathbf{r}) = i\frac{3n_0\lambda^2\Gamma_{ab}}{8\pi}\rho_{ab}\,. \tag{2.24}$$

In Eq. (2.24), we have assumed that the electric field is propagating in the z direction $\hat{\mathbf{e}}_{\mathrm{k}_0} = \hat{\mathbf{e}}_{\mathrm{z}}$. More generally, it can be in any other direction $\hat{\mathbf{e}}_{\mathrm{k}_0} = \sin\theta\cos\varphi\hat{\mathbf{e}}_{\mathrm{x}} + \sin\theta\sin\varphi\hat{\mathbf{e}}_{\mathrm{y}} + \cos\theta\hat{\mathbf{e}}_{\mathrm{z}}$ with θ and φ being the polar and azimuthal angles respectively. When the electric field varies only gradually along the propagating direction, z, the so called paraxial approximation can be formulated as

$$\left|\frac{\partial^2}{\partial \mathrm{z}^2}\right| \ll \left|\frac{\partial^2}{\partial \mathrm{x}^2}\right|, \left|\frac{\partial^2}{\partial \mathrm{y}^2}\right|, \left|2\mathrm{k}_0\frac{\partial}{\partial \mathrm{z}}\right|. \tag{2.25}$$

Then, Eq. (2.24) takes the form

$$\left[\frac{\partial}{\partial z} - \frac{i}{2\mathrm{k}_0}\frac{\partial^2}{\partial \mathbf{r}_\perp^2}\right]\Omega(\mathbf{r}) = i\frac{3n_0\lambda^2\Gamma_{ab}}{8\pi}\rho_{ab}\,, \tag{2.26}$$

Eq. (2.26) is the wave equation describing wave dynamics in atomic media in the paraxial regime. In Eq. (2.26), the second-order derivative in the transverse direction gives rise to diffraction, which would lead to spatial spreading, energy attenuation, and distortion of the electric field. Hence, in general, diffraction is detrimental to the involved dynamics. Depending on specific properties of the macroscopic polarization of the medium, $\mathbf{P}$, a variety of intriguing phenomena can already be found in the paraxial regime, including diffractionless propagation, self-focusing and -defocusing, spatial solitons and modulational instability [9, 10], to mention a few. Furthermore, owing to the mathematical equivalence between the paraxial wave equation and the Schrödinger equation, paraxial optics has also been employed as a testbed for studying fundamental aspects of quantum theory and newly developed concepts in condensed matter physics [42–50, 110–120].

2.1.3 Paraxial optics and the Schrödinger equation

By employing the relation between the polarization and the electric field

$$P(\mathbf{r},t) = \varepsilon_0\chi(\mathbf{r})E(\mathbf{r},t)\,, \tag{2.27}$$

where $\chi(\mathbf{r})$ is the medium susceptibility given by

$$\chi(\mathbf{r}) = \frac{n_0|\mathrm{d}|^2\rho_{ab}}{\varepsilon_0\hbar\Omega(\mathbf{r})}\,, \tag{2.28}$$

we note that the paraxial equation can have a different form

$$\left[\frac{\partial}{\partial z} - \frac{i}{2\mathrm{k}_0}\frac{\partial^2}{\partial \mathbf{r}_\perp^2}\right]\Omega(\mathbf{r}) = i\frac{\mathrm{k}_0}{2}\chi(\mathbf{r})\Omega(\mathbf{r})\,. \tag{2.29}$$

Multiplying both sides by the imaginary unit i yields

$$i\frac{\partial\Omega(\mathbf{r})}{\partial z} = -\frac{1}{2\mathrm{k}_0}\frac{\partial^2}{\partial \mathbf{r}_\perp^2}\Omega(\mathbf{r}) - \frac{\mathrm{k}_0}{2}\chi(\mathbf{r})\Omega(\mathbf{r})\,. \tag{2.30}$$

One can then find that Eq. (2.30) is exactly identical to the mathematical form of the Schrödinger equation describing the time evolution of a massive particle in two dimensions by replacing $z \to t$, while the optical effective mass and potential are defined to be

$$m_{opt} = \hbar \mathrm{k}_0 \,, \tag{2.31a}$$

$$V_{opt}(\mathbf{r}) = -\frac{\hbar \mathrm{k}_0}{2} \chi(\mathbf{r}) \,. \tag{2.31b}$$

Eq. (2.30) is thus called the optical Schröndinger equation. Rising from this fabulous resemblance, it is then not surprising that physical concepts developed in quantum physics such as Bloch oscillation, Bragg scattering, have been migrated to and studied in paraxial optics, and have already been experimentally verified in optical systems [121–126]. Moreover, exciting achievements have also been demonstrated recently in realizing transverse Anderson localization of light [40–45], photonic Floquet topological insulator [46–50], and superfluid motion of light [51, 52], which might be difficult to be observed in condensed matter physics because of lattice defects or thermal fluctuations.

In particular, new developments have been put forward towards the fundamental aspects of quantum theory. In any introductory course of quantum mechanics, one would learn the fundamental axioms characterizing the theory. One of those axioms is that the Hamiltonian should be Hermitian to fulfill the requirements of unitary time-evolution and real eigenvalues for physical quantities. Recently, a new class of non-Hermitian Hamiltonians exhibiting parity-time (PT) reflection symmetry has been explored to show real eigenvalues [53–64]. The marriage of PT-symmetric quantum mechanics and paraxial optics has given birth to various excellent applications, such as implementation of a coherent perfect absorber [115, 127–129], asymmetric power oscillation violating left-right symmetry [112, 113, 130–132], unidirectional invisibility in reflection at the exceptional point [114, 133–136], nonreciprocal light transmission in the presence of nonlinearity [120, 137–139], optical complex crystals [110, 111, 140–144], single-mode laser [116, 117] and loss-induced suppression and revival of lasing [118, 119]. The investigation of PT-symmetric dynamics has also been emerging in atomic systems [145, 146], which we will discuss further in the presence of nonlinear nonlocal effects in Sec. 5.2.

This mathematical isomorphism has not only lead to remarkable refreshments of paraxial optics fused with new ingredients from quantum mechanics, but also allowed the possibility to mimic quantum phenomena which were theoretically introduced but hard to be examined in condensed matter physics, thus deepening our understanding of nature.

2.2 Introduction to classical and quantum nonlocality

2.2.1 Classical nonlocal linear effects in paraxial optics

In the context of paraxial optics, nonlocal linear effects are presented when the polarization $P(\mathbf{r}_\perp, z)$ depends on the electric field not only at $\mathbf{r}_\perp$ but also at other different positions, i.e.,

$$P(\mathbf{r}_\perp, z) = \varepsilon_0 \int_{-\infty}^{\infty} \chi(\mathbf{r}_\perp - \mathbf{r}'_\perp) E(\mathbf{r}'_\perp, z) d\mathbf{r}'_\perp \,. \tag{2.32}$$

Then, the paraxial wave equation is modified to

$$\left[\frac{\partial}{\partial z}-\frac{i}{2\mathrm{k}_0}\frac{\partial^2}{\partial \mathbf{r}_\perp^2}\right]\Omega(\mathbf{r}_\perp,z)=i\frac{\mathrm{k}_0}{2}\int_{-\infty}^{\infty}\chi(\mathbf{r}_\perp-\mathbf{r}_\perp^{'})\Omega(\mathbf{r}_\perp^{'},z)d\mathbf{r}_\perp^{'}\,. \tag{2.33}$$

A simple Fourier transformation from position into momentum space $\mathbf{r}_\perp \to \mathbf{k}_\perp$ yields

$$\left[\frac{\partial}{\partial z}+i\frac{\mathrm{k}_\perp^2}{2\mathrm{k}_0}\right]\Omega_F(\mathbf{k}_\perp,z)=i\frac{\mathrm{k}_0}{2}\chi_F(\mathbf{k}_\perp)\Omega_F(\mathbf{k}_\perp,z)\,. \tag{2.34}$$

Here, $\Omega_F(\mathbf{k}_\perp,z)$ and $\chi_F(\mathbf{k}_\perp)$ are the spatial Fourier transformations of $\Omega(\mathbf{r}_\perp,z)$ and $\chi(\mathbf{r}_\perp)$ from $\mathbf{r}_\perp$ to $\mathbf{k}_\perp$ respectively. Here the spatial Fourier transformation is defined by

$$g_F(\mathbf{k}_\perp,z)=\int_{-\infty}^{\infty}g(\mathbf{r}_\perp,z)e^{-i\mathbf{k}_\perp\cdot\mathbf{r}_\perp}d\mathbf{r}_\perp\,, \tag{2.35}$$

and we have applied the convolution theorem in deriving Eq. (2.34)

$$F[g(\mathbf{r}_\perp)*h(\mathbf{r}_\perp),\mathbf{k}_\perp]=g_F(\mathbf{k}_\perp)h_F(\mathbf{k}_\perp)\,, \tag{2.36}$$

where "$*$" stands for the convolution of $g(\mathbf{r}_\perp)$ and $h(\mathbf{r}_\perp)$. With the help of this nonlocal linear effects, paraxial light propagation can be coherently controlled and manipulated in various ways. For instance, it has been found that thermal motion and collisions in hot atomic systems can introduce nonlocal linear effects, leading to a direct manipulation of the paraxial diffraction in the momentum space, for instance, the exact elimination of paraxial diffraction. An outstanding feature of the elimination of diffraction by nonlocal linear effects is that it operates in momentum space and thus does not depend on the spatial profile of the laser beams. By taking advantage of this extraordinary feature, further applications can be realized, for instance, uniform phase modulation and diffractionless image reproduction between different frequencies, which will be exploited in Chap. 4.

2.2.2 Classical nonlocal nonlinear effects and modulational instability

Apart from nonlocal linear effects, a probably more intriguing and fruitful topic is linked to the nonlocal nonlinear effects, which appear naturally in a wide range of different systems ranging from plasmonics [147, 148], molecular reorientation of nematic liquid crystals [149, 150], to transport processes such as atom diffusion [151], heat conduction in materials with a thermal nonlinearity [152] or phonon heat transfer [153] in spin caloritronics, drift of electric charges [154]. In particular, many-body interacting systems including Bose-Einstein condensates [155–158] and Rydberg atoms [25] may also introduce nonlocal nonlinear effects under certain conditions. Along these lines, a variety of exciting phenomena has been intensively studied, including wave collapse (catastrophic self-focusing) [38, 159] and arrest [160], incoherent spatial solitons [35, 161, 162], beam stabilization [160, 163, 164], enhancement or suppression of modulational instability (MI) [36–39].

Of course it is an impossible mission to consider all the topics in a single thesis. Instead, we constrain ourselves to the MI effect, which is one of the most ubiquitous types of instabilities in nature and serves as a fundamental mechanism associated with wave propagation in nonlinear media. In short, MI stems from an interplay between diffraction/dispersion and local or nonlocal nonlinearity, giving rise to an exponential growth

for small amplitude and phase perturbations with specific frequencies or wavevectors. Consequently, MI may lead to a rapid amplification of sidebands, which breaks up the otherwise uniform wave front and generates fine localized structures (e.g., filamentation [11, 36, 37]). Furthermore, MI in the optical system also sheds light in Rogue waves [165, 166], which is especially concerned in oceanography. Aiming at investigating MI in more detail in nonlocal nonlinear media, we first give the explicit form of the wave equation involving nonlocal nonlinearity. In the scope of light propagation, the paraxial wave equation in the presence of cubic nonlocal nonlinear effects that we are interested in reads

$$\left[\frac{\partial}{\partial z} - \frac{i}{2\mathrm{k}_0}\frac{\partial^2}{\partial \mathbf{r}_\perp^2}\right]\Omega(\mathbf{r}_\perp, z) = iC_{nl}\Omega(\mathbf{r}_\perp, z)\int_{-\infty}^{\infty} K(\mathbf{r}_\perp - \mathbf{r}_\perp^{'})|\Omega(\mathbf{r}_\perp^{'}, z)|^2 d\mathbf{r}_\perp^{'}\,. \tag{2.37}$$

Here $K(\mathbf{r}_\perp)$ stands for the nonlocal response function in the transverse direction and C_{nl} is the nonlinear coefficient which can be either real or complex. In Eq. (2.37), we have omitted the linear effect which is not important here. And we have to mention here that other types of nonlocal nonlinear effects are in principle possible, e.g., the nonlocal response can also depend on the propagation distance z. In the regime where C_{nl} is real and $K(\mathbf{r}_\perp)$ is a real and integrable function, we can apply a linear stability analysis for MI. By doing this, we make the ansatz that Eq. (2.37) permits plane wave solution for a two-dimensional case in the form [36]

$$\Omega(x, z) = \sqrt{\rho_0}e^{ik_0 x - iw_0 z}\,, \tag{2.38}$$

with $\rho_0 > 0$ and k_0, w_0 being real numbers. Then substituting this solution back into Eq. (2.37) leads to the relation between w_0, k_0 and ρ_0

$$w_0 = \frac{k_0^2}{2} - \rho_0 C_{nl} I_K\,, \tag{2.39}$$

where I_K is a real number given by the integral

$$I_K = \int_{-\infty}^{\infty} K(x)dx\,. \tag{2.40}$$

Now suppose that there is a small perturbation added in the plane wave solution

$$\Omega(x, z) = [\sqrt{\rho_0} + u(\xi, \tau) + iv(\xi, \tau)]e^{ik_0 x - iw_0 z}\,, \tag{2.41}$$

with

$$\xi = x - k_0 z \quad \text{and} \quad \tau = z\,, \tag{2.42}$$

where u and v are real functions and $u, v \ll \sqrt{\rho_0}$. Inserting the expression (2.41) into Eq. (2.37) and linearizing around the ansatz (2.38) by keeping the leading order gives the equation

$$\frac{\partial u}{\partial \tau} + i\frac{\partial v}{\partial \tau} = \frac{i}{2}\frac{\partial^2 u}{\partial \xi^2} - \frac{1}{2}\frac{\partial^2 v}{\partial \xi^2} + 2i\rho_0 C_{nl}\int_{-\infty}^{\infty} K(x - x^{'})u(\xi^{'}, \tau)dx^{'}\,. \tag{2.43}$$

Since

$$\int_{-\infty}^{\infty} K(x-x^{'})u(\xi^{'},\tau)dx^{'} = \int_{-\infty}^{\infty} K(\xi-\xi^{'})u(\xi^{'},\tau)d\xi^{'}\,, \tag{2.44}$$

Eq. (2.43) can be split into the real and imaginary parts

$$\frac{\partial u}{\partial \tau} = -\frac{1}{2}\frac{\partial^2 v}{\partial \xi^2}\,, \tag{2.45a}$$

$$\frac{\partial v}{\partial \tau} = \frac{1}{2}\frac{\partial^2 u}{\partial \xi^2} + 2\rho_0 C_{nl}\int_{-\infty}^{\infty} K(\xi-\xi^{'})u(\xi^{'},\tau)d\xi^{'}\,. \tag{2.45b}$$

Introducing the spatial Fourier transform defined by Eq. (2.35), the linearized system Eq. (2.45) is converted to a set of ordinary differential equations in momentum space

$$\frac{\partial}{\partial \tau}\begin{bmatrix} u_F \\ \\ v_F \end{bmatrix} = \begin{bmatrix} 0 & \frac{k^2}{2} \\ \\ -\frac{k^2}{2}+2\rho_0 C_{nl}K_F(k) & 0 \end{bmatrix}\begin{bmatrix} u_F \\ \\ v_F \end{bmatrix}\,. \tag{2.46}$$

The eigenvalues $\lambda(k)$ of the system are then given by

$$\lambda_1(k) = i\sqrt{k^2\left[\frac{k^2}{4}-\rho_0 C_{nl}K_F(k)\right]}\,, \tag{2.47a}$$

$$\lambda_2(k) = -i\sqrt{k^2\left[\frac{k^2}{4}-\rho_0 C_{nl}K_F(k)\right]}\,, \tag{2.47b}$$

where $K_F(k)$ is defined by Eq. (2.35). We then find $\lambda_2(k) = -\lambda_1(k)$. Thus the solution for the perturbation can be written as

$$u_F(k,\tau) = c_1 e^{\lambda_1 \tau} + c_2 e^{\lambda_2 \tau}\,. \tag{2.48}$$

In the following, we will analytically calculate Eq. (2.46) to get the exact solution for the perturbation. Assuming firstly that the initial perturbation takes the form

$$u(\xi,\tau=0) = a_p \cos(k_p \xi)\,, \tag{2.49a}$$

$$v(\xi,\tau=0) = a_p \sin(k_p \xi)\,, \tag{2.49b}$$

where a_p and k_p are the amplitude and wavenumber of the perturbation respectively, and $k_p \neq 0$. Performing spatial Fourier transform on Eq. (2.49) results in

$$u_F(k,\tau=0) = \frac{a_p}{2}\left[\delta(k-k_p)+\delta(k+k_p)\right]\,, \tag{2.50a}$$

$$v_F(k,\tau=0) = \frac{i a_p}{2}\left[\delta(k-k_p)-\delta(k+k_p)\right]\,. \tag{2.50b}$$

Here, $\delta(k)$ is the Dirac delta function. With the initial conditions (2.50) in momentum space, the equations for the coefficients c_1 and c_2 can be derived from Eq. (2.46) and (2.48)

$$c_1 + c_2 = \frac{a_p}{2}\left[\delta(k-k_p)+\delta(k+k_p)\right]\,, \tag{2.51a}$$

$$c_1 - c_2 = q(k)\frac{a_p}{2}\left[\delta(k-k_p) - \delta(k+k_p)\right], \tag{2.51b}$$

where $q(k)$ is defined by

$$q(k) = \frac{ik^2}{2\lambda_1(k)} = \frac{k^2}{\sqrt{k^2\left[k^2 - 4\rho_0 C_{nl} K_F(k)\right]}}, \tag{2.52}$$

when $k^2 - 4\rho_0 C_{nl} K_F(k) \neq 0$. Otherwise we have $\lambda_1(k) = -\lambda_2(k) = 0$ which is related to an exceptional point [167]. Then we find

$$c_1 = \frac{a_p}{4}\left\{[1+q(k)]\delta(k-k_p) + [1-q(k)]\delta(k+k_p)\right\}, \tag{2.53a}$$

$$c_2 = \frac{a_p}{4}\left\{[1-q(k)]\delta(k-k_p) + [1+q(k)]\delta(k+k_p)\right\}. \tag{2.53b}$$

Finally, the solution for the perturbation can be obtained

$$\begin{aligned} u(\xi,\tau) =& \frac{1}{2\pi}\int_{-\infty}^{\infty} u(k,\tau)e^{ik\xi}dk \\ =& \frac{a_p}{4}\left\{[1+q(k_p)]e^{\lambda_1(k_p)\tau}e^{ik_p\xi} + [1-q(-k_p)]e^{\lambda_1(-k_p)\tau}e^{-ik_p\xi}\right\} + \\ & \frac{a_p}{4}\left\{[1-q(k_p)]e^{-\lambda_1(k_p)\tau}e^{ik_p\xi} + [1+q(-k_p)]e^{-\lambda_1(-k_p)\tau}e^{-ik_p\xi}\right\}. \end{aligned} \tag{2.54}$$

In the linear case where $C_{nl} = 0$, the eigenvalues are all imaginary, i.e., $\lambda_1(k) = -\lambda_2(k) = ik^2/2$, then the perturbation will never be amplified and always oscillates along the propagation direction with spatial frequency $k^2/2$. When a local nonlinearity is present, i.e., $C_{nl} \neq 0$ and $K_F(k) = 1$, there will be in principle an exponential growth (i.e., MI) for some specific k when $C_{nl} > 0$ which corresponds to a focusing nonlinearity. The other trivial case gives the normal oscillation when $C_{nl} < 0$, which relates to a defocusing nonlinearity. Nevertheless, the situation can be completely different when a nonlocal nonlinearity is introduced. Depending on the spatial structure of the nonlocal response function $K(\xi)$, it generally involves MI independent of the value of C_{nl}. Moreover, the nonlocal nonlinearity can lead to either enhancement or suppression of MI appeared in the local nonlinear case. For the special example of a symmetric nonlocal response function $K(\ xi)$, its Fourier transform should be also symmetric $K_F(k) = K_F(-k)$. We thus have $\lambda_1(k) = \lambda_1(-k)$ and $q(k) = q(-k)$. Then Eq. (2.54) can be further simplified

$$\begin{aligned} u(\xi,\tau) =& \frac{a_p}{2}\left[\cos(k_p\xi) + iq(k_p)\sin(k_p\xi)\right]e^{\lambda_1(k_p)\tau} \\ & + \frac{a_p}{2}\left[\cos(k_p\xi) - iq(k_p)\sin(k_p\xi)\right]e^{-\lambda_1(k_p)\tau}. \end{aligned} \tag{2.55}$$

Note that $u(\xi,\tau)$ seems to be a complex function at first sight, however, it is actually real, thus fulfilling our initial assumption. Similarly, $v(\xi,\tau)$ can also be attained

$$\begin{aligned} v(\xi,\tau) =& \frac{ia_p}{2q(k_p)}\left[\cos(k_p\xi) + iq(k_p)\sin(k_p\xi)\right]e^{\lambda_1(k_p)\tau} \\ & - \frac{ia_p}{2q(k_p)}\left[\cos(k_p\xi) - iq(k_p)\sin(k_p\xi)\right]e^{-\lambda_1(k_p)\tau}. \end{aligned} \tag{2.56}$$

Note that $v(\xi,\tau)$ is also a real function. It should be emphasized here that the analytical solutions Eqs. (2.54), (2.55) and (2.56) are reasonable only when the ansatz Eq. (2.38) is valid. In other words, this linear analysis remains only meaningful in the mere case where C_{nl} is real and $K(\xi)$ is a real and integrable function. More generally, it can be simply extended to be valid in the region where the product $C_{nl}K(\xi)$ is real and integrable.

Beyond this limit, i.e., in the more intricate case where $C_{nl}K(\xi)$ is complex, however, the linear stability analysis would fail and the corresponding analytical solutions for the perturbation are rather impossible. The physical essence beneath the breakdown of the ansatz Eq. (2.38) and the associated linear analysis attributes to the nonlinear absorption entered in this case, which might give rise to a simultaneous competition against MI. As a result, there exists no plane wave solution, and the perturbation may have unexpected behaviors differing from the MI effect. In order to show this, we have developed a new model in Sec. 5.1 which is capable of describing the MI effect in the presence of nonlinear absorption. Here we present an overview of this model to show its differences and possible advantages against the linear stability analysis. We first rewrite Eq. (2.37) as follows

$$\left(\frac{\partial}{\partial\zeta}-\frac{i}{2}\frac{\partial^2}{\partial\boldsymbol{\xi}^2}\right)\psi(\boldsymbol{\xi},\zeta)=iC_{nl}^{'}\psi(\boldsymbol{\xi},\zeta)\int_{-\infty}^{\infty}K(\boldsymbol{\xi}-\boldsymbol{\xi}^{'})|\psi(\boldsymbol{\xi}^{'},\zeta)|^2d\boldsymbol{\xi}^{'}\,, \tag{2.57}$$

Here, we have rescaled the coordinates using $\boldsymbol{\xi}=\mathbf{r}_\perp/S_t$, $\zeta=z/S_z$, $S_z=\mathrm{k}_pS_t^2$, $\Omega(\boldsymbol{\xi},\zeta)=\Omega_{p0}\psi(\boldsymbol{\xi},\zeta)$ and $C_{nl}^{'}=C_{nl}S_zS_t^2\Omega_{p0}^2$ with S_t and S_z being the scales in the transverse and propagation directions, respectively. Without loss of generality, we consider two-dimensional propagation in the following.

Now considering that a one-dimensional plane wave with an additional cosine perturbation $\psi(\xi_x,\zeta=0)=1+\epsilon_0\cos(\mathrm{k}_x\xi_x)$ (ϵ_0 is real and $\epsilon_0\ll1$) is propagating in the absorptive nonlocal nonlinear media, we shall assume that the output function $\psi(\xi_x,\zeta)$ can be decomposed into a Fourier series consisting of multiples of the k_x component, by observing the simple form of the input wave

$$\psi(\xi_x,\zeta)=\sum_j a_j(\zeta)e^{ijk_x\xi_x}\,, \tag{2.58}$$

Substituting this form into Eq. (2.37) leads to a set of equations for $a_j(\zeta)$

$$\left[\frac{\partial}{\partial\zeta}+\frac{i}{2}j^2k_x^2\right]a_j(\zeta)=iC_{nl}^{'}\sum_{p,q}a_{j-p+q}(\zeta)a_p(\zeta)a_q^*(\zeta)K_F\left[(p-q)k_x\right]\,, \tag{2.59}$$

and $K_F(mk_x)$ is the m-th spatial Fourier transform of the kernel function $K(\xi_x)$, i.e.,

$$K_F(mk_x)=\int_{-\infty}^{\infty}K(\xi_x)e^{-imk_x\xi_x}d\xi_x\,. \tag{2.60}$$

In general, analytical solutions of this set of equations are rather impossible. Practically, the set of equations can be reasonably truncated to a maximum value, i.e., $j\le j_{\max}$, depending on the propagation distance ζ_L. For a short distance where $|a_0(\zeta)|\gg|a_1(\zeta)|$, $j_{\max}$ can be safely limited to $j_{\max}=1$, leading to the following much simplified equations

of motion for $a_0(\zeta)$, $a_1(\zeta)$ and $a_{-1}(\zeta)$

$$\frac{da_0(\zeta)}{d\zeta} = iC_{nl}' K_F(0)|a_0(\zeta)|^2 a_0(\zeta)\,, \tag{2.61a}$$

$$\begin{aligned}\frac{da_1(\zeta)}{d\zeta} =& -\frac{k_x^2}{2}a_1(\zeta) + iC_{nl}'\big[K_F(0)|a_0(\zeta)|^2 a_1(\zeta) \\ &+ K_F(k_x)|a_0(\zeta)|^2 a_1(\zeta) + K_F(k_x)a_0^2(\zeta)a_{-1}^*(\zeta)\big]\,,\end{aligned} \tag{2.61b}$$

$$\begin{aligned}\frac{da_{-1}(\zeta)}{d\zeta} =& -\frac{k_x^2}{2}a_{-1}(\zeta) + iC_{nl}'\big[K_F(0)|a_0(\zeta)|^2 a_{-1}(\zeta) \\ &+ K_F(-k_x)|a_0(\zeta)|^2 a_{-1}(\zeta) + K_F(-k_x)a_0^2(\zeta)a_1^*(\zeta)\big]\,.\end{aligned} \tag{2.61c}$$

For a symmetric kernel function $K(\xi_x) = K(-\xi_x)$, it would result in $K_F(k_x) = K_F(-k_x)$ and the subsequent symmetric nature of the equation of motion for the positive and negative components. And also by noting the fact that the input cosine perturbation indicates that $a_1(0) = a_{-1}(0)$, we then find that $a_1(\zeta) = a_{-1}(\zeta)$. The analytical solutions for $a_0(\zeta)$ and $a_1(\zeta)$ are then obtained

$$a_0(\zeta) = \frac{(1+2\mathrm{Im}[c_0]\zeta)^{i\frac{\mathrm{Re}[c_0]}{2\mathrm{Im}[c_0]}}}{\sqrt{1+2\mathrm{Im}[c_0]\zeta}} = (1+2\mathrm{Im}[c_0]\zeta)^{\frac{ic_0}{2\mathrm{Im}[c_0]}}\,, \tag{2.62a}$$

$$\begin{aligned}a_1(\zeta) =& \epsilon_0(1+2\mathrm{Im}[c_0]\zeta)^{\frac{ic_0}{2\mathrm{Im}[c_0]}} e^{-\frac{ik_x^2\zeta}{2}} \\ &\cdot\Big\{s_1\mathrm{HypergeometricU}\big[\frac{-ic_1}{2\mathrm{Im}[c_0]}, 1+\frac{\mathrm{Im}[c_1]}{\mathrm{Im}[c_0]}, \frac{ik_x^2}{2\mathrm{Im}[c_0]} + ik_x^2\zeta\big] \\ &+ s_2\mathrm{LaguerreL}\big[\frac{ic_1}{2\mathrm{Im}[c_0]}, \frac{\mathrm{Im}[c_1]}{\mathrm{Im}[c_0]}, \frac{ik_x^2}{2\mathrm{Im}[c_0]} + ik_x^2\zeta\big]\Big\}\,,\end{aligned} \tag{2.62b}$$

where $c_0 = C_{nl}' K_F(0)$ and $c_1 = C_{nl}' K_F(k_x)$, and the coefficients s_1 and s_2 are constrained by the initial conditions in Eq. (2.61b)

$$a_1(\zeta = 0) = \epsilon_0\,, \tag{2.63a}$$

$$\left.\frac{da_1}{d\zeta}\right|_{\zeta=0} = -\frac{k_x^2}{2}\epsilon_0 + i\epsilon_0\big[c_0 + 2c_1\big]\,. \tag{2.63b}$$

Detailed procedures to obtain the solutions Eq. (2.62a) can be further found in Sec. 5.1. Owing to the evolved confluent hypergeometric function and generalized Laguerre polynomial, it is hard to reveal the underlying physics inside $a_1(\zeta)$ in an analytical manner. In order to show the competition between MI and nonlocal nonlinear absorption more directly, we then re-solve Eq. (2.61b) in the region of $\zeta \sim 0$, which gives

$$b_1(\zeta) = e^{-(\mathrm{Im}[c_0] - \frac{ik_x^2}{2} + i\mathrm{Re}[c_1])\zeta}\big[s_1 e^{-\lambda(k_x)\zeta} + s_2 e^{\lambda(k_x)\zeta}\big]\,, \tag{2.64}$$

with

$$\lambda(k_x) = \frac{1}{2}\sqrt{4|c_1|^2 + (2\mathrm{Im}[c_0] - ik_x^2 + 2i\mathrm{Re}[c_1])^2}\,. \tag{2.65}$$

Thus the analytical solution for $a_1(\zeta)$ can be much simplified

$$a_1(\zeta) = \epsilon_0(1 + 2\mathrm{Im}[c_0]\zeta)^{\frac{i(c_0+c_1)}{2\mathrm{Im}[c_0]}} e^{-(\mathrm{Im}[c_0]+i\mathrm{Re}[c_1])\zeta}\left[s_1 e^{-\lambda(k_x)\zeta} + s_2 e^{\lambda(k_x)\zeta}\right]. \tag{2.66}$$

From Eq. (2.66) it is clear to see that $\lambda(k)$ is associated to MI which occurs in the absorptive nonlocal nonlinear media. In sharp contrast to the pure dispersive case where $\mathrm{Im}[C_{nl}K_F(k)] = 0$, counterintuitively, MI generally occurs for each k wave component when the nonlinear absorption is present, as indicated in Eq. (2.65). Thanks to the nonlinear absorption introduced by $\mathrm{Im}[c_0]$, it is evident to see the competition between MI and nonlinear absorption. In general, MI can be fully suppressed by the nonlinear absorption and $a_1(\zeta)$ does not experience any real exponential growth throughout its propagation in the medium. Note that in nonlocal nonlinear media where only dispersive effect enters, i.e., $\mathrm{Im}[C_{nl}K_F(k_x)] = 0$, the exponential index $\lambda(k)$ is reduced to

$$\lambda(k_x) = \frac{i}{2}\sqrt{k_x^2[k_x^2 - 4C_{nl}K_F(k_x)]}, \tag{2.67}$$

which is of the same form as Eq. (2.47a) obtained in the linear stability analysis if we set $\rho_0 = 1$. Furthermore, in the local dispersive regime where $K_F(k_x) = 1$ and $C_{nl} = C_{nl}^*$, Eq. (2.67) coincides with the results obtained in Ref. [36, 37]. This will be further exploited in Sec. 5.1.

2.2.3 Quantum nonlocality

After a little taste of classical nonlocal effects in the previous sections, we now move our attention to a more subtle and counterintuitive concept, which is quantum nonlocality. Quantum theory states that there is no way to precisely determine the value for non-commutable physical quantities simultaneously, which is known as the Heisenberg uncertainty principle. However, according to the arguments in the famous paper [8] by Einstein, Podolsky, and Rosen (EPR) in 1935, non-commutable quantities (e.g., position and momentum) can have simultaneous values in a quantum correlated system, under the plausible assumptions "*no action at a distance*" and "*the reality of a physical quantity is the possibility of predicting it with certainty, without disturbing the system*" (together called "local realism"), leading to paradoxical conclusions in comparison with quantum theory. Thus they claimed that the quantum-mechanical description of physical reality is not complete under the seemingly reasonable assumption of "local realism" that they defined. In the same year, Bohr replied in a paper [27] with the same title that the criterion of physical reality formulated by EPR contains an essential ambiguity in quantum physics when the experimental arrangement is specified, attempting to resolve the challenging raised by EPR. However, his philosophical statement was not fully convincing to the physical community [29].

In order to interpret the quantum-mechanical predictions for a system of EPR type, a vast class of hidden-variable theories was suggested. In a hidden-variable theory, the probabilistic nature of quantum mechanics is typically abandoned to meet determinism derived from reality. An exceptional example would be the nonlocal pilot-wave theory developed by De Broglie and Bohm [168, 169], where it postulates an additional guiding equation determining an actual configuration on which the Schrödinger equation evolves. It was hoped that the hidden-variable theory could restore the completeness and determinism to the quantum theory. Until recently, Colbeck and Renner [170] have proven that "*no extension of quantum theory can give more information about the outcomes of*

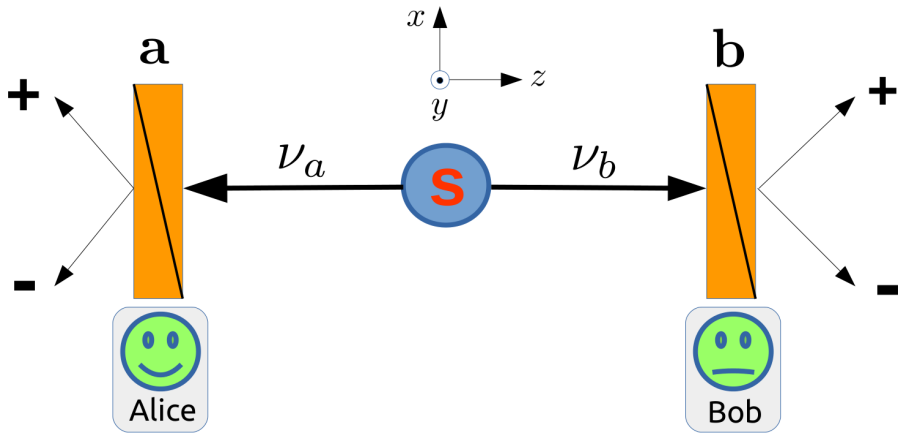

Figure 2.1: A schematic demonstration of experimental test of CHSH inequality. The photon pairs emitted from the source **S** are sent to two remote observers Alice and Bob. Alice and Bob measure the polarization of the two photons along the directions **a** and **b** perpendicular to the z axis respectively, each has two possible outcomes $+$ and $-$. The Bell-like inequality can be violated when the photon pairs are prepared in entangled states.

future measurements than quantum theory itself" under the assumption that measurements can be chosen freely. That is to say, any extension of quantum mechanical theory, whether using hidden variables or otherwise cannot provide a more accurate prediction of outcomes, provided that observers can freely choose the measurement settings. They thus concluded that quantum theory is really complete under the assumption that measurement settings can be chosen freely. Moreover, it has been shown by Pusey, Barrett, and Rudolph [171] that "*any model in which a quantum state represents mere information about an underlying physical state of the system that is objective and independent of the observer, and in which systems that are prepared independently have independent physical states, must make predictions that contradict those of quantum theory*". Inspired by the insights gained from Ref. [171], Colbeck and Renner [172] again pointed out that the wave function of a system is in one-to-one correspondence with its elements of reality based only on the assumption that measurement settings can be chosen freely.

In 1964, Bell [28] proved a direct contradiction between quantum physics and the EPR assumptions, i.e., local realism, thus ruling out a certain class of local hidden-variable theories. In more detail, he demonstrated that in a correlated system certain combinations of expectation values of correlations have upper bounds under local realism, which is smaller than that predicted by quantum mechanics. It is now called Bell inequality and has stimulated several variants [173, 174] which are easier to be tested experimentally, for instance, the Clauser, Horne, Shimony, and Holt (CHSH) inequality [173]. For the sake of a deeper understanding of Bell's inequality, here we provide a simplified illustration of inequalities of Bell's type. As shown in Fig. 2.1, suppose we have a random source emitting pairs of particles, e.g., photons. The pair of photons ν_a and ν_b are sent to two linear polarizers called Alice and Bob, who measure the polarization of the two photons along $\vec{a}$ and $\vec{b}$ perpendicular to the z axis respectively. Each measurement has two possible outcomes, "$+$" or "$-$", and one can measure the single or joint probabilities at various orientations $\vec{a}$ and $\vec{b}$. We then define a conditional joint probability [175]

$$P(x, y|\vec{a}, \vec{b}) = \int d\lambda \rho(\lambda) P_\lambda(x, y|\vec{a}, \vec{b}) \,. \tag{2.68}$$

Here, x and y ($\in \{+,-\}$) represent the outcomes for Alice and Bob respectively. The density function $\rho(\lambda)$ describes a certain distribution of possible states of the source. Each state is determined by λ which denotes a single hidden variable, a set, or even a set of functions. Then we have

$$\int \rho(\lambda) d\lambda = 1\,, \tag{2.69}$$

and $P_\lambda(x, y|\vec{a}, \vec{b})$ stands for the conditional joint probability when *both* Alice has the outcome x *and* Bob has the outcome y at measurement settings $\vec{a}$ *and* $\vec{b}$, and when the source is in state λ. The outcome x for Alice can in principle rely on *not only* her own experiment setting $\vec{a}$ *but also* on Bob's setting $\vec{b}$ and outcome y, and vice versa. The correlation function at specific measurement settings can be written as

$$C(\vec{a}, \vec{b}) = P(+,+|\vec{a}, \vec{b}) - P(+,-|\vec{a}, \vec{b}) - P(-,+|\vec{a}, \vec{b}) + P(-,-|\vec{a}, \vec{b})\,. \tag{2.70}$$

Bell's locality assumption leads to

$$P_\lambda(x, y|\vec{a}, \vec{b}) = P_\lambda^A(x|\vec{a}) P_\lambda^B(y|\vec{b})\,, \tag{2.71}$$

where $P_\lambda^A(x|\vec{a})$ is the single probability for Alice having the outcome x at $\vec{a}$ when the source is in state λ, and $P_\lambda^B(y|\vec{b})$ is the single probability for Bob having the outcome y at $\vec{b}$ when the source is in state λ. Evident from Eq. (2.71), Bell's locality assumption implies that the single probability $P_\lambda^A(x|\vec{a})$ for Alice to have the outcome x is solely determined by the setting $\vec{a}$ she chooses and the state of the source λ, but does not depend on either the outcome y or the setting $\vec{b}$ at Bob's side, and vice versa. Experimentally, the single probability is defined as

$$P_\lambda^A(x|\vec{a}) = \frac{N_A(x|\vec{a})}{\sum_x N_A(x|\vec{a})} = \frac{N_A(x|\vec{a})}{N_A(+|\vec{a}) + N_A(-|\vec{a})}\,, \tag{2.72a}$$

$$P_\lambda^B(y|\vec{b}) = \frac{N_B(y|\vec{b})}{\sum_y N_B(x|\vec{b})} = \frac{N_B(y|\vec{b})}{N_B(+|\vec{b}) + N_B(-|\vec{b})}\,, \tag{2.72b}$$

where $N_A(x|\vec{a})$ [$N_B(y|\vec{b})$] is the number of counts when the measurement gives outcome x [y] for Alice [Bob] at experiment setting $\vec{a}$ [$\vec{b}$]. With the help of Eq. (2.71), we can find that $C(\vec{a}, \vec{b})$ defined in Eq. (2.70) can be changed to

$$\begin{aligned} C(\vec{a}, \vec{b}) &= \int d\lambda \rho(\lambda) [P_\lambda^A(+|\vec{a}) - P_\lambda^A(-|\vec{a})][P_\lambda^B(+|\vec{b}) - P_\lambda^B(-|\vec{b})] \\ &= \int d\lambda \rho(\lambda) P_\lambda^A(\vec{a}) P_\lambda^B(\vec{b})\,, \end{aligned} \tag{2.73}$$

with

$$P_\lambda^A(\vec{a}) = P_\lambda^A(+|\vec{a}) - P_\lambda^A(-|\vec{a})\,, \tag{2.74a}$$

$$P_\lambda^B(\vec{b}) = P_\lambda^B(+|\vec{b}) - P_\lambda^B(-|\vec{b})\,, \tag{2.74b}$$

$P_\lambda^A(\vec{a})$ and $P_\lambda^B(\vec{b})$ are understood as the average outcomes for Alice and Bob, respectively,

thus satisfying

$$|P_\lambda^A(\vec{a})| \leq 1\,, \tag{2.75a}$$
$$|P_\lambda^B(\vec{b})| \leq 1\,. \tag{2.75b}$$

The CHSH inequality can be deduced [176] based on the correlation function defined in Eq. (2.73)

$$\begin{aligned} C(\vec{a},\vec{b}) - C(\vec{a},\vec{b}^{'}) &= \int d\lambda\rho(\lambda)[P_\lambda^A(\vec{a})P_\lambda^B(\vec{b}) - P_\lambda^A(\vec{a})P_\lambda^B(\vec{b}^{'})] \\ &= \int d\lambda\rho(\lambda)\{P_\lambda^A(\vec{a})P_\lambda^B(\vec{b})[1 \pm P_\lambda^A(\vec{a}^{'})P_\lambda^B(\vec{b}^{'})]\} \\ &\quad - \int d\lambda\rho(\lambda)\{P_\lambda^A(\vec{a})P_\lambda^B(\vec{b}^{'})[1 \pm P_\lambda^A(\vec{a}^{'})P_\lambda^B(\vec{b})]\} \\ &\leq \int d\lambda\rho(\lambda)[1 \pm P_\lambda^A(\vec{a}^{'})P_\lambda^B(\vec{b}^{'})] + \int d\lambda\rho(\lambda)[1 \pm P_\lambda^A(\vec{a}^{'})P_\lambda^B(\vec{b})] \\ &= 2 \pm [C(\vec{a}^{'},\vec{b}^{'}) + C(\vec{a}^{'},\vec{b})]\,, \end{aligned} \tag{2.76}$$

where we have applied the relations given in Eq. (2.75). Finally, the inequality reads

$$C(\vec{a},\vec{b}) - C(\vec{a},\vec{b}^{'}) \pm [C(\vec{a}^{'},\vec{b}^{'}) + C(\vec{a}^{'},\vec{b})] \leq 2\,, \tag{2.77}$$

which is the CHSH-type inequality. Throughout the deduction of Eq. (2.77) shown above, only Bell's locality assumption Eq. (2.71) is involved. Thus a violation of inequality (2.77) would indicate problems related to Bell's locality assumption. One might argue that Eq. (2.75) should be also considered as a precondition to derive the final CHSH inequality, thus it should be also considered as an additional assumption. However, Eq. (2.75) is very unlikely to be invalid unless the single probabilities given in Eq. (2.71) can be negative. Experimentally, the conditional joint probability is given by

$$\begin{aligned} P(x,y|\vec{a},\vec{b}) &= \frac{N(x,y|\vec{a},\vec{b})}{\sum_{x,y} N(x,y|\vec{a},\vec{b})} \\ &= \frac{N(x,y|\vec{a},\vec{b})}{N(+,+|\vec{a},\vec{b}) + N(+,-|\vec{a},\vec{b}) + N(-,+|\vec{a},\vec{b}) + N(-,-|\vec{a},\vec{b})}\,, \end{aligned} \tag{2.78}$$

where $N(x,y|\vec{a},\vec{b})$ (here $x,y \in \{+,-\}$) is the number of coincidences when the measurement gives outcomes x for Alice at direction $\vec{a}$ and y for Bob at direction $\vec{b}$ simultaneously. Note that Eq. (2.78) is directly defined by the experiment outcomes and therefore has nothing to do with any assumption. With the aim of Eq. (2.78), the quantity

$$S(\vec{a},\vec{b},\vec{a}^{'},\vec{b}^{'}) = C(\vec{a},\vec{b}) - C(\vec{a},\vec{b}^{'}) + C(\vec{a}^{'},\vec{b}) + C(\vec{a}^{'},\vec{b}^{'})\,, \tag{2.79}$$

can be checked experimentally, and the relation

$$S(\vec{a},\vec{b},\vec{a}^{'},\vec{b}^{'}) \leq 2\,, \tag{2.80}$$

must be satisfied if the assumption of local realism holds. Amazingly, quantum mechanics predicts that the quantity $S(\vec{a},\vec{b},\vec{a}^{'},\vec{b}^{'})$ could be larger than 2 at certain directions $\vec{a}_0,\vec{b}_0,\vec{a}_0^{'},\vec{b}_0^{'}$ when the pairs of photons are prepared in entangled states, thus violating

the CHSH inequality (2.80). And it is not only limited to photons but also any other particles prepared in an entangled state, for instance, electrons, and ions. It is astonishing that a philosophical questioning on the fundamental interpretation of quantum mechanics could be judged by a simple mathematical number. Nevertheless, numerous and notable experiments were performed by different groups in the last fifty years. In all those reliable experiments, results are consistent with quantum theory but contradict local realism, revealing the intrinsically nonlocal nature of quantum theory. The first pioneering experiment was done in 1972 by Freedman and Clauser who employed photon pairs emitted in an atomic cascade [177]. Much more reliable experimental demonstrations were performed by Aspect *et al.* in the early 1980s, who have for the first time measured directly the CHSH inequality with high-efficiency source and time-varying analyzers [30–32]. Even the results favored quantum theory, criticism has been raised that auxiliary assumptions have to be involved. Specifically, the detected pairs in those experiments may not represent a fair sample of all events due to the low efficiency of detectors, and local channels could in principle exist since the two observers are not positioned far away from each other enough to exclude all subliminal communication. Those are at that time two main problems in which one is termed as the detection loophole related to the fair-sampling assumption (alternatively no-enhancement hypothesis [178]) and the other is called the locality loophole relevant to the possible local communication. A few years later, the loophole of local communication has been closed by Weihs *et al.* in 1998, in which the necessary spacelike separation of the observations is achieved not only by sufficient physical distance between the measurement stations but also by ultrafast and random setting of the analyzers and completely independent data registration[33]. Recently, Giustina *et al.* have succeeded to show Bell violation without fair-sampling assumption by experimentally testing the Eberhard form of Bell's inequality which is invulnerable to the fair-sampling assumption [34]. It should be noted that every loophole has only been closed individually, no test has been done to simultaneously close all loopholes. Based on the glorious achievements done in the last fifty years, we would be optimistic to expect a final experiment which will close all the loopholes in the near future.

We have just learned that any local realistic theory leads to bounded values for certain combinations of correlations according to Bell's inequalities, it is then natural to ask the question whether there is also a boundary that quantum correlations cannot exceed? The answer is positive, it has been proven by Cirel'son [179] that quantum theory does not allow the quantity S in the CHSH inequality to be larger than a maximum value, i.e., $S \leq 2\sqrt{2}$. Quantum bounds for inequalities of various types could also be in principle derived. It becomes even more subtle as the correlation behavior is investigated beyond quantum nonlocality. There are mainly two branches in this direction, in which each has lead to remarkable progresses. The first one is to consider the case when abandoning the assumption of locality but preserving the element of reality; Leggett [93] has provided a set of inequalities by assuming the nonlocal realism. The results of recent experimental tests have shown to be consistent with quantum mechanics rather than the Leggett's inequalities [94]. The other one is to study the case when only respecting the special relativity but completely eliminating the assumption of local realism. This refers to the non-signalling principle, which says that Alice's local statistics should not be influenced by Bob's choice of measurement, and reciprocally [96, 175, 180]. One of the outstanding examples retaining the non-signalling principle is the Popescu-Rohrlich (PR) box [95, 96], which was deliberately designed to show that the correlation can reach $S = 4$.

On the road of pursuing an ultimate understanding of quantum theory, people have

also asked deeply if it is possible to construct the quantum theory from certain fundamental physical principles, just like the special relativity which can be naturally deduced from two simple but straightforward axioms that all the inertial frames of reference are equivalent and there is a finite maximum speed for propagation of signals, i.e., the speed of light. There have been thrilling progresses in this direction. For instance, quantum nonlocality has been proposed as one of the axioms of quantum mechanics [95]. A further generalization of the non-signalling principle gives rise to the concept of information causality, which states "*the information gain that Bob can reach about a previously unknown to him data set of Alice, by using all his local resources and m classical bits communicated by Alice, is at most m bits*" [97]. For $m = 0$, it is reduced to the non-signalling principle. In the last decades, there have been pioneering attempts to pick out reasonable candidates of essential physical requirements [98, 99] to uniquely deduce and formulate quantum theory.

2.3 Optical Schrödinger equation in periodic system

2.3.1 Bloch theorem

We first rewrite the optical Schrödinger equation Eq. (2.30) as

$$i\frac{\partial\psi(\boldsymbol{\xi},\zeta)}{\partial\zeta} = -\frac{\partial^2}{\partial\boldsymbol{\xi}^2}\psi(\boldsymbol{\xi},\zeta) - V(\boldsymbol{\xi},\zeta)\psi(\boldsymbol{\xi},\zeta)\,, \tag{2.81}$$

where we have made the rescaling $\mathbf{r}_\perp = S_\perp\boldsymbol{\xi}, z = S_z\zeta$ with $S_z = 2\mathrm{k}_0 S_\perp^2$, and also the replacement $\Omega(\boldsymbol{\xi},\zeta) = \Omega_0\psi(\boldsymbol{\xi},\zeta)$ with Ω_0 being the amplitude. Note here $\boldsymbol{\xi} = (\xi_x, \xi_y)$ represents the scaled coordinates in the transverse plane. The effective potential is thus changed to

$$V(\boldsymbol{\xi},\zeta) = \frac{\mathrm{k}_0}{2}S_z\chi(\mathbf{r}) = \mathrm{k}_0^2 S_\perp^2\chi(\boldsymbol{\xi},\zeta)\,, \tag{2.82}$$

and the optical Hamiltonian is given by

$$H = -\frac{\partial^2}{\partial\boldsymbol{\xi}^2} - V(\boldsymbol{\xi},\zeta)\,. \tag{2.83}$$

We now assume that $V(\boldsymbol{\xi},\zeta)$ does not depend on ζ

$$V(\boldsymbol{\xi},\zeta) = V(\boldsymbol{\xi})\,. \tag{2.84}$$

Thus we can find that the solution of the optical Schrödinger equation can be written as

$$\psi(\boldsymbol{\xi},\zeta) = \phi(\boldsymbol{\xi})e^{-i\beta\zeta}. \tag{2.85}$$

Here β is the eigenvalue of the optical Hamiltonian satisfying

$$H\phi(\boldsymbol{\xi}) = \beta\phi(\boldsymbol{\xi})\,, \tag{2.86}$$

when the optical potential is periodic in $\boldsymbol{\xi}$, i.e.,

$$V(\boldsymbol{\xi}) = V(\boldsymbol{\xi} + \boldsymbol{R})\,, \tag{2.87}$$

where $\boldsymbol{R} = (R_x, R_y)$ is the period of the potential in the transverse plane. It is stated by the Bloch theorem that the eigenfunctions of the optical Schrödinger equation must be of the special form

$$\phi(\boldsymbol{\xi}) = u_{\boldsymbol{k}}(\boldsymbol{\xi}) e^{i\boldsymbol{k}\cdot\boldsymbol{\xi}}\,, \tag{2.88}$$

where $u_{\boldsymbol{k}}(\boldsymbol{\xi}) = u_{\boldsymbol{k}}(\boldsymbol{\xi} + \boldsymbol{R})$ is a periodically modulated function having the periodicity of the potential, and $\boldsymbol{k} = (k_x, k_y)$ is the Bloch wave vector. Literally, the Bloch theorem states [181]

> "***The eigenfunctions of the wave function for a periodic potential are the product of a plane wave exp***$(i\boldsymbol{k}\cdot\boldsymbol{\xi})$ ***times a function*** $u_k(\boldsymbol{\xi})$ ***with the periodicity identical to the potential.***"

In order to understand the Bloch theorem more clearly, we provide a brief proof here. We start by defining a space translation operator $\hat{T}_R$

$$\hat{T}_R\phi(\boldsymbol{\xi}) = \phi(\boldsymbol{\xi} + \boldsymbol{R})\,. \tag{2.89}$$

Note that the translation operator commutes with the optical Hamiltonian since

$$\begin{aligned}
\hat{T}_R H\phi(\boldsymbol{\xi}) &= \big[-\frac{\partial^2}{\partial\boldsymbol{\xi}^2} - V(\boldsymbol{\xi}+\boldsymbol{R})\big]\phi(\boldsymbol{\xi}+\boldsymbol{R}) \\
&= \big[-\frac{\partial^2}{\partial\boldsymbol{\xi}^2} - V(\boldsymbol{\xi})\big]\phi(\boldsymbol{\xi}+\boldsymbol{R}) \\
&= H\hat{T}_R\phi(\boldsymbol{\xi})\,.
\end{aligned} \tag{2.90}$$

Since $\hat{T}_R$ is linear, $\hat{T}_R$ and H share the same eigenbasis

$$\hat{T}_R\phi(\boldsymbol{\xi}) = \lambda_T\phi(\boldsymbol{\xi})\,. \tag{2.91}$$

We then expand the wave function $\phi(\boldsymbol{\xi})$ in plane wave series

$$\phi(\boldsymbol{\xi}) = \sum_{\boldsymbol{q}} C_{\boldsymbol{q}} e^{i\boldsymbol{q}\cdot\boldsymbol{\xi}}\,, \tag{2.92}$$

so the translated wave function reads

$$\hat{T}_R\phi(\boldsymbol{\xi}) = \phi(\boldsymbol{\xi}+R) = \sum_{\boldsymbol{q}} C_{\boldsymbol{q}} e^{i\boldsymbol{q}\cdot(\boldsymbol{\xi}+\boldsymbol{R})}\,. \tag{2.93}$$

From Eq. (2.91) and (2.93) we could find that

$$\lambda_T \sum_{\boldsymbol{q}} C_{\boldsymbol{q}} e^{i\boldsymbol{q}\cdot\boldsymbol{\xi}} = \sum_{\boldsymbol{q}} C_{\boldsymbol{q}} e^{i\boldsymbol{q}\cdot(\boldsymbol{\xi}+\boldsymbol{R})}\,, \tag{2.94}$$

which leads to the fact that $e^{i\boldsymbol{q}\cdot\boldsymbol{R}}$ must be a constant, i.e.,

$$\boldsymbol{q}\cdot\boldsymbol{R} = 2n\pi + \text{const.}\,, \tag{2.95}$$

then we have

$$\boldsymbol{q} = \boldsymbol{G} + \boldsymbol{k}, \qquad \text{with} \quad \boldsymbol{G} \cdot \boldsymbol{R} = 2n\pi\,, \tag{2.96}$$

where $\boldsymbol{G}$ is the reciprocal vectors and $\boldsymbol{k} \cdot \boldsymbol{R} = \text{const.}$. Replacing $\boldsymbol{q}$ in Eq. (2.92) by the relation (2.96) yields

$$\begin{aligned}\phi(\boldsymbol{\xi}) &= \sum_{\boldsymbol{G}} C_{\boldsymbol{G}+\boldsymbol{k}} e^{i(\boldsymbol{G}+\boldsymbol{k})\cdot\boldsymbol{\xi}} = e^{i\boldsymbol{k}\cdot\boldsymbol{\xi}} \sum_{\boldsymbol{G}} C_{\boldsymbol{G}+\boldsymbol{k}} e^{i\boldsymbol{G}\cdot\boldsymbol{\xi}} \\ &= u_{\boldsymbol{k}}(\boldsymbol{\xi}) e^{i\boldsymbol{k}\cdot\boldsymbol{\xi}}\,,\end{aligned} \tag{2.97}$$

where $\boldsymbol{k}$ is called the Bloch wave vector and $u_{\boldsymbol{k}}(\boldsymbol{\xi})$ is the periodically modulated function defined by

$$u_{\boldsymbol{k}}(\boldsymbol{\xi}) = \sum_{\boldsymbol{G}} C_{\boldsymbol{G}+\boldsymbol{k}} e^{i\boldsymbol{G}\cdot\boldsymbol{\xi}}\,. \tag{2.98}$$

It is easy to find that $u_{\boldsymbol{k}}(\boldsymbol{\xi}+\boldsymbol{R}) = u_{\boldsymbol{k}}(\boldsymbol{\xi})$. We then have proven the Bloch theorem. Note that an equivalent statement of the Bloch theorem follows

$$\begin{aligned}\phi(\boldsymbol{\xi}+\boldsymbol{R}) &= \sum_{\boldsymbol{q}} C_{\boldsymbol{q}} e^{i\boldsymbol{q}\cdot(\boldsymbol{\xi}+\boldsymbol{R})} = \sum_{\boldsymbol{G}} C_{\boldsymbol{G}+\boldsymbol{k}} e^{i(\boldsymbol{G}+\boldsymbol{k})\cdot(\boldsymbol{\xi}+\boldsymbol{R})} = e^{i\boldsymbol{k}\cdot\boldsymbol{R}} \sum_{\boldsymbol{G}} C_{\boldsymbol{G}+\boldsymbol{k}} e^{i(\boldsymbol{G}+\boldsymbol{k})\cdot\boldsymbol{\xi}} \\ &= e^{i\boldsymbol{k}\cdot\boldsymbol{R}} \phi(\boldsymbol{\xi})\,.\end{aligned} \tag{2.99}$$

2.3.2 Band structure in periodic system

The eigenvalues of the optical Hamiltonian can be obtained by calculating the eigenvalue equation (2.86). By doing this, we first expand the periodic potential into a Fourier series

$$V(\boldsymbol{\xi}) = \sum_{n} V_{\boldsymbol{G}} e^{i\boldsymbol{G}\cdot\boldsymbol{\xi}}\,, \tag{2.100}$$

where $V_{\boldsymbol{G}}$ is the Fourier coefficient defined by

$$V_{\boldsymbol{G}} = \frac{1}{R} \int_0^{\boldsymbol{R}} V(\boldsymbol{\xi}) e^{-i\boldsymbol{G}\cdot\boldsymbol{\xi}} d\boldsymbol{\xi}\,, \tag{2.101}$$

with $R = |\boldsymbol{R}|$ and $\boldsymbol{G} \cdot \boldsymbol{R} = 2n\pi$. We rewrite the plane-wave series of the wavefunction Eq. (2.97) as

$$\phi(\boldsymbol{\xi}) = \sum_{\boldsymbol{G}} C_{\boldsymbol{G}}(\boldsymbol{k}) e^{i(\boldsymbol{G}+\boldsymbol{k})\cdot\boldsymbol{\xi}}\,. \tag{2.102}$$

With the help of the Fourier expansion (2.100) of the periodic potential $V(\boldsymbol{\xi})$ and the eigenfunction Eq. (2.102), the eigenvalue equation (2.86) reads

$$\sum_{\boldsymbol{G}} C_{\boldsymbol{G}}(\boldsymbol{k})(\boldsymbol{k}+\boldsymbol{G})^2 e^{i(\boldsymbol{G}+\boldsymbol{k})\cdot\boldsymbol{\xi}} - \sum_{\boldsymbol{G},\boldsymbol{G}'} C_{\boldsymbol{G}}(\boldsymbol{k}) V_{\boldsymbol{G}'} e^{i(\boldsymbol{G}+\boldsymbol{G}'+\boldsymbol{k})\cdot\boldsymbol{\xi}} = \beta \sum_{\boldsymbol{G}} C_{\boldsymbol{G}}(\boldsymbol{k}) e^{i(\boldsymbol{G}+\boldsymbol{k})\cdot\boldsymbol{\xi}}\,, \tag{2.103}$$

which leads to the central equation

$$[(\boldsymbol{k}+\boldsymbol{G})^2-\beta]C_{\boldsymbol{G}}(\boldsymbol{k})-\sum_{\boldsymbol{G}'}V_{\boldsymbol{G}'}C_{\boldsymbol{G}-\boldsymbol{G}'}(\boldsymbol{k})=0\,. \tag{2.104}$$

Eq. (2.104) forms a set of algebraic equations determining the eigenvalues of the system. By solving this set of equations we can get the eigenvalue β for each $\boldsymbol{k}$, which is called the band structure. At the same time, the eigenfunction could be also obtained when the coefficients $C_{\boldsymbol{G}}(\boldsymbol{k})$ are calculated. Note that

$$\begin{aligned}\phi_{\boldsymbol{k}+\boldsymbol{G}'}(\boldsymbol{\xi}) &= \sum_{\boldsymbol{G}} C_{\boldsymbol{G}+\boldsymbol{G}'}(\boldsymbol{k})e^{i(\boldsymbol{G}+\boldsymbol{G}'+\boldsymbol{k})\cdot\boldsymbol{\xi}} \quad (\text{with } \boldsymbol{G}'\cdot\boldsymbol{R}=2m\pi)\\ &= \sum_{\boldsymbol{G}''} C_{\boldsymbol{G}''}(\boldsymbol{k})e^{i(\boldsymbol{G}''+\boldsymbol{k})\cdot\boldsymbol{\xi}} \quad (\text{with } \boldsymbol{G}''=\boldsymbol{G}+\boldsymbol{G}')\\ &= \phi_{\boldsymbol{k}}(\boldsymbol{\xi})\,.\end{aligned} \tag{2.105}$$

It is found from Eq. (2.105) that the band structure should also be periodic with the periodicity $\boldsymbol{G}_0$ defined by $\boldsymbol{G}_0\cdot\boldsymbol{R}=2\pi$. We could then limit our interests for the band structure in one period, for example, $\boldsymbol{k}\in[-\boldsymbol{G}_0/2,\boldsymbol{G}_0/2]$.

In principle, there could be an infinite number for the set of equations to determine β and $C_{\boldsymbol{G}}(\boldsymbol{k})$. It is of course formidable to solve this infinite number of equations. Fortunately, in principle, a truncation of higher components is often possible and sufficient to simplify the mathematical calculations. For instance, for a periodic potential in the one-dimensional case

$$V(\xi_x)=V_a\cos^2(G_0\xi_x)+iV_b\sin(2G_0\xi_x)\,, \tag{2.106}$$

with $G_0R_x=2\pi$ and R_x being the periodicity of the potential, V_a and V_b are the amplitudes of the real and imaginary parts of the potential respectively (usually $V_b=0$). Then the algebraic equations can be safely truncated to

$$\boldsymbol{M}\cdot\boldsymbol{C}=0\,, \tag{2.107}$$

with $\boldsymbol{C}=\{C_2(k),C_1(k),C_0(k),C_{-1}(k),C_{-2}(k)\}^T$ and $\boldsymbol{M}$ defined by

$$\boldsymbol{M}=\begin{bmatrix}(k+2G_0)^2-\beta-V_0 & -V_1 & -V_2 & 0 & 0\\ -V_{-1} & (k+G_0)^2-\beta-V_0 & -V_1 & -V_2 & 0\\ -V_{-2} & -V_{-1} & k^2-\beta-V_0 & -V_1 & -V_2\\ 0 & -V_{-2} & -V_{-1} & (k-G_0)^2-\beta-V_0 & -V_1\\ 0 & 0 & -V_{-2} & -V_{-1} & (k-2G_0)^2-\beta-V_0\end{bmatrix}, \tag{2.108}$$

and V_n is given by

$$V_n=\frac{1}{R_x}\int_0^{R_x}V(\xi_x)e^{-inG_0\xi_x}d\xi_x\,. \tag{2.109}$$

The band structure and eigenfunctions can be obtained by simply solving Eq. (2.107) for each $k\in[-G_0/2,G_0/2]$. Normally, the eigenvalues should be real for a Hermitian Hamiltonian which here means $V_b=0$. However, for $V_b\neq0$, $V(\xi_x)$, which is called parity-

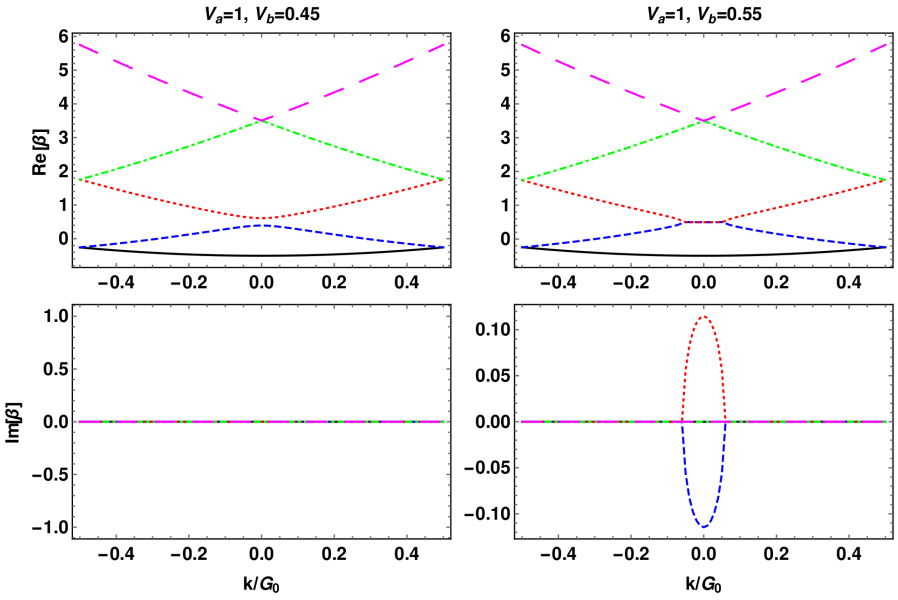

Figure 2.2: Illustration of the band structure for a parity-time symmetric periodic potential. Complex conjugate eigenvalue pairs can appear in the band structure if the ratio V_b/V_a exceeds a certain limit. Here we have chosen $G_0 = 1$.

time symmetric since $V(\xi_x) = V^*(-\xi_x)$, could result in either complex or real eigenvalues depending on the ratio between V_b and V_a, corresponding to a broken or conserved parity-time symmetry [53, 55, 59]. For specific values of V_a and V_b, we have calculated the band structure using Eq. (2.107) as an example shown in Fig. 2.2. It can be seen that complex conjugate eigenvalue pairs enter in the band structure for $V_a = 1$ and $V_b = 0.55$. The properties of the band structure for a parity-time symmetric periodic potential will be further discussed in Sec. 5.2, and we will study light propagation dynamics in detail in the presence of an effective optical potential consisting of both parity-time symmetric and nonlocal nonlinear parts simultaneously.

2.3.3 Band structure in periodic system with nonlocal nonlinear effects

We have shown the procedures how to calculate the band structure of a linear periodic potential in Sec. 2.3.2, however, it only serves an ideal example which manifests the essential physical nature of a periodic system. Practically, there are plenty of situations where different mechanisms could affect the linear periodic potential, for instance, the electronic structure in solids where electron-electron interactions would lead to an effective nonlinear potential. Consequently, the calculation of the band structure becomes demanding and inefficient. In this section we consider a specific case where the nonlocal nonlinear effects come into play. Then the band structure depends not only on the periodic potential but also the nonlocal nonlinear effects governed by the eigenfunction itself. We first write down the optical Schrödinger equation including a nonlocal nonlinear potential as

$$i\frac{\partial\psi(\boldsymbol{\xi},\zeta)}{\partial\zeta} = -\frac{\partial^2}{\partial\boldsymbol{\xi}^2}\psi(\boldsymbol{\xi},\zeta) - V(\boldsymbol{\xi})\psi(\boldsymbol{\xi},\zeta) - C_{nl}\psi(\boldsymbol{\xi},\zeta)\int_{-\infty}^{\infty} K(\boldsymbol{\xi}-\boldsymbol{\xi}')|\psi(\boldsymbol{\xi}',\zeta)|^2 d\boldsymbol{\xi}' \,. \tag{2.110}$$

Thus the eigenvalue equation reads

$$\beta\phi(\boldsymbol{\xi}) = -\frac{\partial^2}{\partial\boldsymbol{\xi}^2}\phi(\boldsymbol{\xi}) - V(\boldsymbol{\xi})\phi(\boldsymbol{\xi}) - C_{nl}\phi(\boldsymbol{\xi})\int_{-\infty}^{\infty} K(\boldsymbol{\xi}-\boldsymbol{\xi}')|\phi(\boldsymbol{\xi}')|^2 d\boldsymbol{\xi}' \,. \tag{2.111}$$

Note that the solutions $\psi(\boldsymbol{\xi},\zeta) = \phi(\boldsymbol{\xi})e^{-i\beta\zeta}$ satisfy Eq. (2.110) only for real β. For complex β, $\psi(\boldsymbol{\xi},\zeta) = \phi(\boldsymbol{\xi})e^{-i\beta\zeta}$, instead, provides an adiabatic approximation to the actual evolution [182, 183].

For a periodic potential $V(\boldsymbol{\xi}) = V(\boldsymbol{\xi}+\boldsymbol{R})$, we can then apply the Bloch theorem to calculate the band structrue. With the ansatz Eq. (2.102), we can first rewrite the nonlocal nonlinear integral in Eq. (2.111) as

$$\begin{aligned}
\int_{-\infty}^{\infty} K(\boldsymbol{\xi}-\boldsymbol{\xi}')|\psi(\boldsymbol{\xi}')|^2 d\boldsymbol{\xi}' &= \int_{-\infty}^{\infty} K(\boldsymbol{\xi}-\boldsymbol{\xi}') \sum_{\boldsymbol{G}',\boldsymbol{G}''} C_{\boldsymbol{G}'}(\boldsymbol{k})C^*_{\boldsymbol{G}''}(\boldsymbol{k}) e^{i(\boldsymbol{G}'-\boldsymbol{G}'')\cdot\boldsymbol{\xi}'} d\boldsymbol{\xi}' \\
&= \sum_{\boldsymbol{G}',\boldsymbol{G}''} C_{\boldsymbol{G}'}(\boldsymbol{k})C^*_{\boldsymbol{G}''}(\boldsymbol{k}) \int_{-\infty}^{\infty} K(\boldsymbol{\xi}-\boldsymbol{\xi}') e^{i(\boldsymbol{G}'-\boldsymbol{G}'')\cdot\boldsymbol{\xi}'} d\boldsymbol{\xi}' \\
&= \sum_{\boldsymbol{G}',\boldsymbol{G}''} C_{\boldsymbol{G}'}(\boldsymbol{k})C^*_{\boldsymbol{G}''}(\boldsymbol{k}) \int_{-\infty}^{\infty} K(\boldsymbol{\xi}'') e^{i(\boldsymbol{G}'-\boldsymbol{G}'')\cdot(\boldsymbol{\xi}-\boldsymbol{\xi}'')} d\boldsymbol{\xi}'' \\
&= \sum_{\boldsymbol{G}',\boldsymbol{G}''} C_{\boldsymbol{G}'}(\boldsymbol{k})C^*_{\boldsymbol{G}''}(\boldsymbol{k}) e^{i(\boldsymbol{G}'-\boldsymbol{G}'')\cdot\boldsymbol{\xi}} \int_{-\infty}^{\infty} K(\boldsymbol{\xi}'') e^{-i(\boldsymbol{G}'-\boldsymbol{G}'')\cdot\boldsymbol{\xi}''} d\boldsymbol{\xi}'' \\
&= \sum_{\boldsymbol{G}',\boldsymbol{G}''} C_{\boldsymbol{G}'}(\boldsymbol{k})C^*_{\boldsymbol{G}''}(\boldsymbol{k}) K_F(\boldsymbol{G}'-\boldsymbol{G}'') e^{i(\boldsymbol{G}'-\boldsymbol{G}'')\cdot\boldsymbol{\xi}} \,,
\end{aligned} \tag{2.112}$$

where $K_F(\boldsymbol{G})$ is the Fourier transformation of the kernel function $K(\boldsymbol{\xi})$. Replacing the nonlocal integral in Eq. (2.111) with Eq. (2.112) gives

$$\begin{aligned}
&\sum_{\boldsymbol{G}} C_{\boldsymbol{G}}(\boldsymbol{k})[(\boldsymbol{k}+\boldsymbol{G})^2-\beta]e^{i(\boldsymbol{G}+\boldsymbol{k})\cdot\boldsymbol{\xi}} - \sum_{\boldsymbol{G},\boldsymbol{G}'} C_{\boldsymbol{G}}(\boldsymbol{k})V_{\boldsymbol{G}'}e^{i(\boldsymbol{G}+\boldsymbol{G}'+\boldsymbol{k})\cdot\boldsymbol{\xi}} \\
&= C_{nl}\sum_{\boldsymbol{G},\boldsymbol{G}',\boldsymbol{G}''} C_{\boldsymbol{G}}(\boldsymbol{k})C_{\boldsymbol{G}'}(\boldsymbol{k})C^*_{\boldsymbol{G}''}(\boldsymbol{k})K_F(\boldsymbol{G}'-\boldsymbol{G}'')e^{i(\boldsymbol{G}+\boldsymbol{G}'-\boldsymbol{G}''+\boldsymbol{k})\cdot\boldsymbol{\xi}} \,.
\end{aligned} \tag{2.113}$$

In order to avoid confusion, here we need to point out that the repeated $\boldsymbol{G}$ and $\boldsymbol{G}'$ which denotes the summations in the three terms in Eq. (2.113) is independent from each other. Finally, the central equation can be derived from Eq. (2.113)

$$\begin{aligned}
&C_{\boldsymbol{G}}(\boldsymbol{k})[(\boldsymbol{k}+\boldsymbol{G})^2-\beta] - \sum_{\boldsymbol{G}'} V_{\boldsymbol{G}'}C_{\boldsymbol{G}-\boldsymbol{G}'}(\boldsymbol{k}) \\
&- C_{nl}\sum_{\boldsymbol{G}',\boldsymbol{G}''} C_{\boldsymbol{G}'''}(\boldsymbol{k})C_{\boldsymbol{G}'}(\boldsymbol{k})C^*_{\boldsymbol{G}''}(\boldsymbol{k})K_F(\boldsymbol{G}'-\boldsymbol{G}'') = 0 \,,
\end{aligned} \tag{2.114}$$

where $\boldsymbol{G}''' = \boldsymbol{G}-\boldsymbol{G}'+\boldsymbol{G}''$. By truncating $\boldsymbol{G}$ to a certain limit $\boldsymbol{G}_{max}$ and then calculating the central equation (2.114), the band structure and the eigenfunctions can be obtained for a periodic potential mixed by a nonlocal nonlinear counterpart. Note that by setting $K_F(\boldsymbol{G}'-\boldsymbol{G}'') = 1$, we arrive at the local nonlinear regime.

Calculation of the band structure turns out to be far more challenging for Eq. (2.114) than for Eq. (2.104), owing to the presence of the nonlocal nonlinear effects. In order

to obtain the band structure, a self-consistent field (SCF) theory [184, 185] is usually employed to solve Eq. (2.114) iteratively. In general, the SCF theory states that the derived wavefunction $\phi(\boldsymbol{\xi})$ of Eq. (2.114) must satisfy the central equation (2.114) which includes the nonlocal nonlinear effects generated by the wavefunction $\phi(\boldsymbol{\xi})$ itself. Mathematically, it means that for an input wavefunction $\psi_{\text{in}}(\boldsymbol{\xi})$ which determines the nonlocal nonlinear effects, the solution of Eq. (2.114), $\psi_{\text{out}}(\boldsymbol{\xi})$, should be identical to the input wavefunction, i.e., $\psi_{\text{in}}(\boldsymbol{\xi}) = \psi_{\text{out}}(\boldsymbol{\xi})$. In particular, it involves the following steps:

1. Choose an initial guess wavefunction, $\psi_{\text{in}}^{(0)}(\boldsymbol{\xi}) = \{C_{\boldsymbol{G}}\}$, and a preselected small number ϵ, e.g., $\epsilon = 10^{-8}$. Set the eigenfunction $\psi_{\text{in}}^{(n)}(\boldsymbol{\xi}) = \psi_{\text{in}}^{(0)}(\boldsymbol{\xi})$.

2. Calculate the nonlocal nonlinear potential determined by $\psi_{\text{in}}^{(n)}(\boldsymbol{\xi})$.

3. Solve the central equation (2.114) to get the eigenvalue β_n and the solution $\psi_{\text{out}}^{(n)}(\boldsymbol{\xi}) = \{C'_{\boldsymbol{G}}\}$.

4. Compare the two input and output wavefunctions $\psi_{\text{in}}^{(n)}(\boldsymbol{\xi})$ and $\psi_{\text{out}}^{(n)}(\boldsymbol{\xi})$. If $\|\psi_{\text{out}}^{(n)}(\boldsymbol{\xi}) - \psi_{\text{in}}^{(n)}(\boldsymbol{\xi})\| \geq \epsilon$, update the input wavefunction, e.g., $\psi_{\text{in}}^{(n+1)}(\boldsymbol{\xi}) = (1-\alpha)\psi_{\text{in}}^{(n)}(\boldsymbol{\xi}) + \alpha\psi_{\text{out}}^{(n)}(\boldsymbol{\xi})$ for a suitable choice of $\alpha \in [0, 1]$, and go to Step 2.

5. If $\|\psi_{\text{out}}^{(n)}(\boldsymbol{\xi}) - \psi_{\text{in}}^{(n)}(\boldsymbol{\xi})\| \leq \epsilon$, stop the iteration. β_n and $\psi_{\text{out}}^{(n)}(\boldsymbol{\xi})$ are then considered as the self-consistent eigenvalue and eigenfunction of Eq. (2.114) respectively.

It seems to be clear that the band structure could be determined in the presence of the nonlocal nonlinear effects by essentially proceeding this iterative calculation for each $\boldsymbol{k} \in [-\boldsymbol{G}_0/2, \boldsymbol{G}_0/2]$. However, mathematical difficulties have been hidden behind these general procedures. Specifically, there is no guarantee that this self-consistent iteration will converge. In other words, it is normally divergent. For the sake of helping convergence, massive mathematical algorithms have been developed to achieve or even improve the convergence of the self-consistent calculation. Among these algorithms are Anderson mixing [186], Broyden's quasi-Newton-Raphson method [187–190], modified Broyden method [191–195], Banach fix-point theorem [196], to mention a few. Since we concentrate on the physical properties of the system, we would skip here the detailed discussion of these exact algorithms. Further rigorous description of these algorithms can be easily found in the given references or other textbooks in related topics.

Chapter 3

Validity of the paraxial approximation

In this chapter, we will first examine the validity of the paraxial approximation by studying beam propagation in an optically written waveguide structure, before we dive into a deeper level to investigate the paraxial propagation dynamics in various systems exhibiting nonlocal linear or nonlinear effects in the following chapters. The waveguide structure, which leads to diffractionless light propagation, is imprinted in a five-level atomic medium driven by an incoherent pump and two spatially dependent control and plane-wave laser fields as introduced in Sec. 3.1. We then first study beam propagation in a single optically written waveguide in Sec. 3.2.1, and find that the paraxial approximation does not provide an accurate description of the probe propagation, given that the beam size is not large enough comparing to its wavelength. Furthermore, we employ coherent control fields consisting of two parallel and one tilted Gaussian beams to produce a branched waveguide structure in Sec. 3.2.2. Beam propagation dynamics is carefully investigated beyond paraxial approximation in this branched waveguide structure, which allows selective steering of the probe beam into different branches. In the end, we summarizes all the results in Sec. 3.3.

3.1 Theoretical model

3.1.1 Equations of motion

The five-level atomic system we consider is shown in Fig. 3.1. This model has been proposed previously in a different context for generating high index of refraction contrast with low absorption [197]. The two transitions $|2\rangle \leftrightarrow |4\rangle$ and $|3\rangle \leftrightarrow |5\rangle$ are driven by two far-detuned coherent laser fields with Rabi frequencies Ω_s and Ω_c respectively, and a weak probe is coupled to both transitions $|1\rangle \leftrightarrow |4\rangle$ and $|4\rangle \leftrightarrow |5\rangle$ with Rabi frequencies Ω_{p1} and Ω_{p2} respectively. An incoherent pump field is applied to transition $|1\rangle \rightarrow |4\rangle$ to provide a population inversion.

The electric fields of the three beams are defined as

$$\boldsymbol{\xi}_j(\boldsymbol{r},t) = \frac{1}{2}E_j(\boldsymbol{r},t)\,\boldsymbol{e}_j\,e^{-i\omega_j t+i\boldsymbol{k}_j\cdot\boldsymbol{r}} + \text{c.c.}\,, \tag{3.1}$$

where $E_j(\boldsymbol{r},t)$, $\boldsymbol{e}_j$, ω_j and $\boldsymbol{k}_j$ are the slowly varying envelopes, the unit polarization vectors, angular frequencies, and wave vectors of the corresponding electric fields respectively. The index $j \in \{p,s,c\}$ labels the three fields. Under the dipole and rotating-wave approximations, the Hamiltonian of the system in the interaction picture can be written as

$$\begin{aligned} H_I/\hbar = &-(\Delta_{p1}-\Delta_s)|2\rangle\langle 2| - (\Delta_{p1}+\Delta_{p2}-\Delta_c)|3\rangle\langle 3| - \Delta_{p1}|4\rangle\langle 4| - (\Delta_{p1}+\Delta_{p2})|5\rangle\langle 5| \\ &-(\Omega_{p1}|4\rangle\langle 1| + \Omega_{p2}|5\rangle\langle 4| + \Omega_s|4\rangle\langle 2| + \Omega_c|5\rangle\langle 3| + \text{H.c.})\,, \end{aligned} \tag{3.2}$$

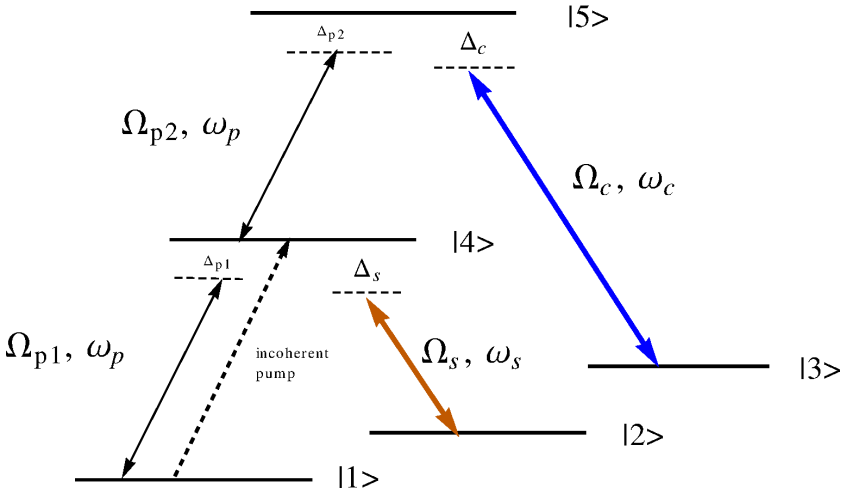

Figure 3.1: The considered scheme of a five-level system. The probe field couples to transitions $|1\rangle \leftrightarrow |4\rangle$ and $|4\rangle \leftrightarrow |5\rangle$ and the two coherent control laser fields Ω_s, Ω_c are far-detuned from respective transition frequencies in order to split states $|4\rangle$ and $|5\rangle$ into desired dressed states. An incoherent pump control field is applied to $|1\rangle \leftrightarrow |4\rangle$ to achieve a population inversion. The control fields modify the probe field coupling to achieve high refractive index contrast with low absorption.

where $\Delta_{p1} = \omega_p - \omega_{41}$, $\Delta_{p2} = \omega_p - \omega_{54}$, $\Delta_s = \omega_s - \omega_{42}$, and $\Delta_c = \omega_c - \omega_{53}$ are the detunings of the laser fields, and the Rabi frequencies of the fields are defined as $\Omega_{p1} = E_p \boldsymbol{e}_p \cdot \boldsymbol{d}_{41}/2\hbar$, $\Omega_{p2} = E_p \boldsymbol{e}_p \cdot \boldsymbol{d}_{54}/2\hbar$, $\Omega_s = E_s \boldsymbol{e}_s \cdot \boldsymbol{d}_{42}/2\hbar$, and $\Omega_c = E_c \boldsymbol{e}_c \cdot \boldsymbol{d}_{53}/2\hbar$, just as we have done in Sec. 2.1. Here, $\boldsymbol{d}_{ij}$ are the dipole moments of the respective transitions, and we have simplified the notation $E_j(\boldsymbol{r}, t)$ to E_j ($j \in \{p, s, c\}$). The master equation of motion follows as

$$\dot{\rho} = -\frac{i}{\hbar}[H_I, \rho] - \mathcal{L}\rho\,, \tag{3.3}$$

and $\mathcal{L}\rho$ represents the incoherent contributions given by

$$\mathcal{L}\rho = \mathcal{L}^{\gamma}_{41}\rho + \mathcal{L}^{\gamma}_{42}\rho + \mathcal{L}^{\gamma}_{53}\rho + \mathcal{L}^{\gamma}_{54}\rho + \mathcal{L}^{d}\rho + \mathcal{L}^{p}\rho\,, \tag{3.4a}$$

$$\mathcal{L}^{\gamma}_{jk}\rho = \frac{\Gamma_{jk}}{2}\left(|j\rangle\langle j|\,\rho + \rho\,|j\rangle\langle j| - 2|k\rangle\langle j|\,\rho\,|j\rangle\langle k|\right)\,, \tag{3.4b}$$

$$\mathcal{L}^{d}\rho = \sum_{j\neq k}\gamma^{d}_{jk}\,|j\rangle\langle k|\,, \tag{3.4c}$$

$$\mathcal{L}^{p}\rho = \frac{p}{2}\left(|1\rangle\langle 1|\,\rho + \rho\,|1\rangle\langle 1| - 2|4\rangle\langle 1|\,\rho\,|1\rangle\langle 4|\right)\,, \tag{3.4d}$$

where $\mathcal{L}^{\gamma}_{jk}\rho$ describes spontaneous emission from $|j\rangle$ to $|k\rangle$ with rate Γ_{jk}. And $\mathcal{L}^{d}\rho$ models additional pure dephasing for ρ_{jk} with rate γ^{d}_{jk} such that the total damping rate of this coherence is $\gamma_{jk} = \gamma^{d}_{jk} + (\Gamma_j + \Gamma_k)/2$, with $\Gamma_j = \sum_k \Gamma_{jk}$ the total decay rate out of state $|j\rangle$. The last contribution $\mathcal{L}^{p}\rho$ describes the incoherent pumping from $|1\rangle$ to $|4\rangle$ with rate p.

The equations of motion for the density matrix elements can easily be derived to give

$$\dot{\rho}_{11} = -p\rho_{11} - i\left(\Omega_{p1}\rho_{14} - \Omega_{p1}\rho_{41}\right) + \Gamma_{41}\rho_{44}\,, \tag{3.5a}$$

$$\dot{\rho}_{22} = -i\Omega_s(\rho_{24} - \rho_{42}) + \Gamma_{42}\rho_{44}\,, \tag{3.5b}$$

$$\dot{\rho}_{44} = p\rho_{11} - (\Gamma_{41} + \Gamma_{42})\,\rho_{44} - i\,(-\Omega_{p1}\rho_{14} - \Omega_s\rho_{24} + \Omega_{p1}\rho_{41} + \Omega_s\rho_{42} + \Omega_{p2}\rho_{45} - \Omega_{p2}\rho_{54}) + \Gamma_{54}\rho_{55}\,, \tag{3.5c}$$

$$\dot{\rho}_{55} = -i\,(-\Omega_c\rho_{35} - \Omega_{p2}\rho_{45} + \Omega_c\rho_{53} + \Omega_{p2}\rho_{54}) - (\Gamma_{53} + \Gamma_{54})\,\rho_{55}\,, \tag{3.5d}$$

$$\dot{\rho}_{42} = i(\Delta_s + i\gamma_{42})\rho_{42} + i\Omega_s(\rho_{22} - \rho_{44}) + i\Omega_{p1}\rho_{12} + i\Omega_{p2}\rho_{52}\,, \tag{3.5e}$$

$$\dot{\rho}_{54} = -\gamma_{54}\rho_{54} - i\,(-\Omega_c\rho_{34} - \Omega_{p2}\rho_{44} + \Omega_{p1}\rho_{51} + \Omega_s\rho_{52} - \Delta_{p2}\rho_{54} + \Omega_{p2}\rho_{55})\,, \tag{3.5f}$$

$$\dot{\rho}_{41} = -\,(p/2 + \gamma_{41})\,\rho_{41} - i\,(-\Omega_{p1}\rho_{11} - \Omega_s\rho_{21} - \Delta_{p1}\rho_{41} + \Omega_{p1}\rho_{44} - \Omega_{p2}\rho_{51})\,, \tag{3.5g}$$

$$\dot{\rho}_{34} = -\gamma_{43}\rho_{34} - i\,(\Omega_{p1}\rho_{31} + \Omega_s\rho_{32} + (\Delta_c - \Delta_{p2})\rho_{34} + \Omega_{p2}\rho_{35} - \Omega_c\rho_{54})\,, \tag{3.5h}$$

$$\dot{\rho}_{52} = -\gamma_{52}\rho_{52} - i\,\{-\Omega_c\rho_{32} - \Omega_{p2}\rho_{42} - (\Delta_s + \Delta_{p2})\rho_{52} + \Omega_s\rho_{54}\}\,, \tag{3.5i}$$

$$\dot{\rho}_{21} = -\,(p/2 + \gamma_{21})\,\rho_{21} - i\,\{(-\Delta_{p1} + \Delta_s)\rho_{21} + \Omega_{p1}\rho_{24} - \Omega_s\rho_{41}\}\,, \tag{3.5j}$$

$$\dot{\rho}_{32} = -\gamma_{32}\rho_{32} - i\,\{(\Delta_c - \Delta_s - \Delta_{p2})\rho_{32} + \Omega_s\rho_{34} - \Omega_c\rho_{52}\}\,. \tag{3.5k}$$

The remaining equations follow from the constraints $\sum_i \rho_{ii} = 1$ and $\rho_{ij} = \rho^*_{ji}$.

3.1.2 Steady-state solution for the linear susceptibility

We assume the probe field to be weak enough to be treated as a perturbation to the system in linear order. With the help of perturbation theory, the related zeroth and first-order contributions for ρ_{ij} are obtained as

$$\rho^{(0)}_{11} = \frac{2\gamma_{42}\Gamma_{41}\Omega_s^2}{p\gamma_{42}^2\Gamma_{42} + p\Gamma_{42}\Delta_s^2 + 2\gamma_{42}\,(2p + \Gamma_{41})\,\Omega_s^2}\,, \tag{3.6a}$$

$$\rho^{(0)}_{22} = \frac{p\,(\gamma_{42}^2\Gamma_{42} + \Gamma_{42}\Delta_s^2 + 2\gamma_{42}\Omega_s^2)}{p\gamma_{42}^2\Gamma_{42} + p\Gamma_{42}\Delta_s^2 + 2\gamma_{42}\,(2p + \Gamma_{41})\,\Omega_s^2}\,, \tag{3.6b}$$

$$\rho^{(0)}_{44} = \frac{2p\gamma_{42}\Omega_s^2}{p\gamma_{42}^2\Gamma_{42} + p\Gamma_{42}\Delta_s^2 + 2\gamma_{42}\,(2p + \Gamma_{41})\,\Omega_s^2}\,, \tag{3.6c}$$

$$\rho^{(0)}_{55} = 0\,, \tag{3.6d}$$

$$\rho^{(1)}_{41} = \frac{\left(\rho^{(0)}_{44} - \rho^{(0)}_{11}\right)\Omega_{p1}}{\Delta_{p1} + i(\gamma_{41} + \frac{p}{2}) + \frac{\Omega_s^2}{\Delta_s - \Delta_{p1} - i(\gamma_{21} + p/2)}}\,, \tag{3.6e}$$

$$\rho^{(1)}_{54} = \frac{A\left(\rho^{(0)}_{44} - \rho^{(0)}_{55}\right)\Omega_{p2}}{B}\,. \tag{3.6f}$$

The explicit expressions for A, B in Eqs. (3.6) are as follows:

$$A = \Delta_{32}\left[\Omega_c^2 - \Omega_s^2 - \Delta_{52}\Delta_{32}\right]\left[-\Delta_{43} + \frac{\Omega_c^2}{\Delta_{32}} + \frac{\Omega_s^2(\Omega_s^2 - \Omega_c^2 - \Delta_{43}\Delta_{32})}{\Delta_{32}(\Omega_c^2 - \Omega_s^2 - \Delta_{52}\Delta_{32})}\right]\,, \tag{3.7a}$$

$$B = \Omega_c^2(\Delta_{32} + \Delta_{54})(\Delta_{43}\Delta_{32} - \Omega_s^2 + \Omega_c^2) + (\Omega_c^2 - \Omega_s^2 - \Delta_{52}\Delta_{32})\left[\Delta_{32}(\Delta_{54}\Delta_{43} - \Omega_c^2) - \Delta_{54}\Omega_s^2\right]\,, \tag{3.7b}$$

with $\Delta_{32} = \Delta_{p2} + \Delta_s - \Delta_c + i\gamma_{32}, \Delta_{43} = \Delta_{p2} - \Delta_c + i\gamma_{43}, \Delta_{52} = \Delta_{p2} + \Delta_s + i\gamma_{52}$ and $\Delta_{54} = \Delta_{p2} + i\gamma_{54}$.

To elucidate the role of the different coupling fields, we first reduce the level structure to a three-level ladder system, by switching off the two far-detuned laser fields Ω_c and Ω_s. Then, the linear susceptibility for the probe simplifies to

$$\chi(\omega_p) = \frac{3n_0\lambda_p^3}{8\pi^2}\left(\frac{\Gamma_{41}(\rho_{44}-\rho_{11})}{\Delta_{p1}+i(\gamma_{41}+\frac{p}{2})}+\frac{\Gamma_{54}(\rho_{55}-\rho_{44})}{\Delta_{p2}+i\gamma_{54}}\right), \tag{3.8}$$

where n_0 is the atomic density and λ_p is the wave length of the probe field. The terms in the right hand side of Eq. (3.8) describe the two individual contributions coming from the two two-level subsystems in the three-level ladder structure. Since we are interested in the beam propagation dynamics within or beyond paraxial approximation, thus the inevitable absorption due to spontaneous decay and dephasing should be minimized as possible. To achieve the desired refractive index modulation without absorption, three conditions should be satisfied in Eq. (3.8) according to Ref. [197]. First, the population inversions on the two transitions should be matched. Second, the decoherence rates should be comparable. Third, the two-photon resonance should be fulfilled for the two transitions. These conditions can be expressed as $\Gamma_{41}(\rho_{44}-\rho_{11}) = \Gamma_{54}(\rho_{55}-\rho_{44})$, $\gamma_{54} = \gamma_{41} + p/2$ and $\Delta_{p1} + \Delta_{p2} = 0$. A maximum refractive index modulation can then be realized if $\gamma_{41} = \pm\Delta_{p1} - p/2$. In this ideal case, the refractive index is increased by a factor of 2, with absorption canceled at the same time. However, it is hard to find a real atomic system in which these conditions are satisfied simultaneously. To relax the stringent conditions, it has been suggested in Ref. [197] to introduce the two far-detuned laser fields coupling $|4\rangle$ and $|5\rangle$ to auxiliary states to induce Stark shifts. The Stark shifts of $|4\rangle$ and $|5\rangle$ together with modifications to the decoherence rates of the Stark sublevels can be controlled by tuning the intensities and detunings of the two laser fields. This way, the two transitions for the probe can be modified to one's advantage. This leads to the five-level scheme shown in Fig. 3.1, in which the two upper states are coupled by two external far-detuned laser fields Ω_s and Ω_c. By appropriately choosing the parameters of these laser fields, one can achieve strong refractive index modulation with minimized absorption or even gain, even in realistic level schemes.

3.1.3 Realization of spatial waveguide-like structures

From Eqs. (3.6), the linear susceptibility of the probe field can be written as

$$\chi^{(1)} = \frac{3n_0\lambda_p^3}{8\pi^2}\left(\frac{\Gamma_{41}\rho_{41}^{(1)}}{\Omega_{p1}}+\frac{\Gamma_{54}\rho_{54}^{(1)}}{\Omega_{p2}}\right). \tag{3.9}$$

We now assume that the control field has a spatial Gaussian profile, i.e.

$$\Omega_s = \Omega_{s0}\, e^{-\frac{x^2}{2w_s^2}}, \tag{3.10}$$

where w_s is the width of the intensity profile. This spatial dependence of the control field creates a modulation of the medium susceptibility in space, which can be managed to induce a waveguide-like structure. In order to achieve maximum refractive index modulation, the peak Rabi frequency of the laser field Ω_s should meet the condition $\Omega_{s0} = \sqrt{2\gamma_{41}\Delta_s}$. Assuming these conditions, the real and imaginary parts of the linear susceptibility, which correspond to the dispersion and absorption of the atomic medium, respectively, are shown in Fig. 3.2(a). Clearly, the real part of the susceptibility resembles a waveguide structure, whereas absorption is low.

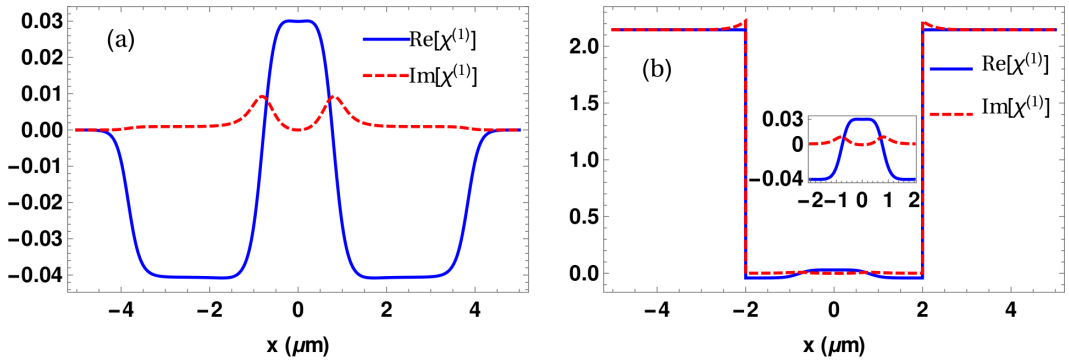

Figure 3.2: Real (blue solid line) and imaginary (red dashed line) parts of the linear susceptibility obtained from Eq. (3.9) as a function of the position in the presence of a Gaussian control field Ω_s. Panel (a) shows results for a constant incoherent pump rate, whereas (b) shows results for spatially dependent pump as explained in the main text. The inset in (b) depicts the detailed structure of the linear susceptibility in the central area which is similar to that in (a). Note that the profile of the real part in the central region forms a waveguide structure. Parameters are chosen as: $n_0 = 1.4 \times 10^{27}$ m^{-3}, $\lambda_p = 813.2$ nm, $\gamma_{54}^d = 0.8$ GHz, $\gamma_{41}^d = \gamma_{42}^d = 0.3$ GHz, $\gamma_{43}^d = 0.2$ GHz, $\gamma_{52}^d = \gamma_{21}^d = \gamma_{32}^d = 0$, $\Gamma_{41} = \Gamma_{42} = 45$ Hz, $\Gamma_{54} = 15$ Hz, $\Delta_{p1} = -\gamma_{41}$, $\Delta_{p2} = 19.7$ GHz, $\Delta_s = 10.0$ GHz, $\Delta_c = 18.0$ GHz, $\Omega_{s0} = \sqrt{2\gamma_{41}\Delta_s}$, $\Omega_c = 5.2$ GHz, $w_s = 1.0$ μm, and $p = 45.9943$ Hz.

The parameters in Fig. 3.2 are chosen to fulfill $\Delta_{p1}, \Delta_s, \gamma_{54}, \gamma_{41} \gg \Gamma_{54}, \Gamma_{41}, p$. In this limit, Eq. (3.6e) can be simplified to

$$\rho_{41}^{(1)} = \frac{\left(\rho_{44}^{(0)} - \rho_{11}^{(0)}\right)\Omega_{p1}}{-\gamma_{41} + i\gamma_{41} + \frac{\Omega_s^2}{\Delta_s + \gamma_{41}}}. \tag{3.11}$$

In the central area of Ω_s defined by Eq. (3.10), the part $\Omega_s^2/(\Delta_s + \gamma_{41}) - \gamma_{41} \simeq \gamma_{41}$ in the dominator of Eq. (3.11), and the refractive index is maximized as desired together with gain. At the same time, the transition $|5\rangle \leftrightarrow |4\rangle$ will give maximum refractive index accompanied with absorption. Those two transitions together result in a maximum refractive index for the probe with almost canceled absorption in the central area of Ω_s as shown in Fig. 3.2(a). In contrast, in the two wings of Ω_s, the refractive index is minimized for transition $|4\rangle \leftrightarrow |1\rangle$ with gain since now $\Omega_s^2/(\Delta_s + \gamma_{41}) - \gamma_{41} \simeq -\gamma_{41}$. Meanwhile, a minimal refractive index followed with absorption is obtained for transition $|5\rangle \leftrightarrow |4\rangle$. In total, a minimal refractive index with little absorption is obtained for the probe.

In order to check the validity of the perturbation approximation in the far-detuned regime, we also calculated the atomic susceptibility to all orders of E_p by numerically solving Eq. (3.5) in steady state. For a weak probe field $\Omega_{p1} \sim \Gamma_{41}$, it is indeed indistinguishable from the linear susceptibility shown in Fig. 3.2(a).

3.1.4 Incoherent pumping

In this section, we discuss the possibility to control the optically written waveguide structure by means of an incoherent pump field. As shown in Fig. 3.2(a), the absorption becomes weaker in the two wings than in the central area. In practical implementations, this may lead to stray fields outside the waveguide region caused by the part of the probe field leaking from the central part of the waveguide-like structure into the weakly absorbing wings. This stray fields could possibly affect or even contaminate the beam

propagation dynamics, and thus rendering the analytical distinguishment of propagation dynamics with or without paraxial propagation to be more challenging. In order to eliminate this leaking light, we propose a spatially dependent incoherent pump field given as follows

$$p(\Omega_s) = \begin{cases} p & \text{if} \quad (\frac{\Omega_s}{\Omega_{s0}})^2 \geqslant e^{-4}\,, \\ 0 & \text{if} \quad (\frac{\Omega_s}{\Omega_{s0}})^2 < e^{-4}\,. \end{cases} \tag{3.12}$$

The resulting linear susceptibility is shown in Fig. 3.2(b), for otherwise same parameters as in (a). It can be seen that the central region featuring the waveguide-like structure remains the same as in Fig. 3.2(a) as expected. In contrast, in both side wings, where $(\Omega_s/\Omega_{s0})^2 < e^{-4}$, the incoherent pump vanishes, such that the atoms remain in the ground state $|1\rangle$ according to Eq. (3.6a). Thus, the medium acts as an absorber outside the waveguide region, and stray-fields are thus reduced. In the following, the spatially-dependent incoherent pump is used in the numerical simulations.

3.2 Propagation dynamics within and beyond the paraxial approximation

The propagation dynamics of the probe field is governed by Maxwell's equations. Without applying the paraxial approximation, the wave equation for the probe field propagating along z direction can be derived as Eq. (2.24) and also as in Ref. [198]. Here we rewrite it as follows

$$\frac{\partial E_p}{\partial z} = \frac{i}{2k_p}(\nabla_\perp^2 + \frac{\partial^2}{\partial z^2})E_p + \frac{ik_p}{2}\chi^{(1)}E_p\,, \tag{3.13}$$

where $k_p = \omega_p/c$ with c the speed of light in vacuum and $\nabla_\perp^2 = \partial^2/\partial x^2 + \partial^2/\partial y^2$. In Eq. (3.13), $i\nabla_\perp^2/2k_p$ accounts for the paraxial diffraction, while $(i/2k_p)\partial^2/\partial z^2$ introduces effects beyond the paraxial approximation. The paraxial propagation equation can be obtained as Eq. (2.26) by dropping $(i/2k_p)\partial^2/\partial z^2$.

In order to obtain the propagation dynamics beyond paraxial approximation in the induced waveguide structure, we make use of the finite-difference time domain (FDTD) technique [199] provided by the software package MEEP [200] to numerically solve Maxwell's equations in the presence of atomic effects. In the case of paraixal propagation dynamics, we drop the term $(i/2k_p)\partial^2 E_p/\partial z^2$ in Eq. (3.13), and then solve the resulting equation using the Strang split operator method [201]. In both numerical simulations, all fields are chosen as continuous waves.

3.2.1 Beam propagation in a single optically induced waveguide

As a first step, we study two-dimensional (2D) light propagation of a Gaussian probe field along z in a single written waveguide. The probe field has a width of $w_p = 1.0$ μm at $z = 0$. The medium is prepared by a Gaussian control laser field Ω_s with width $w_s = 1$ μm at $z = 0$ and specific beam profile given in Eq. (3.10). Note that we do not take into account the spreading of the field Ω_s since we are focused on the propagation dynamics of the probe field. Fig. 3.3 shows the numerical results for the probe propagation for a distance of $z_0 = 20\mu$m (about 2.59 Rayleigh lengths $z_R = 2\pi w_p^2/\lambda_p \simeq 7.73\mu$m). The left panel compares three different cases. (a) shows the probe propagating in free space. Clearly, the diffraction-induced spreading of the probe beam can be seen. In

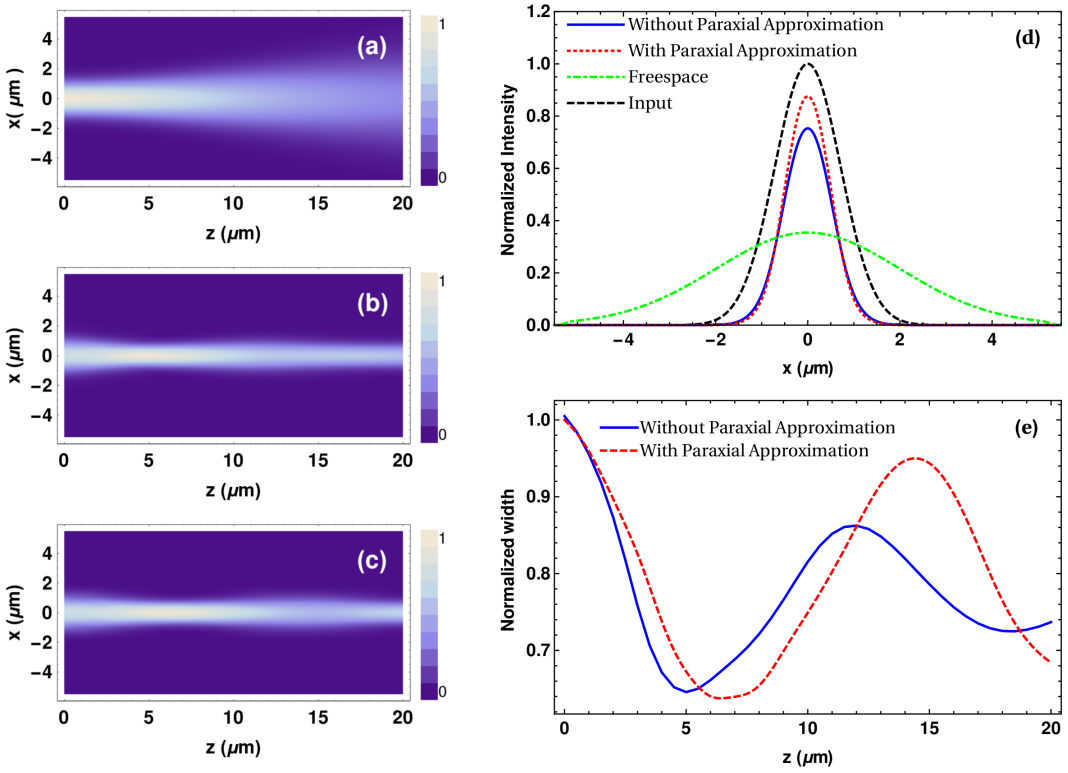

Figure 3.3: Probe propagation within or beyond the paraxial approximation in a single optically written waveguide-like structure. (a) shows the free-space propagation which is taken as a simple example to give the first expression of light propagation, (b) and (c) correspond to the probe propagation beyond or within the paraxial approximation in the five-level atomic medium respectively. Owing to the induced waveguide structure, the probe is mainly confined in the waveguide, except for some stray fields. As already shown in (b) and (c), difference appears between the results with and without paraxial approximation. In more detail, (d) shows the output intensity profile of the probe field after a propagating distance $z_0 = 20$ μm. The input reference is given by the dashed black line. The dot-dashed green line shows the output in free space, the dotted red line denotes the output in the medium with paraxial approximation, and the solid blue line relates to the results beyond paraxial approximation. (e) Transversal width of the probe field as a function of propagation distance z evaluated within (dashed red) and beyond (solid blue) paraxial approximation. From (d) and (e), it is clear that the propagation dynamics cannot be accurately described by the paraixal approximation in this case, suggesting the invalidity of the paraxial approximation. Other parameters are as in Fig. 3.2.

(b), results are shown for the FDTD simulation beyond the paraxial approximation in the atomic medium. It can be seen that the diffraction is suppressed by the waveguide structure introduced by the control beam. Finally, results within paraxial approximation from the Strang technique are shown in (c). While obtaining again a waveguide-like propagation without diffraction, the results differ considerably from those obtained in (b). In particular, the paraxial approximation leads to higher maximum intensity, and also a slower "breathing"-like width modulation throughout the propagation as compared to (b), which are further shown in (d) and (e). In more words, (d) compares the input and outputs of corresponding transverse intensity profiles for the three different cases. It can be seen that in free space, the maximum intensity is considerably attenuated together with a substantial increase in the width to $w_p(z_0) \simeq 2.85\mu$m. When propagating in the waveguide structure beyond the paraxial approximation, the width is slightly narrowed to $w_p(z_0) \simeq 0.75\mu$m, together with a moderate reduction of the maximum intensity.

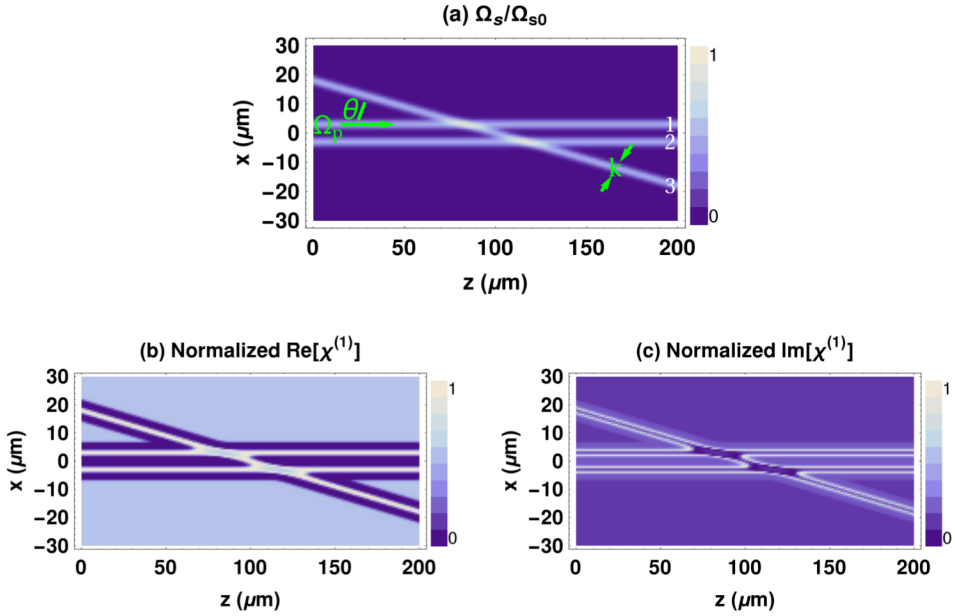

Figure 3.4: Sketch of the branched waveguide structure. (a) shows the spatial profile of Ω_s for $k = 1$. Panels (b) and (c) show the corresponding position-dependent real and imaginary part of the linear susceptibility in the medium. The labels $i \in \{1, 2, 3\}$ in (a) indicate the three output ports corresponding to the i-th control beam Ω_{si}. The size of the medium is chosen as 60 μm $\times$ 200 μm. The other parameters are as in Fig. 3.2.

However, when considering the paraxial approximation, the width is underestimated, and the maximum intensity is overestimated.

An intuitive way to understand the observed diffractionless light propagation is to model the probe as a bunch of rays propagating in a medium rendered by the applied control field into a waveguide structure. As the probe is propagating in the medium, total reflection at the medium boundaries occurs, as the refractive index is larger in the central area than in the two wings as shown by the solid blue line in Fig. 3.2(a). Thus, the main part of the probe intensity is confined in the central area. To substantiate this interpretation, we calculated the width of the probe as a function of propagation distance z, and show the result in Fig. 3.3(e). It can be seen that the width of the probe oscillates periodically throughout the propagation. These oscillations in the width arise from the total refraction. Those rays in the probe which do not meet the condition of total internal reflection leave the central area and are absorbed in the wings. This leads to the reduction in both the energy density and the width of the probe decreases against the propagation distance. Note that Fig. 3.3(e) again shows the difference in the spatial structure of the probe beam with and without the paraxial approximation.

We thus conclude, that even when confined to a single waveguide-like structure and propagating only few Rayleigh lengths, the paraxial approximation does not provide an accurate description of the probe field propagation.

3.2.2 Beam propagation in a branched waveguide structure

We now turn to a more complicated example where the probe field propagates in a branched waveguide structure formed by a field Ω_s consisting of three Gaussian laser

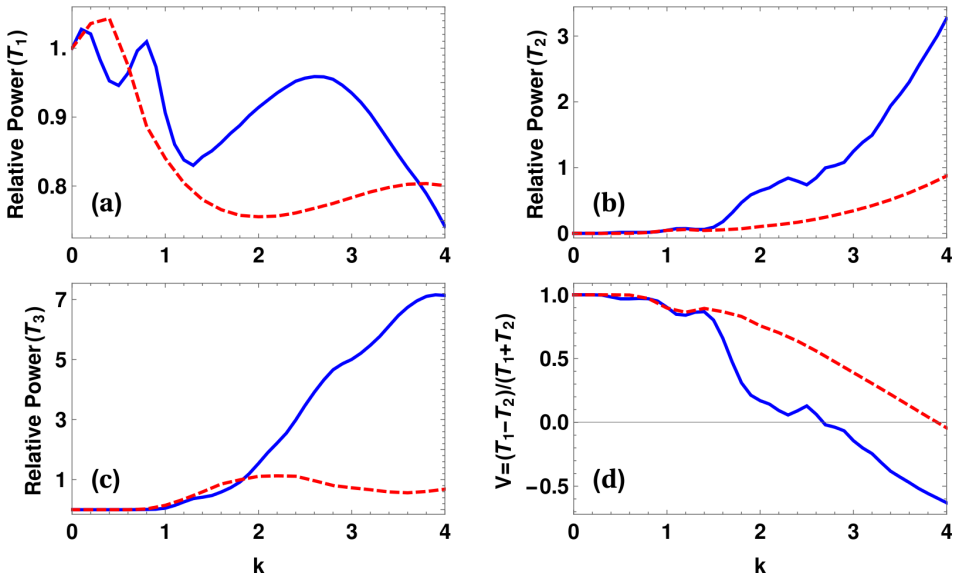

Figure 3.5: (a,b,c) Transmitted powers T_1, T_2, and T_3 at the three output ports indicated in Fig. 3.4(a) after the propagation through the branched waveguide medium. (d) shows the visibility $V = (T_1 - T_2)/(T_1 + T_2)$ for the switching of light between the two output ports 1 and 2. All results are plotted against the relative width of the tilted control beam k. The blue solid (red dashed) line shows results for tilting angle $\tan\theta = 0.18$ ($\tan\theta = 0.26$). The probe beam initially has a Gaussian shape with $w_p = 1.0$ μm. Other parameters are as in Fig. 3.2.

beams with different geometries defined as

$$\Omega_s = \Omega_{s1} + \Omega_{s2} + \Omega_{s3}\,, \tag{3.14a}$$

$$\Omega_{s1} = \Omega_{s0} e^{-\frac{(x-x_0)^2}{2w_s^2}}\,, \tag{3.14b}$$

$$\Omega_{s2} = \Omega_{s0} e^{-\frac{(x+x_0)^2}{2w_s^2}}\,, \tag{3.14c}$$

$$\Omega_{s3} = \Omega_{s0} e^{-\frac{[(x-x_t)\cos\theta + z\sin\theta]^2}{2k^2 w_s^2}}\,. \tag{3.14d}$$

The spatial profile of the field Ω_s is plotted in Fig. 3.4(a). It consists of two parallel beams, intersected by a tilted one. Furthermore, the width w_s, the displacement x_0 of the parallel beams, as well as the displacement x_t of the tilted beam are chosen as 1.0 μm, 3.0 μm, and 18.0 μm, respectively. k is a factor by which the width of the tilted control beam differs from that of the parallel beams. The maximum propagation distance is chosen to be $z_0 = 200$ μm, and the tilting angle for Ω_{s3} is $\tan\theta = 2x_t/z_0$. Using Eqs. (3.6), (3.9) and (3.14), we can obtain the linear susceptibility for the probe, which has real and imaginary parts as shown in Fig. 3.4(b) and (c), respectively. It can be seen that the branched waveguide-like structures are generated in the optical response corresponding to the three beams of Ω_s. Note that in regions where two of the fields Ω_{s1}, Ω_{s2} and Ω_{s3} overlap, the total magnitude of Ω_s is considerably larger than Ω_{s0} of a single field, which means that the conditions for the desired maximum reflective index modulation are not satisfied. This deviation leads to lower spatial dispersion with weak gain as shown in the corresponding regions in Figs. 3.4(b) and (c). As a result, refraction will take place when the probe field enters these regions.

We then consider a Gaussian probe field launching into the waveguide formed by Ω_{s1}

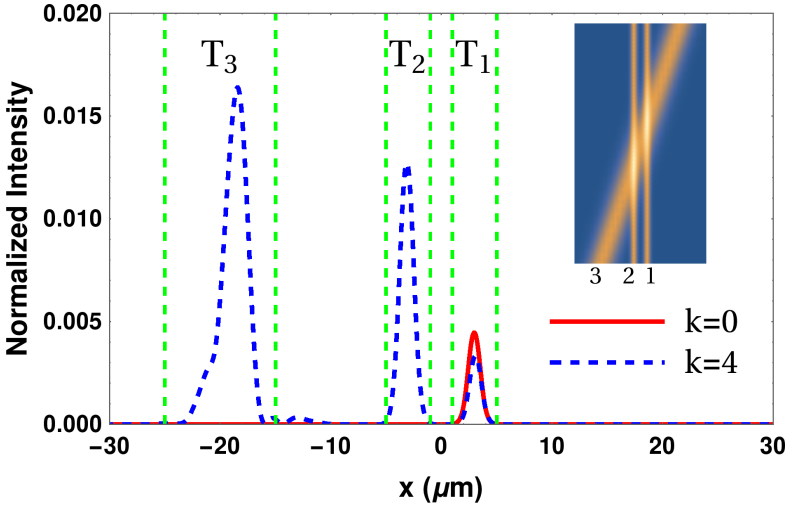

Figure 3.6: Spatial field configuration in the plane transverse to the propagation direction at the output of the medium at $z_0 = 200$ μm. The red solid line shows results without tilted control beam, whereas the blue dashed line shows results including a tilted control with relative width $k = 4$. The vertical green dashed lines indicate the positions of the three output ports. The tilting angle is chosen as $\tan\theta = 0.18$. Other parameters are as in Fig. 3.5.

as depicting in Fig. 3.4(a). As a first step, we have calculated the light propagation without the tilted control field ($\Omega_{s3} = 0$), such that the probe light remains in the upper of the two parallel waveguide structures. We denote this transmitted power after the propagation distance z_0 as P_0. We will normalize part of the results of the following analysis to this reference value P_0, and it is important to remember that P_0 is smaller than the incident power due to attenuation in the waveguide.

We then switch on the tilted control beam, and calculate the field power at the three output ports after the propagation, which we denote as P_i. From these quantities, we calculate the relative transmitted powers $T_i = P_i/P_0$. Here, $i = 1$ corresponds to the upper parallel waveguide, $i = 2$ to the lower parallel waveguide, and $i = 3$ to the tilted waveguide, as shown in Fig. 3.4(a).

Results are shown in Fig. 3.5(a-c) for two different tilting angles $\tan\theta \in \{0.18, 0.26\}$, as a function of the tilted beam width k. Additionally, in (d), the visibility $V = (T_1 - T_2)/(T_1 + T_2)$ is shown, which can be seen as a figure of merit for the switching between the two parallel output ports. While for $k \to 0$, all light is emitted at output port 1 as expected, with increasing k, the light is re-routed towards port 2, with a visibility below -0.6. This indicates that switching of the output port by means of the tilted control field is possible. The corresponding output probe field structure after propagating through the branched waveguide structure without tilted field ($k = 0$) and with $k = 4$ is shown in Fig. 3.6. It clearly shows that the probe pulse in output 2 exceeds that in port 1.

Fig. 3.6 also shows that the output power can be larger than P_0. This is also shown in Figs. 3.5(a-c). The origin of this increase is owing to the slight gain in the overlap regions of the three beams. It should be noted, however, that the overall sum of the total transmitted probe intensity in all three output ports is lower than the input power. Values larger than P_0 only indicate that the transmitted power is larger than the power transmitted through a single optically written waveguide, since part of the absorption is compensated by the gain in the overlap region.

In the following, we provide a simple explanation for the observed light switching to different output ports. If the tilted beam is switched off, the probe field propagates

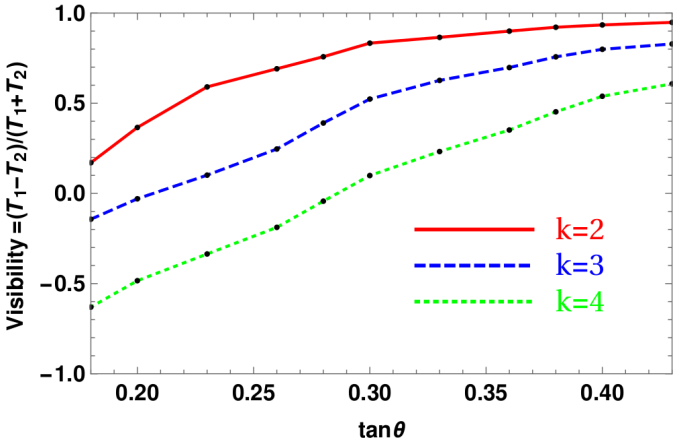

Figure 3.7: Visibility $V = (T_1 - T_2)/(T_1 + T_2)$ as a function of the tilting angle of the control field for three different relative widths of the tilted beam. The upper red solid line shows $k = 2$, the middle blue dashed line $k = 3$, and the lower green dotted line $k = 4$. Other parameters are as in Fig. 3.5.

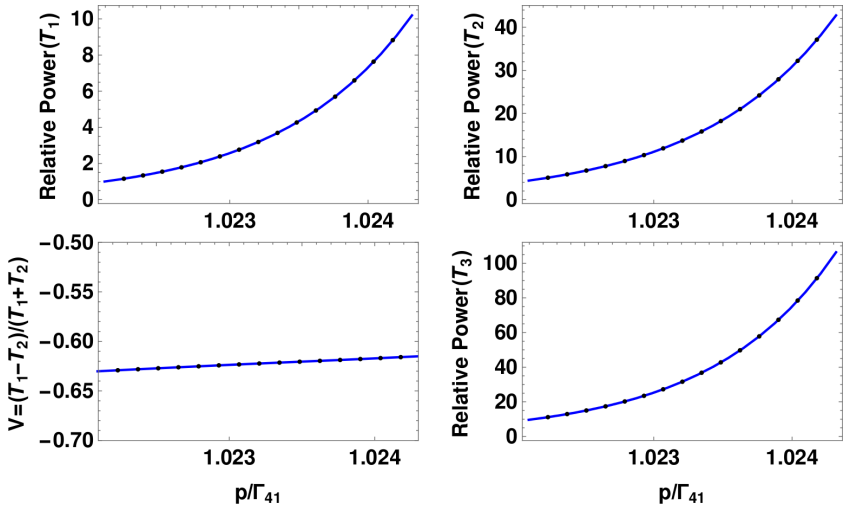

Figure 3.8: The effect of the incoherent pump on the output of the probe. The angle and width of the probe are chosen as $\tan\theta = 0.18$ and $k = 4$ respectively. Other parameters are as in Fig. 3.5.

without diffraction to output port 1 as discussed in the previous section. When the tilted beam Ω_{s3} is turned on, and if suitable parameters are chosen for the tilting angle, the tilted beam width, and the atomic density N, the probe field can be refracted into the tilted beam Ω_{s3}. To understand this, on should note that the region in which two of the three control beams overlap has a real part of the susceptibility varying with the propagation direction z. Due to this variation, as well as due to the missing guiding in perpendicular direction in the overlap region, parts of the probe field can be redirected into the tilted beam. Starting from a tilted beam of vanishing thickness, initially the proportion of redirected light grows with increasing thickness. After the first intersection area, in turn light can be redirected out of the tilted beam into the lower parallel control beam at the second intersection area.

Note that the transmitted power T_1 at output port 1 oscillates with the thickness of the tilted control beam determined by k. This is likely an interference effect. As discussed above, the refractive index varies along the propagation direction z in the waveguide formed by Ω_{s1} in the intersection area. When the probe field enters this area,

some part of it is refracted back and forth repeatedly along the z direction. Depending on k, the interference of the different channels possible for the light changes between (partly) constructive or destructive, thus resulting in the oscillations in T_1.

Qualitatively, one would expect that the probe field can be more easily redirected from Ω_{s1} into the tilted beam Ω_{s3} and subsequently into the lower parallel guide Ω_{s2} if the tilting angle θ is smaller, and if the atomic density N is larger. We have verified this by plotting the transmitted power T_i and visibility V versus the width of Ω_{s3} also for a larger tilting angle $\tan\theta = 0.26$ in Fig. 3.5. It can be seen that the probe transferred into the two output ports 2 and 3 is generally smaller at $\tan\theta = 0.26$ as compared to that at $\tan\theta = 0.18$. We then further calculated the visibility V as a function of the tilting angle $\tan\theta$ for several different widths of the tilted control. Results are shown in Fig. 3.7. It can be seen that V increases as the tilting angle θ increases for all chosen widths of the tilted beam.

It should be noted that since the tilting angle in our case is relatively large ($\tan\theta \in \{0.18, 0.26\}$), the paraxial approximation cannot be applied. This is clearly indicated by the non-vanishing transmitted power T_3 which arises due to effects beyond the paraxial approximation described by the term $(ic/2\omega_p)\partial^2 E_p/\partial z^2$ in Eq. (3.13).

As discussed in Sec. 3.1.4, since we have chosen a relatively weak incoherent pump, the probe will be absorbed as it propagates in the atomic medium. However, the output of the probe can be improved by applying stronger incoherent pumping. Fig. 3.8 shows the transmitted power $T_i (i = 1, 2, 3)$ and visibility V as a function of the incoherent pump rate p. It can be seen that the transmitted powers T_i can be sensitively controlled via the gain introduced by p over a wide range of output powers. Note that due to the slightly longer propagation distance to output port 2 compared to the path to 1, the transmitted power T_2 grows faster than T_1 as the incoherent pump increases. For the same reason, T_3 grows even more rapidly. It is important to note that while the transmitted powers can be controlled, the visibility for the switching remains approximately the same over the whole range of p. This suggests that the visibility is mainly determined by the geometry of the optically written structure, consistent with the waveguide interpretation. In contrast to the absorption and gain properties, this geometry is largely independent of the pumping p, with the exception of slight changes in the beam profiles with p.

3.3 Conclusion

In this chapter, we have investigated light propagation within and beyond paraxial approximation in an optically written waveguide structure induced in a five-level atomic system. The waveguide structure is prepared in a medium tailored with spatially dependent Gaussian control fields and an incoherent pump field. Our initial calculations have shown that already in a single optically written waveguide, accurate results for the beam propagation cannot be obtained within the paraxial approximation when the width of the probe field is too small. The correct propagation dynamics has been attained by numerically calculating the full Maxwell's equations with FDTD method. Moreover, we have demonstrated that a controllable branched-waveguide structure can be optically formed inside the medium by applying a spatially dependent control field consisting of two parallel and one tilted Gaussian beams. Based on the full calculation of Maxwell's equations, it has been found that the tilted beam can be used to selectively steer a probe beam between two different output ports. In the overlapping regions of the Gaussian control beams a rapidly varying refractive index is created that guides the probe beam to propagate in a particular output branch.

Chapter 4

Control of light propagation via nonlocal linear effects

In the previous chapters, we have introduced the concept of nonlocal linear effects and also verified the validity of paraxial approximation. As briefly mentioned in Sec. 2.2, a specific type of nonlocal linear effects can be induced by exploiting thermal atomic motion and collisions of atoms. This nonlocal linear effects are found to have a $\mathbf{k}_\perp$-square dependence in momentum space which could thus be used to exactly eliminate the paraxial diffraction of laser beams with arbitrary spatial profiles. However, strong inevitable absorption in this initially proposed mechanism leads to severe attenuation of the input laser beams, rendering it useless for practical application. In this chapter, we are mainly focused on how to employ this specific nonlocal linear effects to realize light propagation with neither diffraction nor absorption, uniform π phase modulation, image reproduction and frequency conversion. We firstly propose an enhanced scheme to realize diffractionless and lossless light propagation for laser beams with arbitrary profiles, which is given in Sec. 4.1. Based on this enhanced scheme, we find in Sec. 4.2 that it can be further utilized to apply a uniform π phase modulation to the laser beam without changing any other physical properties. Then an extended scheme combined with four-wave mixing process is offered in Sec. 4.3 to demonstrate image reproduction and frequency conversion without diffraction or absorption. Finally, this chapter is closed with a short conclusion in Sec. 4.4.

4.1 Diffractionless and lossless light propagation in thermal atomic vapor

4.1.1 Motivation

All-optical data processing, which can be much more compact and efficient than present-day electronics due to the ultra-high bandwidth and the absence of optical-to-electrical conversion, offers a very promising technique for the next-generation information networks. However, there are some inherent difficulties to be solved before its practical application. One of these obstacles is optical diffraction, which will lead to energy spreading and distortion of an image imprinted on a light beam propagating in free space. Physically, diffraction stems from the unique phase shift acquired from the propagation for each wave component contained in the laser beam. In order to suppress or even remove the diffraction, different methods have been suggested. First, there are particular characteristic spatial modes which satisfy the paraxial wave equation, and therefore can propagate in free space without changes in their transverse profile [202]. These are Airy [203, 204], Bessel [205–207], Mathieu [208, 209] and parabolic (Weber) beams [209–211]. An alternative method is to induce a spatially-varying index of refraction experienced by the propagating light, effectively forming an optically written

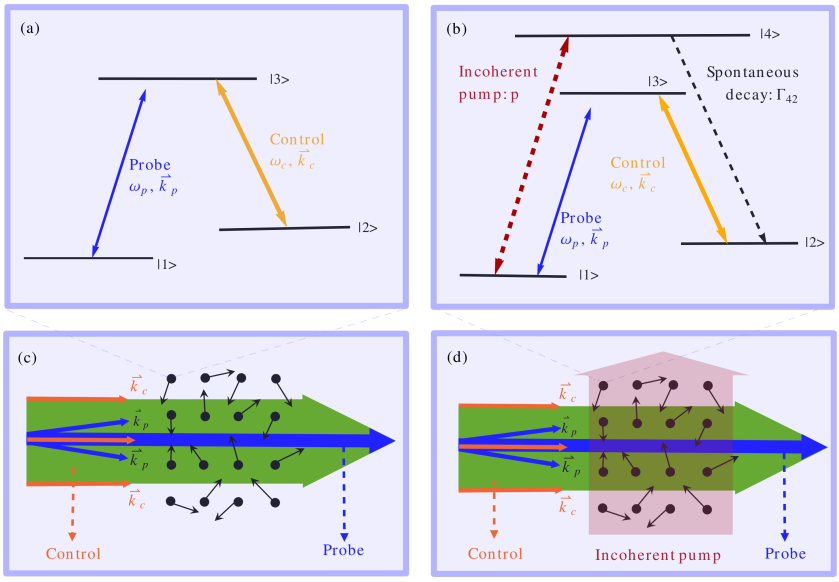

Figure 4.1: The basic three-level lambda atomic system (a) interacting with two co-propagating probe and control fields with the geometric configuration sketched in (c), which has been realized to eliminate optical diffraction by Firstenberg *et al.*, while it is followed by inevitable single-photon absorption due to imperfect EIT. (b) is our proposed four-level double-lambda system in which an additional two-way incoherent plane-wave pump is applied with geometry depicted in (d). In this enhanced scheme, one may not only remove the diffraction but also compensate the single-photon absorption thanks to atomic coherences induced by the incoherent pump and coherent control field together.

waveguide [212–222]. However, those schemes operating in position space typically only allow to propagate specific spatial modes through a particular waveguide, and cannot be applied to multimode fields.

A more powerful approach to eliminate paraxial diffraction of a laser beam encoded with arbitrary image has been recently proposed by Firstenberg *et al.* with successful experimental demonstration in a thermal atomic medium [20–24]. The method takes advantage of the thermal atomic motion and collisions which introduces a specific type of nonlocal linear effects. It is found that this nonlocal linear effects can be employed to exactly cancel paraxial diffraction for laser beams with arbitrary spatial profiles. In more detail, in their three-level lambda system as shown in Fig. 4.1(a) and (c), two co-propagating probe and control fields are applied to form an electromagnetically induced transparency (EIT) configuration. The probe field has an arbitrary spatial profile while the control is set to be a plane-wave field. In terms of atomic response, the atomic motion and collisions introduce a specific type of linear susceptibility which is nonlocal linear in position space and $\mathbf{k}_\perp$-square dependent in momentum space. This nonlocal susceptibility can be manipulated in such a way, that the phase shift for each wave component giving rise to diffraction is exactly canceled. Since the phase shift of each momentum component is eliminated individually, arbitrary images within a certain bandwidth can be propagated without diffraction. However, this method can only eliminate the diffraction of a laser beam imprinted with arbitrary image in a certain condition of negative two-photon detuning between the involved fields, it necessarily involves strong single-photon absorption due to imperfect EIT, and therefore is impractical.

Here we propose an enhanced scheme in which arbitrary images encoded onto a probe field can propagate with canceled diffraction, while the strong absorption is exactly

removed or can even be turned to negative, which means the probe field can be amplified. As shown in Fig. 4.1(b), we simply apply an additional two-way incoherent pump field to couple another transition. It will pump out the populations in the ground state, and then redistribute the populations among the four states. Via the coherent control field, atomic coherences will be induced between state $|2\rangle$ and $|3\rangle$, which leads to constant gain for the probe field. Depending on the intensity of the incoherent pump, the constant single-photon absorption can be completely compensated or even surpassed by the gain from the atomic coherences. Meanwhile, the linear dispersion are still quadratic in $\mathbf{k}_\perp$ except for a different constant offset. Consequently, the probe field can propagate in the prepared thermal medium with neither diffraction nor absorption. The output power of the probe field can be controlled by simply tuning the intensity of the incoherent pump.

4.1.2 Theoretical description of thermal atoms

Our proposed scheme to not only eliminate the paraxial diffraction but also compensate the single-photon absorption employs a four-level system in double-lambda configuration as shown in Fig. 4.1(b). The probe field with Rabi frequency $\Omega_p(\mathbf{r},t)$ and wavevector $\mathbf{k}_p$ couples the transition $|1\rangle \leftrightarrow |3\rangle$ with detuning $\Delta_p = \omega_p - \omega_{31}$, while the transition $|2\rangle \leftrightarrow |3\rangle$ is driven by a control field with Rabi frequency $\Omega_c(\mathbf{r},t)$ and wavevector $\mathbf{k}_c$, the detuning for the control field is defined as $\Delta_c = \omega_c - \omega_{32}$. In addition, a two-way incoherent pump field $p(\mathbf{r})$ [197, 223–225] is applied to the transition $|1\rangle \leftrightarrow |4\rangle$. Due to the effect of the incoherent pump, the populations initially staying in the ground state $|1\rangle$ will be pumped out and then be redistributed among the other three states. Together with the control field, atomic coherences between the two states $|2\rangle$ and $|3\rangle$ will be generated, already in the absence of the probe field. The atomic coherences $\rho_{23}^{(0)}$ leads to gain for the probe field. As a result, the overall absorption for the probe field can be controlled to zero or even negative, by simply tuning the intensity of the incoherent pump field as we show below. The level structure can, for example, be realized in the hyperfine structure of the D1 line of ^{87}Rb. In our numerical analysis, we choose the magnetic sublevels $5\ ^2S_{1/2}, F = 1, m_F = 0$ and $F = 2, m_F = 2$ as the two lower states $|1\rangle$ and $|2\rangle$, while $5\ ^2P_{1/2}, F = 2, m_F = 1$ and $F = 1, m_F = 1$ are set to be the two upper states $|3\rangle$ and $|4\rangle$, respectively.

Following the theoretical description of the three-level lambda system including thermal atomic motion and collisions developed in [21], we define a generalized density-matrix distribution function in space and velocity as

$$\rho(\mathbf{r},\mathbf{v},t) = \sum_j \rho^j(t)\,\delta(\mathbf{r}-\mathbf{r}_j(t))\,\delta(\mathbf{v}-\mathbf{v}_j(t))\,. \tag{4.1}$$

Here, $\rho^j(t)$ is the density matrix for the j-th atom. $\rho(\mathbf{r},\mathbf{v},t)$ is understood as the probability density to find an atom with internal density matrix $\rho(t)$ at position $\mathbf{r}$ and with velocity $\mathbf{v}$. Then, we find

$$\begin{aligned}\frac{\partial\rho(\mathbf{r},\mathbf{v},t)}{\partial t} = &\sum_j \frac{d\rho^j(t)}{dt}\,\delta(\mathbf{r}-\mathbf{r}_j(t))\,\delta(\mathbf{v}-\mathbf{v}_j(t))\\ &+\sum_j \rho^j(t)\,\frac{\partial\delta(\mathbf{r}-\mathbf{r}_j(t))}{\partial t}\,\delta(\mathbf{v}-\mathbf{v}_j(t))\\ &+\sum_j \rho^j(t)\,\delta(\mathbf{r}-\mathbf{r}_j(t))\,\frac{\partial\delta(\mathbf{v}-\mathbf{v}_j(t))}{\partial t}\,.\end{aligned} \tag{4.2}$$

The time evolution of the first term in the right hand side (RHS) of Eq. (4.2) is described by the master equation

$$\begin{aligned}
&\sum_j \frac{d\rho^j(t)}{dt}\,\delta(\mathbf{r}-\mathbf{r}_j(t))\,\delta(\mathbf{v}-\mathbf{v}_j(t)) \\
&=\sum_j \big\{-\frac{i}{\hbar}[H,\rho^j]-L\rho^j\big\}\,\delta(\mathbf{r}-\mathbf{r}_j(t))\,\delta(\mathbf{v}-\mathbf{v}_j(t)) \\
&=-\frac{i}{\hbar}[H,\rho(\mathbf{r},\mathbf{v},t)]-L\rho(\mathbf{r},\mathbf{v},t)\big]\,. \qquad (4.3)
\end{aligned}$$

And for the second term in the RHS of Eq. (4.2), we have

$$\begin{aligned}
&\sum_j \rho^j(t)\,\frac{\partial\delta(\mathbf{r}-\mathbf{r}_j(t))}{\partial t}\,\delta(\mathbf{v}-\mathbf{v}_j(t)) \\
&=\sum_j \rho^j(t)\,\frac{\partial\mathbf{r}_j(t)}{\partial t}\frac{\partial\delta(\mathbf{r}-\mathbf{r}_j(t))}{\partial\mathbf{r}_j}\,\delta(\mathbf{v}-\mathbf{v}_j(t)) \\
&=-\mathbf{v}\cdot\frac{\partial\rho(\mathbf{r},\mathbf{v},t)}{\partial\mathbf{r}}\,. \qquad (4.4)
\end{aligned}$$

When the atomic system is relaxed to the thermal equilibrium state, the last term describing atomic collision in the RHS of Eq. (4.2) can be rewritten as [21]

$$\sum_j \rho^j(t)\,\delta(\mathbf{r}-\mathbf{r}_j(t))\,\frac{\partial\delta(\mathbf{v}-\mathbf{v}_j(t))}{\partial t}=\gamma_c\big[\rho(\mathbf{r},\mathbf{v},t)-\hat{R}(\mathbf{r},t)F(\mathbf{v})\big]\,. \qquad (4.5)$$

Here γ_c denotes the collision rates between atoms. $R(\mathbf{r},t)$ in the RHS stands for the density of atoms in internal state $\rho(t)$ per unit volume at position $\mathbf{r}$

$$R(\mathbf{r},t)=\int\rho(\mathbf{r},\mathbf{v},t)d\mathbf{v}\,, \qquad (4.6)$$

and $F(\mathbf{v})=\mathrm{Exp}[-\mathrm{v}^2/\mathrm{v}_{\mathrm{th}}^2]/\sqrt{\pi}\mathrm{v}_{\mathrm{th}}$ is the Boltzmann distribution for the atoms, $\mathrm{v}_{\mathrm{th}}=\sqrt{2k_bT/m}$ refers to the most probable thermal velocity.

Finally, the equation of motion of the system can be written as

$$\begin{aligned}
\frac{\partial\rho(\mathbf{r},\mathbf{v},t)}{\partial t}&=-\frac{i}{\hbar}[H,\rho(\mathbf{r},\mathbf{v},t)]-L\rho(\mathbf{r},\mathbf{v},t) \\
&\quad-\mathbf{v}\cdot\frac{\partial\rho(\mathbf{r},\mathbf{v},t)}{\partial\mathbf{r}}-\gamma_c\big[\rho(\mathbf{r},\mathbf{v},t)-R(\mathbf{r},t)F(\mathbf{v})\big]\,, \qquad (4.7)
\end{aligned}$$

where H is the Hamiltonian of the system, $L\rho$ represents the relaxation terms including spontaneous decay, dephasing and the incoherent pump, etc.. In the right hand side of Eq. (4.7), the first two terms describe the internal quantum-mechanical evolution, while the other terms characterize the external classical motion including thermal motion and collisions [22]. The relevant equations of motion for the coherences follow as

$$\begin{aligned}
&\big(\frac{\partial}{\partial t}+\mathbf{v}\cdot\frac{\partial}{\partial\mathbf{r}}-i\Delta_p+i\mathbf{k}_p\cdot\mathbf{v}+\frac{p(\mathbf{r})}{2}+\frac{\Gamma_3}{2}+\gamma_c\big)\rho_{31} \\
&=i\Omega_p(\mathbf{r},t)(\rho_{11}-\rho_{33})+i\Omega_c(\mathbf{r},t)\rho_{21}+\gamma_cR_{31}(\mathbf{r},t)F(\mathbf{v})\,, \qquad (4.8a)
\end{aligned}$$

$$(\frac{\partial}{\partial t}+\mathbf{v}\cdot\frac{\partial}{\partial \mathbf{r}}-i\Delta+i\Delta\mathbf{k}\cdot\mathbf{v}+\frac{p(\mathbf{r})}{2}+\gamma_{21}+\gamma_c)\rho_{21}$$
$$=i\Omega_c^*(\mathbf{r},t)\rho_{31}-i\Omega_p(\mathbf{r},t)\rho_{23}+\gamma_c R_{21}(\mathbf{r},t)F(\mathbf{v})\,, \tag{4.8b}$$

where we have abbreviated $\rho_{ij}(\mathbf{r},\mathbf{v},t)$ as ρ_{ij} for convinience, and introduced the two-photon detuning $\Delta=\Delta_p-\Delta_c$ and the wavevector difference $\Delta\mathbf{k}=\mathbf{k}_p-\mathbf{k}_c$. We denote the spontaneous emission rate on transition $|i\rangle\rightarrow|k\rangle$ as Γ_{ik}, and the total decay rate of state $|i\rangle$ as $\Gamma_i=\sum_k\Gamma_{ik}$. The decoherence between the two ground states $|1\rangle$ and $|2\rangle$ is given by γ_{21}.

For simplicity, we approximate the control field $\Omega_c(\mathbf{r},t)$ and the pump field $p(\mathbf{r})$ as plane-wave fields, which means $\Omega_c(\mathbf{r},t)=\Omega_c$ and $p(\mathbf{r})=p$. Then, the steady-state density-matrix distribution function in the zeroth-order of the probe field can be obtained as [22]

$$\begin{aligned}\rho_{ij}^{(0)}(\mathbf{r},\mathbf{v},t\rightarrow\infty)&=\sum_m\rho_{ij}^{(0)}\,\delta(\mathbf{r}-\mathbf{r}_m(t))\,\delta(\mathbf{v}-\mathbf{v}_m(t))\\&=\sum_{m,N\rightarrow\infty}\frac{N}{V}F(\mathbf{v}_m)\rho_{ij}^{(0)}\,\delta(\mathbf{r}-\mathbf{r}_m(t))\,\delta(\mathbf{v}-\mathbf{v}_m(t))\frac{V}{N}\Delta\mathbf{v}_m\\&=n_0\int F(\mathbf{v}_m)\rho_{ij}^{(0)}\,\delta(\mathbf{r}-\mathbf{r}_m(t))\,\delta(\mathbf{v}-\mathbf{v}_m(t))d\mathbf{r}_m d\mathbf{v}_m\\&=n_0\rho_{ij}^{(0)}F(\mathbf{v})\,.\end{aligned} \tag{4.9}$$

Here, $n_0=N/V$ is the atomic density and $\rho_{ij}^{(0)}$ is the zero-order density matrix element of an atom at rest. Under those approximations, the equations of motion for the first-order coherences can be derived from Eq. (4.8)

$$(\frac{\partial}{\partial t}+\mathbf{v}\cdot\frac{\partial}{\partial \mathbf{r}}-i\Delta_p+i\mathbf{k}_p\cdot\mathbf{v}+\frac{p}{2}+\frac{\Gamma_3}{2}+\gamma_c)\rho_{31}^{(1)}$$
$$=i\Omega_p(\mathbf{r},t)(\rho_{11}^{(0)}-\rho_{33}^{(0)})n_0F(\mathbf{v})+i\Omega_c(\mathbf{r},t)\rho_{21}^{(1)}+\gamma_c R_{31}^{(1)}(\mathbf{r},t)F(\mathbf{v})\,, \tag{4.10a}$$

$$(\frac{\partial}{\partial t}+\mathbf{v}\cdot\frac{\partial}{\partial \mathbf{r}}-i\Delta+i\Delta\mathbf{k}\cdot\mathbf{v}+\frac{p}{2}+\gamma_{21}+\gamma_c)\rho_{21}^{(1)}$$
$$=i\Omega_c^*(\mathbf{r},t)\rho_{31}^{(1)}-i\Omega_p(\mathbf{r},t)\rho_{23}^{(0)}n_0F(\mathbf{v})+\gamma_c R_{21}^{(1)}(\mathbf{r},t)F(\mathbf{v})\,. \tag{4.10b}$$

In order to get an analytical expression for $R_{31}^{(1)}(\mathbf{k},\omega)$, which determine the thermal atomic effect on the probe propagation dynamics, we first integrate Eqs. (4.10b) over velocity

$$(\frac{\partial}{\partial t}-i\Delta+\frac{p}{2}+\gamma_{21})R_{21}^{(1)}(\mathbf{r},t)+(\frac{\partial}{\partial \mathbf{r}}+i\Delta\mathbf{k})\mathbf{J}_{21}(\mathbf{r},t)$$
$$=i\Omega_{c1}^*R_{31}^{(1)}(\mathbf{r},t)-in_0\Omega_p(\mathbf{r},t)\rho_{23}^{(0)}\,, \tag{4.11}$$

where we have defined the current density of the density-matrix distribution function

$$\mathbf{J}_{ij}(\mathbf{r},t)=\int\mathbf{v}\rho_{ij}^{(1)}(\mathbf{r},\mathbf{v},t)d\mathbf{v}\,, \tag{4.12}$$

in Eq. (4.10b), when the Dicke limit is satisfied, i.e., $\gamma=\gamma_c+p/2+\gamma_{21}-i\Delta$ is dominant,

we can approximately rewrite $\rho(\mathbf{r},\mathbf{v},t)$ to first order in γ

$$\begin{aligned}\rho_{21}^{(1)}(\mathbf{r},\mathbf{v},t) &= \rho_{21}^{(1,0)}(\mathbf{r},\mathbf{v},t) + \frac{1}{\gamma}\rho_{21}^{(1,1)}(\mathbf{r},\mathbf{v},t) \\ &= R_{21}^{(1)}(\mathbf{r},t)F(\mathbf{v}) + \frac{1}{\gamma}\rho_{21}^{(1,1)}(\mathbf{r},\mathbf{v},t)\,. \end{aligned} \tag{4.13}$$

By integrating Eq.(4.13), we can then find that

$$0 = \int \mathbf{v}\rho_{21}^{(1,0)}(\mathbf{r},\mathbf{v},t)d\mathbf{v}\,, \tag{4.14a}$$

$$\mathbf{J}_{21}(\mathbf{r},t) = \frac{1}{\gamma}\int \mathbf{v}\rho_{21}^{(1,1)}(\mathbf{r},\mathbf{v},t)d\mathbf{v}\,, \tag{4.14b}$$

we expand $\rho_{21}^{(1)}(\mathbf{r},\mathbf{v},t)$ as in Eq. (4.13) and multiply Eq. (4.10b) by $\mathbf{v}$, then integrate over velocity. Using the relations in Eq. (4.14) and taking the leading term in γ, the following equation for $\mathbf{J}_{21}(\mathbf{r},t)$ is given as

$$\mathbf{J}_{21}(\mathbf{r},t) = -D\big(\frac{\partial}{\partial\mathbf{r}} + i\Delta\mathbf{k}\big)R_{21}^{(1)}(\mathbf{r},t) + i\frac{\Omega_{c1}^*}{\gamma}\mathbf{J}_{31}(\mathbf{r},t)\,, \tag{4.15}$$

where D is defined as $D = v_{\mathrm{th}}^2/\gamma$. To derive Eq. (4.15) we have used the relation [22]

$$\int \mathbf{v}^2\frac{\partial}{\partial\mathbf{r}}R_{21}^{(1)}(\mathbf{r},t)F(\mathbf{v})d\mathbf{v} = \mathrm{v}_{\mathrm{th}}^2\frac{\partial}{\partial\mathbf{r}}R_{21}^{(1)}(\mathbf{r},t)\,, \tag{4.16}$$

substituting $\mathbf{J}_{21}(\mathbf{r},t)$ in Eq. (4.11) by Eq. (4.15) we have

$$\begin{aligned}&\big[\frac{\partial}{\partial t} - i\Delta + \frac{p}{2} + \gamma_{21} - D\big(\frac{\partial}{\partial\mathbf{r}} + i\Delta\mathbf{k}\big)^2\big]R_{21}^{(1)}(\mathbf{r},t) \\ &= i\Omega_{c1}^*R_{31}^{(1)}(\mathbf{r},t) - in_0\Omega_p(\mathbf{r},t)\rho_{23}^{(0)} - i\big(\frac{\partial}{\partial\mathbf{r}} + i\Delta\mathbf{k}\big)\cdot\frac{\Omega_{c1}^*}{\gamma}\mathbf{J}_{31}(\mathbf{r},t)\,, \end{aligned} \tag{4.17}$$

the last term containing $\mathbf{J}_{31}(\mathbf{r},t)$ in Eq. (4.17) usually can be neglected when $|\Omega_c| \ll |\gamma|$. Furthermore, even when this condition is not satisfied, this term can be still neglected when both the spatial variations $\partial/\partial\mathbf{r}$ and $\Delta\mathbf{k}$ remains in the transverse directions, perpendicular to $\mathbf{k}_p$, since $\mathbf{J}_{31}(\mathbf{r},t)$ is parallel to $\mathbf{k}_p$ [22]. Then Eq. (4.17) is simplified to

$$\begin{aligned}&\big[\frac{\partial}{\partial t} - i\Delta + \frac{p}{2} + \gamma_{21} - D\big(\frac{\partial}{\partial\mathbf{r}} + i\Delta\mathbf{k}\big)^2\big]R_{21}^{(1)}(\mathbf{r},t) \\ &= i\Omega_{c1}^*R_{31}^{(1)}(\mathbf{r},t) - in_0\Omega_p(\mathbf{r},t)\rho_{23}^{(0)}\,. \end{aligned} \tag{4.18}$$

Here we consider the common case of slowly-varying envelope approximation(SVEA), where the temporal and spatial variations in the envelope of probe and signal field are much smaller than the decoherence rate and the wave number. Correspondingly, it results in the SVEA for the spatial-temporal evolution of density-matrix distribution function $R_{31}^{(1)}(\mathbf{r},t)$, which means

$$\Big|\frac{\partial}{\partial t} + \mathbf{v}\cdot\frac{\partial}{\partial\mathbf{r}}\Big| \ll \Big|\frac{p}{2} + \frac{\Gamma_3}{2} - i\Delta_p + i\mathbf{k}_p\cdot\mathbf{v}\Big|\,, \tag{4.19a}$$

In Eq. (4.10a), we can then neglect the temporal and spatial variations, and only take the dominant part of $\rho_{21}^{(1)}(\mathbf{r},\mathbf{v},t) = R_{21}^{(1)}(\mathbf{r},t)F(\mathbf{v})$, then integrate over velocities, the expression for $R_{31}^{(1)}(\mathbf{r},z,\mathbf{v},t)$ is found

$$R_{31}^{(1)}(\mathbf{r},t) = iK_{31}\left[n_0(\rho_{11}^{(0)} - \rho_{33}^{(0)})\Omega_p(\mathbf{r},t) + \Omega_{c1}R_{21}^{(1)}(\mathbf{r},t)\right], \tag{4.20}$$

where K_{31} is defined as follows

$$G_{31} = \int \frac{F(\mathbf{v})}{\Delta_p - \mathbf{k}_p\cdot\mathbf{v} + i(\frac{p}{2} + \frac{\Gamma_3}{2} + \gamma_c)}d\mathbf{v}\,, \tag{4.21a}$$

$$K_{31} = \frac{iG_{31}}{1 - i\gamma_c G_{31}}\,. \tag{4.21b}$$

When $\Delta_p \ll p/2 + \Gamma_3 + \gamma_c$, i.e., near the one-photon resonance where most experiments were done, the imaginary parts of K_{31} are much smaller than its rear part. In the following, we treat K_{31} as real number. In the paraxial approximation, the changes in the envelopes along z direction are much smaller than that in the transverse plane, so we may replace $\mathbf{r} \to (\mathbf{r}_\perp, z)$ and $\partial/\partial\mathbf{r} \to \partial/\partial\mathbf{r}_\perp$ in Eq. (4.18), and then Fourier transform them from $(\mathbf{r}_\perp, t)$ to $(\mathbf{k}_\perp, \omega)$. We can then immediately find the final expression for $R_{31}^{(1)}(\mathbf{k}_\perp, z, \omega)$

$$R_{31}^{(1)}(\mathbf{k}_\perp,z,\omega) = iK_{31}n_0\Omega_p(\mathbf{k}_\perp,z,\omega)\big(\rho_{11}^{(0)} - \rho_{33}^{(0)} + \frac{\Gamma_c(\rho_{11}^{(0)} - \rho_{33}^{(0)}) + i\Omega_c\rho_{23}^{(0)}}{i(\omega+\Delta) - \Gamma_1 - D(\mathbf{k}_\perp + \Delta\mathbf{k})^2}\big)\,, \tag{4.22}$$

where we have set the power broadening $\Gamma_c = K_{31}\Omega_c^2$ and $\Gamma_1 = p/2 + \gamma_{21} + \Gamma_c$. For a continuous wave, we can set $\omega = 0$ in Eq. (4.22). In the case for a small wavevector difference between Ω_p and Ω_c, $\Delta\mathbf{k}$ could be neglected, i.e., $\Delta\mathbf{k} = 0$. Finally we find the expression for $R_{31}^{(1)}(\mathbf{k}_\perp, z, \omega)$

$$R_{31}^{(1)}(\mathbf{k}_\perp,z,\omega) = iK_{31}n_0\Omega_p(\mathbf{k}_\perp,z,\omega)\big(\rho_{11}^{(0)} - \rho_{33}^{(0)} + \frac{\Gamma_c(\rho_{11}^{(0)} - \rho_{33}^{(0)}) + i\Omega_c\rho_{23}^{(0)}}{i(\omega+\Delta) - \Gamma_1 - D\mathrm{k}_\perp^2}\big)\,, \tag{4.23}$$

then the linear susceptibility in momentum space reads

$$\begin{aligned}\chi(\mathbf{k}_\perp) &= \frac{3\lambda_p^3\Gamma_{31}}{8\pi^2}\frac{R_{31}^{(1)}(\mathbf{k}_\perp,\omega=0)}{\Omega_p(\mathbf{k}_\perp,z,\omega=0)} \\ &= i\alpha\big(\rho_{11}^{(0)} - \rho_{33}^{(0)} + \frac{\Gamma_c(\rho_{11}^{(0)} - \rho_{33}^{(0)}) + i\Omega_c\rho_{23}^{(0)}}{i\Delta - \Gamma_1 - D\mathrm{k}_\perp^2}\big)\,.\end{aligned} \tag{4.24}$$

where we have $\alpha = 3\lambda_p^3\Gamma_{31}K_{31}n_0/(8\pi^2)$. It can be observed that from Eq. (4.23) that the atomic response in fact leads to a specific type of nonlocal linear effects by Fourier transforming it back in to position space

$$R_{31}^{(1)}(\mathbf{r}_\perp,z) = \frac{8\pi^2}{3\lambda_p^3\Gamma_{31}}\int \chi_F(\mathbf{r}_\perp - \mathbf{r}_\perp^{'})\Omega_p(\mathbf{r}_\perp^{'},z)d\mathbf{r}_\perp^{'}\,, \tag{4.25}$$

wehre $\Omega_p(\mathbf{r}_\perp, z)$ is the slowly varying envelope of the probe field and $\chi_F(\mathbf{r}_\perp)$ is the

Fourier transformation of $\chi(\mathbf{k}_\perp)$ defined as

$$\chi_F(\mathbf{r}_\perp) = \int_{-\infty}^{\infty} \chi(\mathbf{k}_\perp) e^{i\mathbf{k}_\perp \cdot \mathbf{r}_\perp} d\mathbf{k}_\perp \,. \tag{4.26}$$

4.1.3 Laser beam propagation with arbitrary spatial profiles

Since we want to study the propagation dynamics of the probe beam, we need first to get the propagation equation which governs the dynamics of the probe field. As we have discussed in Sec 2.2, the propagation equation in paraxial approximation for the probe beam including the atomic effect can be written

$$\begin{aligned}\left(\frac{\partial}{\partial z} - \frac{i}{2\mathrm{k}_p}\frac{\partial^2}{\partial \mathbf{r}_\perp^2}\right)\Omega_p(\mathbf{r}_\perp, z) &= i\frac{3\lambda_p^2\Gamma_{31}}{8\pi} R_{31}^{(1)}(\mathbf{r}_\perp, z) \\ &= i\frac{\mathrm{k}_p}{2}\int \chi_F(\mathbf{r}_\perp - \mathbf{r}_\perp^{'})\Omega_p(\mathbf{r}_\perp^{'}, z) d\mathbf{r}_\perp^{'} \,,\end{aligned} \tag{4.27}$$

with $\chi_F(\mathbf{r}_\perp)$ defined in Eq. (4.26). In momentum space it reads

$$\left(\frac{\partial}{\partial z} + i\frac{\mathrm{k}_\perp^2}{2\mathrm{k}_p}\right)\Omega_p(\mathbf{k}_\perp, z) = i\frac{\mathrm{k}_p}{2}\chi(\mathbf{k}_\perp)\Omega_p(\mathbf{k}_\perp, z) \,, \tag{4.28}$$

where $\Omega_p(\mathbf{k}_\perp, z)$ is the Fourier transform $\Omega_p(\mathbf{r}_\perp, z)$ in the plane (x, y) transverse to the propagation direction z. The second term $\sim \mathrm{k}_\perp^2$ on the left hand side is responsible for the paraxial diffraction of the probe beam throughout its propagation. It is immediately clear that diffraction can be exactly eliminated, if the linear dispersion $\mathrm{Re}[\chi(\mathbf{k}_\perp)]$ is quadratic in $\mathrm{k}_\perp^2$ and the linear absorption $\mathrm{Im}[\chi(\mathbf{k}_\perp)]$ remains as a constant [21, 22].

4.1.3.1 Without incoherent pump

We have calculated the linear susceptibility $\chi(\mathbf{k}_\perp)$ depending on $\mathrm{k}_\perp^2$ due to atomic motion. In this section, we will show that it leads to elimination of paraxial diffraction under specified circumstances. First, we consider the case when there is no incoherent pump field, which means that $\rho_{11}^{(0)} = 1, \rho_{33}^{(0)} = 0, \rho_{23}^{(0)} = 0$. Then the linear susceptibility $\chi(\mathbf{k}_\perp)$ can be simplified to

$$\chi(\mathbf{k}_\perp) = i\alpha\left(1 + \frac{\Gamma_c}{i\Delta - \Gamma_0 - D_0\mathrm{k}_\perp^2}\right) , \tag{4.29}$$

where we have $\Gamma_0 = \gamma_{21} + \Gamma_c$ and $D_0 = \mathrm{v}_{\mathrm{th}}^2/(\gamma_c + \gamma_{21} - i\Delta)$. We then find that it is exactly the same as discussed in Ref. [21, 22]. In the region where $\mathrm{k}_\perp \ll \mathrm{k}_0$ with $\mathrm{k}_0 = \sqrt{\Gamma_0\gamma_c/\mathrm{v}_{\mathrm{th}}^2}$, Eq. (4.29) can be written in order of $\mathrm{k}_\perp^2$

$$\chi(\mathbf{k}_\perp) = \chi^{(0)} + \chi^{(1)}\frac{\mathrm{k}_\perp^2}{\mathrm{k}_0^2} + O(\mathrm{k}_\perp^4) \,, \tag{4.30}$$

where $\chi^{(0)}$ and $\chi^{(1)}$ are coefficients only determined by the choice of Δ. At negative two-photon detuning $\Delta = -\Gamma_0$, we then find that $\mathrm{Im}[\chi^{(1)}] = 0$ and $\mathrm{Re}[\chi^{(1)}] = \alpha\Gamma_c/2\Gamma_0$. Compared to the propagation equation Eq. (4.28), it can be clearly seen that the paraxial

diffraction can be exactly canceled when

$$\frac{1}{\mathrm{k}_p^2} = \frac{\mathrm{Re}[\chi^{(1)}]}{\mathrm{k}_0^2} = \frac{\alpha\Gamma_c}{2\Gamma_0\mathrm{k}_0^2}\,. \tag{4.31}$$

Since this elimination of diffraction is operated in momentum space and thereby does not depend on the spatial profile of the probe field, it means that arbitrary images imprinted on the probe can propagate without diffraction. However, the probe field will experience inevitable single-photon absorption, due to the negative two-photon detuning deviating from the EIT resonance which is necessary for the elimination of diffraction. The constant absorption coefficient can be derived

$$\beta = \frac{\mathrm{k}_p}{2}\mathrm{Im}[\chi^{(0)}] = \frac{\mathrm{k}_p}{2}\alpha(1-\frac{\Gamma_c}{2\Gamma_0}) \simeq \frac{\mathrm{k}_p}{4}\alpha\,, \tag{4.32}$$

the probe field will be exponentially decreased $\sim e^{-\beta z}$ along the propagation direction. For the ^{87}Rb D1 line with atomic density $n_0 \sim 4\times10^{11}\mathrm{cm}^{-3}$ which is the lowest atomic density required for the elimination of diffraction, we have $\beta \simeq 1.37\mathrm{cm}^{-1}$, indicating that the probe will be severely attenuated after a rather short propagation distance. It lays as a main obstacle for practical application.

4.1.3.2 With incoherent pump

Actually, the severe absorption due to the negative two-photon detuning can be completely compensated by the gain from atomic coherences, which is induced by the incoherent pump together with the control field. At first glance of Eq. (4.8), both ρ_{31} and ρ_{21} suffer an additional decoherence effect due to the applied incoherent pump, which may lead to even stronger absorption for the probe field. While it is not the case, since the populations of the ground state $|1\rangle$ is pumped out and then redistributed among total four states by the incoherent pump together with the control field. Then, the coherent control field generates atomic coherences $\rho_{23}^{(0)}$ between metastable state $|2\rangle$ and excited state $|3\rangle$, which gives gain to the probe. We then calculate the steady-state populations and coherences in the zeroth order of Ω_p. For a resonant control field where $\Delta_c = 0$, the relevant elements $\rho_{ij}^{(0)}$ is obtained

$$\rho_{11}^{(0)} = \frac{4\Gamma_{31}(p+\Gamma_4)\Omega_c^2}{p\Gamma_3^2\Gamma_{42}+4[2p(\Gamma_{31}+\Gamma_{42})+\Gamma_{31}\Gamma_4]\Omega_c^2}\,, \tag{4.33a}$$

$$\rho_{33}^{(0)} = \frac{4p\Gamma_{42}\Omega_c^2}{p\Gamma_3^2\Gamma_{42}+4[2p(\Gamma_{31}+\Gamma_{42})+\Gamma_{31}\Gamma_4]\Omega_c^2}\,, \tag{4.33b}$$

$$\rho_{23}^{(0)} = \frac{-i2p\Gamma_3\Gamma_{42}\Omega_c}{p\Gamma_3^2\Gamma_{42}+4[2p(\Gamma_{31}+\Gamma_{42})+\Gamma_{31}\Gamma_4]\Omega_c^2}\,. \tag{4.33c}$$

These are further plotted in Fig. 4.2. It is clear that the populations $\rho_{11}^{(0)}$ in the ground state decreases as the incoherent pump increases, at the same time, the populations $\rho_{33}^{(0)}$ in the exited state and atomic coherences $\rho_{23}^{(0)}$ increase. It means that on the one hand the single-photon absorption depending on the population difference $\rho_{11}^{(0)}-\rho_{33}^{(0)}$ is decreased, on the other hand it can be further compensated by the induced atomic coherences $\rho_{23}^{(0)}$. To clearly show that not only the paraxial diffraction can be exactly removed but also the strong absorption can also be completely compensated when applying the incoherent

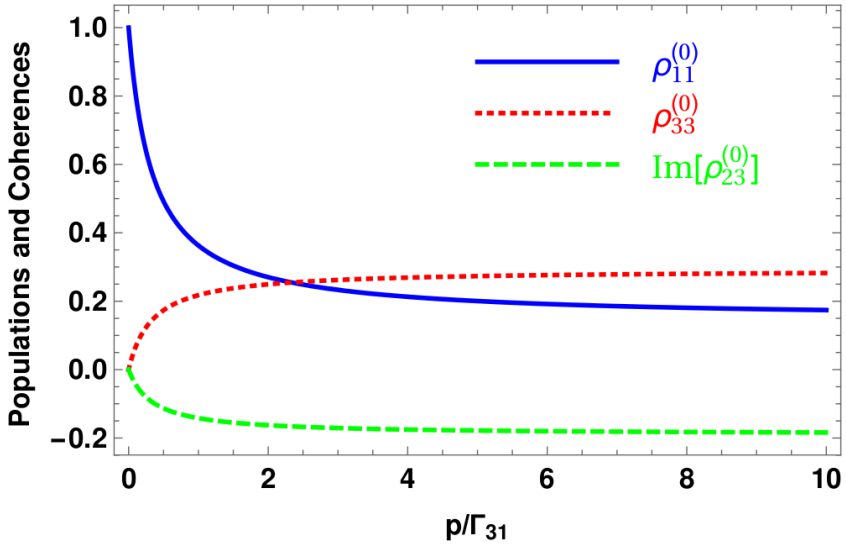

Figure 4.2: The populations $\rho_{11}^{(0)}, \rho_{33}^{(0)}$ and coherence $\mathrm{Im}[\rho_{23}^{(0)}]$ as a function of the amplitude of the incoherent pump. Parameters are: $\Gamma = 2\pi \times 5.75$ MHz, $\Gamma_{31} = \Gamma/4, \Gamma_{32} = \Gamma/6, \Gamma_{41} = \Gamma/12, \Gamma_{42} = \Gamma/2, \gamma_{21} = 0.001\Gamma_{31}, \Omega_c = 1.4\Gamma_{31}$.

pump, we rewrite Eq. (4.24) in order of $\mathrm{k}_\perp^2$

$$\chi(\mathbf{k}_\perp) = \chi_p^{(0)} + \chi_p^{(1)} \frac{\mathrm{k}_\perp^2}{\mathrm{k}_1^2} + O(\mathrm{k}_\perp^4)\,, \tag{4.34}$$

where we have

$$\chi_p^{(0)} = i\alpha(\rho_{11}^{(0)} - \rho_{33}^{(0)} + \frac{\Gamma_c(\rho_{11}^{(0)} - \rho_{33}^{(0)}) + i\Omega_c\rho_{23}^{(0)}}{i\Delta - \Gamma_1})\,, \tag{4.35a}$$

$$\chi_p^{(1)} = i\alpha\Gamma_1\gamma_{c1}\frac{\Gamma_c(\rho_{11}^{(0)} - \rho_{33}^{(0)}) + i\Omega_c\rho_{23}^{(0)}}{(\gamma_{c1} - i\Delta)(i\Delta - \Gamma_1)^2}\,, \tag{4.35b}$$

$$\mathrm{k}_1 = \sqrt{\frac{\Gamma_1\gamma_{c1}}{\mathrm{v}_{\mathrm{th}}^2}} = \frac{1}{\mathrm{v}_{\mathrm{th}}}\sqrt{(\gamma_c + \frac{p}{2} + \gamma_{21})(\Gamma_c + \frac{p}{2} + \gamma_{21})}\,, \tag{4.35c}$$

and we have set $\gamma_{c1} = p/2 + \gamma_c + \gamma_{21}$. In the region $\mathrm{k}_\perp \ll \mathrm{k}_1$, the linear susceptibility is proportional to $\mathrm{k}_\perp^2$ except for a constant term. Especially, when we chose a negative detuning

$$\Delta = -\sqrt{\frac{\gamma_{c1}}{\gamma_{c1} + 2\Gamma_1}}\Gamma_1\,, \tag{4.36}$$

then the imaginary part of $\chi_p^{(1)}$ which may lead to diffusion for the probe field can be set to zero. Furthermore, we find the condition for the diffraction cancellation

$$\frac{1}{\mathrm{k}_p^2} = \frac{\mathrm{Re}[\chi_p^{(1)}]}{\mathrm{k}_1^2} = -\alpha\Gamma_1\gamma_{c1}\Delta\frac{[\Gamma_c(\rho_{11}^{(0)} - \rho_{33}^{(0)}) + i\Omega_c\rho_{23}^{(0)}](\Gamma_1^2 - \Delta^2 + 2\gamma_{c1}\Gamma_1)}{(\gamma_{c1}^2 + \Delta^2)(\Gamma_1^2 + \Delta^2)^2\mathrm{k}_1^2}\,. \tag{4.37}$$

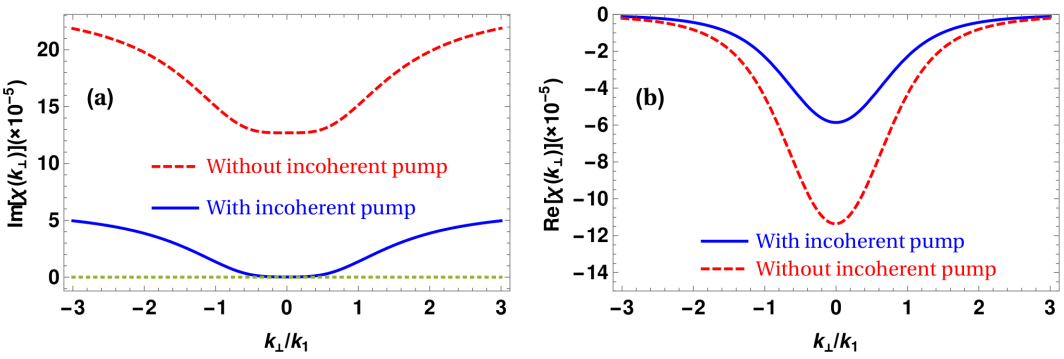

Figure 4.3: The motion-induced linear susceptibility $\chi(\mathbf{k}_\perp)$ in momentum space with or without the incoherent pump field. In the central region $\mathrm{k}_\perp/\mathrm{k}_1 \ll 1$, the linear absorption $\mathrm{Im}[\chi(\mathbf{k}_\perp)]$ (a) remains as a constant in the case of no incoherent pump, indicating strong absorption for the probe field. When the incoherent pump is applied, the constant absorption is reduced to zero due to gain from atomic coherences $\rho_{23}^{(0)}$. At the same time, the dispersion $\mathrm{Re}[\chi(\mathbf{k}_\perp)]$ (b) is still quadratic in $\mathrm{k}_\perp$ in this region for both cases except for different constant offsets. Then the probe field will experience diffractionless and lossless propagation in the prepared thermal medium. Parameters are: $n_0 = 1.5 \times 10^{12}$ cm$^{-3}, \lambda_p = 795$ nm$, T = 300$ $K, \mathrm{v_{th}} = 240$ m/s$, \Delta\mathrm{k} = 22.8$ m$^{-1}, \gamma_c = 2000\ \Delta\mathrm{k} \cdot \mathrm{v_{th}}, p = 0.65\Gamma_{31}$. Other parameters are as in Fig. 4.2.

More interestingly, the constant absorption is give by

$$\mathrm{Im}[\chi_p^{(0)}] = \alpha(\rho_{11}^{(0)} - \rho_{33}^{(0)} - \Gamma_1 \frac{\Gamma_c(\rho_{11}^{(0)} - \rho_{33}^{(0)}) + i\Omega_c\rho_{23}^{(0)}}{\Delta^2 + \Gamma_1^2}), \tag{4.38}$$

now it is determined by the competition between one-photon absorption $\propto \rho_{11}^{(0)} - \rho_{33}^{(0)}$ due to negative two-photon detuning and the gain induced by the atomic coherence $\rho_{23}^{(0)}$. By appropriately choosing parameters, the constant absorption can be reduced to zero or even negative, which means the probe field can be amplified. We then plot the linear susceptibility $\chi(\mathbf{k}_\perp)$ in momentum space as shown in Fig. 4.3 by the solid blue line. In the central area $\mathrm{k}_\perp \ll \mathrm{k}_1$, the linear absorption $\mathrm{Im}[\chi(\mathbf{k}_\perp)]$ is exactly reduced to zero, while the dispersion $\mathrm{Re}[\chi(\mathbf{k}_\perp)]$ is still quadratic in $\mathbf{k}_\perp$ except for a constant offset. As a comparison, we also plot the linear susceptibility without incoherent pump as shown in Fig. 4.3 by the dashed red line. If all the components of the probe in momentum space are located in the central region $\mathrm{k}_\perp/\mathrm{k}_0 \ll 1$, then the paraxial diffraction of the probe field can be precisely eliminated by the linear dispersion. Since the absorption is also removed, the probe field will propagate without diffraction and attenuation throughout the thermal medium.

4.1.3.3 Image propagation

In principle, our enhanced scheme can be generally realized in any thermal atomic system in which a double-lambda level structure could be found. However, since we have not considered the collective interaction [226] between atoms in our scheme, it means that the atomic gas should be dilute. In order to have a low atomic density, we then find that the spontaneous decay rate Γ_{42} should be much larger than Γ_{41} to minimize the populations staying in the upper state $|4\rangle$ which does not interact with the probe field. Moreover, the coupling between atoms and the probe field should be as strong as possible to further reduce the atomic density, it means that a large dipole moment

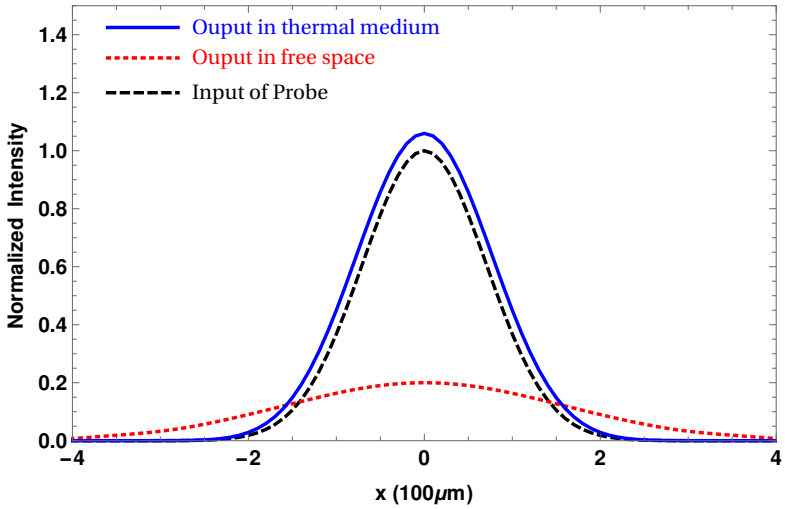

Figure 4.4: A Gaussian probe field with transverse profile $\Omega_p(x,y) = \Omega_{p0}\text{Exp}[-(x^2+y^2)/(2\text{w}_p^2)]$ propagates in free space and in the thermal medium, for a propagation distance $z = 2z_R$. Here we only show the slice at $y = 0$. The probe remains almost unchanged through propagating in the thermal medium with canceled paraxial diffraction and slightly amplified peak intensity. Parameters are: $\text{w}_p = 100\ \mu m$, others are the same as in Fig. 4.3.

$\vec{\mu}_{31}$ is required. Fortunately, the hyperfine structure of ^{87}Rb D1 line could meet the requirements: magnetic sublevels $5\ ^2S_{1/2}, F = 1, m_F = 0$ and $F = 2, m_F = 2$ are chosen to be the two lower states $|1\rangle$ and $|2\rangle$, and $5\ ^2P_{1/2}, F = 2, m_F = 1$ and $F = 1, m_F = 1$ are chosen to be the two upper states $|3\rangle$ and $|4\rangle$ respectively. A strong right-handed circularly polarized laser field can be applied to couple the transition $|2\rangle \leftrightarrow |3\rangle$ to act as the control field, with a weak left-handed circularly polarized field coupling the transition $|1\rangle \leftrightarrow |3\rangle$ to be the probe field. It can be easily implemented in current experimental settings. The parameters of those transitions, as shown in Fig. 4.2, are used throughout the analytical and numerical calculations of the present work.

We then numerically solved Eq. (4.28) together with Eq. (4.24), and then Fourier transformed into real space to simulate the probe propagation in the thermal medium. Fig. 4.4 shows a Gaussian probe beam with initial profile $\Omega_p(x,y) = \Omega_{p0}\text{Exp}[-(x^2+y^2)/(2\text{w}_p^2)]$ ($\text{w}_p = 100\mu m$) propagates both in free space and in the thermal medium using the proposed setup after two Rayleigh lengths ($z_R = 2\pi\text{w}_p^2/\lambda_p = 7.90\text{cm}$). Here we only take the slice $y = 0$ to clearly show the differences of propagation dynamics between the two cases. The transmitted peak intensity of the probe is decreased by a factor of $1/[1+(z/z_R)^2] = 1/5$ with a broadened width $\text{w}_p(z = 2z_R) = \sqrt{1+(z/z_R)^2} = \sqrt{5}\text{w}_p$ in free space due to paraxial diffraction. While propagating in the prepared thermal medium, the Gaussian spatial profile of the probe is preserved, the output of the probe is almost unchanged with width $\text{w}_p(z = 2z_R) = 1.074\text{w}_p$ and a slightly amplified peak intensity by a factor of 1.063. Thanks to the nonlocal linear effects introduced by the atomic motion and the incoherent pump, the paraxial diffraction of the probe is eliminated with no absorption. Since some of wave components of the Gaussian probe in momentum space are outside from the central area $\text{k}_\perp/\text{k}_0 \ll 1$, they acquire extra phases while propagating in the medium due to high-order diffraction $\sim O(\text{k}_\perp^4)$, leading to the insignificantly broadened width $\text{w}_p(z = 2z_R) = 1.074\text{w}_p$. In order to demonstrate that arbitrary image encoded on the probe field can propagate without diffraction and loss in our scheme, we further simulated a two-dimensional image imprinted on the probe

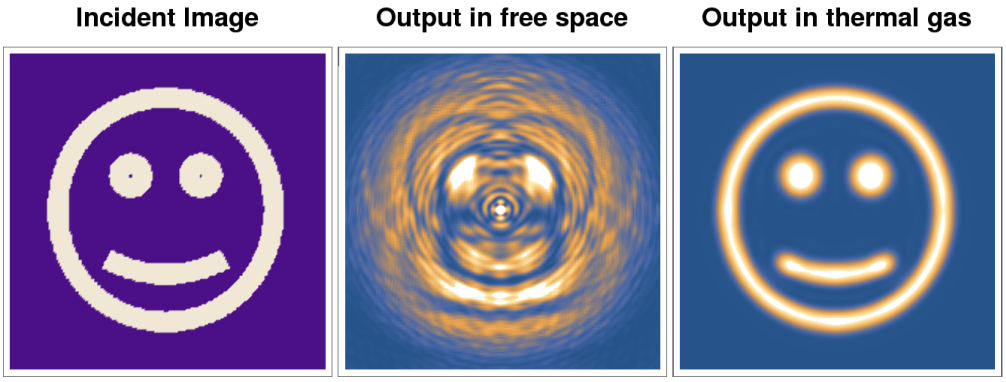

Figure 4.5: A smiley face encoded on the probe field propagates in free-space and in the medium. Obviously the image is severely distorted in free-space while is faily preserved in the medium. The image size is 20×20 with a scale of $100\ \mu m$. Other parameters are the same as in Fig. 4.3.

field propagating two Rayleigh lengths in the thermal medium. The results are shown in Fig. 4.5. Note that the image is represented by an array of values "0" and "1" in the transverse plane, thus including wave components with large transverse wave vectors. We can immediately find that the image is totally distorted while propagating in free space. However, as propagating in the prepared thermal medium, the image is fairly preserved. Moreover, the intensity of the image remains almost the same, except for weak amplifications in the edges due to both the residual diffraction of wave components with large wavevectors and also the higher-order diffraction of the wave components in momentum space.

4.1.3.4 Effect of the incoherent pump field

From Eq. (4.37) and (4.38), one can find that the incoherent pump does not only affect the power but also the width of the output probe. We also numerically calculated the transmitted power and width of a Gaussian probe versus the amplitude of the incoherent pump, after propagating two Rayleigh lengths in the prepared thermal medium. The results are shown in Fig. 4.6. It can be seen from Fig. 4.6(a) that the transmitted power of the probe is very sensitive to the amplitude of the incoherent pump. For a weak incoherent pump, the probe is severely attenuated since the single-photon absorption due to imperfect EIT is still much stronger than the coherent scattering from atomic coherences; for strong incoherent pump, the coherent scattering becomes dominant, leading to significant amplification of the probe as shown in Fig. 4.6(a). However, the transmitted width of the probe only weakly depends on the amplitude of the incoherent pump as shown in Fig. 4.6(b). The small increases in the slightly broadened width is due to the breakdown of the condition for elimination of diffraction shown in Eq. (4.37). we then find that the output power of the probe can be controlled without changing the output width very much, by simply tuning the intensity of the incoherent pump. It also suggests that the possible inhomogeneities in the incoherent pump field, which may arise due to absorption in the medium, will not significantly affect the outgoing spatial profile and the diffractionless propagation.

4.1.4 Discussions

In our numerical calculations, we have assumed parameters of the D1 line of ^{87}Rb, which has been widely used in current experiments. But in principle, our scheme can be

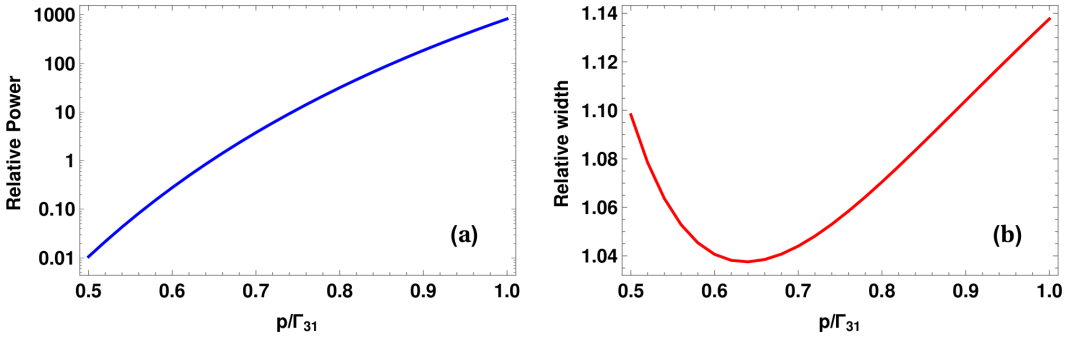

Figure 4.6: The relative output power (a) and width (b) of a Gaussian probe versus the amplitude of the two-way incoherent pump p after propagating two Rayleigh lengths in the thermal medium. Other parameters are the same as in Fig. 4.3.

realized in any thermal atomic system in which a double-Λ level structure can be found. However, since we have not considered direct interactions between the atoms [227, 228] in our scheme, the atomic gas should be dilute enough to neglect them. In order to allow our scheme to work at lower atomic densities, we found that it is favorable if a large ratio Γ_{42}/Γ_{41} between spontaneous decay rates minimizes the population in the upper state $|4\rangle$ which does not interact with the probe field. Moreover, the coupling between the atoms and the probe field should be as strong as possible to further reduce the required atomic density, such that a large dipole moment $\vec{\mu}_{31}$ is favorable.

As discussed above, we initially employed the two-way incoherent pump field to redistribute the populations and induce atomic coherences already at zeroth order in the probe field, which would lead to reduction of one-photon absorption. Surprisingly, we found that the pump field has several more positive effects beyond our initial purpose. First, the incoherent pump further alleviates the demand for strong collision rates to achieve the Dicke limit. Second, since k_1 defined in Eq. (4.35c) which sets the transverse wave number scale in Eq. (4.34) grows rapidly as the incoherent pump increases, the series expansion in the transverse momentum becomes more accurate with the pump field, resulting in both a further improvement of diffraction elimination and a reduction of the higher-order diffraction for the probe field. Third, the pump field introduces one more degree of freedom to control probe propagation.

For a short summary of this section, we have proposed an enhanced scheme in which a probe field encoded with arbitrary images propagates without diffraction and absorption in a double-lambda thermal atomic system. In the scheme, we applied an additional two-way incoherent pump to redistribute the populations and then to generate an additional zero-order atomic coherences together with the coherent control field. The single-photon absorption due to imperfect EIT condition can be compensated by the gain from the generated atomic coherences, while the paraxial diffraction is eliminated by the $\mathrm{k}_\perp$-square dependent dispersion at the same time, resulting in diffractionless and lossless propagation for the probe field. This $\mathrm{k}_\perp$-square dependent dispersion stems from the nonlocal linear effects induced by thermal atomic motion and collisions. Since the elimination of diffraction operates in momentum space, it is thus suitable for the probe carrying with arbitrary spatial profiles. We also discussed the possible experimental implementation in atomic ^{87}Rb with the hyperfine structure of D1 line.

4.2 Uniform phase modulation with vanishing diffraction or absorption

4.2.1 Motivation

Light propagation through matter is governed by the refractive index. Consequently, manipulation and control of the refractive index has been a topic of substantial interest over the last decades. A particular promising candidate is atomic gases, which offer great flexibility in designing the optical response, and thus in controlling the propagation of light. The linear refractive index can be enhanced in a straightforward way by tuning the light carrier frequency close to an atomic resonance. But in this case, the enhancement is accompanied with strong absorption, prohibiting most applications. A number of methods have been proposed to overcome this limitation to change the refractive index without absorption [197, 229–239]. Currently, experiments are limited to refractive index variations of order $\Delta n \simeq 10^{-4}$ [231, 237], but there are theoretical suggestions to improve the enhancement (see, e.g., Ref. [239] and references therein).

In general, the spatial evolution of the light fields in the medium will give rise to energy attenuation and spatial distortion due to paraxial diffraction. As a consequence, additional unwanted nonuniform phase shifts will be induced by the diffraction over the transverse plane perpendicular to the propagation direction. These effects become particularly important if long propagation distances are required, and if the manipulation of the refractive index depends on the intensities of the involved laser fields.

This raises the question, whether it is possible to realize uniform phase modulation for laser beams with arbitrary spatial profiles. One approach to achieve this goal is

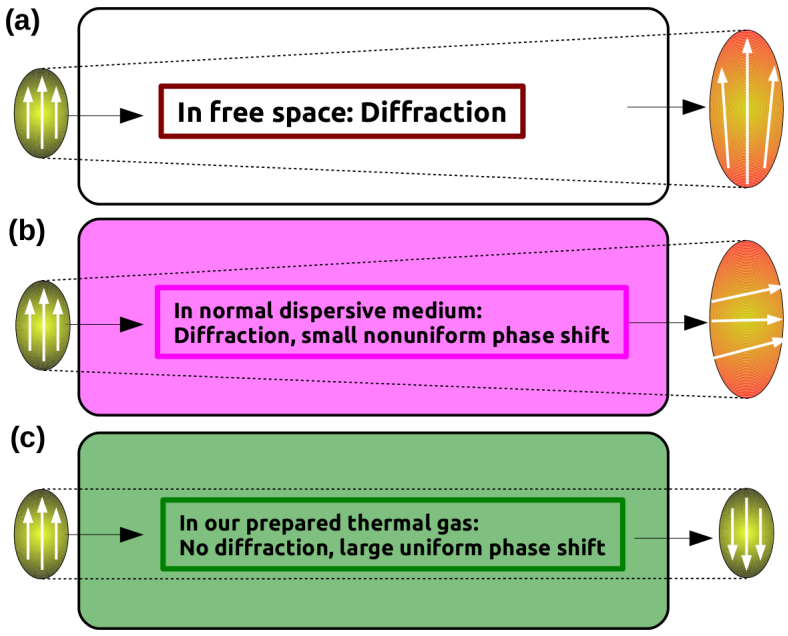

Figure 4.7: Schematic illustration for phase modulation acquired by a laser field throughout propagation in different media. The arrows indicate the phase distribution of the laser field. (a) In free space, diffraction leads to spatial spreading and a small nonuniform phase distribution in the transverse plane. (b) In a regular dispersive medium, spatial spreading and nonuniform phase distortion due to diffraction occur. (c) In the setup discussed here, a strong spatially uniform phase shift is achieved, together with cancellation of paraxial diffraction.

to reduce the diffraction. As we have already learned from Sec. 4.1, a novel scheme to explore the effect of atomic motion and collisions to eliminate paraxial diffraction of laser beams with arbitrary spatial shapes was theoretically proposed [20–22, 240], and also experimentally verified [23, 24] by Firstenberg *et al.*. It is not restricted to particular spatial profiles, since it operates on the light in the transverse momentum space thanks to the nonlocal nature of the atomic response, directly canceling the effect of diffraction for each of the transverse momentum components individually. Interestingly, in this method, the thermal motion of atoms does not act as a perturbation, but are rather exploited to reduce the paraxial diffraction.

Motivated by this, here, we address the question whether the homogeneity of the phase modulation can be improved by effects of thermal atomic motion and collisions. To this end, based on the results obtained in Sec. 4.1, we propose a setup which allows to achieve strong controllable uniform phase shifts over short propagation distances. We predict refractive index changes of order $\Delta n \simeq 10^{-4}$ with vanishing absorption at atomic density $\sim 1.5 \times 10^{12}\mathrm{cm}^{-3}$. The phase modulation is based on the linear susceptibility of the atomic vapor and therefore does not depend on the intensity of the laser beam. Furthermore, this uniform phase modulation can be easily controlled by tuning the intensities of the applied laser and incoherent pump fields. These advantages are illustrated in Fig. 4.7.

4.2.2 Phase modulation for laser beams with arbitrary spatial profiles

4.2.2.1 nonlocal linear susceptibility of the thermal medium

The atomic medium configuration is shown in Fig. 4.1(b). As having already derived in Sec. 4.1.2, the nonlocal linear effects of the thermal atoms in momentum space reads

$$\chi(\mathbf{k}_\perp) = i\alpha \left(\rho_{11}^{(0)} - \rho_{33}^{(0)} + \frac{\Gamma_c(\rho_{11}^{(0)} - \rho_{33}^{(0)}) + i\Omega_c \rho_{23}^{(0)}}{i\Delta - \Gamma_1 - D\mathrm{k}_\perp^2} \right) . \tag{4.39}$$

Before we start to study the uniform phase modulation induced by the nonlocal linear effects, we would like to first briefly review the physical mechanism of elimination of diffraction and absorption as discussed in detail in Sec. 4.1. In order to show this, we then repeat the expansion of Eq. (4.39) in $\mathrm{k}_\perp$ and obtain

$$\chi(\mathbf{k}_\perp) = c_0 + c_1 \frac{\mathrm{k}_\perp^2}{\mathrm{k}_1^2} + O(\mathrm{k}_\perp^4) , \tag{4.40}$$

where

$$c_0 = i\alpha \left(\rho_{11}^{(0)} - \rho_{33}^{(0)} + \frac{\Gamma_c(\rho_{11}^{(0)} - \rho_{33}^{(0)}) + i\Omega_c \rho_{23}^{(0)}}{i\Delta - \Gamma_1} \right) , \tag{4.41a}$$

$$c_1 = i\alpha\Gamma_1\gamma_{c1} \frac{\Gamma_c(\rho_{11}^{(0)} - \rho_{33}^{(0)}) + i\Omega_c \rho_{23}^{(0)}}{(\gamma_{c1} - i\Delta)(i\Delta - \Gamma_1)^2} , \tag{4.41b}$$

$$\mathrm{k}_1 = \sqrt{\frac{\Gamma_1\gamma_{c1}}{\mathrm{v}_{\mathrm{th}}^2}} = \frac{1}{\mathrm{v}_{\mathrm{th}}} \sqrt{(\gamma_c + \frac{\mathrm{p}}{2} + \gamma_{21})(\Gamma_c + \frac{\mathrm{p}}{2} + \gamma_{21})} . \tag{4.41c}$$

In the regime $\mathrm{k}_\perp \ll \mathrm{k}_1$, the constant term c_0 leads to uniform absorption and dispersion, while the $\mathrm{k}_\perp^2$-dependent term proportional to c_1 results in atomic-motion induced

absorption and elimination of diffraction. As already discussed in Sec. 4.1, a suitable value for the two-photon detuning

$$\Delta = -\sqrt{\frac{\gamma_{c1}}{\gamma_{c1} + 2\Gamma_1}}\Gamma_1 \,, \tag{4.42}$$

can be chosen to remove the $\mathrm{k}_\perp^2$-dependent absorption which gives rise to diffusion, i.e. $\mathrm{Im}[c_1] = 0$. Furthermore, diffraction is canceled if

$$\frac{1}{\mathrm{k}_p^2} = \frac{\mathrm{Re}[c_1]}{\mathrm{k}_1^2} = -\alpha\Gamma_1\gamma_{c1}\Delta\frac{[\Gamma_c(\rho_{11}^{(0)} - \rho_{33}^{(0)}) + i\Omega_c\rho_{23}^{(0)}](\Gamma_1^2 - \Delta^2 + 2\gamma_{c1}\Gamma_1)}{(\gamma_{c1}^2 + \Delta^2)(\Gamma_1^2 + \Delta^2)^2\mathrm{k}_1^2} \,. \tag{4.43}$$

Combined with Eqs. (4.28) and (4.39), we finally obtain the propagation equation

$$\frac{\partial}{\partial z}\Omega_p(\mathbf{k}_\perp, z) = i\frac{\mathrm{k}_p}{2}c_0\Omega_p(\mathbf{k}_\perp, z) \,. \tag{4.44}$$

This equation is readily solved as

$$\Omega_p(r_\perp, z) = \Omega_p(r_\perp, z = 0)\, e^{\frac{i}{2}\mathrm{k}_p c_0 z} \,. \tag{4.45}$$

Eq. (4.45) shows that the probe field will propagate through the thermal medium preserving its spatial profile, i.e., without diffraction. By changing the incoherent pump and the control field, the constant absorption proportional to $\mathrm{Im}[c_0]$ can be tuned to zero or even negative values. As a result, at zero absorption, the probe field only experiences an uniform phase shift proportional to $\mathrm{Re}[c_0]$ during the propagation while all other physical properties remain the same.

4.2.2.2 Uniform phase modulation without diffraction or absorption

From Eq. (4.45) we find that uniform phase shifts can be achieved without affecting any other properties of the probe field, such as the spatial profile or the power, for appropriate parameter choices. This phase shift can be written as

$$\phi_s = \frac{1}{2}\mathrm{k}_p\Delta n z \,, \tag{4.46a}$$

$$\Delta n = \mathrm{Re}[c_0] \,, \tag{4.46b}$$

which does not depend on the shape or the intensity of the probe field, and thus is universal. The derivation of Eq. (4.45) relied on several approximations. In order to investigate the validity of these approximations, we next simulate the propagation dynamics of the probe field in the prepared thermal medium by numerically solving Eq. (4.28) together with Eq. (4.39). The result is subsequently Fourier transformed back to real space. For a proof-of-principle demonstration, the incident probe field is assumed to have a Gaussian spatial profile

$$\Omega_p(x, y, z = 0) = \Omega_{p0}e^{-(x^2+y^2)/(2w_p^2)} \,, \tag{4.47}$$

the initial width of the Gaussian probe is set to $w_p = 100\mu m$, which is within the paraxial regime. We assume the same parameters of the D1 line of ^{87}Rb for the thermal atoms as used in Sec. 4.1. We further choose a propagation distance of one Rayleigh length $z_R = 2\pi w_p^2/\lambda_p$ which for the present parameters evaluates to about 7.90cm. Results

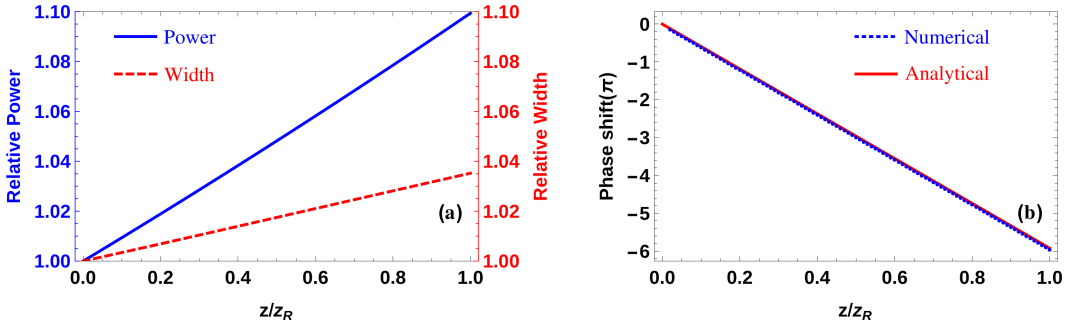

Figure 4.8: (a) Power and spatial width of the Gaussian probe beam as function of the propagation distance. Note the small plot range of only few percent relative change, suggesting that the probe field power and width remain approximately unchanged. (b) The accumulated phase shift as a function of propagation distance. π-phase flips can be achieved already in a small fraction of the Rayleigh length z_R. Parameters are: $n_0 = 1.5 \times 10^{12}$ cm$^{-3}, \lambda_p = 795$ nm, $T = 300$ K, $\mathsf{v_{th}} = 240$ m/s, $\Delta\mathsf{k} = 22.8$ m$^{-1}, \gamma_c = 2000$ $\Delta\mathsf{k} \cdot \mathsf{v_{th}}, \Gamma = 2\pi \times 5.75$ MHz, $\Gamma_{31} = \Gamma/4, \Gamma_{32} = \Gamma/6, \Gamma_{41} = \Gamma/12, \Gamma_{42} = \Gamma/2, \gamma_{21} = 0.001\Gamma_{31}, \Omega_c = 1.4\Gamma_{31}, \mathsf{p} = 0.65\Gamma_{31}$.

are depicted in Fig. 4.8. As can be seen from panel (a), the Gaussian shape of the probe is maintained throughout the propagation in the thermal vapor, except for a small broadening by up to 3.5% due to the residual higher-order diffraction $\sim O(\mathrm{k}_\perp^4)$. The probe is also weakly amplified as the propagation distance increases, since we have chosen a relatively strong incoherent pump field such that the gain from the atomic coherences exceeds the reduced single-photon absorption. Note that more precise tuning of the parameters results in a further reduction of the broadening and amplification. After having established that the shape and intensity remain essentially unchanged, we turn to the phase, which is shown in Fig. 4.8(b). While propagating through the thermal atoms, a phase shift starting from 0 up to almost -6π is imprinted onto the probe beam within the single Rayleigh length. Already after $z_f \simeq 0.168 z_R \simeq 1.33$cm, which is a small fraction of the Rayleigh length, a π-phase flip can be achieved. This phase modulation can readily be understood, since the non-zero two-photon detuning results in a deviation from the EIT resonance, such that a nonzero linear dispersion is obtained for the probe field. This nonzero linear dispersion leads to a change in the refractive index of order $\Delta n \simeq -0.6 \times 10^{-4}$ for the chosen parameters. It is important to note that the π-phase flip is accomplished due to the specific type of the nonlocal linear effects, and is therefore independent of the spatial shape and power of the incident probe field.

4.2.2.3 Effect of the intensity of the control field

The phase modulation can be controlled not only by the propagation distance, but also by other parameters such as the intensities of the control and pump fields, as illustrated by Eqs. (4.46), (4.41a) and (4.33). In this section, we study the effect of the intensity of the control field. Results are shown in Fig. (4.9) for a Gaussian probe field, which propagates in the thermal medium for a distance equal to one Rayleigh length. In the absence of the control field ($\Omega_c = 0$), since the atoms have been optically pumped out from the ground state $|1\rangle$ to $|2\rangle$ by the incoherent pump, there is no interaction between the atoms and the probe field any more. Then the probe propagation proceeds as in free space. As shown in Fig. 4.9(a), the probe field acquires a small phase shift due to the diffraction term, while the power remains the same and the width is broadened to $w(z = z_R) = \sqrt{2} w_p$ as depicted in Fig. 4.9(b) by the red dashed line. Increasing Ω_c,

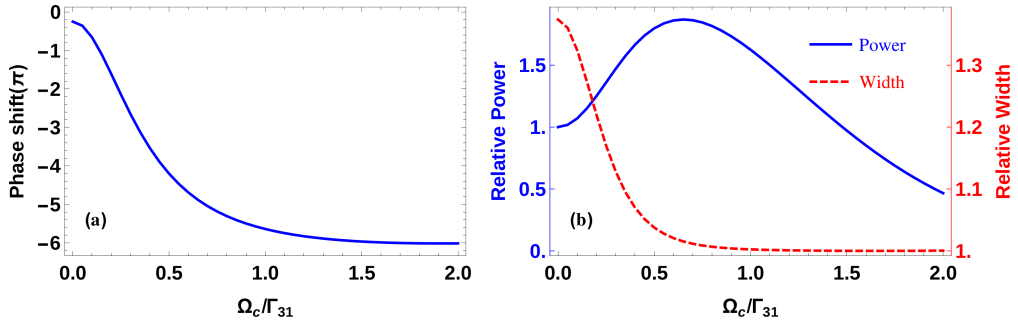

Figure 4.9: (a) Phase shift of the transmitted Gaussian probe field against the intensity of the control after propagating one Rayleigh length in the thermal atomic gas. (b) The power and width of the outgoing probe field as a function of the control. Other parameters are as in Fig. 4.8.

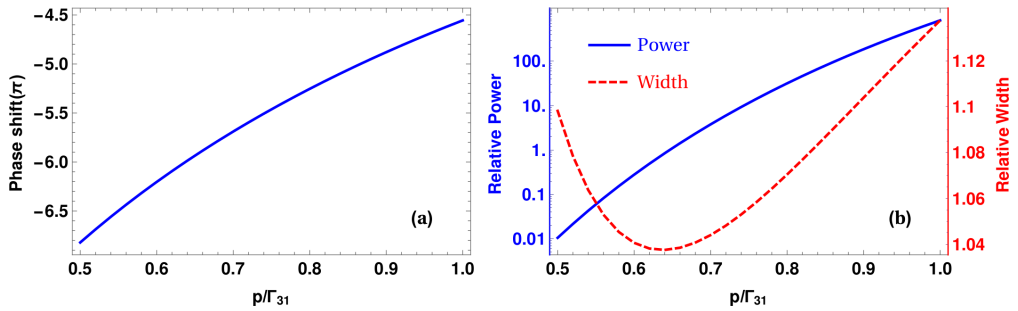

Figure 4.10: (a) Phase shift of the output Gaussian probe field as a function of the incoherent pump rate after propagating one Rayleigh length in the thermal atomic gas. (b) The power and width of the outgoing probe field as function of the incoherent pump rate. Other parameters are as in Fig. 4.8.

the phase shift can be gradually tuned, due to the Ω_c-dependent constant dispersion $\mathrm{Re}[c_0]$ (i.e., the changes in refractive index, Δn). At Ω_c exceeding about $1.5\,\Gamma_{31}$, the phase shift becomes approximately independent of Ω_c since $\mathrm{Re}[c_0]$ has saturated to its minimum [but maximum absolute value, see Fig. 4.9(a)]. By dynamically changing the control field, the phase shift can also be switched between two values. For example, a controllable phase shift of π could be realized by toggling Ω_c between $0.47\Gamma_{31}$ and $0.7\Gamma_{31}$. The relative phase shift imprinted onto the probe beam between these two intensities is π. Due to the switching, output probe field intensity slightly changes (relative power increases from 1.76 to 1.86), and the probe beam width is broadened by less than 8%.

4.2.2.4 Effect of the incoherent pump field

Next to the control field power, the phase shift can also be tuned via the amplitude of the incoherent pump field, which we studied here. Results are shown in Fig. 4.10 for a Gaussian probe field propagating in the thermal medium for a distance equal to one Rayleigh length. We find that the absolute value of the acquired phase shift is approximately inversely proportional to the incoherent pump rate p as shown in Fig. 4.10(a). Thus, a particular phase change can also be achieved by choosing a suitable pump strength. At lower pump rates, the width of the outgoing probe field decreases with increasing p, and reaches a minimum roughly at $\mathrm{p} = 0.65\Gamma_{31}$ at which the condition for diffraction cancellation is satisfied. For other values of p, the paraxial diffraction is either over- or under-compensated, resulting in a broadened width for the output probe. Since the populations and coherences sensitively depend on the incoherent pump power as indicated in

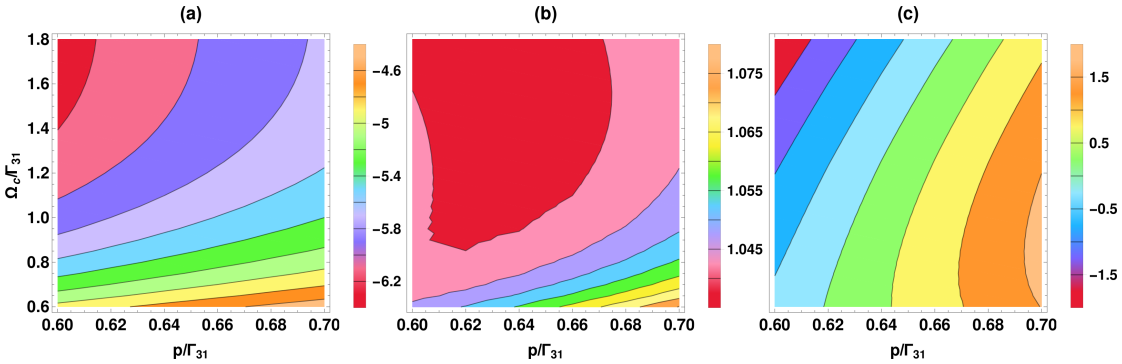

Figure 4.11: (a) Phase shift (in unit of π) of the output Gaussian probe field plotted against the intensities of the control and incoherent pump fields after propagating one Rayleigh length in the thermal atomic gas. Particular phase modulations can be achieved in various ways by tuning the control and incoherent pump simultaneously. (b) and (c) show the corresponding relative power ($\ln[P_{\text{out}}/P_{\text{in}}]$) and width ($w_{\text{out}}/w_p$) of the outgoing probe field. Other parameters are the same as in Fig. 4.8.

Eq. (4.33), the output power of the probe field strongly depends on the incoherent pump rate, as shown in Fig. 4.10(b).

4.2.2.5 Combining control field and incoherent pump field

More generally, the phase shift can be tuned by simultaneously changing the control field and incoherent pump field intensities. This way, results can further be improved compared to the control of only one of the two variables. An example is shown in Fig. 4.11 for a Gaussian probe field propagating one Rayleigh length in the thermal medium. Again it can be seen that particular phase modulations can be easily realized. For example, if a π-modulation via switching between phase shifts of -6π and -5π is chosen, then the width of the outgoing probe beam remains almost the same for the two values, with residual broadening less than 7%. Note that the output power of the probe field is much more sensitive to the incoherent pump rate than to the control field, since the redistribution of population and generation of coherences which lead to reduction of the single-photon absorption crucially depend on the intensity of the incoherent pump.

4.2.3 Spatial uniformity of the phase modulation

Throughout the calculations up to now, the phase value is extracted at the point of peak intensity of the probe field (i.e., at $x = y = 0$). Ideally, the phase imprinted onto the probe field should be uniformly distributed in the plane transverse to the propagation direction, since there is only an overall constant dispersion term affecting the propagation dynamics. However, the dispersion introduced by the residual diffraction in the region beyond $\mathrm{k}_\perp \ll \mathrm{k}_1$ and higher-order diffraction $\sim O(\mathrm{k}_\perp^4)$ can lead to small variations in the phase distribution over the transverse plane. This can be further improved by increasing k_1 defined in Eq. 4.41(d). As an example, we calculated the phase distribution over the transverse plane after a propagation distance $z_f = 0.168 z_R$ in free space, in a cold EIT medium, and in our thermal gas. Results are shown in Fig. 4.12(a)-(c). After this propagation distance z_f, the probe beam has accumulated a nearly uniform phase shift of π in the thermal medium, with the phase differences in the transverse plane smaller than 0.2% as shown in Fig. 4.12(f). In the cold EIT medium, we chose a rather small probe detuning as given in Fig. 4.12 in order to reduce the absorption due to the deviation

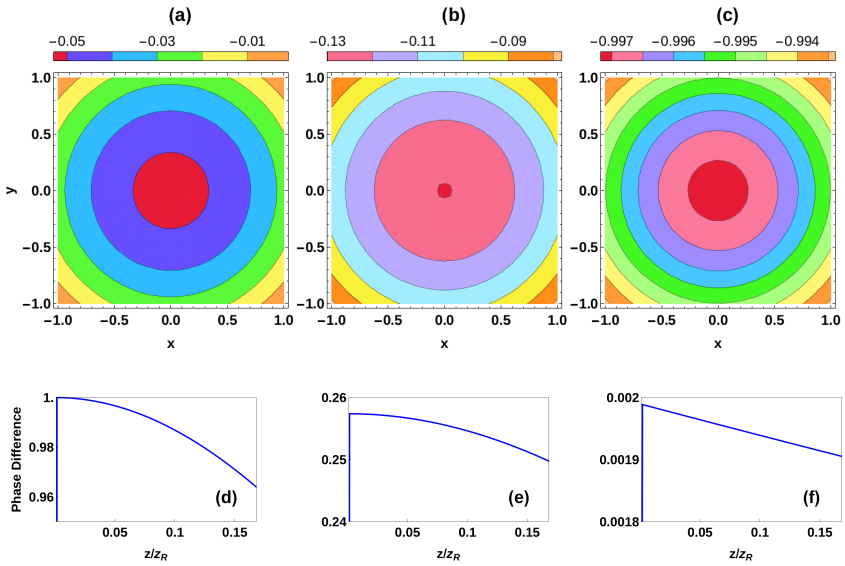

Figure 4.12: Spatial phase variation of the probe field in the transverse plane in units of π after a propagation distance $z_f = 0.168 z_R$. Results are shown for free space (a), a cold EIT medium (b), and the thermal vapor considered here (c). The parameters chosen for the cold EIT medium are the same as in Fig.(4.8) except for $T = 0K, \gamma_c = 0, \gamma_{21} = 0, \mathrm{p} = 0, \Delta_p = -0.001\Gamma_{31}$. In the thermal vapor, the probe acquires an almost uniform phase π, as compared to a small nonuniform phase gained in the cold EIT medium or in free space. (d)-(f) show the phase difference, which is defined as $(\phi[x = y = 0] - \phi[x = y = w_p])/(\phi[x = y = 0] + \phi[x = y = w_p])$, as a function of propagation distance for the three cases. The starting points for z in (d)-(f) are $z = 0.001 z_R$, since at $z = 0$ the phase difference for all cases should be 0. Other parameters are the same as in Fig. 4.8.

from the two-photon resonance, the acquired phase modulation is up to -0.13π, and accompanied with a phase difference larger than 25% as shown in Fig. 4.12(e).

4.2.4 Discussions

As discussed in Sec. 4.1.4, the introduced two-way incoherent pump field has proved that it has more positive effects far beyond our initial purpose to compensate the one-photon absorption. We would stress further here that since k_1 defined in Eq. (4.41d) which sets the transverse wave number scale in Eq. (4.40) grows rapidly as the incoherent pump increases, the series expansion in the transverse momentum becomes more accurate for an increasing pump field, resulting in a reduction of the differences in the phase distribution of the probe field across the transverse plane.

In summary, we have studied the possibility of achieving large uniform phase shifts by exploiting the atomic motion and collisions in a thermal atomic medium which gives rise to a specific type of nonlocal linear effects. At the time when uniform phase shift for the probe field is realized, the spatial distribution and the beam intensity of the probe remain approximately unchanged. The phase shift is obtained via a refractive index manipulation of order $\Delta n = -0.6 \times 10^{-4}$ at a rather low atomic density. Our scheme is applicable for probe fields with arbitrary spatial profiles within a certain transverse momentum bandwidth, and is independent of the probe field intensity. The phase shift can be controlled via the intensity of the control and incoherent pump fields. Furthermore, our proposal is feasible in current experimental settings as discussed in Sec. 4.1. In principle, our scheme can be extended to the low-photon level, as long as the noise induced by the gain mechanism remains low enough [241, 242].

4.3 Diffractionless image reproduction and frequency conversion

4.3.1 Motivation

A promising route towards the implementation of all-optical information processing or future quantum technologies is to combine different technologies into a hybrid system. This way, the different core functionalities can be realized using different methods, exploiting their individual advantages. But the various technologies typically operate at different characteristic frequencies, such that efficient frequency conversion is usually required. Such frequency conversion can be accomplished using nonlinear four-wave mixing (FWM) processes [9], which have already been widely studied and applied in various settings. Example are conventional up- and down-frequency conversion to generate vacuum-ultraviolet (VUV) or extreme-ultraviolet (XUV) [243–247] or far infrared (IR) [248–251] light.

But since FWM is a nonlinear process, it sensitively depends on the intensities of the applied fields, and thereby on the propagation dynamics [252] and on the transverse intensity profile of the applied fields. It is well-known, however, that light beams propagating in free space rapidly spread, together with a distortion of the transverse beam profile due to diffraction. The origin for diffraction is that each momentum component of the propagating beam acquires a different phase shift throughout the propagation. Diffraction is a fundamental limitation in particular for the creation, detection or propagation of small images, due to the large momentum bandwidth. The effect of diffraction thus is not only to destroy the information carried in the transverse beam profile, but also to distort any nonlinear processes such as FWM, due to the modification of the spatial intensity profiles. This raises the question, whether diffraction can be manipulated in a way such that nonlinear processes can be effective.

As discussed in Sec. 4.1 and 4.2, the thermal motion and collisions of atoms is found by Firstenberg *et al.* [20–24] to be capable of generating a specific type of nonlocal linear response, which can result in exact elimination of paraxial diffraction of laser beams carrying with arbitrary spatial profiles. In Sec. 4.1 and 4.2, we have put forward this approach further in which the necessarily involved absorption is alleviated by employing a two-way incoherent pump field. Stimulated by this, we then ask ourselves that if it is possible to accomplish difffractionless and lossless image reproduction between different frequencies when nonlinear processes are involved. The question is perfectly answered in this section.

With the knowledge gained in the previous sections, we here propose a method to transfer and frequency-convert an arbitrary image encoded in the spatial profile of a probe field onto a signal field using four-wave mixing in a thermal atomic vapor exhibiting nonlocal linear effects. We demonstrate how diffraction can be removed in this conversion process, by exploiting the atomic motion to cancel the paraxial diffraction of both the probe and signal fields simultaneously. Furthermore, we show that an additional incoherent two-way pump field can be employed to improve the performance in various ways. It redistributes populations in zeroth order of the probe field, which together with the applied control fields leads to the formation of additional coherences. This on the one hand allows us to cancel linear absorption with nonlinear gain such that the laser beam intensities are maintained throughout the propagation. On the other hand, the pump field broadens the transverse momentum bandwidth in which more wave components can be propagated without diffraction, such that smaller spatial structures become accessible. Third, the pump leads to modified propagation dynamics of the probe and

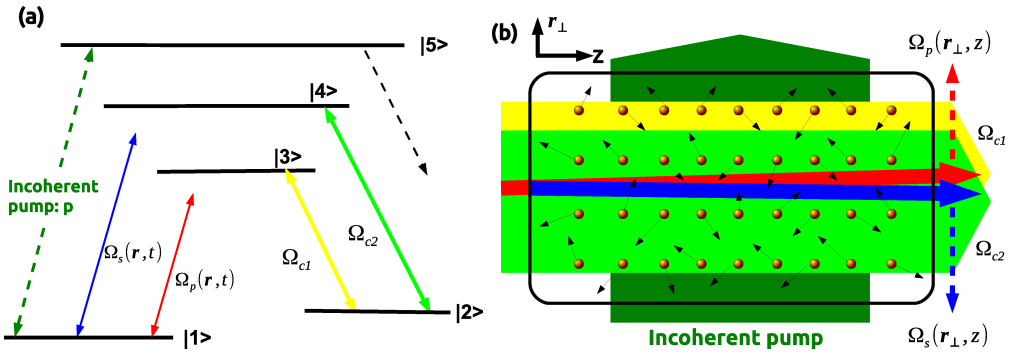

Figure 4.13: Schematic setup proposed to realize diffractionless image reproduction via four-wave mixing in a thermal atom vapor. (a) In the considered five-level model, the lower three states in Λ-configuration form the basic EIT setup for the probe propagation. The fourth state together with an additional control beam lead to a four-level double-Λ system, which enables four-wave mixing to generate an additional signal field. Finally, a two-way incoherent pump field is applied to the fifth auxiliary state. In effect, the single-photon absorption for both the probe and signal fields are reduced, and the four-wave mixing process is enhanced. (b) Co-linear propagation of the four coherent fields in the thermal atomic medium to satisfy the phase matching condition. Due to atomic motion, the paraxial diffraction of arbitrary profiles of both probe and signal fields can be eliminated over a certain bandwidth of the transverse beam profile. Eventually, the incident image encoded onto the probe is copied to the FWM signal field, which also propagates without diffraction.

signal fields which improves the FWM process, such that residual broadening and absorption of those two fields before the FWM equilibrium is reached are minimized. We analyze our setup first for Gaussian probe beams, and finally show that arbitrary images can be propagated and frequency-converted without diffraction. All results are based on ^{87}Rb at room temperature.

4.3.2 The four-wave mixing process in thermal atoms

We consider a five-level atomic system as shown in Fig. 4.13(a), which is designed as follows. The three levels $|1\rangle$, $|2\rangle$ and $|3\rangle$ form a Λ-shaped EIT setup. Transition $|1\rangle \leftrightarrow |3\rangle$ is driven by a weak probe field with Rabi frequency $\Omega_p(\mathbf{r},t) = \vec{\mu}_{31} \cdot \vec{e}_p E_p(\mathbf{r},t)/2\hbar$, while a resonant control field with Rabi frequency $\Omega_{c1}(\mathbf{r},t) = \vec{\mu}_{32} \cdot \vec{e}_{c1} E_{c1}(\mathbf{r},t)/2\hbar$ is applied to transition $|2\rangle \leftrightarrow |3\rangle$. This Λ-type setup is enlarged to a double-Λ-system by applying a second resonant control field with Rabi frequency $\Omega_{c2}(\mathbf{r},t) = \vec{\mu}_{42} \cdot \vec{e}_{c2} E_{c2}(\mathbf{r},t)/2\hbar$ to transition $|2\rangle \leftrightarrow |4\rangle$. The fourth transition $|1\rangle \leftrightarrow |4\rangle$ is not driven by an external field, but due to four-wave mixing, a signal field $\Omega_s(\mathbf{r},t) = \vec{\mu}_{41} \cdot \vec{e}_s E_s(\mathbf{r},t)/2\hbar$ can be generated from this transition throughout the propagation of the light fields through the medium. Finally, we apply a two-way incoherent pump field [197, 223–225] to the transition $|1\rangle \leftrightarrow |5\rangle$, which together with spontaneous decay from $|5\rangle$ into the other states effectively forms a one-way pumping from $|1\rangle$ into the other atomic states. Here, $\vec{\mu}_{ij}$ is the dipole moment between states $|i\rangle$ and $|j\rangle$ $(i,j \in \{1,2,3,4\})$. E_n and $\vec{e}_n$ are the slowly varying envelopes and unit polarization vectors of the electric fields with $n \in \{p, s, c1, c2\}$. The incoherent pump field induces a redistribution of the populations in zeroth order of the probe field, which together with the control fields leads to the formation of additional atomic coherences. These coherences turns out to favorably affect the propagation dynamics in a non-trivial way.

As discussed in more detail later, the required level scheme can be realized, for instance, in ^{87}Rb, with magnetic sublevels $5^2S_{1/2}, F = 1, m_F = -1$ and $F = 2, m_F = -2$

as the two lower states $|1\rangle$ and $|2\rangle$, and $5^2P_{1/2}, F = 2, m_F = -1$ and $F = 1, m_F = -1$ as the two upper states $|3\rangle$ and $|5\rangle$, respectively. State $|4\rangle$ can be chosen as $5\ ^2P_{3/2}, F = 2, m_F = -2$. We use the parameters of this implementation as summarized in the caption of Fig. 4.14 for the numerical calculations presented below.

The equation of motion of the system has already been given by Eq. (4.7), for convenience we write it down here again

$$\frac{\partial\rho(\mathbf{r},\mathbf{v},t)}{\partial t} = -\frac{i}{\hbar}[H,\rho(\mathbf{r},\mathbf{v},t)] - L\rho(\mathbf{r},\mathbf{v},t) - \mathbf{v}\cdot\frac{\partial\rho(\mathbf{r},\mathbf{v},t)}{\partial\mathbf{r}} - \gamma_c\{\rho(\mathbf{r},\mathbf{v},t) - R(\mathbf{r},t)F(\mathbf{v})\}\,, \tag{4.48}$$

where H is the Hamiltonian of the system, and $L\rho$ represents the incoherent internal dynamics including spontaneous decay, dephasing and the incoherent pumping field. Next to these quantum mechanical contributions, the external classic motion leads to additional terms with γ_c as the collision rate between atoms. Specifically, the third term addresses the thermal motion, and the last term is related to the phase-changing collisions between atoms.

To determine the medium susceptibilities, from Eq. (4.48), we can derive the corresponding density matrix equations of motion for the FWM process in the undepleted-pump limit to give

$$\left(\frac{\partial}{\partial t} + \mathbf{v}\cdot\frac{\partial}{\partial\mathbf{r}} - i\Delta_s + i\mathbf{k}_s\cdot\mathbf{v} + \frac{p(\mathbf{r})}{2} + \frac{\Gamma_4}{2} + \gamma_c\right)\rho_{41}$$
$$= i\Omega_s(\mathbf{r},t)(\rho_{11}-\rho_{44}) - i\Omega_p(\mathbf{r},t)\rho_{43} + i\Omega_{c2}(\mathbf{r},t)\rho_{21} + \gamma_c R_{41}(\mathbf{r},t)F(\mathbf{v})\,, \tag{4.49a}$$

$$\left(\frac{\partial}{\partial t} + \mathbf{v}\cdot\frac{\partial}{\partial\mathbf{r}} - i\Delta_p + i\mathbf{k}_p\cdot\mathbf{v} + \frac{p(\mathbf{r})}{2} + \frac{\Gamma_3}{2} + \gamma_c\right)\rho_{31}$$
$$= i\Omega_p(\mathbf{r},t)(\rho_{11}-\rho_{33}) - i\Omega_s(\mathbf{r},t)\rho_{34} + i\Omega_{c1}(\mathbf{r},t)\rho_{21} + \gamma_c R_{31}(\mathbf{r},t)F(\mathbf{v})\,, \tag{4.49b}$$

$$\left(\frac{\partial}{\partial t} + \mathbf{v}\cdot\frac{\partial}{\partial\mathbf{r}} - i\Delta + i\Delta\mathbf{k}\cdot\mathbf{v} + \frac{p(\mathbf{r})}{2} + \gamma_{21} + \gamma_c\right)\rho_{21}$$
$$= i\Omega_{c1}^*(\mathbf{r},t)\rho_{31} + i\Omega_{c2}^*(\mathbf{r},t)\rho_{41} - i\Omega_p(\mathbf{r},t)\rho_{23} - i\Omega_s(\mathbf{r},t)\rho_{24} + \gamma_c R_{21}(\mathbf{r},t)F(\mathbf{v})\,. \tag{4.49c}$$

Note we have simplified the notation of $\rho_{ij}(\mathbf{r},\mathbf{v},t)$ to ρ_{ij}. Further,

$$\Delta = \Delta_p - \Delta_{c1}\,, \quad \text{and} \tag{4.50}$$

$$\Delta\mathbf{k} = \mathbf{k}_p - \mathbf{k}_{c1}\,, \tag{4.51}$$

are the two-photon detuning and the wavevector difference between Ω_p and Ω_{c1}. The phase-matching conditions are

$$\Delta_s = \Delta_p - \Delta_{c1} + \Delta_{c2}\,, \tag{4.52}$$

$$\mathbf{k}_s = \mathbf{k}_p - \mathbf{k}_{c1} + \mathbf{k}_{c2}\,. \tag{4.53}$$

Here, Δ_i and $\mathbf{k}_i$ are the detuning from the corresponding transition and wave vector of the field with Rabi frequency $\Omega_i(\mathbf{r},t)$ ($i \in \{p,s,c1,c2\}$), $p(\mathbf{r})$ is the incoherent pump rate, $\Gamma_i = \sum_k \Gamma_{ik}$ the total spontaneous emission rate from state $|i\rangle$ with Γ_{ik} the partial

one from $|i\rangle$ to $|k\rangle$, and γ_{21} denotes the ground state dephasing.

For simplicity, we focus on the case in which the two control fields and the incoherent pump can be treated as plane waves, such that $\Omega_{c1}(\mathbf{r}) = \Omega_{c1}$, $\Omega_{c2}(\mathbf{r}) = \Omega_{c2}$, and $p(\mathbf{r}) = p$. Moreover, we expand the system to leading order of the weak probe and FWM signal fields. In zeroth order, the steady-state density-matrix distribution function is obtained as in Eq. (4.9)

$$\rho_{ij}^{(0)}(\mathbf{r}, \mathbf{v}, t \to \infty) = n_0 \rho_{ij}^{(0)} F(\mathbf{v}) \,, \tag{4.54}$$

where n_0 is the atomic density, and $\rho_{ij}^{(0)}$ is the zero-order density-matrix element of an atom at rest. Note that $\rho_{ij}^{(0)}$ can be easily calculated from the steady-state master equations by setting $\Omega_{p(s)} = 0$.

The first-order equations of motion follow from Eq. (4.49) as

$$\begin{aligned}
&\left(\frac{\partial}{\partial t} + \mathbf{v}\cdot\frac{\partial}{\partial \mathbf{r}} - i\Delta_s + i\mathbf{k}_s\cdot\mathbf{v} + \frac{p}{2} + \frac{\Gamma_4}{2} + \gamma_c\right)\rho_{41}^{(1)} \\
&= i\Omega_s(\mathbf{r},t)(\rho_{11}^{(0)} - \rho_{44}^{(0)})n_0 F(\mathbf{v}) - i\Omega_p(\mathbf{r},t)\rho_{43}^{(0)} n_0 F(\mathbf{v}) + i\Omega_{c2}\rho_{21}^{(1)} + \gamma_c R_{41}^{(1)}(\mathbf{r},t)F(\mathbf{v}) \,,
\end{aligned} \tag{4.55a}$$

$$\begin{aligned}
&\left(\frac{\partial}{\partial t} + \mathbf{v}\cdot\frac{\partial}{\partial \mathbf{r}} - i\Delta_p + i\mathbf{k}_p\cdot\mathbf{v} + \frac{p}{2} + \frac{\Gamma_3}{2} + \gamma_c\right)\rho_{31}^{(1)} \\
&= i\Omega_p(\mathbf{r},t)(\rho_{11}^{(0)} - \rho_{33}^{(0)})n_0 F(\mathbf{v}) - i\Omega_s(\mathbf{r},t)\rho_{34}^{(0)} n_0 F(\mathbf{v}) + i\Omega_{c1}\rho_{21}^{(1)} + \gamma_c R_{31}^{(1)}(\mathbf{r},t)F(\mathbf{v}) \,,
\end{aligned} \tag{4.55b}$$

$$\begin{aligned}
&\left(\frac{\partial}{\partial t} + \mathbf{v}\cdot\frac{\partial}{\partial \mathbf{r}} - i\Delta + i\Delta\mathbf{k}\cdot\mathbf{v} + \frac{p}{2} + \gamma_{21} + \gamma_c\right)\rho_{21}^{(1)} \\
&= i\Omega_{c1}^{*}\rho_{31}^{(1)} + i\Omega_{c2}^{*}\rho_{41}^{(1)} - i\Omega_p(\mathbf{r},t)\rho_{23}^{(0)} n_0 F(\mathbf{v}) - i\Omega_s(\mathbf{r},t)\rho_{24}^{(0)} n_0 F(\mathbf{v}) + \gamma_c R_{21}^{(1)}(\mathbf{r},t)F(\mathbf{v}) \,.
\end{aligned} \tag{4.55c}$$

From Eqs. (4.55), the general solution for $R_{ij}^{(1)}(\mathbf{k},\omega)$ can be obtained by Fourier transforming from $(\mathbf{r},t)$ coordinates to $(\mathbf{k},\omega)$ space, and solving the resulting algebraic equations for $\rho_{ij}^{(1)}(\mathbf{k},\omega)$. The result for $\rho_{ij}^{(1)}(\mathbf{k},\omega)$ is integrated over velocity to give a set of equations for $R_{ij}^{(1)}(\mathbf{k},\omega)$. Solving the resulting equations leads to an expression for $R_{ij}^{(1)}(\mathbf{k},\omega)$. While $R_{ij}^{(1)}(\mathbf{k},\omega)$ can be obtained from these straightforward procedures, its final expressions are too complicated to gain deeper physical understanding of the FWM process.

Therefore, we apply a different procedure. To this end, we first integrate Eq. (4.55c) over velocity and obtain

$$\begin{aligned}
&\left(\frac{\partial}{\partial t} - i\Delta + \frac{p}{2} + \gamma_{21}\right) R_{21}^{(1)}(\mathbf{r},t) + \left(\frac{\partial}{\partial \mathbf{r}} + i\Delta\mathbf{k}\right)\mathbf{J}_{21}(\mathbf{r},t) \\
&= i\Omega_{c1}^{*} R_{31}^{(1)}(\mathbf{r},t) + i\Omega_{c2}^{*} R_{41}^{(1)}(\mathbf{r},t) - i n_0 \Omega_p(\mathbf{r},t)\rho_{23}^{(0)} - i n_0 \Omega_s(\mathbf{r},t)\rho_{24}^{(0)} \,,
\end{aligned} \tag{4.56}$$

where we have defined the current density of the density-matrix distribution function

$$\mathbf{J}_{ij}(\mathbf{r},t) = \int \mathbf{v}\rho_{ij}^{(1)}(\mathbf{r},\mathbf{v},t)d\mathbf{v} \,. \tag{4.57}$$

For dominating

$$\gamma = \gamma_c + \frac{p}{2} + \gamma_{21} - i\Delta\,, \tag{4.58}$$

which is in the Dicke limit [21], we can expand $\rho(\mathbf{r},\mathbf{v},t)$ to first order in γ as

$$\begin{aligned}\rho_{21}^{(1)}(\mathbf{r},\mathbf{v},t) &= \rho_{21}^{(1,0)}(\mathbf{r},\mathbf{v},t) + \frac{1}{\gamma}\rho_{21}^{(1,1)}(\mathbf{r},\mathbf{v},t) \\ &= R_{21}^{(1)}(\mathbf{r},t)F(\mathbf{v}) + \frac{1}{\gamma}\rho_{21}^{(1,1)}(\mathbf{r},\mathbf{v},t)\,,\end{aligned} \tag{4.59}$$

and obtain

$$0 = \int \mathbf{v}\rho_{21}^{(1,0)}(\mathbf{r},\mathbf{v},t)d\mathbf{v}\,, \tag{4.60a}$$

$$\mathbf{J}_{21}(\mathbf{r},t) = \frac{1}{\gamma}\int \mathbf{v}\rho_{21}^{(1,1)}(\mathbf{r},\mathbf{v},t)d\mathbf{v}\,. \tag{4.60b}$$

Next, we multiply Eq. (4.55c) by $\mathbf{v}$, and integrate over velocity. Expanding to the leading term in γ and inserting the relations in Eq. (4.60), we obtain the following equation for $\mathbf{J}_{21}(\mathbf{r},t)$

$$\mathbf{J}_{21}(\mathbf{r},t) = -D\left(\frac{\partial}{\partial\mathbf{r}} + i\Delta\mathbf{k}\right)R_{21}^{(1)}(\mathbf{r},t) + i\left(\frac{\Omega_{c1}^*}{\gamma}\mathbf{J}_{31}(\mathbf{r},t) + \frac{\Omega_{c2}^*}{\gamma}\mathbf{J}_{41}(\mathbf{r},t)\right)\,. \tag{4.61}$$

Here, $D = \mathrm{v}_{\mathrm{th}}^2/\gamma$, and to derive Eq. (4.61) we have used the relation [21]

$$\int \mathbf{v}^2\frac{\partial}{\partial\mathbf{r}}R_{21}^{(1)}(\mathbf{r},t)F(\mathbf{v})d\mathbf{v} = \mathrm{v}_{\mathrm{th}}^2\frac{\partial}{\partial\mathbf{r}}R_{21}^{(1)}(\mathbf{r},t)\,. \tag{4.62}$$

Inserting Eq. (4.61) into Eq. (4.56), we find

$$\begin{aligned}&\left[\frac{\partial}{\partial t} - i\Delta + \frac{p}{2} + \gamma_{21} - D(\frac{\partial}{\partial\mathbf{r}} + i\Delta\mathbf{k})^2\right]R_{21}^{(1)}(\mathbf{r},t) \\ &= i\Omega_{c1}^*R_{31}^{(1)}(\mathbf{r},t) + i\Omega_{c2}^*R_{41}^{(1)}(\mathbf{r},t) - in_0\Omega_p(\mathbf{r},t)\rho_{23}^{(0)} - in_0\Omega_s(\mathbf{r},t)\rho_{24}^{(0)} \\ &\quad - i\left(\frac{\partial}{\partial\mathbf{r}} + i\Delta\mathbf{k}\right)\cdot\left(\frac{\Omega_{c1}^*}{\gamma}\mathbf{J}_{31}(\mathbf{r},t) + \frac{\Omega_{c2}^*}{\gamma}\mathbf{J}_{41}(\mathbf{r},t)\right)\,.\end{aligned} \tag{4.63}$$

In Eq. (4.63), the last terms containing $\mathbf{J}_{31}(\mathbf{r},t), \mathbf{J}_{41}(\mathbf{r},t)$ can be neglected if $|\Omega_{c1}|, |\Omega_{c2}| \ll |\gamma|$, which is typically satisfied in relevant setups. Furthermore, even when this condition is not valid, these terms can still be neglected if both the spatial variations $\partial/\partial\mathbf{r}$ and $\Delta\mathbf{k}$ remain in the transverse plane, perpendicular to $\mathbf{k}_p$ and $\mathbf{k}_s$ [21]. Then Eq. (4.63) reduces to

$$\begin{aligned}&\left[\frac{\partial}{\partial t} - i\Delta + \frac{p}{2} + \gamma_{21} - D(\frac{\partial}{\partial\mathbf{r}} + i\Delta\mathbf{k})^2\right]R_{21}^{(1)}(\mathbf{r},t) \\ &= i\Omega_{c1}^*R_{31}^{(1)}(\mathbf{r},t) + i\Omega_{c2}^*R_{41}^{(1)}(\mathbf{r},t) - in_0\Omega_p(\mathbf{r},t)\rho_{23}^{(0)} - in_0\Omega_s(\mathbf{r},t)\rho_{24}^{(0)}\,.\end{aligned} \tag{4.64}$$

In the slowly-varying envelope approximation (SVEA), the temporal and spatial vari-

ations of the envelope of probe and signal fields are assumed to be much smaller than the decoherence rate and the wave number. For the spatial-temporal evolution of the density-matrix distribution function $R_{31}^{(1)}(\mathbf{r},t), R_{41}^{(1)}(\mathbf{r},t)$, SVEA leads to the conditions

$$\left|\frac{\partial}{\partial t}+\mathbf{v}\cdot\frac{\partial}{\partial \mathbf{r}}\right| \ll \left|\frac{p}{2}+\frac{\Gamma_4}{2}-i\Delta_s+i\mathbf{k}_s\cdot\mathbf{v}\right|, \tag{4.65a}$$

$$\left|\frac{\partial}{\partial t}+\mathbf{v}\cdot\frac{\partial}{\partial \mathbf{r}}\right| \ll \left|\frac{p}{2}+\frac{\Gamma_3}{2}-i\Delta_p+i\mathbf{k}_p\cdot\mathbf{v}\right|. \tag{4.65b}$$

Neglecting the temporal and spatial variations and only taking the dominant part of $\rho_{21}^{(1)}(\mathbf{r},\mathbf{v},t) = R_{21}^{(1)}(\mathbf{r},t)F(\mathbf{v})$ in Eqs. (4.55a) and (4.55b), we obtain expressions for $R_{31}^{(1)}(\mathbf{r},\mathbf{v},t)$ and $R_{41}^{(1)}(\mathbf{r},\mathbf{v},t)$ by integrating over velocity

$$R_{41}^{(1)}(\mathbf{r},t) = iK_{41}\left[n_0(\rho_{11}^{(0)}-\rho_{44}^{(0)})\Omega_s(\mathbf{r},t)-n_0\rho_{43}^{(0)}\Omega_p(\mathbf{r},t)\ +\Omega_{c2}R_{21}^{(1)}(\mathbf{r},t)\right], \tag{4.66a}$$

$$R_{31}^{(1)}(\mathbf{r},t) = iK_{31}\left[n_0(\rho_{11}^{(0)}-\rho_{33}^{(0)})\Omega_p(\mathbf{r},t)-n_0\rho_{34}^{(0)}\Omega_s(\mathbf{r},t)\ +\Omega_{c1}R_{21}^{(1)}(\mathbf{r},t)\right], \tag{4.66b}$$

where K_{41} and K_{31} are defined as

$$K_{31} = \frac{iG_{31}}{1-i\gamma_c G_{31}}, \tag{4.67a}$$

$$K_{41} = \frac{iG_{41}}{1-i\gamma_c G_{41}}, \tag{4.67b}$$

$$G_{31} = \int \frac{F(\mathbf{v})}{\Delta_s-\mathbf{k}_s\cdot\mathbf{v}+i(\frac{p}{2}+\frac{\Gamma_3}{2}+\gamma_c)}d^3\mathbf{v}, \tag{4.67c}$$

$$G_{41} = \int \frac{F(\mathbf{v})}{\Delta_p-\mathbf{k}_p\cdot\mathbf{v}+i(\frac{p}{2}+\frac{\Gamma_4}{2}+\gamma_c)}d^3\mathbf{v}, \tag{4.67d}$$

and K_{31} and K_{41} are related to the single-photon spectra for both fields and can be treated as real numbers at near resonance [21]. Near the one-photon resonance $\Delta_p \ll p/2+\Gamma_3+\gamma_c$ and $\Delta_s \ll p/2+\Gamma_4+\gamma_c$, the imaginary parts of K_{31} and K_{41} are much smaller than their respective real parts, and we neglect the imaginary parts in the following.

Following the paraxial approximation, we separate the transverse and longitudinal coordinates, $\mathbf{r}\to(\mathbf{r}_\perp,z)$, and neglect changes along the propagation direction, $\partial/\partial\mathbf{r}\to\partial/\partial\mathbf{r}_\perp$. Next, we Fourier transform Eqs. (4.64) and (4.66) from $(\mathbf{r}_\perp,t)$ to $(\mathbf{k}_\perp,\omega)$, and obtain the final expressions for $R_{31}^{(1)}(\mathbf{k}_\perp,z,\omega)$ and $R_{41}^{(1)}(\mathbf{k}_\perp,z,\omega)$ as follows

$$\begin{aligned}R_{31}^{(1)}(\mathbf{k}_\perp,z,\omega) = {}& iK_{31}n_0\Omega_p(\mathbf{k}_\perp,z,\omega)\left[\rho_{11}^{(0)}-\rho_{33}^{(0)}+\frac{\Gamma_{c1}(\rho_{11}^{(0)}-\rho_{33}^{(0)})+i\Omega_{c1}\rho_{23}^{(0)}-\Gamma_b\rho_{43}^{(0)}}{i(\omega+\Delta)-\Gamma_1-D(\mathbf{k}_\perp+\Delta\mathbf{k})^2}\right]\\ &+iK_{31}n_0\Omega_s(\mathbf{k}_\perp,z,\omega)\left[-\rho_{34}^{(0)}+\frac{\Gamma_b(\rho_{11}^{(0)}-\rho_{44}^{(0)})+i\Omega_{c1}\rho_{24}^{(0)}-\Gamma_{c1}\rho_{34}^{(0)}}{i(\omega+\Delta)-\Gamma_1-D(\mathbf{k}_\perp+\Delta\mathbf{k})^2}\right],\end{aligned} \tag{4.68a}$$

$$R_{41}^{(1)}(\mathbf{k}_\perp,z,\omega) = iK_{41}n_0\Omega_s(\mathbf{k}_\perp,z,\omega)\left[\rho_{11}^{(0)}-\rho_{44}^{(0)}+\frac{\Gamma_{c2}(\rho_{11}^{(0)}-\rho_{44}^{(0)})+i\Omega_{c2}\rho_{24}^{(0)}-\Gamma_a\rho_{34}^{(0)}}{i(\omega+\Delta)-\Gamma_1-D(\mathbf{k}_\perp+\Delta\mathbf{k})^2}\right]$$

$$+ iK_{41}n_0\Omega_p(\mathbf{k}_\perp, z, \omega)\Big[-\rho_{43}^{(0)} + \frac{\Gamma_a(\rho_{11}^{(0)} - \rho_{33}^{(0)}) + i\Omega_{c2}\rho_{23}^{(0)} - \Gamma_{c2}\rho_{43}^{(0)}}{i(\omega+\Delta) - \Gamma_1 - D(\mathbf{k}_\perp + \Delta\mathbf{k})^2}\Big], \tag{4.68b}$$

where $\Gamma_1 = p/2 + \gamma_{21} + \Gamma_{c1} + \Gamma_{c2}$, with power broadening contributions of the two control fields $\Gamma_{c1} = K_{31}\Omega_{c1}^2$, $\Gamma_{c2} = K_{41}\Omega_{c2}^2$, $\Gamma_a = K_{31}\Omega_{c1}^*\Omega_{c2}$ and $\Gamma_b = K_{41}\Omega_{c1}\Omega_{c2}^*$. For continuous wave fields, we can set $\omega = 0$ in Eqs. (4.68). In the case of a small wavevector difference between Ω_p and Ω_{c1}, $\Delta\mathbf{k}$ can be neglected, i.e., $\Delta\mathbf{k} = 0$.

Finally, we note that the propagation equations for the two probe and signal fields in paraxial approximation can be written as

$$\left(\frac{\partial}{\partial z} - \frac{i}{2\mathrm{k}_p}\frac{\partial^2}{\partial \mathbf{r}_\perp^2}\right)\Omega_p(\mathbf{r}_\perp, z) = i\frac{3\lambda_p^2\Gamma_{31}}{8\pi}R_{31}^F(\mathbf{r}_\perp, z)\,, \tag{4.69a}$$

$$\left(\frac{\partial}{\partial z} - \frac{i}{2\mathrm{k}_s}\frac{\partial^2}{\partial \mathbf{r}_\perp^2}\right)\Omega_s(\mathbf{r}_\perp, z) = i\frac{3\lambda_s^2\Gamma_{41}}{8\pi}R_{41}^F(\mathbf{r}_\perp, z)\,, \tag{4.69b}$$

where λ_p [λ_s] is the wavelength of the probe [signal] field, and n_0 is the atomic density. And the atomic responses in position space are given by the corresponding Fourier transformation

$$R_{31}^F(\mathbf{r}_\perp, z) = \int_{-\infty}^{\infty} R_{31}^{(1)}(\mathbf{k}_\perp, z, \omega = 0)e^{i\mathbf{k}_\perp\cdot\mathbf{r}_\perp}d\mathbf{r}_\perp \tag{4.70a}$$

$$R_{41}^F(\mathbf{r}_\perp, z) = \int_{-\infty}^{\infty} R_{41}^{(1)}(\mathbf{k}_\perp, z, \omega = 0)e^{i\mathbf{k}_\perp\cdot\mathbf{r}_\perp}d\mathbf{r}_\perp\,. \tag{4.70b}$$

By comparing Eqs. (4.68) with Eqs. (4.70), we can then find again that nonlocal linear effects appear owing to the thermal motion and collisions of atoms. In the following, we will show that this specific nonlocal effects can lead to high-fidelity image reproduction between different frequencies because of its well-known capability to eliminate diffraction.

4.3.3 Image reproduction and frequency conversion

In order to derive analytical expressions, we assume the undepleted pump approximation for the strong control fields, such that they only acquire phase shifts as a result of self- and cross- phase modulation during the FWM process. Consequently, the propagation dynamics for the probe and signal fields is mainly determined by their coupled paraxial wave equations. We then Fourier transform the propagation equations in Eq. (4.69) into momentum space and obtain

$$\left(\frac{\partial}{\partial z} + i\frac{\mathrm{k}_\perp^2}{2\mathrm{k}_p}\right)\Omega_p(\mathbf{k}_\perp, z) = i\frac{\mathrm{k}_p}{2}\left[\chi_p(\mathbf{k}_\perp)\Omega_p(\mathbf{k}_\perp, z) + \chi_{sp}(\mathbf{k}_\perp)\Omega_s(\mathbf{k}_\perp, z)\right], \tag{4.71a}$$

$$\left(\frac{\partial}{\partial z} + i\frac{\mathrm{k}_\perp^2}{2\mathrm{k}_s}\right)\Omega_s(\mathbf{k}_\perp, z) = i\frac{\mathrm{k}_s}{2}\left[\chi_s(\mathbf{k}_\perp)\Omega_s(\mathbf{k}_\perp, z) + \chi_{ps}(\mathbf{k}_\perp)\Omega_p(\mathbf{k}_\perp, z)\right]. \tag{4.71b}$$

Here, k_p [k_s] is the wave number of the probe [signal] field. The terms $i\mathrm{k}_\perp^2/2\mathrm{k}_{p(s)}$ characterize the paraxial diffraction of the probe (signal) field, and lead to spatial broadening and energy spreading throughout the field propagation, thereby severely distorting the spatial profiles of the incident fields. The linear response of the atomic medium to

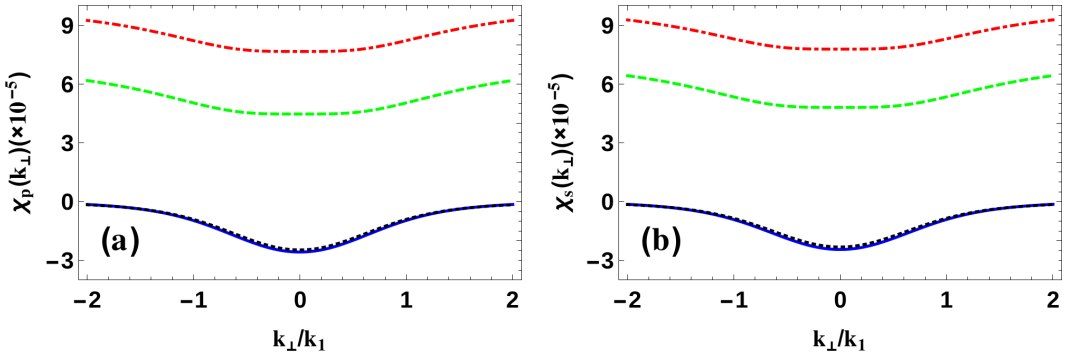

Figure 4.14: Motion-induced linear susceptibilities for the probe (a) and signal (b) fields in momentum space. The figures show the linear dispersion without incoherent pump field (black dotted line) and with incoherent pump field (solid blue curve). It can be seen that the dispersion is essentially unaffected in the presence of the pump and remains approximately quadratic in the central region $\mathbf{k}_\perp \ll \mathbf{k}_1$. In contrast, the linear absorption with (dashed green curve) and without (dot-dashed red curve) are strongly reduced by the pump. Parameters are $\lambda_p = 795$ nm, $\lambda_s = 780$ nm, $\Gamma_{D1} = 2\pi \times 5.75$ MHz, $\Gamma_{D2} = 2\pi \times 6.07$ MHz, $\Gamma_{31} = \Gamma_{D1}/4$,$\Gamma_{32} = \Gamma_{D1}/6$, $\Gamma_{41} = \Gamma_{D2}/4$, $\Gamma_{42} = \Gamma_{D2}/6$, $\Gamma_{51} = \Gamma_{D1}/12$, $\Gamma_{52} = \Gamma_{D2}/2$, $\gamma_{21} = 0.001\Gamma_{31}$, $T = 300\ K$, $v_{th} = 240$ m/s, $\Delta k = 22.8\ m^{-1}$, $\Omega_{c1} = 1.55\Gamma_{32}$, $\Omega_{c2} = 1.43\Gamma_{42}$, $\Delta_{c1} = 0$, $\Delta_{c2} = 0$, and $\Delta_p = \Delta$. With incoherent pump field, $n_0 = 1.32 \times 10^{18}\ m^{-3}$, $\gamma_c = 1600\Delta k \cdot v_{th}$, and $p = 0.7\Gamma_{31}$. Without incoherent pump field, $n_0 = 6.2 \times 10^{17}\ m^{-3}$, $\gamma_c = 30000\Delta k \cdot v_{th}$, and $p = 0$. In both cases, parameters are chosen such that the diffraction for both probe and signal fields can be eliminated, and that the transverse momentum scales with and without pump are comparable, $k_0 \approx k_1$.

the probe and signal fields are given by $\chi_p(\mathbf{k}_\perp)$ and $\chi_s(\mathbf{k}_\perp)$ respectively, while $\chi_{ps}(\mathbf{k}_\perp)$ $[\chi_{sp}(\mathbf{k}_\perp)]$ characterizes the nonlinear forward [backward] FWM process from Ω_p $[\Omega_s]$ to Ω_s $[\Omega_p]$.

We can see from Eqs. (4.71) that each wave vector component of the probe field is proportionally transfered onto the signal field and vice versa. Therefore, eventually images carried by the transverse degrees of freedom of the probe field can be copied to the signal field via the interplay of the FWM processes. In this transfer, the relative intensities of the output probe and signal fields depend on their coupling strengths to the atomic medium. As shown in the following, the combination of the linear and nonlinear responses of the thermal vapor can be manipulated in such a way that it exactly eliminates the diffraction of both fields due to atomic motion when the FWM process reaches the equilibrium. As a result, the initial spatial profile of the probe field is then reproduced and thereby frequency converted essentially without diffraction to the signal field during the FWM process.

4.3.3.1 Linear and nonlinear susceptibilities

The expressions for the linear susceptibilities χ_p, χ_s and nonlinear susceptibilities χ_{ps}, χ_{sp} given could then be readily derived

$$\chi_p(\mathbf{k}_\perp) = i\frac{3\lambda_p^3 K_{31} n_0 \Gamma_{31}}{8\pi^2}\left(\rho_{11}^{(0)} - \rho_{33}^{(0)} + \frac{\Gamma_{c1}(\rho_{11}^{(0)} - \rho_{33}^{(0)}) + i\Omega_{c1}\rho_{23}^{(0)} - \Gamma_b\rho_{43}^{(0)}}{i\Delta - \Gamma_1 - D\mathrm{k}_\perp^2}\right), \quad (4.72a)$$

$$\chi_s(\mathbf{k}_\perp) = i\frac{3\lambda_s^3 K_{41} n_0 \Gamma_{41}}{8\pi^2}\left(\rho_{11}^{(0)} - \rho_{44}^{(0)} + \frac{\Gamma_{c2}(\rho_{11}^{(0)} - \rho_{44}^{(0)}) + i\Omega_{c2}\rho_{24}^{(0)} - \Gamma_a\rho_{34}^{(0)}}{i\Delta - \Gamma_1 - D\mathrm{k}_\perp^2}\right), \quad (4.72b)$$

$$\chi_{sp}(\mathbf{k}_\perp) = i\frac{3\lambda_p^3 K_{31} n_0 \Gamma_{31}}{8\pi^2}\left(-\rho_{34}^{(0)} + \frac{\Gamma_b(\rho_{11}^{(0)} - \rho_{44}^{(0)}) + i\Omega_{c1}\rho_{24}^{(0)} - \Gamma_{c1}\rho_{34}^{(0)}}{i\Delta - \Gamma_1 - D\mathrm{k}_\perp^2}\right), \tag{4.72c}$$

$$\chi_{ps}(\mathbf{k}_\perp) = i\frac{3\lambda_s^3 K_{41} n_0 \Gamma_{41}}{8\pi^2}\left(-\rho_{43}^{(0)} + \frac{\Gamma_a(\rho_{11}^{(0)} - \rho_{33}^{(0)}) + i\Omega_{c2}\rho_{23}^{(0)} - \Gamma_{c2}\rho_{43}^{(0)}}{i\Delta - \Gamma_1 - D\mathrm{k}_\perp^2}\right), \tag{4.72d}$$

In this section, we show how the atomic motion can be exploited to eliminate the paraxial diffraction of both probe and signal fields. We start with the case without the incoherent pump field, i.e., $p = 0$. Then, $\rho_{11}^{(0)} = 1$ is the only non-vanishing zeroth-order density matrix element, and Eqs. (4.72) simplify to

$$\chi_p(\mathbf{k}_\perp) = i\frac{3\lambda_p^3 K_{31} n_0 \Gamma_{31}}{8\pi^2}\left(1 + \frac{\Gamma_{c1}}{i\Delta - \Gamma_0 - D_0\mathrm{k}_\perp^2}\right), \tag{4.73a}$$

$$\chi_s(\mathbf{k}_\perp) = i\frac{3\lambda_s^3 K_{41} n_0 \Gamma_{41}}{8\pi^2}\left(1 + \frac{\Gamma_{c2}}{i\Delta - \Gamma_0 - D_0\mathrm{k}_\perp^2}\right), \tag{4.73b}$$

$$\chi_{sp}(\mathbf{k}_\perp) = i\frac{3\lambda_p^3 K_{41} n_0 \Gamma_{31}}{8\pi^2}\frac{\Gamma_b}{i\Delta - \Gamma_0 - D_0\mathrm{k}_\perp^2}, \tag{4.73c}$$

$$\chi_{ps}(\mathbf{k}_\perp) = i\frac{3\lambda_s^3 K_{41} n_0 \Gamma_{41}}{8\pi^2}\frac{\Gamma_a}{i\Delta - \Gamma_0 - D_0\mathrm{k}_\perp^2}, \tag{4.73d}$$

where $\Gamma_0 = \gamma_{21} + \Gamma_{c1} + \Gamma_{c2}$ and $D_0 = \mathrm{v}_{\mathrm{th}}^2/(\gamma_c + \gamma_{21} - i\Delta)$. Setting $\Omega_{c2} = 0$ such that state $|4\rangle$ is not accessed, the system reduces to a three-level Λ-type setup, and we recover the result for $\chi_p(\mathbf{k}_\perp)$ of Ref. [21, 22]. In the region $\mathrm{k}_\perp \ll \mathrm{k}_0$, Eqs. (4.73) can be approximated to first order in $\mathrm{k}_\perp^2$

$$\chi_p(\mathbf{k}_\perp) = \frac{3\lambda_p^3 K_{31} n_0 \Gamma_{31}}{8\pi^2}\left[i\left(1 - \frac{\Gamma_{c1}}{2\Gamma_0}\right) - \frac{\Gamma_{c1}}{2\Gamma_0}\left(1 - \frac{\mathrm{k}_\perp^2}{\mathrm{k}_0^2}\right)\right], \tag{4.74a}$$

$$\chi_s(\mathbf{k}_\perp) = \frac{3\lambda_s^3 K_{41} n_0 \Gamma_{41}}{8\pi^2}\left[i\left(1 - \frac{\Gamma_{c2}}{2\Gamma_0}\right) - \frac{\Gamma_{c2}}{2\Gamma_0}\left(1 - \frac{\mathrm{k}_\perp^2}{\mathrm{k}_0^2}\right)\right], \tag{4.74b}$$

$$\chi_{sp}(\mathbf{k}_\perp) = \frac{3\lambda_p^3 K_{41} n_0 \Gamma_{31}}{8\pi^2}\frac{\Gamma_b}{2\Gamma_0}\left[-1 - i + \frac{\mathrm{k}_\perp^2}{\mathrm{k}_0^2}\right], \tag{4.74c}$$

$$\chi_{ps}(\mathbf{k}_\perp) = \frac{3\lambda_s^3 K_{41} n_0 \Gamma_{41}}{8\pi^2}\frac{\Gamma_a}{2\Gamma_0}\left[-1 - i + \frac{\mathrm{k}_\perp^2}{\mathrm{k}_0^2}\right]. \tag{4.74d}$$

Here, $\mathrm{k}_0 = \sqrt{\Gamma_0/D_{\mathrm{r}0}}$ with $D_{\mathrm{r}0} = \mathrm{v}_{\mathrm{th}}^2/\gamma_c$, where we have neglected γ_{21} since it is much smaller than γ_c. We have also set $\Delta = -\Gamma_0$ in order to remove the dependence of the imaginary parts of the linear and nonlinear susceptibilities on $\mathrm{k}_\perp^2$. Note that the real parts proportional to $\mathrm{k}_\perp^2$ remain positive in the central region $\mathrm{k}_\perp \ll \mathrm{k}_0$. Results for the linear and nonlinear susceptibilities in Eq. (4.73) as a function of $\mathrm{k}_\perp$ are shown in Figs. 4.14 and 4.15. Note that in order to facilitate a comparison of the shapes of the response curves, in these figures, we have chosen parameters in such a way that $\mathrm{k}_0 \approx \mathrm{k}_1$, i.e., the scales of the transverse wave vectors with and without the incoherent pump are approximately the same. k_1 is defined later as Eq. (4.76) and is reduced to k_0 in the absence of the incoherent pump. In the central area $\mathrm{k}_\perp \ll \mathrm{k}_1$, the linear

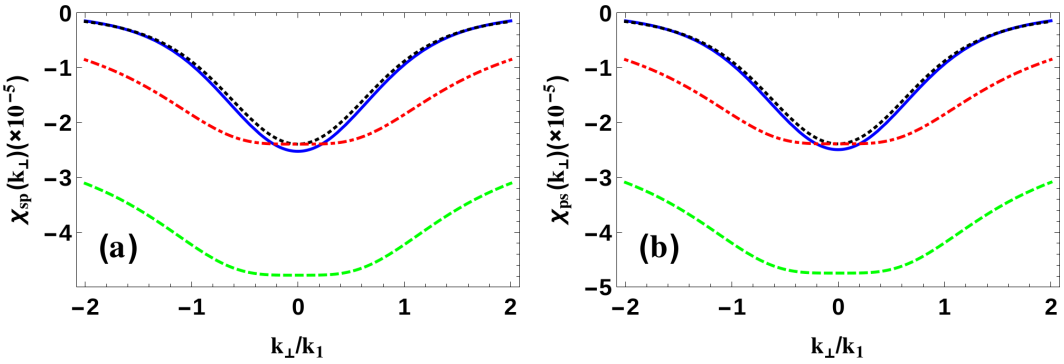

Figure 4.15: Motion-induced nonlinear susceptibilities related to the forward (a) and backward (b) FWM processes. The figures show the nonlinear dispersion without incoherent pump field (black dotted line) and with incoherent pump field (solid blue curve). As for the linear susceptibilities, the dispersion is essentially unaffected by the pump and remains approximately quadratic in the central region $\mathbf{k}_\perp \ll \mathbf{k}_1$. In contrast, the nonlinear absorption with (dashed green curve) and without (dot-dashed red curve) is strongly modified by the incoherent pump. Parameters can be chosen such that the nonlinear and the linear absorption cancel each other for a suitable choice of the pump field. Parameters are as in Fig. 4.14.

and nonlinear dispersions are quadratic in $\mathrm{k}_\perp$ with a constant offset (black dotted line). Recalling the propagation equations in paraxial approximation for the probe and signal fields Eqs. (4.71), we immediately find that the combination of linear and nonlinear susceptibilities has a suitable functional dependence to cancel the effect of diffraction throughout the propagation, provided that the two fields have the same spatial structure. Indeed, as shown later, the FWM process duplicates the spatial shape of the probe onto the signal field. Since the elimination of diffraction operates over a certain momentum range, it does not depend on the spatial profile of both fields within a certain bandwidth range. Within this bandwidth, diffraction of arbitrary spatial structure can be removed by the atomic motion.

This elimination of the diffraction, however, is accompanied by strong single-photon absorption as shown in Fig. 4.14 by the dot-dashed red curve. This significant attenuation of the output intensities of both fields is inevitable without the incoherent pump field, since a negative two-photon detuning $\Delta = -\Gamma_0$ deviating from the EIT resonance condition is required for the cancellation of diffraction. This forms a major obstacles for practical applications of the present scheme.

We next consider the effect of the incoherent pump field, which redistributes the populations in the five-level system. Subsequently, the control fields create additional coherences already in the absence of the probe and signal fields. The aim of this control is to cancel the single-photon absorption, without perturbing the diffraction cancellation. The zero-order populations and coherences $\rho_{ij}^{(0)}$ for motionless atoms can be obtained by solving the steady-state master equation. The analytic exact expressions for $\rho_{ij}^{(0)}$ are too complicated to be shown here. Instead, we show the relevant $\rho_{ij}^{(0)}$ as a function of the incoherent pump field strength in Fig. 4.16. As the amplitude of the incoherent pump increases, the population of the initial ground state $|1\rangle$ decreases, while that of the other states increases. Due to the two coherent control fields, atomic coherences are established in the lower double-Λ system. For resonant control fields $\Delta_{c1} = \Delta_{c2} = 0$ as considered in the following, $\rho_{23}^{(0)}$ and $\rho_{24}^{(0)}$ are purely imaginary while $\rho_{34}^{(0)}$ is real. In the

region $\mathrm{k}_\perp \ll \mathrm{k}_1$, we can expand Eqs. (4.72) to first order in $\mathrm{k}_\perp^2$ to give

$$\chi_i(\mathbf{k}_\perp) \approx \chi_i^{(0)} + \chi_i^{(1)} \frac{\mathrm{k}_\perp^2}{\mathrm{k}_1^2} + O(\mathrm{k}_\perp^4)\,, \tag{4.75}$$

with $i \in \{s, p, sp, ps\}$ and the critical transverse wave number scale is set by

$$\mathrm{k}_1 = \sqrt{\frac{\Gamma_1}{D_{\mathrm{r}1}}} = \frac{1}{\mathrm{v}_{\mathrm{th}}} \sqrt{\left(\frac{p}{2} + \Gamma_{c1} + \Gamma_{c2}\right)\left(\frac{p}{2} + \gamma_c\right)}\,, \tag{4.76}$$

where $D_{\mathrm{r}1} = \mathrm{v}_{\mathrm{th}}^2/\gamma_{c1}$ and $\gamma_{c1} = \gamma_c + p/2 + \gamma_{21}$, and we have neglected γ_{21}. We find that k_1 grows rapidly with increasing incoherent pump rate p, which enables operation of the diffractionless image propagation over a larger transverse wave number bandwidth compared to the case without incoherent pump field. Specifically, we obtain

$$\chi_p(\mathbf{k}_\perp) = \frac{3\lambda_p^3 K_{31} n_0 \Gamma_{31}}{8\pi^2} \Bigg\{ i(\rho_{11}^{(0)} - \rho_{33}^{(0)}) + \frac{\Gamma_{c1}(\rho_{11}^{(0)} - \rho_{33}^{(0)}) + i\Omega_{c1}\rho_{23}^{(0)} - \Gamma_b \rho_{43}^{(0)}}{\Gamma_1} \Bigg[-\frac{1+i}{1+\alpha^2} + \frac{\alpha(2\Gamma_1 + \gamma_{c1})^2}{2(\gamma_{c1} + \Gamma_1)^2} \frac{\mathrm{k}_\perp^2}{\mathrm{k}_1^2} \Bigg] \Bigg\}\,, \tag{4.77a}$$

$$\chi_s(\mathbf{k}_\perp) = \frac{3\lambda_s^3 K_{31} n_0 \Gamma_{41}}{8\pi^2} \Bigg\{ i(\rho_{11}^{(0)} - \rho_{44}^{(0)}) + \frac{\Gamma_{c2}(\rho_{11}^{(0)} - \rho_{44}^{(0)}) + i\Omega_{c2}\rho_{24}^{(0)} - \Gamma_a \rho_{34}^{(0)}}{\Gamma_1} \Bigg[-\frac{1+i}{1+\alpha^2} + \frac{\alpha(2\Gamma_1 + \gamma_{c1})^2}{2(\gamma_{c1} + \Gamma_1)^2} \frac{\mathrm{k}_\perp^2}{\mathrm{k}_1^2} \Bigg] \Bigg\}\,, \tag{4.77b}$$

$$\chi_{sp}(\mathbf{k}_\perp) = \frac{3\lambda_p^3 K_{41} n_0 \Gamma_{31}}{8\pi^2} \Bigg\{ -i\rho_{34}^{(0)} + \frac{\Gamma_b(\rho_{11}^{(0)} - \rho_{44}^{(0)}) + i\Omega_{c1}\rho_{24}^{(0)} - \Gamma_{c1} \rho_{34}^{(0)}}{\Gamma_1} \Bigg[-\frac{1+i}{1+\alpha^2} + \frac{\alpha(2\Gamma_1 + \gamma_{c1})^2}{2(\gamma_{c1} + \Gamma_1)^2} \frac{\mathrm{k}_\perp^2}{\mathrm{k}_1^2} \Bigg] \Bigg\}\,, \tag{4.77c}$$

$$\chi_{ps}(\mathbf{k}_\perp) = \frac{3\lambda_s^3 K_{41} n_0 \Gamma_{41}}{8\pi^2} \Bigg\{ -i\rho_{43}^{(0)} + \frac{\Gamma_a(\rho_{11}^{(0)} - \rho_{33}^{(0)}) + i\Omega_{c2}\rho_{23}^{(0)} - \Gamma_{c2} \rho_{43}^{(0)}}{\Gamma_1} \Bigg[-\frac{1+i}{1+\alpha^2} + \frac{\alpha(2\Gamma_1 + \gamma_{c1})^2}{2(\gamma_{c1} + \Gamma_1)^2} \frac{\mathrm{k}_\perp^2}{\mathrm{k}_1^2} \Bigg] \Bigg\}\,, \tag{4.77d}$$

with

$$\alpha = \sqrt{\frac{\gamma_{c1}}{2\Gamma_1 + \gamma_{c1}}}\,. \tag{4.78}$$

In order to remove the dependence on $\mathrm{k}_\perp^2$ for the imaginary parts of the linear and nonlinear susceptibilities and at the same time keep the real parts positive in the central area $\mathrm{k}_\perp \ll \mathrm{k}_1$ as desired, we have calculated the condition for the two-photon detuning

$$\Delta = -\alpha\Gamma_1\,. \tag{4.79}$$

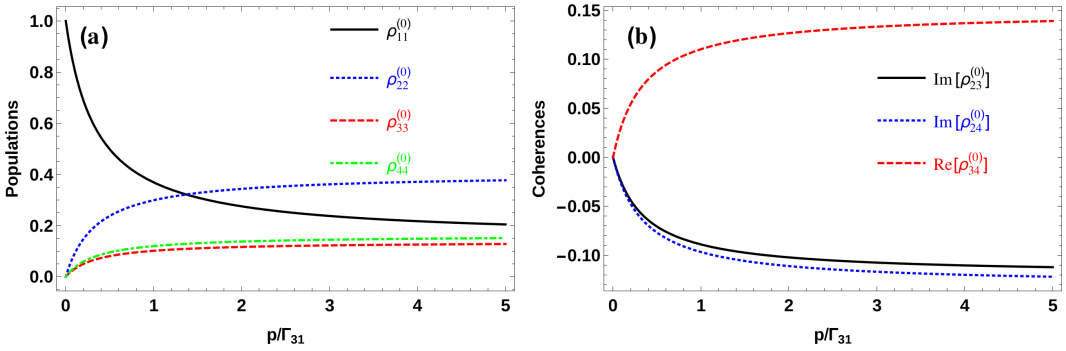

Figure 4.16: (a) Zeroth-order populations $\rho_{ii}^{(0)}(i = 1, 2, 3, 4)$ and (b) coherences $\rho_{ij}^{(0)}(i \neq j)$ for a motionless atom as a function the amplitude of the two-way incoherent pump field. At zero pump amplitude, the atoms are in the ground state $|1\rangle$. As the amplitude of the incoherent pump increases, atoms are gradually redistributed among the other four states, and atomic coherences arise between $|2\rangle$, $|3\rangle$ and $|4\rangle$ due to interactions with the two coherent control fields Ω_{c1} and Ω_{c2}. Parameters are as in Fig. 4.14.

In Figs. 4.14 and 4.15, we also show the imaginary and real parts of the linear and nonlinear susceptibilities against the transverse wave vector $\mathrm{k}_\perp$ in the presence of the incoherent pump field. It can be seen that the single-photon absorption has been considerably reduced due to the incoherent pump (dashed green curve), together with an increase of the nonlinear gain. Still, both the linear and the nonlinear absorption remain approximately constant in the central area $\mathrm{k}_\perp \ll \mathrm{k}_1$. At the same time, the linear and nonlinear dispersions (solid blue curve) are proportional to $\mathrm{k}_\perp^2$ except for constant offsets, and remain essentially unchanged compared to the case without incoherent pumping. We thus conclude that the parameters can be chosen such that the paraxial diffraction of the both probe and the signal fields can be approximately eliminated after the FWM process has reached its equilibrium, but with significant reduction of absorption compared to the case without pump.

It should be noted that it is not possible to fully compensate the single-photon absorption for both signal and probe fields using only the linear gain from the atomic coherences, since $\rho_{43}^{(0)}$ $[\rho_{34}^{(0)}]$ in $\chi_p(\mathbf{k}_\perp)$ $[\chi_s(\mathbf{k}_\perp)]$ will partially cancel out the gain effect of $\rho_{23}^{(0)}$ $[\rho_{24}^{(0)}]$ as shown in Eqs. (4.77a) and (4.77b). However, Fig. 4.14 shows that together with the nonlinear gain from the FWM process, the loss can be eliminated or even over-compensated.

We have discussed the essential mechanism for the elimination of the paraxial diffraction of arbitrary spatial profiles of both probe and signal fields during the FWM process. Eqs. (4.71) and (4.77) show that each wave vector component of the probe field is proportionally transfered onto the signal field and vice versa. Therefore, eventually the incident image carried by the probe field is copied to the signal via the interplay of the FWM processes. In this process, the relative intensities of the output probe and signal fields depends on their coupling strengths to the atomic medium.

To study the propagation dynamics, we numerically solve Eqs. (4.71) together with (4.72), which means we have included all the higher-order contributions in the numerical calculations. In the first step, we start with a Gaussian probe field

$$\Omega_p(\mathrm{r}_\perp, z = 0) = \Omega_{p0} e^{-\frac{(x^2+y^2)}{2\mathrm{w}_{p0}^2}}, \tag{4.80}$$

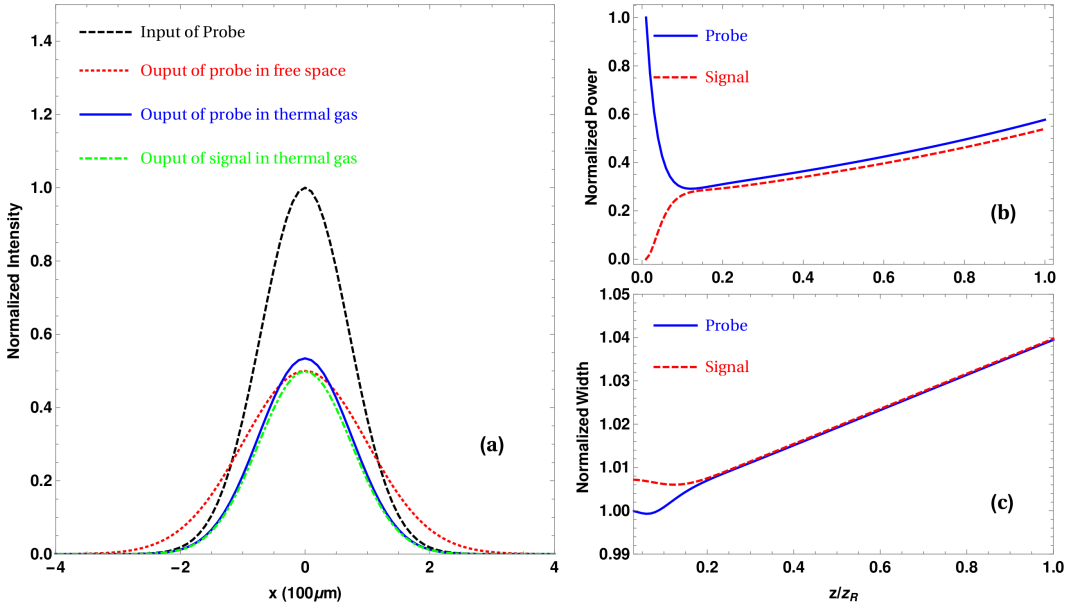

Figure 4.17: (a) Transverse intensity profiles of a two-dimensional Gaussian probe beam after propagation over one Rayleigh length for the one-dimensional slice $y = 0$. The different curves compare the profile of the probe beam in free space with those of the probe and FWM signal beams in the thermal medium. The intensities of all beams are scaled such that the peak intensity of the input probe field also shown in the figure is normalized. It can be seen that the power of the input beam is distributed between the probe and FWM signal beam, and that in the thermal medium, diffraction is significantly reduced compared to the free space case. (b) and (c) show the normalized power and width of the probe and FWM signal as a function of the propagation distance. Note that the starting point for z in (c) is $z = 0.03z_R$, as at small propagation distance, the signal field is very weak as shown in (b), such that the width cannot easily be extracted. Parameters are the same as in Fig. 4.14.

the initial width of the probe beam is $\mathrm{w}_{p0} = 100\mu$m. Results are shown in Fig. 4.17 for the $y = 0$ subspace. In (a), after a propagation over one Rayleigh length $z_R = 2\pi\mathrm{w}_{p0}^2/\lambda_p = 7.905$cm, in free space the transmitted probe beam is broadened to $\mathrm{w}_p(z = z_R) = \sqrt{2}\mathrm{w}_{p0}$ due to paraxial diffraction. Accordingly, the intensity is decreased by factor of $1/2$. In the thermal vapor using the setup proposed here, the width of the outgoing probe field remains almost constant $\mathrm{w}_p(z = z_R) \approx 1.0395\mathrm{w}_{p0}$, while the intensity is reduced to $\Omega_p(z = z_R) \approx 0.537\Omega_{p0}$. The output of the generated FWM signal field has a Gaussian spatial structure with width $\mathrm{w}_s(z = z_R) \approx 1.0397\mathrm{w}_{p0}$ and relative intensity $\Omega_s(z = z_R) \approx 0.502\Omega_{p0}$ similar to the output probe field. In Fig. 4.17(b) and (c), the relative widths and powers of both fields are shown as a function of the propagation distance z. In the first stage of the propagation, the forward FWM process is dominant and transfers energy from the probe to the signal field. At about $z_B \approx 0.15z_R$, the forward and backward FWM processes are balanced. At this point, the normalized width of both signal and probe fields has changed by less than one percent from the width of the initial probe field. In this initial propagation part, linear single-photon absorption dominates, and the total power contained in both signal and probe fields together is attenuated. Beyond $z > z_B$, the nonlinear gain over-compensates the linear loss, such that the probe and signal intensity grows slightly. This growth in power is accompanied by a small growth in the widths of signal and probe fields, which is related to higher-order diffraction $\sim O(\mathrm{k}_\perp^4)$ in the linear and nonlinear dispersions. These are

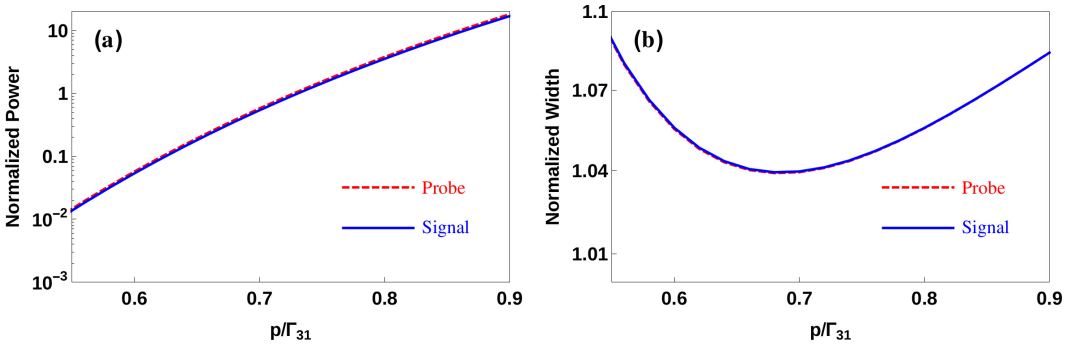

Figure 4.18: The normalized output powers (a) and widths (b) of a Gaussian probe and the generated FWM signal field as a function of the amplitude of the two-way incoherent pump p, after a propagation distance of one Rayleigh length in the prepared thermal medium. It can be seen that the output probe and FWM signal fields widths and powers approach each other. Furthermore, the intensities of both fields are very sensitive to the incoherent pump, meanwhile, the related widths weakly depend on the incoherent pump. Throughout the whole propagation, the widths of the two beams remains essentially unchanged, as can be seen from the small scale on the y axis of (b). Parameters are the same as in Fig. 4.14.

relevant, as the spatial frequency spectrum of the incident pulse contains contributions at wave vectors outside the central region $\mathbf{k}_\perp \ll \mathrm{k}_1$.

4.3.3.2 Effect of the incoherent pump on the propagation dynamics

To further analyze the effect of the incoherent pump on the propagation dynamics, we calculated the output power and width of both probe and signal fields as a function of the pump intensity. Results are shown in Fig. 4.18 for a Gaussian probe field. We find that while the output power of the two fields can be controlled via the pump field over a large range, the output width only weakly depends on the pump amplitude. This suggests that possible inhomogeneities in the incoherent pump field, which could, for example, arise due to absorption in the medium, will not significantly affect the outgoing spatial beam profiles and the diffractionless propagation in the medium. We further find that the balanced distribution of the outgoing power between signal and probe field is preserved over a broad range of pump strengths as well.

While the initial purpose of the incoherent pump field was to induce atomic coherences via the control fields in zeroth order of the probe and signal field, we find that it has further less obvious positive effects on the system dynamics. First, the single-photon absorption without pump can be compensated or even turned into gain by the combination of reduced linear absorption and nonlinear gain from the atomic coherences. This suggests that the FWM process, which sensitively depends on the relative intensities of all applied fields, equilibrates in a rather short propagation distance. Consequently, not only the efficiency of the FWM process is significantly improved, but also the broadening of both probe and signal fields due to residual diffraction before the FWM equilibrium is reached is considerably decreased. Second, the incoherent pump further alleviates the demand for strong collision rates to achieve the Dicke limit $\Delta \mathrm{kv_{th}} \ll \gamma_{c1} = \gamma_c + \frac{p}{2}$, as γ_{c1} is enhanced by the pump rate p. Third, since k_1 defined in Eq. (4.76) which sets the transverse wave number scales in Eq. (4.75) and Figs. 4.14 and 4.15 grows rapidly as the incoherent pump increases, probe and signal fields with a larger transverse bandwidth, and in turn smaller spatial size can be propagated through the medium without diffraction in the thermal medium.

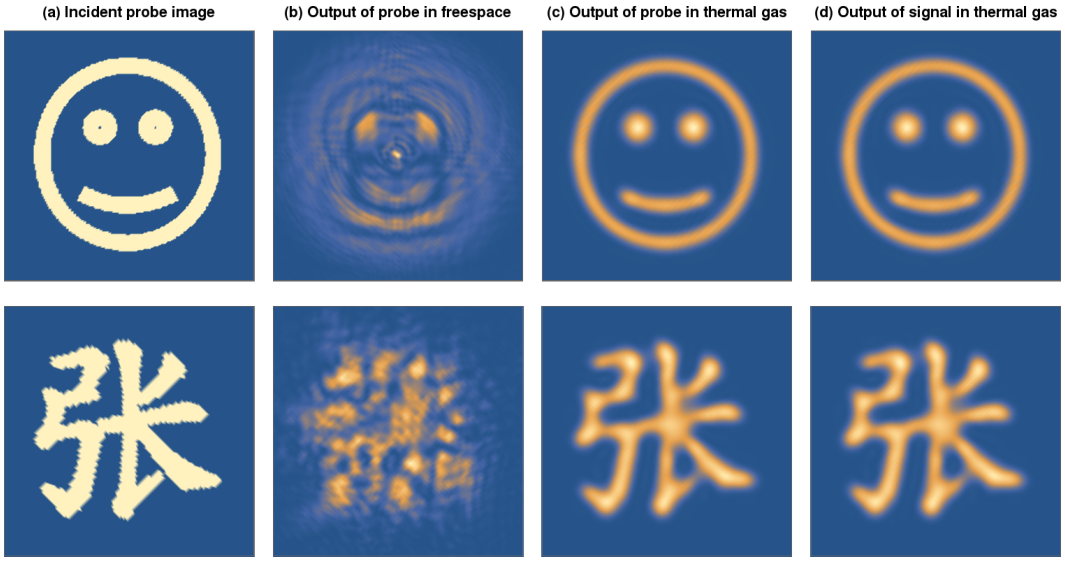

Figure 4.19: Diffractionless propagation and frequency conversion of arbitrary images. The original two-dimensional images encoded onto the transverse profile of the probe beam are shown in column (a). In free space, the image is severely distorted after propagation over one Rayleigh length, as shown in column (b). In our suitably tailored thermal medium, the probe beam profile is preserved, see column (c). Additionally, the same profile is converted onto the signal field via the FWM process as given in column (d). the image size is given by 20×20 with a scale of $100\mu m$. Other parameters are as in Fig. 4.14.

4.3.3.3 Diffractionless image conversion of arbitrary profiles

In order to demonstrate that our setup can operate on arbitrary images encoded onto the probe field, we finally propagated two-dimensional images shown in Fig. 4.19 through the thermal atom vapor. The incident images are represented by an array of values "0" and "1" in the transverse plane, which leads to the somewhat rough edges visible in Fig. 4.19(a). We first test our scheme by propagating a smiley face as depicted in the upper panel of Fig. 4.19. In free space, as expected we find that the smiley face is totally distorted after propagating one Rayleigh length, see column (b). But in the thermal vapor, the image encoded onto the probe beam is well preserved due to the cancellation of the diffraction as shown in column (c). In comparison to the initial image, the sharp edges have been smoothed out, as they contain high-frequency transverse wave vector components outside the central susceptibility area $\mathbf{k}_\perp \ll \mathbf{k}_1$. At the same time, the image is transfered to the signal field via the FWM process, see column (d). We then propagates an even more complicated Chinese character in both frees pace and our prepared thermal medium as shown in the lower panel of Fig. 4.19, the results again demonstrates clearly the difffractionless light propagation and image conversion in the tailored thermal medium.

4.3.4 Discussions

In this section, we have proposed a scheme to realize diffractionless image reproduction and frequency conversion based on four-wave mixing in a thermal atomic vapor. Phase matching is achieved despite the thermal motion, which is exploited to achieve diffractionless image reproduction. In order to compensate the usually inevitable absorption, we applied an additional two-way incoherent pump field. It on the one hand modi-

fies the linear and nonlinear absorption such that overall, the probe and signal fields propagate without attenuation. Besides those positive effects that the incoherent pump brings into the system as discussed in Sec. 4.1, it further leads to a rapid equilibration of the FWM process, which sensitively depends on the intensities of all applied fields. Thereby, an image frequency conversion with negligible diffraction in the initial transient dynamics is achieved. We have shown that our method is capable of transmitting and frequency-converting complex two-dimensional images without diffraction, requiring only short propagation distances of less than one Rayleigh length.

Throughout this section, we used parameters of the hyperfine structure of ^{87}Rb for the results, which is an atomic species routinely used in laboratories and therefore well suited for proof-of-principle experiments. But our setup can also be generalized to different systems, e.g., to achieve conversion to other frequencies. The main considerations which led us to ^{87}Rb are as follows. A major restriction on the parameters arises from the fact that the Doppler effect effectively reduces the coupling between the thermal vapor and the laser fields. Therefore, usually a relatively high atomic density ($> 10^{12}$ cm^{-3}) is required to achieve sufficient medium response to cancel the diffraction, which can lead to unwanted effects such as additional nonlinear processes or collective interactions [227]. In order to reduce the required atomic density, the population in the upper state $|5\rangle$ should be minimized, which acts only as an auxiliary state in order to effectively convert the incoherent two-way pump field into a one-way pumping. For this, the spontaneous decay rate Γ_{52} should ideally be much larger than Γ_{51}. Additionally, the couplings between atoms and the probe and signal fields should be as strong as possible to further reduce the atomic density, such that large dipole moment for $\vec{\mu}_{31}$ and $\vec{\mu}_{41}$ are desirable. Lastly, the simultaneous elimination of diffraction for both fields in the same thermal vapor demands for matched coupling strengths, which further limits the choice of suitable $\vec{\mu}_{31}$ and $\vec{\mu}_{41}$.

In the previous calculations, we have chosen the propagation distances up to a Rayleigh length which is related to a specific probe beam waist. The reason that we do so is to clearly show and compare the differences in propagation dynamics of the probe and signal beams between in free space and in our prepared thermal atomic medium. Of course, it is not limited to the chosen parameters and the propagation dynamics of the two fields at longer propagation distances can also be calculated. Indeed, we have done some numerical calculations where different propagation distances are taken. And the results for different propagation distances look quite similar. The differences are that the outgoing probe and signal fields are amplified further due to the gain from the incoherent pump and are companied with a little larger widths because of the higher-order diffraction, as we increases the propagation distances.

One might be interested in the relations between the widths of the two outgoing fields and the width of the incoming probe. It implicitly depends on how well Eq. (4.72) can be approximated to Eqs. (4.74) and (4.77). If the width of the incident probe is too small such that there are some wave components whose transverse wave vectors are outside the region $k_\perp \ll k_1$. Then we can find that the imaginary parts of the susceptibilities cannot be treated as constants as shown in Figs. 4.14 and 4.15, which means that diffusion processes will take place and leads to broadening and distortion of the probe and signal fields. In the other hand, the real parts of the susceptibilities cannot be well approximated in the form as given in Eq. (4.75), it results in residual diffractions and stronger higher-order diffractions to the two fields. For larger size of the incident probe field which corresponds to smaller scale of its wave vectors, those effects such as diffusion, residual diffraction and higher-order diffraction can be sufficiently suppressed.

A related work by Katzir *et al.* [253], who independently of us developed another method to eliminate paraxial diffraction using a FWM process. Interestingly, while the level schemes at first sight look rather similar, the involved physical processes are entirely different. The setup by Katzir *et al.* and ours share the main principle of operating in the transverse wave vector space $\mathbf{k}_\perp$, such that diffraction of arbitrary images encoded onto the probe beam can be manipulated. But in contrast to the present work, Katzir *et al.* do not rely on the dependence of $\mathbf{k}_\perp$ induced by the thermal motion of atoms, but instead exploit a new mechanism based on the phase-matching condition of a suitably tailored FWM process. In their scheme, a probe field with arbitrary transverse profile and a plane-wave control field interact with a three-level Λ system in EIT configuration. The control field further acts as a pump field to form an active Raman gain (ARG) [254, 255] process, which leads to generation of a *conjugate* FWM signal field. Since for each wave component the produced conjugate signal field has an opposite phase dependence on the transverse wavevector as compared to the probe field, the diffraction for both fields can be tuned such that they cancel each other. As a result, the spatial profile of the probe field is well preserved, and copied to the signal field as in our proposal, while avoiding absorption via the nonlinear gain.

The two related yet different setups clearly highlight how versatile and intriguing the light propagation through atomic vapors becomes in particular if setups beyond the standard three-level EIT setup are considered, and pave the way for further studies operating in the transverse momentum space applicable to arbitrary images.

4.4 Conclusions

In this chapter, we have studied to coherently control light propagation in thermal atomic vapor exhibiting nonlocal linear effects. It has already been found that the specific type of nonlocal linear effects induced by atomic motion and collisions has a $\mathbf{k}_\perp$-square dependent susceptibility in momentum space. By suitably choosing the related parameters, the $\mathbf{k}_\perp$-square dependent susceptibility could lead to an exact elimination of paraxial diffraction of laser beams encoded with arbitrary spatial profiles. The original illustration of the elimination of diffraction evolves inevitable strong absorption owing to necessary two-photon detuning in a there-level thermal atomic system, thus rendering it impractical. Here, we first proposed an enhanced scheme in a four-level system cooperating with an additional incoherent pump, in which light encoded with arbitrary images could propagates without either diffraction or absorption. Based on this enhanced scheme, we find that the tailored medium can give rise to an uniform and considerable phase modulation for the probe light, and a π phase shift is easily accomplished within few Rayleigh lengths. Furthermore, we extended this specific type of nonlocal linear effects to realize diffractionless and lossless image reproduction between different frequencies. And theoretical calculations have already shown that this image reproduction can be successfully implemented for arbitrary images.

Apart from atomic motion and collisions, other mechanisms leading to nonlocal linear effects remains to be open. The knowledge gained from this chapter further reveals the ability of nonlocal linear effects to control light propagation in momentum space, thus being versatile to arbitrary spatial profiles. Beyond, the paraxial propagation equation can be manipulated to realize a direct transition from pure diffractive to diffusive, which could be employed to mimic heat transferring processes or imaginary time propagation of the Schrödinger equation, based on the close connection to the heat or Schrödinger equations as we have mentioned in Sec. 2.3.

Chapter 5

Propagation dynamics in the presence of nonlocal nonlinear effects

After the study of coherent control of light propagation via nonlocal linear effects, we move our interests in this chapter to investigate light propagation dynamics in the presence of nonlocal nonlinear effects induced in interacting Rydberg atoms. In Sec. 5.1, we study light propagation dynamics in thermal Rydberg atoms. In particular, we develop a novel model in Sec. 5.1.2 to describe the thermal Rydberg atoms interacting with laser fields with the input from the last chapter. Based on the analytical form for the nonlocal nonlinear atomic response obtained under certain crucial approximations, we proceed to study the propagation dynamics in Sec. 5.1.3 in both the near-resonant and far-detuned regimes, and find mainly that simultaneous competition appears between the nonlocoal nonlinear absorption and modulational instability (MI) for each wave component, leadint to suppression of MI eventually. Moreover, in Sec. 5.2, we investigate PT-symmetric dynamics in cold interacting Rydberg atoms. Specifically, we propose in Sec. 5.2.2 a promising approach to generate an optical PT-symmetric periodic potential by employing electromagnetically induced transparency and active Raman gain in two different atomic species. In Sec. 5.2.3, the band structure is calculated both in the linear case and in the presence of nonlocal nonlinear effects, indicating phase transition from unbroken to broken PT-symmetry phase which is further analyzed in Sec.5.2.4. The resulting propagation dynamics in either unbroken or broken PT-symmetry phase is given in Sec. 5.2.5. In the end, a short conclusion is given in Sec. 5.3.

5.1 Nonlocal nonlinear effects in thermal interacting Rydberg atoms

5.1.1 Introduction to Rydberg atoms

Rydberg atoms, a peculiar type of atoms excited to high-lying energy states with large principal quantum number [256] were discovered more than a century ago, possessing incredibly "exaggerated" dipole moments and therefore long-range dipole-dipole interactions (DDI), and they have attracted intensive interests due to its potential applications in diverse fields. After the seminar works put forward in the beginning of 2000s [73, 257, 258], the last decade has witnessed remarkable progresses in the multidisciplinary studies of ultracold Rydberg atoms. Considering the uncountable accomplishments and yet fast-evolving developments, one would never be able to provide a comprehensive overview of all topics related to Rydberg atoms. Instead, we can only try our best to outline the very topics in recent years. In this direction, a series of beautiful experiments and theoretical explorations have shown the powerful capabilities of ultracold Rydberg atoms in illustrating local or nonlocal nonlinear effects [25, 26, 65–69], Rydberg blockade [70–72], effective strong mutual interactions between photons [26, 259, 260],

Wigner crystallization of single photons [261], fractional quantum Hall state of Rydberg polaritons [262] benefiting from the unique properties of the dipole-dipole interactions, to mention a few. Moreover, the availability of strong long-range interaction in Rydberg atoms has also enabled promising applications in quantum information processing [73, 74] including long-range quantum gate [257, 263–266], quantum simulator for many-body physics [267], adiabatic quantum computation [268], and many-particle entanglement [65, 263, 269–271].

It is fair to say that all those successes are deeply rooted in how precise we can model the cold Rydberg atoms involving collective interactions. In parallel with the great deal of achievements mentioned above, much efforts has been devoted to the theoretical models that can successfully describe the interacting ultracold Rydberg atoms under certain circumstances. Due to interactions, it is typically required to solve the N-body problem in which the computational complexity scales exponentially in N, and it is even impossible to implement the numerical simulations for a large N, hence simplified approaches to approximately describe the interacting Rydberg atoms are necessary. Among these the most simple one is the mean-field theory [75–78] which decomposes the interatomic two-body correlations into product of individual density matrix elements based on the Hartree-Fock approximation [185]. While appearing to be appealingly straightforward and simplified, however, the resulting nonlinear equations of motion for single atoms would give rise to an unphysical distance-independent energy shift for any finite Rydberg excitation [79]. To take into account the two-body correlations, a model called cluster expansion [25, 79, 80] has been developed, in which the higher-order correlations (e.g., the three-body correlations) are truncated to different products of low-order density matrix elements, under the assumption that the three-body correlation is very weak in comparison with the lower two-body correlation. Obviously, this model breaks down in the case of higher atomic densities, at which three-body correlations become significant. Furthermore, a rate equation model [69, 81–84] has been proposed. It relies on the approximation that all single-atom coherences can be adiabatically eliminated in the master equation and the interatomic interactions are merely translated to energy shifts of the Rydberg state of individual atoms. Though this model reveals its validity in the regime of large atomic densities, it fails as soon as the damping of the coherences is comparable to the Rydberg excitation dynamics and cannot provide further knowledge of the interatomic correlations. In all those models, thermal motion effects is reasonably neglected due to the typically short time scale ($\sim \mu s$), low temperature ($\sim \mu$K) and due to the dominant role of the coherent many-body dynamics in dilute ultracold Rydberg atoms.

At the same time when exceptional advances have been made in ultracold Rydberg atoms, there have been experiments conducted in the thermal Rydberg atoms [85–92], where evidences for long-range coherent DDI have been shown. In these pioneering experiments, there are typically two off-resonant probe and control fields interacting with the thermal atoms, such that the two-photon transition to the Rydberg states is excited near its resonance. Under this configuration, the theoretical description can be tremendously simplified [25] since the time evolution of the intermediate state can be safely adiabatically eliminated, and the individual atoms can be modeled as two-level systems. However, already in this much simplified picture the theoretical models mentioned above seem to be failed to describe the involved dynamics. In a theoretical point of view, many unconsidered physical mechanisms could attribute to the breakdown of present models, for example, Doppler effect, atomic collision effects, etc., in which maybe one of the most challenges is how to relax the complexity introduced by the

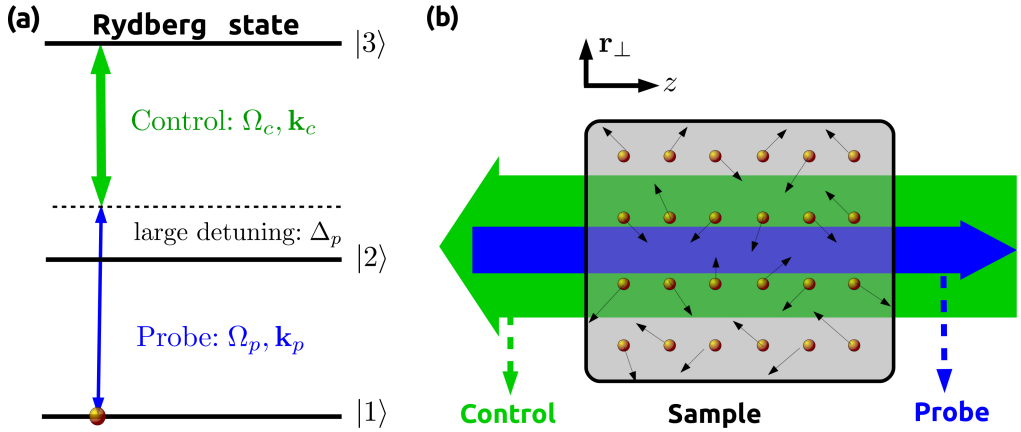

Figure 5.1: The three-level scheme for a single atom (a) interacting with counter-propagating probe and control fields (b). The two single-photon transitions $|1\rangle \leftrightarrow |2\rangle$ and $|2\rangle \leftrightarrow |3\rangle$ are driven by the two far-detuned probe and control fields with Rabi frequencies Ω_c and Ω_p respectively, while the two-photon transition from $|1\rangle$ to the high-lying Rydberg state $|3\rangle$ is near resonant.

time-varying DDI caused by atomic motion in the thermal regime.

It seems the right time to search a proper and robust model describing the thermal interacting Rydberg atoms. In a first step, based on the crucial approximation that the variations in the time-varying DDI can be neglected, here we develop a model to characterize the steady-state dynamics under far-off single-photon transition configuration, where practical approximations have been employed to derive an analytical expression for the nonlocal nonlinear response of the thermal Rydberg atoms. For a check of consistency, we find that our model recovers the results obtained in a recent paper [25] for ultracold Rydberg atoms as the temperature approaches zero, and also indicates further counterintuitive behaviors with respect to that in ultracold Rydberg atoms.

5.1.2 Theoretical model for thermal Rydberg atoms

We consider a ladder-type three-level atomic system as shown in Fig. 5.1. The ground state $|1\rangle$ is coupled to the intermediate state $|2\rangle$ by a weak probe field Ω_p with frequency ω_p and wavevector $\mathbf{k}_p$, which is further driven by a strong control field Ω_c with frequency ω_c and wavevector $\mathbf{k}_c$ to a high-lying Rydberg state $|3\rangle$. The frequencies of the two fields are chosen such that the two-photon transition from $|1\rangle$ to $|3\rangle$ is driven at near-resonance, thus forming an electromagnetically induced transparency (EIT) configuration. In contrast, the single-photon transitions $|1\rangle \leftrightarrow |2\rangle$ and $|2\rangle \leftrightarrow |3\rangle$ are chosen to be either near or far-off resonant. The single-photon detunings are defined as $\Delta_p = \omega_p - \omega_{21}$ for the probe and $\Delta_c = \omega_c - \omega_{32}$ for the control field. To model the thermal interacting Rydberg atoms and obtain the subsequent atomic response to the probe field, we first define a collective transition operator in terms of atomic transition operators distributed in space $\mathbf{r}$ and velocity $\mathbf{v}$ as

$$\hat{\sigma}_{\alpha\beta}(\mathbf{r},\mathbf{v},t) = \sum_j \hat{\sigma}^j_{\alpha\beta}(t)\,\delta(\mathbf{r}-\mathbf{r}_j(t))\,\delta(\mathbf{v}-\mathbf{v}_j(t))\,, \tag{5.1}$$

in analogy to a similar density distribution function developed in [21, 240]. Here, $\hat{\sigma}^j_{\alpha\beta}(t)$ is the atomic transition operator for the j-th atom defined as $\hat{\sigma}^j_{\alpha\beta}(t) = |\alpha^j(t)\rangle\langle\beta^j(t)|$,

and δ represents the Dirac delta function. It obeys the Heisenberg equation

$$\frac{d\hat{\sigma}^j_{\alpha\beta}(t)}{dt} = \frac{i}{\hbar}[H, \hat{\sigma}^j_{\alpha\beta}(t)] - L\hat{\sigma}^j_{\alpha\beta}(t) \,, \tag{5.2}$$

where i is the imaginary unit $i = \sqrt{-1}$, H is the Hamiltonian of the system, and $L\hat{\sigma}^j_{\alpha\beta}(t)$ denotes the incoherent processes including spontaneous decay and dephasing. We start from the collective transition operator $\hat{\sigma}_{\alpha\beta}(\mathbf{r}, \mathbf{v}, t)$ introduced in Eq. (5.1). Then, we find

$$\begin{aligned}\frac{\partial\hat{\sigma}_{\alpha\beta}(\mathbf{r}, \mathbf{v}, t)}{\partial t} = &\sum_j \frac{d\hat{\sigma}^j_{\alpha\beta}(t)}{dt}\, \delta(\mathbf{r} - \mathbf{r}_j(t))\, \delta(\mathbf{v} - \mathbf{v}_j(t)) \\ &+ \sum_j \hat{\sigma}^j_{\alpha\beta}(t)\, \frac{\partial\delta(\mathbf{r} - \mathbf{r}_j(t))}{\partial t}\, \delta(\mathbf{v} - \mathbf{v}_j(t)) \\ &+ \sum_j \hat{\sigma}^j_{\alpha\beta}(t)\, \delta(\mathbf{r} - \mathbf{r}_j(t))\, \frac{\partial\delta(\mathbf{v} - \mathbf{v}_j(t))}{\partial t} \,. \end{aligned} \tag{5.3}$$

For the second term in the RHS of this equation, we have

$$\begin{aligned}&\sum_j \hat{\sigma}^j_{\alpha\beta}(t)\, \frac{\partial\delta(\mathbf{r} - \mathbf{r}_j(t))}{\partial t}\, \delta(\mathbf{v} - \mathbf{v}_j(t)) \\ &= \sum_j \hat{\sigma}^j_{\alpha\beta}(t)\, \frac{\partial\mathbf{r}_j(t)}{\partial t} \frac{\partial\delta(\mathbf{r} - \mathbf{r}_j(t))}{\partial\mathbf{r}_j}\, \delta(\mathbf{v} - \mathbf{v}_j(t)) \\ &= -\mathbf{v} \cdot \frac{\partial\hat{\sigma}_{\alpha\beta}(\mathbf{r}, \mathbf{v}, t)}{\partial\mathbf{r}} \,. \end{aligned} \tag{5.4}$$

Assuming that the atomic system is relaxed to the thermal equilibrium state, the last term describing atomic collisions in the RHS of Eq. (5.3) can be rewritten as

$$\sum_j \hat{\sigma}^j_{\alpha\beta}(t)\, \delta(\mathbf{r} - \mathbf{r}_j(t))\, \frac{\partial\delta(\mathbf{v} - \mathbf{v}_j(t))}{\partial t} = \gamma_c[\hat{\sigma}_{\alpha\beta}(\mathbf{r}, \mathbf{v}, t) - \hat{R}_{\alpha\beta}(\mathbf{r}, t)F(\mathbf{v})] \,. \tag{5.5}$$

Here, $F(\mathbf{v}) = \mathrm{Exp}[-\mathrm{v}^2/\mathrm{v}_p^2]/(\sqrt{\pi}\mathrm{v}_p)^3$ is the Boltzmann distribution function, with $\mathrm{v}_p = \sqrt{2k_BT/m}$ being the most probable thermal velocity, and γ_c is the collision rate. The latter is chosen to be proportional to the thermal velocity $\gamma_c \propto \mathrm{v}_p$ and therefore $\gamma_c \propto \sqrt{T}$. We further defined the collective transition operator $\hat{R}_{\alpha\beta}(\mathbf{r}, t)$ as

$$\hat{R}_{\alpha\beta}(\mathbf{r}, t) = \int \hat{\sigma}_{\alpha\beta}(\mathbf{r}, \mathbf{v}, t) d\mathbf{v} \,. \tag{5.6}$$

This finally leads to the equations of motion of the system which reads

$$\begin{aligned}\frac{\partial\hat{\sigma}_{\alpha\beta}(\mathbf{r}, \mathbf{v}, t)}{\partial t} = &\frac{i}{\hbar}[H, \hat{\sigma}_{\alpha\beta}(\mathbf{r}, \mathbf{v}, t)] - L\hat{\sigma}_{\alpha\beta}(\mathbf{r}, \mathbf{v}, t) \\ &- \mathbf{v} \cdot \frac{\partial\hat{\sigma}_{\alpha\beta}(\mathbf{r}, \mathbf{v}, t)}{\partial\mathbf{r}} \\ &- \gamma_c[\hat{\sigma}_{\alpha\beta}(\mathbf{r}, \mathbf{v}, t) - \hat{R}_{\alpha\beta}(\mathbf{r}, t)F(\mathbf{v})] \,. \end{aligned} \tag{5.7}$$

In the right hand side (RHS) of Eq. (5.7), the first term describes the internal quantum-mechanical evolution, while the next two terms characterize external classical effects such as thermal motion and atomic collisions, respectively [21]. In the following, we simplify the notations $\hat{\sigma}^j_{\alpha\beta}(t), \hat{\sigma}_{\alpha\beta}(\mathbf{r},\mathbf{v},t)$ as $\hat{\sigma}^j_{\alpha\beta}, \hat{\sigma}_{\alpha\beta}$ for convenience. For the geometry depicted in Fig. 5.1, the Hamiltonian of the j-th atom then can be written as

$$\begin{aligned} H_j = &-\Omega_p(\mathbf{r}_j,t)\hat{\sigma}^j_{21} - \Omega_c(\mathbf{r}_j,t)\hat{\sigma}^j_{32} + H.c. \\ &- (\Delta_p - \mathbf{k}_p\cdot\mathbf{v}_j)\hat{\sigma}^j_{22} - (\Delta - \Delta\mathbf{k}\cdot\mathbf{v}_j)\hat{\sigma}^j_{33} + \sum_{l<j} V_{jl}(t)\hat{\sigma}^j_{33}\hat{\sigma}^l_{33}\,, \end{aligned} \tag{5.8}$$

where $\Delta = \Delta_p - \Delta_c$ is the two-photon detuning, and $\Delta\mathbf{k} = \mathbf{k}_p - \mathbf{k}_c$ is the wavevector difference between the two laser fields. In Eq. (5.8), the last term in the RHS represents the dipole-dipole interaction between the Rydberg atoms, in particular, a van-der-Waals type potential [84] is chosen to describe the interaction effects,

$$V_{jl}(t) = \frac{C_6}{\left|\mathbf{r}_j(t) - \mathbf{r}_l(t)\right|^6}\,. \tag{5.9}$$

The total Hamiltonian for the thermal Rydberg atoms then is the sum over all single-particle Hamiltonian

$$H = \sum_j H_j\,. \tag{5.10}$$

In order to obtain the atomic response of the thermal Rydberg gas to the incident probe field, we derive the equations of motions

$$\frac{\partial\hat{\sigma}^j_{12}}{\partial t} = i[\Omega_p(\mathbf{r}_j,t)(\hat{\sigma}^j_{11} - \hat{\sigma}^j_{22}) + \Omega_c(\mathbf{r}_j,t)\hat{\sigma}^j_{13} + \Delta_{12}(\mathbf{v}_j)\hat{\sigma}^j_{12}]\,, \tag{5.11a}$$

$$\frac{\partial\hat{\sigma}^j_{13}}{\partial t} = i[-\Omega_p(\mathbf{r}_j,t)\hat{\sigma}^j_{23} + \Omega_c(\mathbf{r}_j,t)\hat{\sigma}^j_{12} + \Delta_{13}(\mathbf{v}_j)\hat{\sigma}^j_{13}] - i\sum_{l\neq j} V_{jl}(t)\hat{\sigma}^j_{13}\hat{\sigma}^l_{33}\,, \tag{5.11b}$$

Similarly, for the collective transition operators, we find

$$\begin{aligned} (\frac{\partial}{\partial t} + \mathbf{v}\cdot\frac{\partial}{\partial\mathbf{r}})\hat{\sigma}_{12} = &\, i[\Delta_{12}(\mathbf{v}) + i\gamma_c]\hat{\sigma}_{12} + i\Omega_p(\mathbf{r},t)(\hat{\sigma}_{11} - \hat{\sigma}_{22}) + i\Omega_c(\mathbf{r},t)\hat{\sigma}_{13} \\ &+ \gamma_c\hat{R}_{12}(\mathbf{r},t)F(\mathbf{v})\,, \end{aligned} \tag{5.12a}$$

$$\begin{aligned} (\frac{\partial}{\partial t} + \mathbf{v}\cdot\frac{\partial}{\partial\mathbf{r}})\hat{\sigma}_{13} = &\, i[\Delta_{13}(\mathbf{v}) + i\gamma_c]\hat{\sigma}_{13} + i\Omega_c(\mathbf{r},t)\hat{\sigma}_{12} - i\Omega_p(\mathbf{r},t)\hat{\sigma}_{23} + \gamma_c\hat{R}_{13}(\mathbf{r},t)F(\mathbf{v}) \\ &- i\sum_{j<l} V_{jl}(t)\hat{\sigma}^j_{13}\hat{\sigma}^l_{33}\delta(\mathbf{r}-\mathbf{r}_j)\delta(\mathbf{v}-\mathbf{v}_j)\,. \end{aligned} \tag{5.12b}$$

Here we have defined $\Delta_{12}(\mathbf{u}) = \Delta_p - \mathbf{k}_p\cdot\mathbf{u} + i\gamma_{12}$ and $\Delta_{13}(\mathbf{u}) = \Delta - \Delta\mathbf{k}\cdot\mathbf{u} + i\gamma_{13}$ with $\mathbf{u}\in\{\mathbf{v}_j,\mathbf{v}\}$. In general, Eqs. (5.12) are very challenging to solve due to the dipole-dipole interaction terms, even in the "frozen gas" limit $V_{jl}(t) = V_{jl}(t=0)$. For a first step, here we limit ourselves to the far-detuned regime where $\Delta_p, \Delta_c \gg \mathrm{k}_p\mathrm{v}_p, \Omega_p, \gamma_{12}, \gamma_{13}, \gamma_c$ as well as the weak probe limit $\Omega_c \gg \Omega_p$, where it was shown that an analytical solution in the steady state is possible at $T = 0$ [25]. In this far-detuned regime, we could approximate

$\langle\hat{\sigma}_{11}^j\rangle \simeq 1, \langle\hat{\sigma}_{22}^j\rangle \simeq 0, \langle\hat{\sigma}_{23}^j\rangle \simeq 0$, and find

$$\langle\hat{\sigma}_{11}\rangle = \sum_j \langle\hat{\sigma}_{11}^j\rangle \delta(\mathbf{r}-\mathbf{r}_j)\delta(\mathbf{v}-\mathbf{v}_j) = n_0 F(\mathbf{v})\,, \tag{5.13a}$$

$$\langle\hat{\sigma}_{22}\rangle = 0\,, \tag{5.13b}$$

$$\langle\hat{\sigma}_{23}\rangle = 0\,, \tag{5.13c}$$

where $n_0 = N/V$ is the atomic density, and we have applied the relation

$$\begin{aligned}\sum_j f(\mathbf{r}_j,\mathbf{v}_j) &= \sum_{j,N\to\infty} \frac{N}{V} F(\mathbf{v}_j) f(\mathbf{r}_j,\mathbf{v}_j) \frac{V}{N}\Delta\mathbf{v}_j \\ &= n_0 \int f(\mathbf{r}_j,\mathbf{v}_j) F(\mathbf{v}_j) d^3\mathbf{r}_j d^3\mathbf{v}_j\,. \end{aligned} \tag{5.14}$$

Next we assume the involved laser fields are continuous-waves, i.e., $\Omega_p(\mathbf{r},t) = \Omega_p(\mathbf{r})$ and $\Omega_c(\mathbf{r},t) = \Omega_c(\mathbf{r})$, and that the beam diameter of $\Omega_c(\mathbf{r})$ is much larger than that of $\Omega_p(\mathbf{r})$ such that $\Omega_c(\mathbf{r}) \simeq \Omega_c$ and Ω_c can be chosen as real. With these considerations, Eq. (5.11) and (5.12) can be simplified to

$$\frac{\partial\hat{\sigma}_{12}^j}{\partial t} = i\big[\Omega_p(\mathbf{r}_j) + \Omega_c\hat{\sigma}_{13}^j + \Delta_{12}(\mathbf{v}_j)\hat{\sigma}_{12}^j\big]\,, \tag{5.15a}$$

$$\frac{\partial\hat{\sigma}_{13}^j}{\partial t} = i\big[\Omega_c\hat{\sigma}_{12}^j + \Delta_{13}(\mathbf{v}_j)\hat{\sigma}_{13}^j\big] - i\sum_{l\neq j} V_{jl}(t)\hat{\sigma}_{13}^j\hat{\sigma}_{33}^l\,, \tag{5.15b}$$

$$\big(\frac{\partial}{\partial t} + \mathbf{v}\cdot\frac{\partial}{\partial\mathbf{r}}\big)\hat{\sigma}_{12} = i\big[\Delta_{12}(\mathbf{v}) + i\gamma_c\big]\hat{\sigma}_{12} + i\Omega_p(\mathbf{r})n_0F(\mathbf{v}) + i\Omega_c\hat{\sigma}_{13} + \gamma_c\hat{R}_{12}(\mathbf{r},t)F(\mathbf{v})\,, \tag{5.15c}$$

$$\begin{aligned}\big(\frac{\partial}{\partial t} + \mathbf{v}\cdot\frac{\partial}{\partial\mathbf{r}}\big)\hat{\sigma}_{13} &= i\big[\Delta_{13}(\mathbf{v}) + i\gamma_c\big]\hat{\sigma}_{13} + i\Omega_c\hat{\sigma}_{12} + \gamma_c\hat{R}_{13}(\mathbf{r},t)F(\mathbf{v}) \\ &\quad - i\sum_{j<l} V_{jl}(t)\hat{\sigma}_{13}^j\hat{\sigma}_{33}^l\delta(\mathbf{r}-\mathbf{r}_j)\delta(\mathbf{v}-\mathbf{v}_j)\,. \end{aligned} \tag{5.15d}$$

In the far-detuned regime, $\hat{\sigma}_{12}^j$ can be adiabatically eliminated, leading to

$$\hat{\sigma}_{12}^j = -\frac{\Omega_p(\mathbf{r}_j) + \Omega_c\hat{\sigma}_{13}^j}{\Delta_{12}(\mathbf{v}_j)}\,. \tag{5.16}$$

Plugging Eq. (5.16) into Eq. (5.15b), we find

$$\frac{\partial\hat{\sigma}_{33}^j}{\partial t} = \frac{\partial\hat{\sigma}_{31}^j}{\partial t}\hat{\sigma}_{13}^j + \hat{\sigma}_{31}^j\frac{\partial\hat{\sigma}_{13}^j}{\partial t} \simeq -2\gamma_{13}\hat{\sigma}_{33}^j\,. \tag{5.17}$$

For a Rydberg atom, the lifetime of the high-lying Rydberg state $|3\rangle$ is much longer than that of the intermediate state $|2\rangle$, which means $\gamma_{13} \ll \gamma_{12}, \Omega_c$. Thus, $\hat{\sigma}_{33}^j$ decays much slower than the other terms and can be treated as stationary on the level of its

dynamics. With this approximation, we find

$$\begin{aligned}\frac{\partial(\hat{\sigma}_{13}^{j}\hat{\sigma}_{33}^{l})}{\partial t} =& \frac{\partial\hat{\sigma}_{13}^{j}}{\partial t}\hat{\sigma}_{33}^{l} + \hat{\sigma}_{13}^{j}\frac{\partial\hat{\sigma}_{33}^{l}}{\partial t} \simeq \frac{\partial\hat{\sigma}_{13}^{j}}{\partial t}\hat{\sigma}_{33}^{l}\,, \\ \simeq& -\frac{i\Omega_p(\mathbf{r}_j)\Omega_c\hat{\sigma}_{33}^{l} + i\Omega_c^2\hat{\sigma}_{13}^{j}\hat{\sigma}_{33}^{l}}{\Delta_{12}(\mathbf{v}_j)} + i\Delta_{13}(\mathbf{v}_j)\hat{\sigma}_{13}^{j}\hat{\sigma}_{33}^{l} - iV_{jl}(t)\hat{\sigma}_{13}^{j}\hat{\sigma}_{33}^{l}\,, \end{aligned} \tag{5.18}$$

where we have neglected the higher order terms $\sum_{m\neq j,l} V_{jm}(t)\hat{\sigma}_{13}^{j}\hat{\sigma}_{33}^{m}\hat{\sigma}_{33}^{l}$ which are of order $O(\Omega_p^5)$. In general, due to the presence of the time-dependent dipole-dipole interaction $V_{jl}(t)$ in thermal Rydberg atoms, it turns out to be difficult to solve Eq. (5.18), even for a steady-state solution. In order to be able to continue with the analytical derivation, we assume

$$V_{jl}(t) = V_{jl}(0)\,, \tag{5.19}$$

such that the dipole-dipole interaction between different atoms is considered to be time-independent. We have to address here that there is no formal justification for this approximation, which might limit the validity of our model in the general case. However, for a dense atomic ensemble in thermal equilibrium, in a mean-field approximation one can expect that the interaction of one atom with its surrounding atoms on average remains constant, i.e., $\sum_l V_{jl}(t)/N = V_{jl}(0)$.

Making use of the key model assumption Eq. (5.19), a steady-state solution for $\hat{\sigma}_{13}^{j}\hat{\sigma}_{33}^{l}$ can be obtained from Eq. (5.18)

$$\hat{\sigma}_{13}^{j}\hat{\sigma}_{33}^{l} = \frac{-\Omega_c\Omega_p(\mathbf{r}_j)\hat{\sigma}_{33}^{l}}{\Omega_c^2 - \Delta_{12}(\mathbf{v}_j)\Delta_{13}(\mathbf{v}_j) + V_{jl}(0)\Delta_{12}(\mathbf{v}_j)}\,. \tag{5.20}$$

Setting $\partial\hat{\sigma}_{13}^{j}/\partial t = 0$, we further find

$$\hat{\sigma}_{13}^{j} = \frac{\Omega_c\Omega_p(\mathbf{r}_j)}{\Delta_{12}(\mathbf{v}_j)\Delta_{13}(\mathbf{v}_j) - \Omega_c^2}\left[1 - \Delta_{12}(\mathbf{v}_j)\sum_{l\neq j}\frac{V_{jl}(0)\hat{\sigma}_{33}^{l}}{\Omega_c^2 - \Delta_{12}(\mathbf{v}_j)\Delta_{13}(\mathbf{v}_j) + V_{jl}(0)\Delta_{12}(\mathbf{v}_j)}\right], \tag{5.21}$$

and thus

$$\hat{\sigma}_{33}^{j} = \hat{\sigma}_{31}^{j}\hat{\sigma}_{13}^{j} \simeq \frac{\Omega_c^2\left|\Omega_p(\mathbf{r}_j)\right|^2}{\left|\Delta_{12}(\mathbf{v}_j)\Delta_{13}(\mathbf{v}_j) - \Omega_c^2\right|^2}\,. \tag{5.22}$$

In the derivation of Eq. (5.22), we have also neglected the higher-order contributions $O(\Omega_p^4)$. Substituting Eq. (5.20) and (5.22) back into Eq. (5.15d) results in

$$\begin{aligned}\mathbf{v}\cdot\frac{\partial\hat{\sigma}_{13}}{\partial\mathbf{r}} =& i\left[\Delta_{13}(\mathbf{v}) + i\gamma_c\right]\hat{\sigma}_{13} + i\Omega_c\hat{\sigma}_{12} + \gamma_c\hat{R}_{13}(\mathbf{r},t)F(\mathbf{v}) \\ &+ i\sum_j\sum_{l\neq j}\frac{\Omega_c\Omega_p(\mathbf{r}_j)V_{jl}(0)\delta(\mathbf{r}-\mathbf{r}_j)\delta(\mathbf{v}-\mathbf{v}_j)}{\Omega_c^2 - \Delta_{12}(\mathbf{v}_j)\Delta_{13}(\mathbf{v}_j) + V_{jl}(0)\Delta_{12}(\mathbf{v}_j)}\frac{\Omega_c^2\left|\Omega_p(\mathbf{r}_l)\right|^2}{\left|\Delta_{12}(\mathbf{v}_l)\Delta_{13}(\mathbf{v}_l) - \Omega_c^2\right|^2}\,. \end{aligned} \tag{5.23}$$

Applying Eq. (5.14) to this equation, one finds

$$\mathbf{v}\cdot\frac{\partial\hat{\sigma}_{13}}{\partial\mathbf{r}} = i\big[\Delta_{13}(\mathbf{v})+i\gamma_c\big]\hat{\sigma}_{13}+i\Omega_c\hat{\sigma}_{12}+\gamma_c\hat{R}_{13}(\mathbf{r},t)F(\mathbf{v}) + i\,n_0^2\,\Omega_c^3\,A\,F(\mathbf{v})\Omega_p(\mathbf{r})\int\frac{V(\mathbf{r}-\mathbf{r}')\big|\Omega_p(\mathbf{r}')\big|^2d^3\mathbf{r}'}{\Omega_c^2-\Delta_{12}(\mathbf{v})\Delta_{13}(\mathbf{v})+V(\mathbf{r}-\mathbf{r}')\Delta_{12}(\mathbf{v})}\,, \tag{5.24}$$

where $V(0)=V(t=0)$ is replaced by $V(\mathbf{r}-\mathbf{r}')$, and

$$A=\int\frac{F(\mathbf{v})}{|\Delta_{12}(\mathbf{v})\Delta_{13}(\mathbf{v})-\Omega_c^2|^2}d^3\mathbf{v}\,. \tag{5.25}$$

Setting $\partial\hat{\sigma}_{12}^j/\partial t=0$ in Eq. (5.15c), the steady-state solution for $\hat{\sigma}_{12}$ becomes

$$\mathbf{v}\cdot\frac{\partial\hat{\sigma}_{12}}{\partial\mathbf{r}} = i\big[\Delta_{12}(\mathbf{v})+i\gamma_c\big]\hat{\sigma}_{12}+i\Omega_p(\mathbf{r})n_0F(\mathbf{v})+i\Omega_c\hat{\sigma}_{13}+\gamma_c\hat{R}_{12}(\mathbf{r},t)F(\mathbf{v})\,. \tag{5.26}$$

The involved dynamics of the probe field is now completely determined by Eqs.(5.24), (5.26) and the propagation equation. Moreover, in the paraxial regime, where the slowly-varying envelope approximation (SVEA) in the spatial dimension is valid, we have

$$\left|\mathbf{v}\cdot\frac{\partial}{\partial\mathbf{r}}\right|\ll|\Delta_{12}(\mathbf{v})+i\gamma_c|,|\Delta_{13}(\mathbf{v})+i\gamma_c|\,. \tag{5.27}$$

With this approximation, Eqs. (5.24) and (5.26) yield

$$[\Delta_{12}(\mathbf{v})+i\gamma_c]\hat{\sigma}_{12}+\Omega_p(\mathbf{r})n_0F(\mathbf{v})+\Omega_c\hat{\sigma}_{13}-i\gamma_c\hat{R}_{12}(\mathbf{r})F(\mathbf{v})=0\,, \tag{5.28a}$$

$$[\Delta_{13}(\mathbf{v})+i\gamma_c]\hat{\sigma}_{13}+\Omega_c\hat{\sigma}_{12}-i\gamma_c\hat{R}_{13}(\mathbf{r},t)F(\mathbf{v})+n_0^2\Omega_c^3AF(\mathbf{v})B(\mathbf{r},\mathbf{v})\Omega_p(\mathbf{r})=0\,, \tag{5.28b}$$

where we have defined a kernel function depending on $\mathbf{r}$ and $\mathbf{v}$ as

$$B(\mathbf{r},\mathbf{v})=\int\frac{V(\mathbf{r}-\mathbf{r}')\big|\Omega_p(\mathbf{r}')\big|^2d^3\mathbf{r}'}{\Omega_c^2-\Delta_{12}(\mathbf{v})\Delta_{13}(\mathbf{v})+V(\mathbf{r}-\mathbf{r}')\Delta_{12}(\mathbf{v})}\,. \tag{5.29}$$

Integrating Eq. (5.28) over $\mathbf{v}$, we find

$$\mathbf{k}_p\cdot\hat{\mathbf{J}}_{12}(\mathbf{r}) =(\Delta_p+i\gamma_{12})\hat{R}_{12}(\mathbf{r})+n_0\Omega_p(\mathbf{r})+\Omega_c\hat{R}_{13}(\mathbf{r})\,, \tag{5.30a}$$

$$\Delta\mathbf{k}\cdot\hat{\mathbf{J}}_{13}(\mathbf{r}) =i\gamma_{13}\hat{R}_{13}(\mathbf{r})+\Omega_c\hat{R}_{12}(\mathbf{r})+n_0^2\Omega_c^3A\Omega_p(\mathbf{r})f_1(\mathbf{r})\,, \tag{5.30b}$$

where we have set the two-photon detuning $\Delta=0$ for simplicity, and $\hat{\mathbf{J}}_{\alpha\beta}(\mathbf{r})$ and $f_1(\mathbf{r})$ are defined as

$$\hat{\mathbf{J}}_{\alpha\beta}(\mathbf{r})=\int\hat{\sigma}_{\alpha\beta}(\mathbf{r},\mathbf{v})\mathbf{v}d^3\mathbf{v}\,, \tag{5.31}$$

$$f_1(\mathbf{r})=\int F(\mathbf{v})B(\mathbf{r},\mathbf{v})d^3\mathbf{v}\,. \tag{5.32}$$

In Eq. (5.28b), when the residual Doppler effect $\Delta\mathrm{k}\mathrm{v}_p$ becomes dominant, we can expand

$\hat{\sigma}_{13}(\mathbf{r},\mathbf{v})$ to first order in $\Delta\mathrm{k}\mathrm{v}_p$, which yields

$$\hat{\sigma}_{13}(\mathbf{r},\mathbf{v}) \simeq \hat{R}_{13}(\mathbf{r})F(\mathbf{v}) + \frac{\hat{\sigma}_{13}^{(1)}(\mathbf{r},\mathbf{v})}{\Delta\mathrm{k}\mathrm{v}_p}\,. \tag{5.33}$$

This leads to

$$\hat{\mathbf{J}}_{13} = \frac{1}{\Delta\mathrm{k}\mathrm{v}_p}\int \hat{\sigma}_{13}^{(1)}(\mathbf{r},\mathbf{v})\,d^3\mathbf{v}\,. \tag{5.34}$$

Expanding $\hat{\sigma}_{13}(\mathbf{r},\mathbf{v})$ as in Eq. (5.33), multiplying by $\mathbf{v}$ in Eq. (5.28b), integrating over $\mathbf{v}$, and keeping the leading order in $\Delta\mathrm{k}\mathrm{v}_p$, we find

$$\Delta\mathrm{k}^2\mathrm{v}_p^2\hat{R}_{13}(\mathbf{r}) - i(\gamma_{12}+\gamma_c)\Delta\mathbf{k}\cdot\hat{\mathbf{J}}_{13}(\mathbf{r}) = \Omega_c\Delta\mathbf{k}\cdot\hat{\mathbf{J}}_{12}(\mathbf{r}) + n_0^2\Omega_c^3 A\Omega_p(\mathbf{r})f_2(\mathbf{r})\,. \tag{5.35}$$

Here, $f_2(\mathbf{r})$ is given by

$$f_2(\mathbf{r}) = \int F(\mathbf{v})B(\mathbf{r},\mathbf{v})\Delta\mathbf{k}\cdot\mathbf{v}\,d^3\mathbf{v}\,. \tag{5.36}$$

In experimental settings, a common choice of the laser field geometry is near-collinear propagation, i.e., $\mathbf{k}_p \parallel \mathbf{k}_c \parallel \Delta\mathbf{k}$. Then from Eq. (5.30) and (5.35), $\hat{R}_{13}(\mathbf{r})$ can be obtained as

$$\begin{aligned}\hat{R}_{13}(\mathbf{r}) =& \frac{\frac{\Delta\mathrm{k}}{\mathrm{k}_p}\Omega_c(\Delta_p+i\gamma_{12}) + i\Omega_c(\gamma_{13}+\gamma_c)}{\Delta\mathrm{k}^2\mathrm{v}_p^2 - \frac{\Delta\mathrm{k}}{\mathrm{k}_p}\Omega_c^2 + \gamma_{13}(\gamma_{13}+\gamma_c)}\hat{R}_{12}(\mathbf{r}) \\ &+ \frac{\frac{\Delta\mathrm{k}}{\mathrm{k}_p}n_0\Omega_c\Omega_p(\mathbf{r}) + n_0^2\Omega_c^3 A\Omega_p(\mathbf{r})[f_2(\mathbf{r}) + i(\gamma_c+\gamma_{13})f_1(\mathbf{r})]}{\Delta\mathrm{k}^2\mathrm{v}_p^2 - \frac{\Delta\mathrm{k}}{\mathrm{k}_p}\Omega_c^2 + \gamma_{13}(\gamma_{13}+\gamma_c)}\,.\end{aligned} \tag{5.37}$$

In Eq. (5.28a), we approximate $\hat{\sigma}_{13}(\mathbf{r},\mathbf{v}) \simeq \hat{R}_{13}(\mathbf{r})F(\mathbf{v})$ and integrate over $\mathbf{v}$, leading to

$$\hat{R}_{13}(\mathbf{r}) = \frac{1}{\Omega_c}\Big[-n_0\Omega_p(\mathbf{r}) + \frac{i\gamma_c G - 1}{G}\hat{R}_{12}(\mathbf{r})\Big]\,, \tag{5.38}$$

with

$$G = \int \frac{F(\mathbf{v})}{\Delta_p - \mathbf{k}_p\cdot\mathbf{v} + i(\gamma_{12}+\gamma_c)}\,. \tag{5.39}$$

Finally, the solution for $\hat{R}_{12}(\mathbf{r})$ can be derived from Eq. (5.37) and (5.38). The coherence $\rho_{21}(\mathbf{r})$ which determines the atomic response reads

$$\begin{aligned}\rho_{21}(\mathbf{r}) = \langle\hat{R}_{12}(\mathbf{r})\rangle &= \frac{M}{D}\Omega_p(\mathbf{r}) + \frac{1}{D}n_0^2\Omega_c^4 A\Omega_p(\mathbf{r})\big[i(\gamma_{13}+\gamma_c)f_1(\mathbf{r}) + f_2(\mathbf{r})\big] \\ &= \frac{M}{D}\Omega_p(\mathbf{r}) + i\frac{(\gamma_{13}+\gamma_c)n_0^2\Omega_c^4 A}{D}\Omega_p(\mathbf{r})\int K(\mathbf{r}-\mathbf{r}')\big|\Omega_p(\mathbf{r}')\big|^2 d\mathbf{r}'\,,\end{aligned} \tag{5.40}$$

with

$$D = [\Delta \mathrm{k}^2 \mathrm{v}_p^2 - \frac{\Delta \mathrm{k}}{\mathrm{k}_p}\Omega_c^2 + \gamma_{13}(\gamma_{13}+\gamma_c)]\frac{i\gamma_c G - 1}{G} - [\frac{\Delta \mathrm{k}}{\mathrm{k}_p}(\Delta_p + \gamma_{12}) + i(\gamma_{13}+\gamma_c)]\Omega_c^2\,, \tag{5.41a}$$

$$M = [\Delta \mathrm{k}^2 \mathrm{v}_p^2 + \gamma_{13}(\gamma_{13}+\gamma_c)]n_0\,, \tag{5.41b}$$

$$K(\mathbf{r}) = \int \frac{(1 - i\frac{\Delta \mathbf{k}\cdot\mathbf{v}}{\gamma_{13}+\gamma_c})F(\mathbf{v})V(\mathbf{r})d^3\mathbf{v}}{\Omega_c^2 - \Delta_{12}(\mathbf{v})\Delta_{13}(\mathbf{v}) + V(\mathbf{r})\Delta_{12}(\mathbf{v})}\,. \tag{5.41c}$$

Here G and A are related to the Doppler-averaging single- and two- photon spectra respectively, and $K(\mathbf{r})$ corresponds to the dipole-dipole interaction modified by the thermal atomic motion. In the limit $T \to 0$, $\rho_{21}(\mathbf{r})$ reduces to

$$\begin{aligned}\rho_{21}(\mathbf{r}) = &\frac{i\gamma_{13}n_0}{\Omega_c^2 - i\gamma_{13}\Delta_{12}}\Omega_p(\mathbf{r}) \\ &- \frac{n_0^2\Omega_c^4\Omega_p(\mathbf{r})}{(\Omega_c^2 - i\gamma_{13}\Delta_{12})|\Omega_c^2 - i\gamma_{13}\Delta_{12}|^2}\int \frac{V(\mathbf{r}-\mathbf{r}')|\Omega_p(\mathbf{r}')|^2}{\Omega_c^2 - i\gamma_{13}\Delta_{12} + \Delta_{12}V(\mathbf{r}-\mathbf{r}')}d^3\mathbf{r}'\,,\end{aligned} \tag{5.42}$$

we note that the result in this particular limit perfectly agrees with the findings obtained in ultracold Rydberg gases [25], as we expected. Note here $\Delta_{12} = \Delta_p + i\gamma_{12}$.

5.1.3 Propagation dynamics in thermal interacting Rydberg atoms

The propagation dynamics of the probe beam is governed by the Maxwell's equations, which in the paraxial regime can be derived as Eq. (2.26), which reads

$$\left(\frac{\partial}{\partial\zeta} - \frac{i}{2}\frac{\partial^2}{\partial\boldsymbol{\xi}^2}\right)\Omega_p(\boldsymbol{\xi},\zeta) = i\frac{3\lambda_p^2\Gamma_{21}S_z}{8\pi}\rho_{21}(\boldsymbol{\xi},\zeta)\,. \tag{5.43}$$

Here, we have rescaled the coordinates using $\boldsymbol{\xi} = \mathbf{r}_\perp/S_t$, $\zeta = z/S_z$ and $S_z = \mathrm{k}_p S_t^2$, with S_t and S_z being the scales in the transverse and propagation directions, respectively. Since we consider a continuous-wave probe field, the evolution of the probe in the ζ direction is much slower than that of $K(\boldsymbol{\xi},\zeta)$. Therefore, in the nonlocal integral Eq. (5.40), we can apply the local approximation in ζ-direction as $\Omega_p(\boldsymbol{\xi}',\zeta') \simeq \Omega_p(\boldsymbol{\xi}',\zeta)$ [25]. Substituting the atomic response Eq. (5.40) into Eq. (5.43) then results in

$$\left(\frac{\partial}{\partial\zeta} - \frac{i}{2}\frac{\partial^2}{\partial\boldsymbol{\xi}^2}\right)\psi(\boldsymbol{\xi},\zeta) = i\left[C_l + C_{nl}\int_{-\infty}^{\infty}K_s(\boldsymbol{\xi}-\boldsymbol{\xi}')|\psi(\boldsymbol{\xi}',\zeta)|^2 d\boldsymbol{\xi}'\right]\psi(\boldsymbol{\xi},\zeta)\,, \tag{5.44}$$

where we have set $\Omega_p(\boldsymbol{\xi},\zeta) = \Omega_{p0}\psi(\boldsymbol{\xi},\zeta)$. The scaled kernel function $K_s(\boldsymbol{\xi})$ is given in the following

$$K_s(\boldsymbol{\xi}) = \int \frac{(1 - i\frac{\Delta \mathrm{k}\mathrm{v}_p v}{\gamma_{13}+\gamma_c})e^{-v^2}dvd\eta}{\frac{\Delta_{12}(\mathrm{v})}{\Delta_p} + \frac{\Omega_c^2 S_t^6}{\Delta_p C_6}[1 - \frac{\Delta_{12}(\mathrm{v})\Delta_{13}(\mathrm{v})}{\Omega_c^2}](\boldsymbol{\xi}^2+\eta^2)^3}\,, \tag{5.45}$$

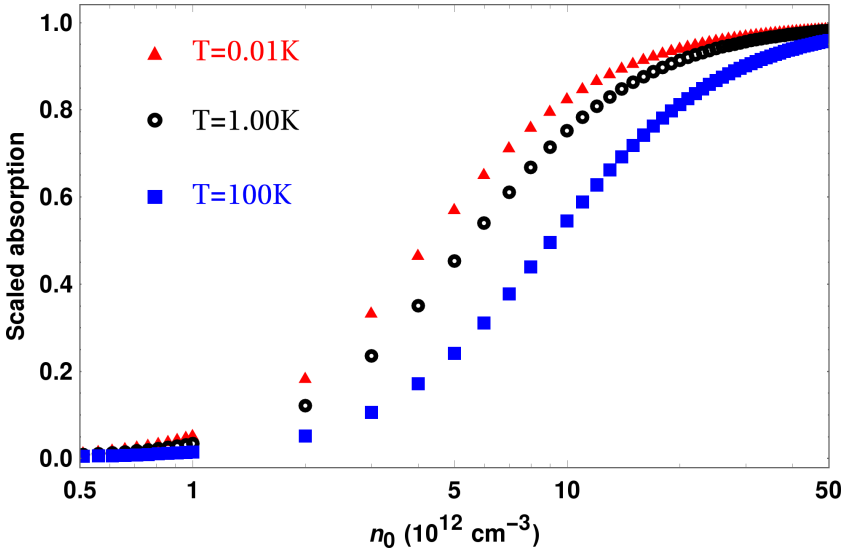

Figure 5.2: Scaled absorption against the atomic density at different temperatures. Related parameters are: $\lambda_p = 0.795\ \mu m, \lambda_c = 0.48\ \mu m, \Gamma_{21} = 2\pi \times 5.75$ MHz, $\gamma_{12} = \Gamma_{21}/2, \gamma_{13} = 0.001\gamma_{21}, \gamma_c = 0.01|\Delta \mathrm{k}|\mathrm{v}_p, \Delta_p = \Delta_c = 0, \Omega_{p0} = 2\pi \times 0.5$ GHz, $\Omega_c = 2\pi \times 10$ GHz, $C_6 = 140$ GHz $\mu m^6, S_t = 40\ \mu m, z_L = 1\ cm$.

with $\mathrm{v} = \mathrm{v}_p v$ and

$$C_l = \frac{3\lambda_p^2 \Gamma_{21} S_z M}{8\pi D}, \tag{5.46a}$$

$$C_{nl} = \frac{3i\lambda_p \Gamma_{21}(\gamma_{13} + \gamma_c) A \Omega_c^4 S_t^5 n_0^2 \Omega_{p0}^2}{4\sqrt{\pi} D \Delta_p}. \tag{5.46b}$$

5.1.3.1 Local nonlinear propagation dynamics

At first glance, our analytical solutions seems to be only applicable in the regime of large single-photon detuning where the adiabatic elimination is valid. However, in principle, we could still obtain a steady-state solution, even in the regime where the single-photon transitions are near-resonant. Thus the analytical analysis still holds in this regime, where the nonlinear absorption plays a major role in the propagation dynamics. We could thus neglect the nonlocal effects in Eq. (5.40), i.e., $\Omega_p(\mathbf{r}') = \Omega_p(\mathbf{r})$ [25].

In the absence of dipole-dipole interactions, i.e., $C_6 = 0$, the atomic medium becomes nearly transparent for the probe field because of the EIT configuration. However, in the presence of the interaction, the nonlinear absorption is introduced. The thermal atomic motion induces a Doppler averaging over all atoms with different velocities, which we expect to effectively weaken the nonlinear absorption (see also Sec. 5.1.3.2). To analyze the nonlinear absorption, we numerically solve Eqs. (5.40) and (5.43) to obtain the propagation dynamics for a Gaussian-shaped probe field $\Omega_p(\boldsymbol{\xi}) = \Omega_{p0} e^{-\xi^2/2}$, from which the scaled absorption against the atomic density n_0 can be derived. Here, the scaled absorption is defined as the actual absorption divided by the two-level absorption obtained for $\Omega_c = 0$. Results at different temperatures are shown in Fig. 5.2. The propagation distance is chosen as $z_L = 1.0\ cm$, close to one Rayleigh length $z_R = 1.26\ cm$. In Fig. 5.2, the scaled absorption increases nonlinearly as a function of n_0, which is in qualitative agreement with previous calculations [67, 69] and experiments [272] obtained

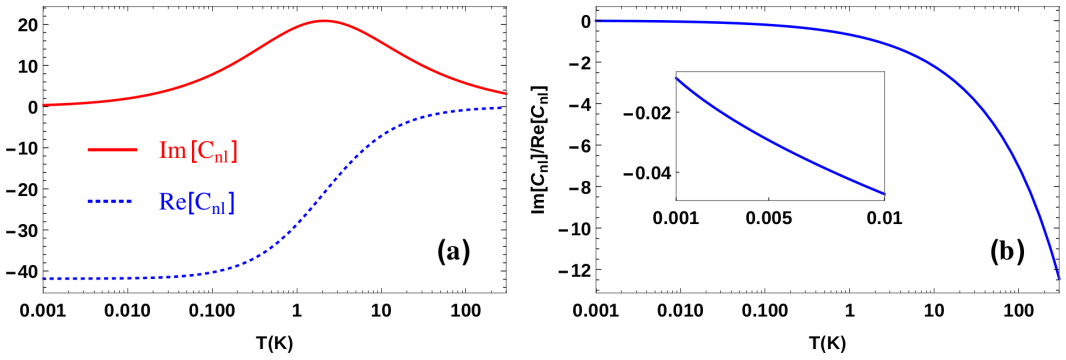

Figure 5.3: (a) The nonlinear coefficient C_{nl} and (b) the ratio between its real and imaginary parts $\mathrm{Im}[C_{nl}]/\mathrm{Re}[C_{nl}]$ against the temperature T. The inset shows the values of the ratio at lower temperature, the small values indicate that $\mathrm{Im}[C_{nl}]$ can be neglected when $T \to 0$. Parameters are: $n_0 = 1.0 \times 10^{20}\ m^{-3}, \Delta_p = 2\pi \times 1.2$ GHz, $\Delta_c = -\Delta_p$, and $S_t = 5R_c$ with R_c being the blockade radius $R_c = (|C_6\Delta_p|/\Omega_c^2)^{1/6} \simeq 0.8\ \mu m$. Other parameters are the same as in Fig. 5.2.

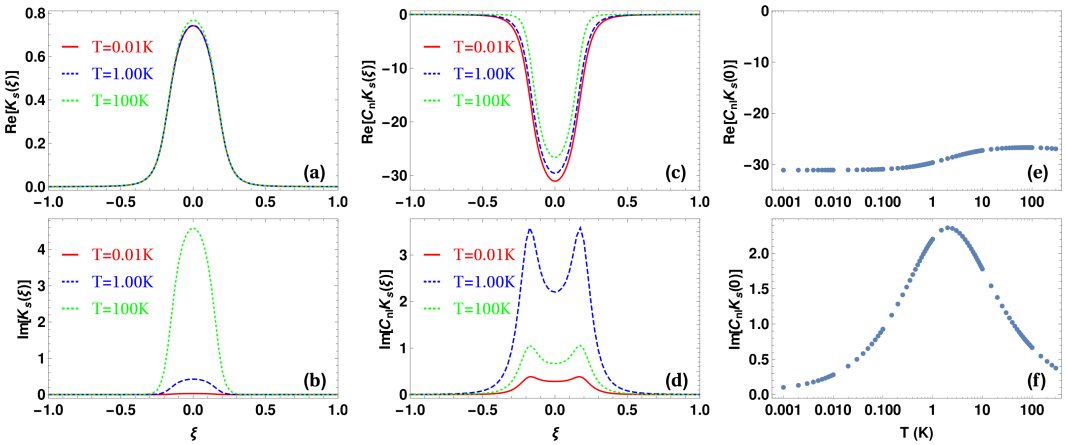

Figure 5.4: The real (a) and imaginary (b) parts of the nonlocal response function $K_s(\xi)$ and the real (c) and imaginary (d) parts of $C_{nl}K_s(\xi)$ at different temperatures. $C_{nl}K_s(0)$ as a function of T is plotted in (e) and (f). Note that $\mathrm{Im}[C_{nl}K_s(0)]$ first grows and then decreases as T rises. Parameters are the same as in Fig. 5.3.

in ultracold Rydberg gases. Furthermore, as expected, the nonlinear absorption at any specific atomic density is decreased due to the Doppler averaging as the temperature rises.

5.1.3.2 Nonlocal nonlinear propagation dynamics

Next, we consider the far-detuned regime where the single-photon detunings dominate, i.e., $\Delta_p \gg \mathrm{k}_p\mathrm{v}_p$, γ_{12}, Ω_p. In this regime, the local approximation is only valid in the propagation direction [25], i.e., $\Omega_p(\mathbf{r}') = \Omega_p(\mathbf{r}'_\perp)$ in Eq. (5.40). Furthermore, note that in Eq. (5.45) it is evident that $K_s(\boldsymbol{\xi})$ is symmetric in the transverse plane (ξ_x, ξ_y), so in the following we will focus on the x direction which is denoted by $\xi = \xi_x$ for simplicity. The propagation dynamics is mainly characterized by the nonlocal coefficient C_{nl} and the scaled nonlocal response $K_s(\xi)$. In low-temperature Rydberg atoms, we find $|\mathrm{Im}[C_{nl}]| \ll |\mathrm{Re}[C_{nl}]|$ such that C_{nl} can be approximated as a real number, see Fig. 5.3. Then, the real and imaginary parts $\mathrm{Re}[K_s(\xi)]$ and $\mathrm{Im}[K_s(\xi)]$ are directly related to the nonlocal nonlinear dispersion and absorption, respectively. At low temperatures,

the nonlocal nonlinear absorption determined by $\mathrm{Im}[K_s(\xi)]$ is small as compared to the nonlocal nonlinear dispersion determined by $\mathrm{Re}[K_s(\xi)]$, see Fig. 5.4(a) and (b). Consequently, the modulational instability (MI) [36, 37] caused by the nonlocal nonlinear dispersion is expected to crucially influence the probe propagation dynamics, as discussed in Ref. [25].

As T increases, we find that C_{nl} and $K_s(\xi)$ change in a characteristic way, influencing the propagation dynamics. As shown in Fig. 5.3, $\mathrm{Im}[C_{nl}]$ first grows and then decreases, while $\mathrm{Re}[C_{nl}]$ decreases monotonically in magnitude. After carefully checking Eq. (5.46b), we find that this can be mainly attributed to the collision rate γ_c which is a function of T.

Corresponding results for $K_s(\xi)$ are shown in Fig. 5.4(a) and (b) for three different temperatures $T \in \{0.01\mathrm{K}, 1\mathrm{K}, 100\mathrm{K}\}$. The real part $\mathrm{Re}[K_s(\xi)]$ remains essentially unchanged against the temperature. However, the imaginary part $\mathrm{Im}[K_s(\xi)]$ increases strongly with the temperature, while maintaining approximately its shape as a function of ξ. This can be understood in a velocity-dependent dressed-state picture. In the far-off resonant regime where $\Delta_p > 0$, part of the atoms have velocities which Doppler-shift their transition frequency to be close to the single-photon resonance. This fraction increases with the mean velocity and thus the temperature, thus leading to a narrowed and amplified spectrum for the probe as summing over the contributions of all atoms [273]. As a result, the amplitude of $K_s(\xi)$ for the nonlocal nonlinear interaction increases with T. In contrast, close to the one-photon resonance $\Delta_p \simeq 0$, an increasing Doppler shift progressively moves the atom transition frequencies out of resonance with increasing temperature, thus resulting in a broadened and attenuated spectrum for the probe field when summing over the contributions from all atoms with different velocities. Therefore, in this case, an increasing temperature T reduces the linear and nonlinear absorption for the probe field, as already discussed in Sec. 5.1.3.1. Finally, we now turn to analyze the combined nonlocal contribution $C_{nl}K_s(\xi)$, as shown in Figs. 5.4(c) and (d). We find that as T increases, $\mathrm{Re}[C_{nl}K_s(\xi)]$ remains essentially unchanged. However, $\mathrm{Im}[C_{nl}K_s(\xi)]$ first increases with growing temperature, assumes a maximum, and subsequently decreases again in magnitude. To further illustrate this behavior, we show the central value $C_{nl}K_s(0)$ against T in Fig. 5.4(e) and (f). Again, the maximum of the imaginary part of the nonlocal contribution at intermediate temperatures is clearly visible. By comparing the dependence of C_{nl} and $K_s(\xi)$ on the temperature, it is found that this behavior is mainly due to C_{nl} and therefore related to the temperature-dependent collision rate $\gamma_c \propto \sqrt{T}$.

In order to see how the propagation dynamics varies with the temperature, we numerically calculated the probe propagation at different temperatures. The input probe is chosen as a Gaussian $\psi(\xi_x, \xi_y) = e^{-(\xi_x^2+\xi_y^2)/2w_p^2} e^{i\phi(\xi_x,\xi_y)}$, where the random phase function $\phi(\xi_x, \xi_y)$ introduces the spatial noises which would induce the MI effect. Results are shown in Fig. 5.5. Owing to the MI, spatially localized spikes emerge in the output profile of the probe field. As the temperature rises, the output intensity first decreases and subsequently grows again, which is consistent with Fig. (5.4). Note that at first sight, this figure might give the impression that the width of the probe output profile increases with the nonlinear absorption. However, this is an artefact of the different scalings in the plots. Instead, while the absorption changes the beam profile, the width does not increase. Because of the nonlocal nonlinear absorption introduced by $\mathrm{Im}[C_{nl}K(\xi)]$, a linear analytical analysis would not be applicable for the MI effect. In order to understand

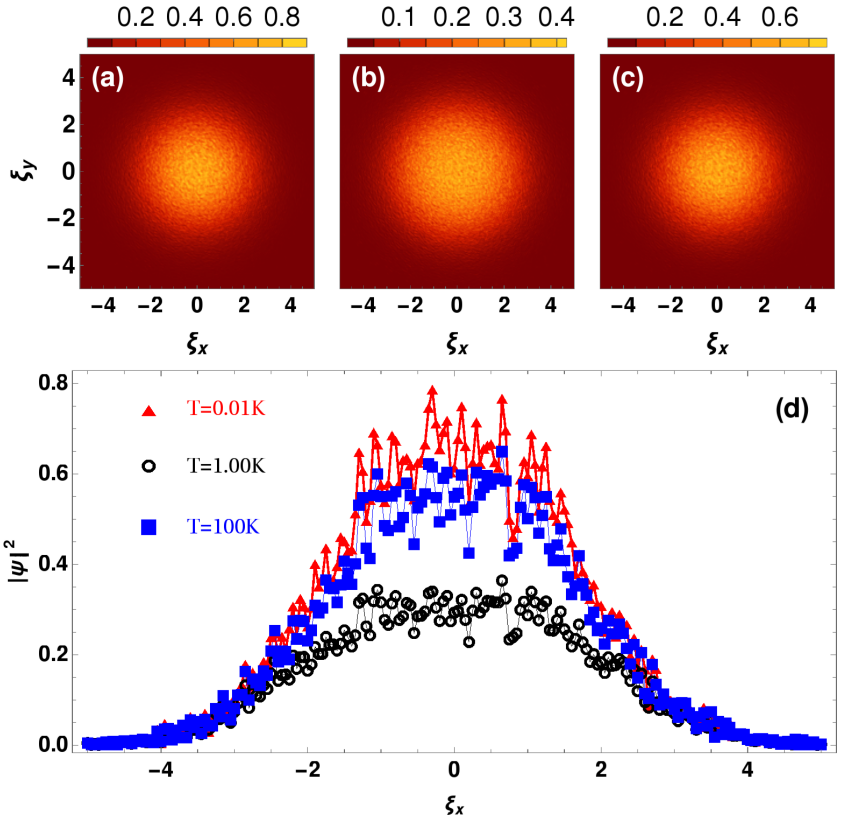

Figure 5.5: The output intensity profiles of the probe in the thermal Rydberg atoms at different temperatures $T = 0.01K$ (a), $T = 1K$ (b), and $T = 100K$ (c), while the corresponding slices at $\xi_y = 0$ are shown in (d). The highly localized spikes is due to the MI effect. Parameters are: $S_t = 20R_c, \mathrm{k}_0 = 2\pi/S_t, w_p = 2, \zeta_L = 1/16$ which is equal to $z_L \simeq 127.3\ \mu m$, others are the same as in Fig. 5.3.

the MI effect more clearly, we define a weighted spatial Fourier spectrum

$$f(\mathrm{k}) = \left| \frac{F[\psi(\xi_x, \xi_y = 0, \zeta), \xi_x, \mathrm{k}]}{F[\psi(\xi_x, \xi_y = 0, \zeta = 0), \xi_x, \mathrm{k}]} \right|, \tag{5.47}$$

with $F[\psi, \xi_x, \mathrm{k}]$ denoting the spatial Fourier transform of ψ from ξ_x to k. We calculated $f(\mathrm{k})$ for three different temperatures and for specific wave components k. Results are shown in Fig. 5.6. It can be seen from the momentum space spectrum in (a) that there are some k components which are enhanced, while others are not. Note that enhancements only become visible in this measure if they are strong enough to overcome the nonlinear absorption. We have to mention at this point that it may not be proper to claim that only these components which satisfies $f(\mathrm{k}) > 1$ exhibit the MI effect, according to the acquired knowledge from a model which we will develop later and which we use to describe the MI in absorptive media. Note that $f(\mathrm{k})$ is asymmetric due to the introduced random noise ϕ. Setting $\phi = 0$, a symmetric spectrum $f(\mathrm{k})$, which is not shown here, has been obtained. We further performed calculations of $f(\mathrm{k})$ as a function of T for three specific components $\mathrm{k} \in \{-0.36\mathrm{k}_0, 0.24\ \mathrm{k}_0, 6.59\mathrm{k}_0\}$, the results in Fig. 5.6(b) show that they first decreases, and then increases again, providing a direct signature of the effect of the temperature-dependent nonlocal nonlinear absorption in thermal interacting Rydberg atoms.

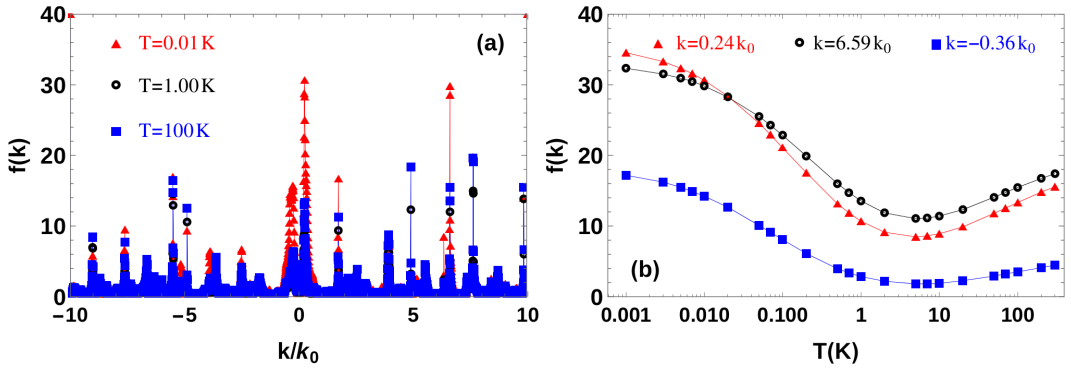

Figure 5.6: In order to show the MI, a corresponding weighted Fourier spectrum $f(\mathrm{k})$ of the output probe at $\xi_y = 0$ is given in (a), while the spectrum as a function of temperature T is plotted in (b) for three specific wave components $\mathrm{k} = -0.36\mathrm{k}_0, 0.24\mathrm{k}_0, 6.59\mathrm{k}_0$. Parameters are: $S_t = 20R_c, \mathrm{k}_0 = 2\pi/S_t, w_p = 2, \zeta_L = 1/16$ which is equal to $z_L \simeq 127.3\ \mu m$, others are the same as in Fig. 5.3.

Owing to the simultaneous presence of the MI effect and the nonlocal nonlinear absorption, there will be competition between these two mechanisms, thus one would expect that the weighted spatial wave components of $f(\mathrm{k})$ may not simply give an exponential dependence on the propagation distance. In order to show this, we then propagate a two-dimensional plane wave with an additional cosine perturbation $\psi(\xi, \zeta = 0) = 1 + \epsilon_0 \cos(\mathrm{k}_x \xi)$ with ϵ_0 being real and $\epsilon_0 \ll 1$. We can assume that the output function $\psi(\xi, \zeta)$ can be approximated by a Fourier expansion

$$\psi(\xi, \zeta) = \sum_j a_j(\zeta) e^{ijk_x\xi}\,. \tag{5.48}$$

Substituting this form back into Eq. (5.44) leads to a set of equations for $a_j(\zeta)$

$$\left[\frac{\partial}{\partial\zeta} + \frac{i}{2}j^2k_x^2\right] a_j(\zeta) = iC_{nl} \sum_{p,q} a_{j-p+q}(\zeta) a_p(\zeta) a_q^*(\zeta) K_F\left[(p-q)k_x\right]\,, \tag{5.49}$$

where we have applied the relation similar to Eq. (2.112)

$$\begin{aligned}\int_{-\infty}^{\infty} K(\xi - \xi')|\psi(\xi')|^2 d\xi' &= \int_{-\infty}^{\infty} K(\xi - \xi') \sum_{p,q} a_p(\zeta) a_q^*(\zeta) e^{i(p-q)k_x\xi'} d\xi' \\ &= \sum_{p,q} a_p(\zeta) a_q^*(\zeta) K_F((p-q)k_x) e^{i(p-q)k_x\xi_x}\,,\end{aligned} \tag{5.50}$$

and $K_F(mk_x)$ is the m-th spatial Fourier transform of the scaled kernel function $K_s(\xi)$ defined by

$$K_F(mk_x) = \int_{-\infty}^{\infty} K_s(\xi) e^{-imk_x\xi} d\xi\,. \tag{5.51}$$

In general, it is rather impossible to obtain analytical solutions of this set of equations. Fortunately, the set of equations can be reasonably truncated to a maximum value, i.e., $j \le j_{\max}$, depending on the propagation distance ζ_L. For a short distance where $|a_0(\zeta)| \gg |a_1(\zeta)|$, $j_{\max}$ can be safely limited to $j_{\max} = 1$, leading to the following

simplified equations of motion for $a_0(\zeta)$, $a_1(\zeta)$ and $a_{-1}(\zeta)$

$$\frac{da_0(\zeta)}{d\zeta} = iC_{nl}K_F(0)|a_0(\zeta)|^2 a_0(\zeta)\,, \tag{5.52a}$$

$$\begin{aligned}\frac{da_1(\zeta)}{d\zeta} =& -\frac{k_x^2}{2}a_1(\zeta) + iC_{nl}\big[K_F(0)|a_0(\zeta)|^2 a_1(\zeta) \\ &+ K_F(k_x)|a_0(\zeta)|^2 a_1(\zeta) + K_F(k_x)a_0^2(\zeta)a_{-1}^*(\zeta)\big]\,,\end{aligned} \tag{5.52b}$$

$$\begin{aligned}\frac{da_{-1}(\zeta)}{d\zeta} =& -\frac{k_x^2}{2}a_{-1}(\zeta) + iC_{nl}\big[K_F(0)|a_0(\zeta)|^2 a_{-1}(\zeta) \\ &+ K_F(-k_x)|a_0(\zeta)|^2 a_{-1}(\zeta) + K_F(-k_x)a_0^2(\zeta)a_1^*(\zeta)\big]\,.\end{aligned} \tag{5.52c}$$

From Eq. (5.52a) the analytical solution for $a_0(\zeta)$ can be found by first rewriting $a_0(\zeta) = f(\zeta)e^{ig(\zeta)}$, which decomposes Eq. (5.52a) into two parts

$$\frac{df(\zeta)}{d\zeta} = -\mathrm{Re}[c_0]f^3(\zeta)\,, \tag{5.53a}$$

$$\frac{dg(\zeta)}{d\zeta} = \mathrm{Im}[c_0]f^2(\zeta)\,, \tag{5.53b}$$

where we have set $C_{nl}K_F(0) = c_0 = \mathrm{Re}[c_0] + \mathrm{Im}[c_0]i$. The solution of Eq. (5.53) can be easily obtained

$$a_0(\zeta) = \frac{(1+2\mathrm{Im}[c_0]\zeta)^{i\frac{\mathrm{Re}[c_0]}{2\mathrm{Im}[c_0]}}}{\sqrt{1+2\mathrm{Im}[c_0]\zeta}} = (1+2\mathrm{Im}[c_0]\zeta)^{\frac{ic_0}{2\mathrm{Im}[c_0]}}\,. \tag{5.54}$$

We can find from Eq. (5.54) that $a_0(\zeta)$ decreases against the propagation distance due to the nonlocal nonlinear absorption $\mathrm{Im}[c_0]$. In the case of $\mathrm{Im}[c_0] \to 0$, Eq. (5.54) is reduced to

$$a_0(\zeta) = \lim_{\mathrm{Im}[c_0]\to 0}(1+2\mathrm{Im}[c_0]\zeta)^{\frac{ic_0}{2\mathrm{Im}[c_0]}} = e^{ic_0\zeta}\,, \tag{5.55}$$

which indicates that $a_0(\zeta)$ will experience no absorption except for a linear phase modulation against the propagation distance. For a symmetric kernel function $K(\xi_x) = K(-\xi_x)$, it would result in $K_F(k_x) = K_F(-k_x)$ and the subsequent symmetric nature of the equations of motion for the positive and negative components. And also by noting the fact that the input cosine perturbation indicates that $a_1(0) = a_{-1}(0)$, we then find that $a_1(\zeta) = a_{-1}(\zeta)$. Then Eq. (2.61b) can be further simplified to

$$\frac{da_1(\zeta)}{d\zeta} = i\big[-\frac{k_x^2}{2} + (c_0+c_1)|a_0(\zeta)|^2\big]a_1(\zeta) + ic_1a_0^2(\zeta)a_1^*(\zeta)\,, \tag{5.56}$$

and we have set $C_{nl}K_F(k_x) = c_1$. Substituting the solution of $a_0(\zeta)$ in Eq. (5.54) into the equation above and rewriting $a_1(\zeta)$ as

$$a_1(\zeta) = \epsilon_0 b_1(\zeta)e^{-\frac{ik_x^2\zeta}{2} + i\frac{c_0+c_1}{2\mathrm{Im}[c_0]}\ln(1+2\mathrm{Im}[c_0]\zeta)}\,, \tag{5.57}$$

Eq. (5.56) is changed to

$$\frac{db_1(\zeta)}{d\zeta} = \frac{ic_1 b_1^*(\zeta)}{1+2\mathrm{Im}[c_0]\zeta} e^{ik_x^2\zeta - i\frac{\mathrm{Re}[c_1]}{\mathrm{Im}[c_0]}\ln(1+2\mathrm{Im}[c_0]\zeta)} . \tag{5.58}$$

Taking the complex conjugate of Eq. (5.58) and then replacing b_1^* leads to

$$\frac{d^2 b_1}{d\zeta^2} = \left[ik_x^2 - \frac{2(\mathrm{Im}[c_0] + i\mathrm{Re}[c_1])}{1+2\mathrm{Im}[c_0]\zeta}\right]\frac{db_1}{d\zeta} + \frac{|c_1|^2 b_1}{(1+2\mathrm{Im}[c_0]\zeta)^2} . \tag{5.59}$$

Finally, the solution of $b_1(\zeta)$ can be obtained

$$\begin{aligned} b_1(\zeta) = (1+2\mathrm{Im}[c_0]\zeta)^{\frac{-ic_1}{2\mathrm{Im}[c_0]}} \{ & s_1 \mathrm{HypergeometricU}[\frac{-ic_1}{2\mathrm{Im}[c_0]}, 1+\frac{\mathrm{Im}[c_1]}{\mathrm{Im}[c_0]}, \frac{ik_x^2}{2\mathrm{Im}[c_0]} + ik_x^2\zeta] \\ & + s_2 \mathrm{LaguerreL}[\frac{ic_1}{2\mathrm{Im}[c_0]}, \frac{\mathrm{Im}[c_1]}{\mathrm{Im}[c_0]}, \frac{ik_x^2}{2\mathrm{Im}[c_0]} + ik_x^2\zeta]\} , \end{aligned} \tag{5.60}$$

and the coefficients s_1 and s_2 are constrained by the initial conditions

$$b_1(\zeta = 0) = 1 , \tag{5.61a}$$

$$\left.\frac{db_1}{d\zeta}\right|_{\zeta=0} = ic_1 . \tag{5.61b}$$

The analytical solution for $a_1(\zeta)$ is then obtained

$$\begin{aligned} a_1(\zeta) = & \epsilon_0 (1+2\mathrm{Im}[c_0]\zeta)^{\frac{ic_0}{2\mathrm{Im}[c_0]}} e^{-\frac{ik_x^2\zeta}{2}} \\ & \cdot \Big\{ s_1 \mathrm{HypergeometricU}[\frac{-ic_1}{2\mathrm{Im}[c_0]}, 1+\frac{\mathrm{Im}[c_1]}{\mathrm{Im}[c_0]}, \frac{ik_x^2}{2\mathrm{Im}[c_0]} + ik_x^2\zeta] \\ & + s_2 \mathrm{LaguerreL}[\frac{ic_1}{2\mathrm{Im}[c_0]}, \frac{\mathrm{Im}[c_1]}{\mathrm{Im}[c_0]}, \frac{ik_x^2}{2\mathrm{Im}[c_0]} + ik_x^2\zeta]\Big\} . \end{aligned} \tag{5.62}$$

The analytical results are then compared to the numerical calculations as given in Fig. 5.7(a). We can immediately find that the results from the developed model Eq. (5.48) have a perfect agreement with the numerical calculations of Eq. (5.44) for $k_x = 6.59k_0$. Further comparisons for other spatial frequencies have also shown that the model gives precisely the same results as obtained from the numerical calculations. Moreover, we can find a regular oscillating behavior which stems from the competition between MI and the nonlocal nonlinear absorption. But note that the competition between these two effects does not necessarily lead to oscillation for every component. Owing to the involved confluent hypergeometric function and generalized Laguerre polynomial, it is hard to reveal the underlying physics inside $a_1(\zeta)$ in an analytical manner. In order to show the competition between MI and nonlocal nonlinear absorption more directly, we then re-solve Eq. (5.59) in the region of $\zeta \sim 0$, which gives

$$b_1(\zeta) = e^{-(\mathrm{Im}[c_0] - \frac{ik_x^2}{2} + i\mathrm{Re}[c_1])\zeta}\left[s_1 e^{-\lambda(k_x)\zeta} + s_2 e^{\lambda(k_x)\zeta}\right] , \tag{5.63}$$

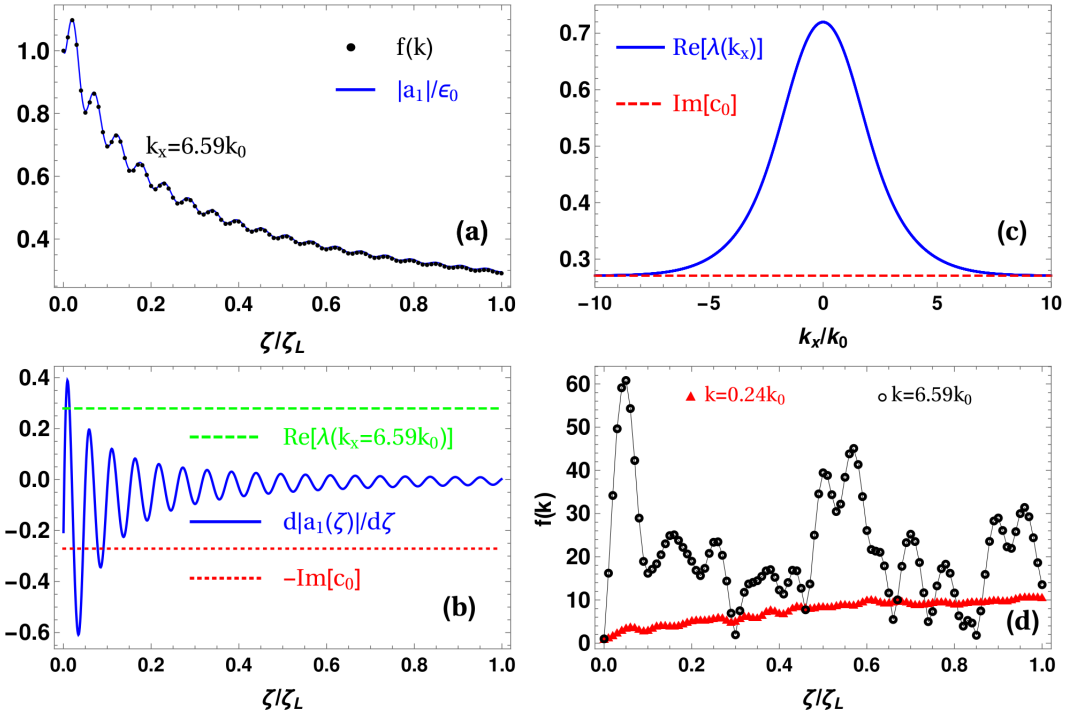

Figure 5.7: Comparison of numerical and analytical results. In (a), we show the wave component of the weighted spectrum $f(\mathrm{k})$ against propagation distance for an incident probe which is a plane wave added by a cosine perturbation as given in the main text, while the associated first derivative related to the growth rate is given in (b). The MI exponential growth rate $\mathrm{Re}[\lambda(k_x)]$ given in Eq. (5.64) is calculated in (c) for different k_x, the positive $\mathrm{Re}[\lambda(k_x)]$ suggests that MI exists for any wave component k_x. In (d), for a more complicated input probe profile as previously used in Fig. 5.5, the regular behavior of the evolution of specific components intends to be random due to the interaction between various wave components. Parameters are $T = 1.0K$, others are the same as in Fig. 5.6.

with

$$\lambda(k_x) = \frac{1}{2}\sqrt{4|c_1|^2 + (2\mathrm{Im}[c_0] - ik_x^2 + 2i\mathrm{Re}[c_1])^2}\,, \tag{5.64}$$

thus the analytical solution for $a_1(\zeta)$ can be much simplified

$$\begin{aligned} a_1(\zeta) =& \epsilon_0(1 + 2\mathrm{Im}[c_0]\zeta)^{\frac{i(c_0+c_1)}{2\mathrm{Im}[c_0]}} \\ & \cdot e^{-(\mathrm{Im}[c_0]+i\mathrm{Re}[c_1])\zeta}\left[s_1 e^{-\lambda(k_x)\zeta} + s_2 e^{\lambda(k_x)\zeta}\right]. \end{aligned} \tag{5.65}$$

From Eq. (5.65) it is clear to observe that $\lambda(k)$ is associated to the MI appeared in the absorptive nonlocal nonlinear media. In sharp contrast to the pure dispersive case where $\mathrm{Im}[C_{nl}K_F(k)] = 0$, counterintuitively, MI generally occurs for each k wave component when the nonlinear absorption is presented, as indicated in Eq. (5.64). Thanks to the nonlinear absorption introduced by $\mathrm{Im}[c_0]$, it is evident to see the competition between MI and the nonlinear absorption.

One might argue that the growth for the perturbation can only be present around $\zeta \sim 0$ where Eq. (5.65) is valid. However, this is not the case, the rate of change for $|a_1(\zeta)|$ calculated in Fig. 5.7(b) shows that it can be larger than 0 beyond $\zeta \sim 0$ and is in general above $-\mathrm{Im}[c_0]$ and below $\mathrm{Re}[\lambda(k_x)]$, indicating the enhancement of the

perturbation can survive for quite a large propagation distance. The values outside $\mathrm{Im}[c_0] \leq d|a_1(\zeta)|/d\zeta \leq \mathrm{Re}[\lambda(k_x)]$ are due to the coefficients determined by Eq. (5.61).

For an even more complicated input probe profile including many wave components, this regular oscillation may not been seen, since from Eq. (5.44) we can find that all wave components are interacting with each other. The resulting dependence on propagation distance for a specific component is then much more intricate and unpredictable. Fig. 5.7(d) shows two of the wave components against the propagation distance in the same input probe profile previously used in Fig. 5.5. It is obvious to see that the behaviors of the component $k_x = 6.59k_0$ is strongly amplified in a somewhat random manner against the propagation distance and differs from that in the simple case shown in Fig. 5.7(a). We attribute the origin of this "randomness" behavior to the interactions with all other wave components contained in the incident Gaussian probe. This randomness seems to be decreased for the wave component with a smaller k_x. This is possibly due to the fact that components with a small k_x have a larger initial amplitude in the Gaussian probe, and they are further associated with a stronger MI growth rate as shown in Fig. 5.7(c), thus the effect of other components becomes less important.

5.1.4 Discussions

In our model describing the thermal interacting Rydberg atoms, we have made a crucial approximation that the time variation in $V(t)$ is neglected. The crucial approximation might limit the potential applications of the present model. However, in an atomic ensemble in thermal equilibrium which is just the case considered here, by noting the fact that atoms are homogeneously distributed in position space, we would expect that the average DDI effect could remain unvaried $\sum_l V_{jl}(t)/N = V_{jl}(0)$ for a time scale much larger than R_c/v_p. Of course, this statement needs further a strict theoretical proof, and it should be a next step to improve the validity of our model.

In conclusion, we developed a model to describe the thermal Rydberg atoms interacting with two probe and control laser fields. Under a crucial approximation that the variations in the time-varying DDI is neglected, we found that an analytical expression for the atomic response can be derived, which gives the same results as previously obtained in ultracold Rydberg atoms [25] as we set the temperature $T = 0$ in our model. In the near-resonant case where the single-photon detuning is small, we find that the nonlinear absorption dominating the probe propagation is weakened when the temperature grows. In contrast, in the off-resonant regime preserving resonant two-photon transition, the nonlocal nonlinear response which is defined as the nonlinear coefficient multiplied by the nonlocal kernel function has shown a completely different behavior. The real part of the nonlinear coefficient is decreasing and the imaginary part is initially growing and then decreasing when the temperature rises. This can be mainly attributed to the collision rates which we assumed to be dependent on the temperature, i.e., $\gamma_c \propto \sqrt{T}$. Meanwhile, the real part of the nonlocal kernel function remains almost unchanged and the imaginary part gets enhanced. This is explained in a velocity-dependent dressed-state picture. Altogether, the nonlocal nonlinear dispersion remains almost unchanged while the nonlocal nonlinear absorption gets first decreased and then enhanced as the temperature increases. Consequently, the modulational instability is first suppressed and then recovered as the temperature grows, which is confirmed later by both a numerical Fourier analysis of the output probe field and an analytical model to describe the MI in nonlinear media with absorption. Furthermore, it is found that each wave component is associated with a positive MI growth rate in absorptive nonlocal nonlinear media, which competes with the nonlocal nonlinear absorption, and is eventually suppressed.

5.2 Parity-time symmetric dynamics in cold interacting Rydberg atoms

5.2.1 Introduction to Parity-time symmetry

It is well known that in canonical quantum mechanics the Hamiltonian $\hat{H}$ must be Hermitian, which guarantees real expectation values of physical quantities and probability conservation (i.e., unitary time evolution). However, as stated by Bender [59], the fact that $\hat{H}$ should be Hermitian is rather a mathematical axiom. When it is replaced by a less restrictive but physically more transparent condition which is called space-time reflection (PT) symmetry, the resulting energy spectrum can be still real when $\hat{H}$ is PT symmetric, by definition, i.e., $\hat{H} = \hat{P}\hat{T}\hat{H}\hat{P}\hat{T}$ [53–59, 63, 64]. Here the parity reflection and time-reversal operators are defined respectively by their action on the position and momentum operators $\hat{x}$ and $\hat{p}$ [59] as

$$\hat{P}\hat{x}\hat{P} = -\hat{x}\,, \quad \hat{P}\hat{p}\hat{P} = -\hat{p}\,, \tag{5.66a}$$

$$\hat{T}\hat{x}\hat{T} = \hat{x}\,, \qquad \hat{T}\hat{p}\hat{T} = -\hat{p}\,, \qquad \hat{T}i\hat{T} = -i\,. \tag{5.66b}$$

Here i is the imaginary unit defined as $i = \sqrt{-1}$. Note that Eq. (5.66) only applies for the systems whose classical position x and momentum p are real. In the following, we shall restrict our discussions to these systems. From Eq. (5.66), we can find that $\hat{P}$ is a linear operator while $\hat{T}$ is antilinear, and $\hat{P}$ commutes with $\hat{T}$, i.e., $[\hat{P}, \hat{T}] = 0$. A PT symmetric $\hat{H}$ would also mean $[\hat{H}, \hat{P}\hat{T}] = 0$. Owing to the antilinear nature of $\hat{P}\hat{T}$, $\hat{H}$ and $\hat{P}\hat{T}$ may not share the same eigenfunction basis even though they commute with each other. Subsequently, a PT symmetric $\hat{H}$ is not sufficient to ensure a real energy eigenvalue. Real energy eigenvalues exist only if every eigenfunction of the parity-time (PT) symmetric $\hat{H}$ is also an eigenfunction of $\hat{P}\hat{T}$ simultaneously. This can be illustrated by a short deduction by first supposing that $\hat{H}$ and $\hat{P}\hat{T}$ share a common eigenfunction, which means

$$\hat{P}\hat{T}|\phi\rangle = \lambda|\phi\rangle\,, \tag{5.67a}$$

$$\hat{H}|\phi\rangle = E|\phi\rangle\,. \tag{5.67b}$$

Here $|\phi\rangle$ is the shared eigenfunction for both $\hat{H}$ and $\hat{P}\hat{T}$, and λ, E are the corresponding eigenvalues, respectively. Note that $(\hat{P}\hat{T})^2 = \mathbf{1}$, which leads to $\lambda^*\lambda = 1$. Thus the eigenvalue λ is nothing but a pure phase

$$\lambda = e^{i\theta}\,. \tag{5.68}$$

Without loss of generality, we now make a transformation on the eigenfunction by absorbing the phase factor given in Eq. (5.68)

$$|\psi\rangle = |\phi\rangle e^{i\theta}\,, \tag{5.69}$$

then the eigenequation (5.67) is modified to

$$\hat{P}\hat{T}|\psi\rangle = |\psi\rangle\,, \tag{5.70a}$$

$$\hat{H}|\psi\rangle = E|\psi\rangle\,. \tag{5.70b}$$

From Eq. (5.70), it is easy to know that

$$\hat{P}\hat{T}\hat{H}|\psi\rangle = \hat{P}\hat{T}E|\psi\rangle = E^*|\psi\rangle\,, \tag{5.71a}$$

$$\hat{H}\hat{P}\hat{T}|\psi\rangle = \hat{H}|\psi\rangle = E|\psi\rangle\,, \tag{5.71b}$$

since $[\hat{H}, \hat{P}\hat{T}] = 0$, we finally find from Eq. (5.71) that $E^* = E$, i.e., the eigenvalue of $\hat{H}$ is real. A PT symmetric H sharing a common eigenfunction basis is regarded as having an unbroken PT symmetry, leading to a complete real spectrum. Conversely, it is called that the PT symmetry of $\hat{H}$ is broken whenever it does not share the same eigenfunction basis with $\hat{P}\hat{T}$, and consequently complex eigenvalues enter in the spectrum [59]. Furthermore

$$\hat{H}\hat{P}\hat{T}|\psi'\rangle = \hat{P}\hat{T}\hat{H}|\psi'\rangle = \hat{P}\hat{T}E|\psi'\rangle = E^*\hat{P}\hat{T}|\psi'\rangle\,, \tag{5.72}$$

where $|\psi'\rangle$ is only the eigenfunction of $\hat{H}$. It is clear in Eq. (5.72) that if $|\psi'\rangle$ is an eigenfunction of the PT symmetric $\hat{H}$ associated with complex eigenvalue E then $\hat{P}\hat{T}|\psi'\rangle$ is also an eigenfunction of $\hat{H}$ with complex conjugate eigenvalue E^*. In other words, complex eigenvalues appear always in complex conjugate pairs in the energy spectrum.

Since the kinetic part of $\hat{H}$ commutes with $\hat{P}\hat{T}$, a PT symmetric Hamiltonian requires necessarily that the potential $V(x)$ presented in $\hat{H}$ should be symmetric under the successive actions of $\hat{P}$ and $\hat{T}$, i.e., $\hat{P}\hat{T}V(x) = V^*(-x) = V(x)$. In general, for a linear potential $V(x)$ which does not depend on the wave function, it is found that the spectrum is completely real if the ratio between the imaginary and real parts of the potential given in the Hamiltonian is below a certain threshold, while complex conjugate paired eigenvalues appear in the spectrum if the ratio exceeds this threshold. At the transition, the system can exhibit exceptional points [132, 167, 274–278], at which two or even more eigenstates coalesce. The word "coalesce" here means that both the eigenvalues and the eigenstates become identical. PT-symmetry has also been extended to diverse fields of theoretical physics, e.g., geometric phase in time-dependent PT-symmetric quantum mechanics [279, 280], quantum field theory [56, 59, 281–287], non-Hermitian Anderson models [288], open quantum systems [289, 290]. Although there are still ongoing debates on the impact of PT symmetry in those fields, the integration of PT-symmetry related notions to paraxial optics has triggered fascinating applications in optical systems such as coherent perfect absorber [115, 127–129], asymmetric power oscillation violating left-right symmetry [112, 113, 130–132], unidirectional invisibility in reflection at the exceptional point [114, 133–136], nonreciprocal light transmission such as optical isolator in the presence of nonlinearity [120, 137–139], Bloch oscillation, Bragg scattering, double or negative reflection and nonreciprocal diffraction in optical complex crystals [110, 111, 140–144], single-mode laser [116, 117] and loss-induced suppression and revival of lasing [118, 119]. PT-symmetric dynamics have also been recently investigated in atomic systems [145, 146]. It should be addressed here that the PT symmetric Hamiltonian could lead to possible contradiction [291] colliding with another physical assumption called non-signalling principle [96, 175, 180] in quantum entangled systems.

From the discussions above, one might be aware of the fact that PT symmetry is neither a necessary nor a sufficient condition for the Hamiltonian to have a real energy spectrum. Actually, there are non-Hermitian Hamiltonians which do not respect PT symmetry but can still have a real spectrum [292, 293]. It has stimulated further theoretical exploration on general characterization of non-Hermitian Hamiltonian with a real spectrum, Mostafazadeh has proven in a series of papers [60–62, 294, 295] that the necessary condition for the reality of the spectrum of a non-Hermitian Hamiltonian $\hat{H}$

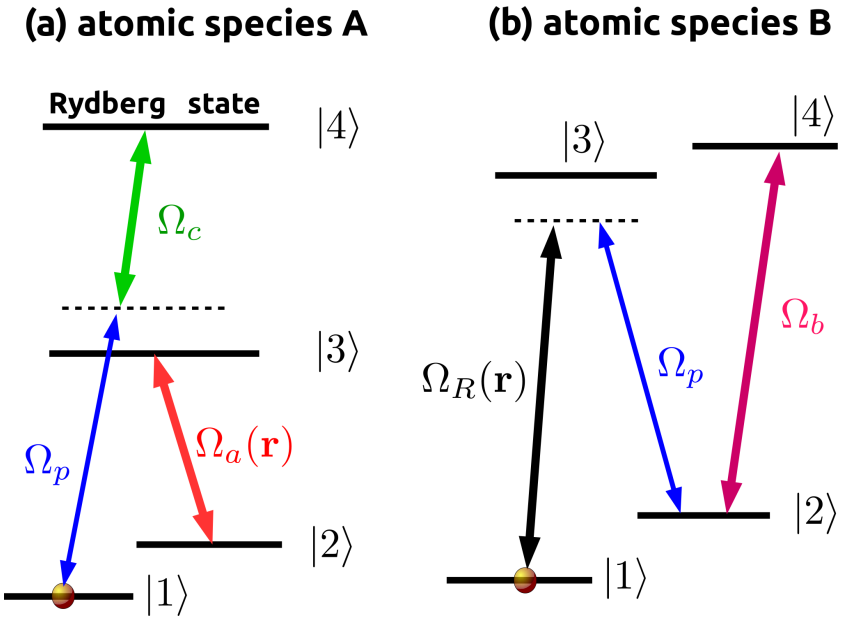

Figure 5.8: The schematic demonstration proposed to generate PT-symmetric periodical potential together with nonlocal nonlinear effects. In (a), atoms A have a four-level invert-Y-type level structure interacting with three laser fields, the probe Ω_p, the control Ω_c and the partial standing-wave field $\Omega_a(\mathbf{r})$. The probe and control fields form an EIT configuration in which the single-photon transitions are far-detuned for both fields. An auxiliary $\Omega_a(\mathbf{r})$ is then introduced to generate periodic modulation in the transverse plane. As a result, atoms A mainly give rise to a linear periodic dispersion and nonlocal nonlinear effects for the probe field. Moreover, atoms B involve a four-level N-type level structure driven by the same Ω_p, a partial stranding-wave Raman field $\Omega_R(\mathbf{r})$ and an additional coherent field Ω_b. The left three-level lambda system introduces an ARG process which leads to gain for the probe field, and it is further modified by Ω_b. In a word, atoms B are responsible for the linear periodic absorption for the probe field. Thus, the combination of atoms A and B results in a linear PT-symmetric periodic potential and nonlocal nonlinear effects for the probe field.

is that $\hat{H}$ must satisfy

$$\hat{H}^\dagger = \hat{\eta}\hat{H}\hat{\eta}^{-1}, \tag{5.73}$$

here $\hat{\eta}$ is a Hermitian invertible linear operator. $\hat{H}$ that fulfills Eq. (5.73) is termed as "pseudo Hermitian", and has a subsequent antilinear symmetry which is responsible for the presence of either real eigenvalues or complex conjugate pairs [62].

5.2.2 Optical periodic potential respecting parity-time symmetry

The considered system employed to produce parity-time symmetric potential is shown in Fig. 5.8. It consists of two different atomic species A and B which both populate on the ground state. In atomic species A, there is a four-level invert-Y-type level structure which includes a lower lambda electromagnetically induced transparency (EIT) configuration and a fourth high-lying Rydberg state which introduces the nonlocal nonlinear effects into the system via dipole-dipole interactions. It interacts with three external laser fields including a probe Ω_p, a control field Ω_c, and a partial standing wave $\Omega_a(\mathbf{r}) = \Omega_{a0}[1+\epsilon_a\cos(\mathbf{k}_a\cdot\mathbf{r})]$ ($\epsilon_a \ll 1$). The standing wave is formed in the transverse plane normal to the propagation direction. There is a large single-photon detuning for both probe and control fields in order to reduce the nonlocal nonlinear absorption introduced by the

dipole-dipole interactions, while the two-photon transition for the probe and control is chosen to be near resonant. In the far detuned regime, the linear and nonlinear dispersion would be the dominant role of atomic species A on the probe field. Furthermore, the near-resonant partial standing wave $\Omega_a(\mathbf{r})$ is then applied to trigger linear dispersion modulation. Atomic species B contains a four-level N-type level structure as shown in Fig. 5.8(b), interacting with also three laser fields which are the partial standing-wave Raman field $\Omega_R(\mathbf{r}) = \Omega_{R0}[1 + \epsilon_b \sin(\mathbf{k}_b \cdot \mathbf{r})]$ ($\epsilon_b \ll 1$), the probe Ω_p and an additional coherent field Ω_b. The left three-level lambda configuration forms an active-Raman gain (ARG) process which leads to gain for the probe field. The field Ω_b would further split the metastable state $|2\rangle$ into two sublevels and create two consequent ARG channels for the probe. Thus the main effect of atomic species B on the probe Ω_p would be gain, which is then periodically modulated by the standing Raman field $\Omega_R(\mathbf{r})$. Altogether, the atomic response is periodically modulated in both absorption and dispersion. Thus a parity-time symmetric potential can be possibly formed in the atomic systems when appropriate parameters are chosen. Actually, we have chosen ^{87}Rb and ^{85}Rb as atom species A and B, respectively, which are widely employed to implement experimental realizations.

As having generalized the idea how to create the parity-time symmetric potential above, we now proceed to calculate the atomic susceptibility for both atoms A and B from the master equation. For the i-th atom A, the interacting Hamiltonian is given by

$$\begin{aligned} H_{a,i} =& -\Omega_p \sigma_{31}^{a,i} - \Omega_c \sigma_{43}^{a,i} - \Omega_a(\mathbf{r}) \sigma_{32}^{a,i} + H.c. \\ & - (\Delta_{pa} - \Delta_a) \sigma_{22}^{a,i} - \Delta_{pa} \sigma_{33}^{a,i} - (\Delta_{pa} + \Delta_c) \sigma_{44}^{a,i} \\ & + \sum_{i<j} V_{ij}^a \sigma_{44}^{a,i} \sigma_{44}^{a,j} \,, \end{aligned} \tag{5.74}$$

here σ_{ij} is the atomic operator, Δ_{pa}, Δ_c and Δ_a are the single-photon detuning from the corresponding transitions for the three fields respectively. Furthermore, the last term in $H_{a,i}$ describes the dipole-dipole interactions in the high-lying Rydberg states, which would introduce the nonlocal nonlinear effects. Explicitly, here we choose V_{ij}^a as in Sec. 5.1

$$V_{ij}^a = \frac{C_6}{|\mathbf{r}_i - \mathbf{r}_j|^6} \,, \tag{5.75}$$

which is the van der Waals interaction [84]. Then the total Hamiltonian for atoms A interacting with laser fields reads

$$H_A = \sum_i H_{a,i} \,, \tag{5.76}$$

the equations of motion for the relevant density matrix elements for the i-th atom A follows

$$\frac{d\sigma_{13}^{a,i}}{dt} = i[-\Omega_p \sigma_{33}^{a,i} + \Omega_p \sigma_{11}^{a,i} + \Omega_a(\mathbf{r}) \sigma_{12}^{a,i} + \Delta_{13}^A \sigma_{13}^{a,i} + \Omega_c \sigma_{14}^{a,i}] \,, \tag{5.77a}$$

$$\frac{d\sigma_{12}^{a,i}}{dt} = i[-\Omega_p \sigma_{32}^{a,i} + \Omega_a(\mathbf{r}) \sigma_{13}^{a,i} + \Delta_{12}^A \sigma_{13}^{a,i}] \,, \tag{5.77b}$$

$$\frac{d\sigma_{14}^{a,i}}{dt} = i[-\Omega_p\sigma_{34}^{a,i} + \Omega_c\sigma_{13}^{a,i} + \Delta_{14}^{A}\sigma_{14}^{a,i} - \sum_{i<j} V_{ij}^{a}\sigma_{14}^{a,i}\sigma_{44}^{a,j}]\,, \tag{5.77c}$$

where we have set $\Delta_{13}^{A} = \Delta_{pa} + i\gamma_{13}^{A}, \Delta_{12}^{A} = \Delta_{pa} - \Delta_a + i\gamma_{12}^{A}$ and $\Delta_{14}^{A} = \Delta_{pa} + \Delta_c + i\gamma_{14}^{A}$, and γ_{ij}^{A} denotes the dephasing rate between the transition $|i\rangle \leftrightarrow |j\rangle$ for atom A. The steady-state solution of Eq. (5.77) can be obtained by first adiabatically eliminating the time evolution for $\sigma_{13}^{a,i}$ since the probe field is chosen to be far-detuned from the associated transition. Detailed procedures to calculate the atomic responses are quite similar to that done in Sec. 5.1, here we would rather give the final expression of the atomic susceptibility, while the detailed calculations is neglected. In particular, we have

$$\rho_{31}^{A}(\mathbf{r}) = \sum_i \langle\sigma_{13}^{a,i}\rangle = \rho_{31}^{A,\mathrm{L}}(\mathbf{r}) + \rho_{31}^{A,\mathrm{NL}}(\mathbf{r})\,, \tag{5.78a}$$

$$\rho_{31}^{A,\mathrm{L}}(\mathbf{r}) = \frac{\Delta_{12}^{A}\Delta_{14}^{A}n_A\Omega_p(\mathbf{r})}{M}\,, \tag{5.78b}$$

$$\rho_{31}^{A,\mathrm{NL}}(\mathbf{r}) = -\frac{(\Delta_{12}^{A})^2|\Delta_{12}^{A}|^2 n_A^2\Omega_c^4\Omega_p(\mathbf{r})}{M|M|^2}\int \frac{V(\mathbf{r}-\mathbf{r}')|\Omega_p(\mathbf{r}')|^2 d^3\mathbf{r}'}{[\Omega_a^2(\mathbf{r}) - \Delta_{12}^{A}\Delta_{13}^{A}][\Delta_{14} - V(\mathbf{r}-\mathbf{r}')] + \Delta_{12}^{A}\Omega_c^2}\,, \tag{5.78c}$$

with $M = \Delta_{14}^{A}(\Omega_a^2(\mathbf{r}) - \Delta_{12}^{A}\Delta_{13}^{A}) + \Delta_{12}^{A}\Omega_c^2$. Here $\rho_{31}^{A,\mathrm{L}}$ stands for the linear response for atoms A, and $\rho_{31}^{A,\mathrm{NL}}$ represents the nonlocal nonlinear effects induced by the dipole-dipole interactions. Note that ρ_{31}^{A} is reduced to the results obtained in [25] by setting $\Omega_a(\mathbf{r}) = 0$.

With a similar procedure, the equations of motion for the related density matrix elements of atoms B can be derived

$$\dot{\rho}_{12}^{B} = i[\Omega_R(\mathbf{r})\rho_{32}^{B} - \Omega_p\rho_{13}^{B} - \Omega_b\rho_{14}^{B}] + i\Delta_{12}^{B}\rho_{12}^{B}\,, \tag{5.79a}$$

$$\dot{\rho}_{13}^{B} = i[\Omega_R(\mathbf{r})\rho_{33}^{B} - \Omega_R(\mathbf{r})\rho_{11}^{B} - \Omega_p\rho_{12}^{B}] + i\Delta_{13}^{B}\rho_{13}^{B}\,, \tag{5.79b}$$

$$\dot{\rho}_{32}^{B} = i[\Omega_R(\mathbf{r})\rho_{12}^{B} + \Omega_p\rho_{22}^{B} - \Omega_p\rho_{33}^{B} - \Omega_b\rho_{34}^{B}] + i\Delta_{32}^{B}\rho_{32}^{B}\,, \tag{5.79c}$$

$$\dot{\rho}_{14}^{B} = i[\Omega_R(\mathbf{r})\rho_{34}^{B} - \Omega_b\rho_{12}^{B}] + i\Delta_{14}^{B}\rho_{14}^{B}\,, \tag{5.79d}$$

$$\dot{\rho}_{34}^{B} = i[\Omega_R(\mathbf{r})\rho_{14}^{B} + \Omega_p\rho_{24}^{B} - \Omega_b\rho_{32}^{B}] + i\Delta_{34}^{B}\rho_{34}^{B}\,, \tag{5.79e}$$

then we can calculate the steady-state solution of Eq. (5.79), which reads

$$\rho_{32}^{B}(\mathbf{r}) = -\frac{n_B\rho_{13}^{B}[\Omega_b^2 - \Omega_R^2(\mathbf{r}) + \Delta_{14}^{B}\Delta_{34}^{B}]\Omega_R(\mathbf{r})\Omega_p(\mathbf{r})}{\Delta_{12}^{B}\Delta_{32}^{B}\Delta_{14}^{B}\Delta_{34}^{B} - Q_1\Omega_b^2 - Q_2\Omega_R^2(\mathbf{r}) + [\Omega_R^2(\mathbf{r}) - \Omega_b^2]^2}\,, \tag{5.80}$$

where $\rho_{13}^{B} = \Omega_R(\mathbf{r})/\Delta_{13}^{B}, \Delta_{13}^{B} = -\Delta_R + i\gamma_{13}^{B}, \Delta_{12}^{B} = \Delta_{pb} - \Delta_R + i\gamma_{12}^{B}, \Delta_{32}^{B} = \Delta_{pb} + i\gamma_{32}^{B}, \Delta_{14}^{B} = \Delta_{pb} - \Delta_R - \Delta_b + i\gamma_{14}^{B}, \Delta_{34}^{B} = \Delta_{pb} - \Delta_b + i\gamma_{34}^{B}$, $Q_1 = \Delta_{12}^{B}\Delta_{14}^{B} + \Delta_{32}^{B}\Delta_{34}^{B}$ and $Q_2 = \Delta_{12}^{B}\Delta_{32}^{B} + \Delta_{14}^{B}\Delta_{34}^{B}$. As before, here Δ_R, Δ_{pa} and Δ_b are the associated single-photon detuning for the Raman, probe and additional coherent fields in atoms B respectively, and γ_{ij}^{B} is the dephasing rate for the corresponding transition.

Finally, we find that the atomic effects from both atoms A and B on the probe field

can be written as

$$\rho(\mathbf{r}) = \rho_{\mathrm{L}}(\mathbf{r}) + \rho_{\mathrm{NL}}(\mathbf{r}) , \tag{5.81a}$$

$$\rho_{\mathrm{L}}(\mathbf{r}) = \rho_{31}^{A,\mathrm{L}}(\mathbf{r}) + \rho_{32}^{B}(\mathbf{r}) , \tag{5.81b}$$

$$\rho_{\mathrm{NL}}(\mathbf{r}) = \rho_{31}^{A,\mathrm{NL}}(\mathbf{r}) . \tag{5.81c}$$

Before we proceed to investigate physical properties of the system in a deeper level, we first make a transformation of the paraxial propagation equation (2.26) which describes the probe propagation dynamics in atomic systems as

$$i\frac{\partial\psi(\boldsymbol{\xi},\zeta)}{\partial\zeta} = -\frac{\partial^2\psi(\boldsymbol{\xi},\zeta)}{\partial\boldsymbol{\xi}^2} + V_{\mathrm{L}}(\boldsymbol{\xi})\psi(\boldsymbol{\xi},\zeta) - C_{nl}\int_{-\infty}^{\infty} K_s(\boldsymbol{\xi}-\boldsymbol{\xi}')|\psi(\boldsymbol{\xi}',\zeta)|^2 d\boldsymbol{\xi}' , \tag{5.82}$$

where we have rescaled the coordinates $\boldsymbol{\xi} = \mathbf{r}_\perp/S_t, \zeta = z/S_z$ and $S_z = 2\mathrm{k}_p S_t^2$, with S_t and S_z being the scales in the transverse and propagation directions, respectively, and we have also set $\Omega_p(\boldsymbol{\xi},\zeta) = \Omega_{p0}\psi(\boldsymbol{\xi},\zeta)$. As discussed in Sec. 5.1, Eq. (5.82) correctly describes the propagation dynamics for the probe field in the far-detuned regime, i.e., $\Delta_{pa}, \Delta_c \ll \Gamma_{31}$. Furthermore, we consider the two partial standing waves residing in the transverse plane, i.e., $\mathbf{k}_a \cdot \vec{\mathbf{e}}_z = 0$ and $\mathbf{k}_b \cdot \vec{\mathbf{e}}_z = 0$. Other quantities given in Eq. (5.82) are as following

$$C_{nl} \simeq -\frac{3\lambda_p^2\Gamma_{31}(\Delta_{12}^A)^2|\Delta_{12}^A|^2 n_A^2\Omega_c^4\Omega_{p0}^2 S_t^3 S_z R_c}{8\pi M|M|^2(\Delta_{pa}^2-\Omega_{a0}^2)} , \tag{5.83a}$$

$$K_s(\boldsymbol{\xi}) \simeq \int_{-\infty}^{\infty} \frac{1}{1+\mathrm{Sign}[Q][(\frac{S_t\boldsymbol{\xi}}{R_c})^2+\zeta^2]^3+i\delta} d\zeta , \tag{5.83b}$$

$$Q = \frac{\Delta_{pa}\Omega_c^2 - \Delta_1(\Delta_{pa}^2-\Omega_{a0}^2)}{C_6(\Delta_{pa}^2-\Omega_{a0}^2)} , \tag{5.83c}$$

$$\delta = \frac{\gamma_{13}^A\Delta_{pa}}{\Delta_{pa}^2-\Omega_{a0}^2} , \tag{5.83d}$$

and $R_c = |Q|^{\frac{1}{6}}$ is the blockade radius for the interacting Rydberg atoms, Sign$[Q]$ stands for the sign function. In the nonlocal integral of Eq. (5.82), we have also applied the local approximation for the probe field in the propagation direction which is valid at the far-detuning regime, specifically, $\psi(\boldsymbol{\xi}',\zeta') \simeq \psi(\boldsymbol{\xi}',\zeta)$ as in Ref. [25]. Furthermore, for $\epsilon_a \ll 1$, the position-dependent part of $\Omega_a(\mathbf{r})$ is several orders of magnitude smaller than the other terms in the nonlocal nonlinear response $K_s(\boldsymbol{\xi})$ and thus has been neglected. And considering the symmetric nature of $K_s(\boldsymbol{\xi})$ and the subsequent symmetry of Eq. (5.82), we then focus on the one-dimensional dynamics, i.e., $\boldsymbol{\xi} \to \xi$. In the far-detuned regime we have $\delta \ll 1$, which indicates an insignificant nonlocal nonlinear absorption.

It is evident that the paraxial propagation equation (5.82) is mathematically equivalent to the Schrödinger equation including nonlocal nonlinear effects, with the optical Hamiltonian defined by

$$H = -\frac{\partial^2}{\partial\xi^2} + V_{\mathrm{L}}(\xi) + V_{\mathrm{NL}}(\xi,\zeta) , \tag{5.84a}$$

$$V_{\mathrm{L}}(\xi) = -\frac{3\lambda_p^2\Gamma_{21}S_z}{8\pi\Omega_p(\xi,\zeta)}[\rho_{31}^{A,\mathrm{L}}(\xi)+\rho_{32}^{B}(\xi)]\,, \tag{5.84b}$$

$$V_{\mathrm{NL}}(\xi,\zeta) = -C_{nl}\int_{-\infty}^{\infty} K_s(\xi-\xi')|\psi(\xi',\zeta)|^2 d\xi'\,. \tag{5.84c}$$

We first consider that the amplitude of the probe field is so weak such that $V_{\mathrm{NL}}(\xi)\simeq 0$, thus the optical Hamiltonian for the system reads

$$H = -\frac{\partial^2}{\partial\xi^2} + V_{\mathrm{L}}(\xi)\,. \tag{5.85}$$

As we discussed in the previous section, a PT symmetric H necessarily requires the relation for the potential

$$V_{\mathrm{L}}(\xi) = V_{\mathrm{L}}^{*}(-\xi)\,. \tag{5.86}$$

In order to create a PT symmetric potential which satisfy Eq. (5.86), we first expand the two terms in $V_{\mathrm{L}}(\xi)$ in orders of ϵ_a, ϵ_b respectively

$$\rho_{31}^{A,\mathrm{L}}(\xi) = \rho_{31}^{A,\mathrm{L0}} + \rho_{31}^{A,\mathrm{L1}}\cos(k_a\xi) + \rho_{31}^{A,\mathrm{L2}}\cos^2(k_a\xi) + \cdots\,, \tag{5.87a}$$

$$\rho_{32}^{B}(\xi) = \rho_{32}^{B,0} + \rho_{32}^{B,1}\sin(k_b\xi) + \rho_{32}^{B,2}\sin^2(k_b\xi) + \cdots\,, \tag{5.87b}$$

where ϵ_a and ϵ_b have been absorbed into the related coefficients. Ideally, a PT symmetric potential can be formed when

$$\mathrm{Im}[\rho_{31}^{A,\mathrm{L0}} + \rho_{32}^{B,0}] = 0\,, \tag{5.88a}$$

$$\mathrm{Im}[\rho_{31}^{A,\mathrm{L}n}] = 0 \quad \text{for} \quad n \geq 1\,, \tag{5.88b}$$

$$\mathrm{Re}[\rho_{32}^{B,n}] = 0 \quad \text{for odd } n \text{ and } n \geq 1\,, \tag{5.88c}$$

$$\mathrm{Im}[\rho_{32}^{B,n}] = 0 \quad \text{for even } n \text{ and } n \geq 1\,. \tag{5.88d}$$

Then, $\rho_{\mathrm{L}}(\mathbf{r})$ is modified to

$$\begin{aligned}\rho_{\mathrm{L}}(\xi) =& \mathrm{Re}[\rho_{31}^{A,\mathrm{L0}} + \rho_{32}^{B,0}] + \mathrm{Re}[\rho_{31}^{A,\mathrm{L1}}]\cos(k_a\xi) + \mathrm{Re}[\rho_{31}^{A,\mathrm{L2}}]\cos^2(k_a\xi) + \cdots \\ & i\mathrm{Im}[\rho_{32}^{B,1}]\sin(k_b\xi) + \mathrm{Re}[\rho_{32}^{B,2}]\sin^2(k_b\xi) + i\mathrm{Im}[\rho_{32}^{B,3}]\sin^3(k_b\xi) + \cdots\,.\end{aligned} \tag{5.89}$$

We can easily find that $\rho_{\mathrm{L}}(\xi) = \rho_{\mathrm{L}}^{*}(-\xi)$ in the equation above. Practically, it is of course difficult to satisfy all the conditions given in Eqs. (5.88). Alternatively, we concern about the first two contributions of the expansions which play the main role in $V_{\mathrm{L}}(\xi)$, the high-order effects are much smaller and thus can be neglected. It then results in a much simplified version of Eqs. (5.88)

$$\mathrm{Im}[\rho_{31}^{A,\mathrm{L0}} + \rho_{32}^{B,0}] = 0\,, \tag{5.90a}$$

$$\mathrm{Re}[\rho_{31}^{A,\mathrm{L1}}],\ \mathrm{Im}[\rho_{32}^{B,1}] \gg \mathrm{Im}[\rho_{31}^{A,\mathrm{L1}}],\ \mathrm{Re}[\rho_{32}^{B,1}]\,. \tag{5.90b}$$

In order to minimize the higher-order contributions, further constraints should be also

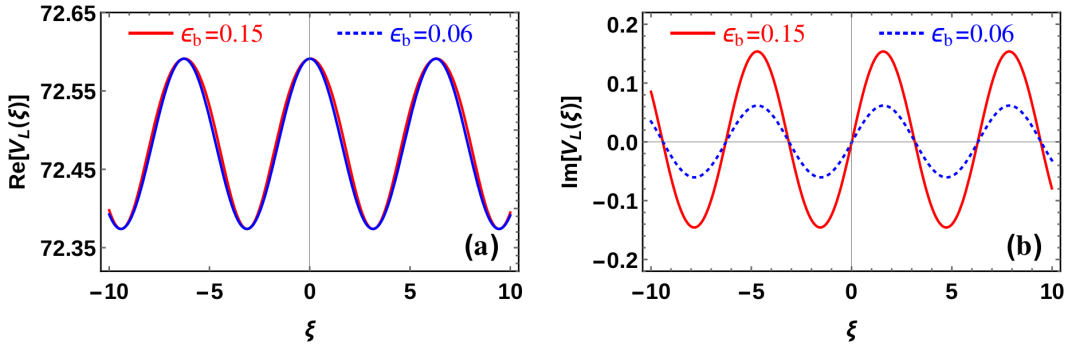

Figure 5.9: The real (a) and imaginary (b) parts of the parity-time symmetric optical potential $V_{\rm L}(\xi)$ formed in the atomic systems consisting of passive atoms A and active atoms B. Relevant parameters are: $\gamma_{13}^A = \Gamma_{31}/2, \gamma_{12}^A = 0, \gamma_{14}^A = 0.01\Gamma_{31}, \Omega_c = 5.0\Gamma_{31}, \Delta_c = -80\Gamma_{31}, \Omega_{a0} = 15.0\Gamma_{31}, \Delta_a = 0, \Delta_{pa} = -\Delta_c + \Delta_1, \Delta_1 = -4.0\Gamma_{31}, \gamma_{13}^B = \gamma_{23}^B = \gamma_{14}^B = \Gamma_{31}/2, \gamma_{12}^B = 0, \gamma_{34}^B = \Gamma_{31}, \Omega_R = 4.7\Gamma 31, \Omega_b = 0.5\Gamma_{31}, \Delta_b = 0, \Delta_{pb} = \Delta_{pa} + \Delta_D, \Delta_R = \Delta_{pb} + \Delta_2, \Delta_2 = -0.52\Gamma 31, \Delta_D = 3.0357$ GHz$, \Gamma_{31} = 2\pi \times 6.0$ MHz$, \lambda_p = 7.94767 \times 10^{-7}$ $m, C_6 = 140.0$ GHz $\cdot\ \mu m^6, n_0 = 5.0 \times 10^{19}$ $m^{-3}, n_A = \eta_A n_0, n_B = \eta_B n_0, \eta_A = 0.966896, \eta_B = 0.033104, S_t = 10.0$ $\mu m, k_a = k_b = 2\pi/S_t$. In addition, we have $\epsilon_a = 0.02$, and ϵ_b is given in both (a) and (b).

added

$$\mathrm{Re}[\rho_{31}^{A,\mathrm{L}1}],\ \mathrm{Im}[\rho_{31}^{B,1}] \gg |\rho_{31}^{A,\mathrm{L}2}|,\ |\rho_{32}^{B,2}|\,. \tag{5.91}$$

After satisfying these two conditions (5.90) and (5.91), we then finally plot the real and imaginary parts of $V_{\rm L}(\xi)$ in Fig. 5.9 for two different cases where ϵ_b are different. Indeed, $V_{\rm L}(\xi)$ in Fig. 5.9 is PT symmetric for both cases. Note that the real parts in (a) are not exactly identical to each other owing to the higher-order effects. And again, the higher-order effects are insignificant here and have little to do with the PT-symmetric dynamics.

5.2.3 Band structure of the optical system

According to the Bloch theorem, the eigenfunctions of the wave function for a periodic potential can be written as $\psi_k(\xi) = u_k(\xi)e^{ik\xi}$, in which k is the Bloch wave number and

$$u_k(\xi) = \sum_n C_n(k)e^{inG_0\xi}\,, \tag{5.92}$$

has the periodicity equal to the potential. And the eigenvalues of the system, which is known as the band structure, should be also periodical in the reciprocal space. Here G_0 is the reciprocal wavevector defined as $G_0 = \mathrm{Max}(k_a, k_b)$. Then the eigenvalue equation for Eq. (5.82) reads

$$\beta\psi_k(\xi) = -\frac{\partial^2\psi_k(\xi)}{\partial\xi^2} + V_{\rm L}(\xi)\psi_k(\xi) - C_{nl}\int_{-\infty}^{\infty} K_s(\xi-\xi')|\psi_k(\xi')|^2 d\xi'\,, \tag{5.93}$$

where β is the eigenvalue of the system, which is also called the propagation constant in the context of optics. Note that for real β, $\psi(\xi,\zeta) = \psi_k(\xi)e^{-i\beta\zeta}$ is the exact solution for the nonlocal nonlinear Schrödinger equation (5.82). However, for complex β, $\psi(\xi,\zeta) = \psi_k(\xi)e^{-i\beta\zeta}$ represents only an adiabatic approximation to Eq. (5.82) [182, 183]. Applying

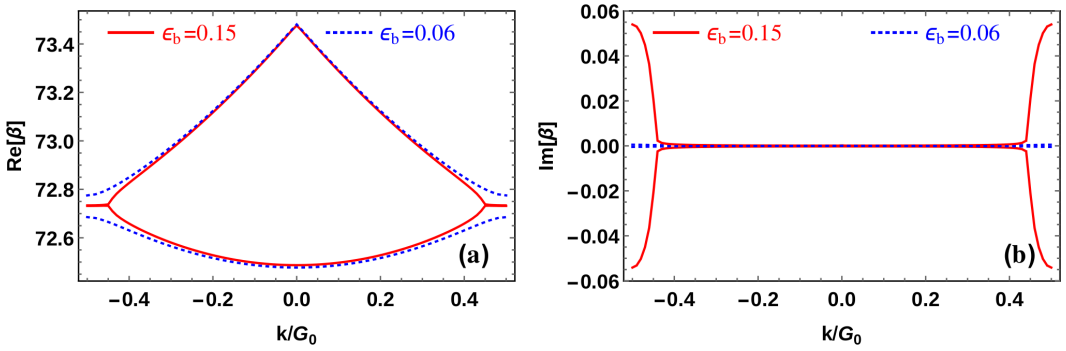

Figure 5.10: The eigenvalues in the first Brillion zone for the linear PT symmetric periodic potential in Fig. 5.9. Here we only show the first two bands. For small $\epsilon_b = 0.06$, the band structure is purely real, corresponding to an unbroken PT-symmetric phase. However, when ϵ_b increases to 0.15, complex values arise from the band edge, relating to a broken PT-symmetric phase. Parameters are the same as in Fig. 5.9.

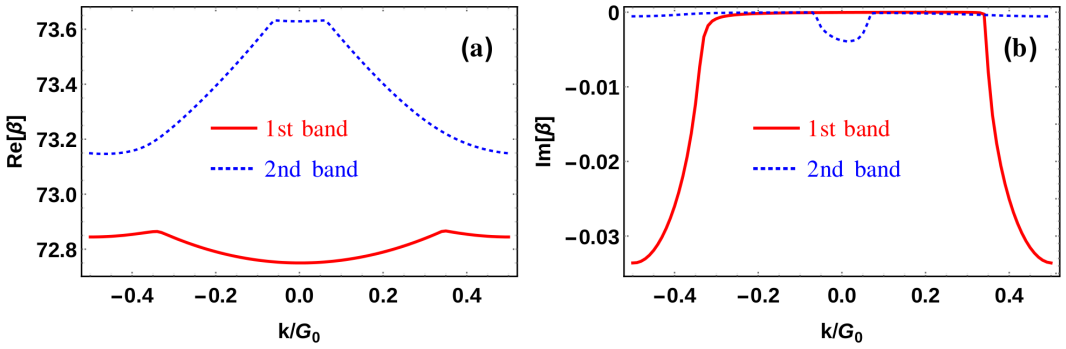

Figure 5.11: The eigenvalues in the first two bands in the first Brillion zone for the optical potential in the presence of the nonlocal nonlinear effects. In (a), the real parts of the eigenvalues exhibit repulsion between the first two bands, while the associated imaginary values emerge in the edge of the first band and in the center of the second band as in (b). Parameter are $\epsilon_b = 0.06$ and $\Omega_{p0} = 0.1\Gamma_{31}$, others are the same as in Fig. 5.9.

the Bloch theorem to Eq. (5.93), it results in the central equation as derived in Sec. 2.3.3

$$C_n(k)[(k+nG_0)^2-\beta] - \sum_m C_{n-m}(k)V_m = C_{nl}\sum_{p,q} C_{n-p+q}(k)C_p(k)C_q^*(k)K_F[(p-q)G_0]\,, \tag{5.94}$$

where V_m is the m-th Fourier coefficient of the linear potential $V_{\mathrm{L}}(\xi)$, and $K_F(nG_0)$ is the n-th Fourier transform of $K_s(\xi)$ which is defined by

$$K_F(nG_0) = \int_{-\infty}^{\infty} K_s(\xi)e^{-inG_0\xi}d\xi\,. \tag{5.95}$$

In order to obtain the eigenvalues and eigenfunctions, we have to calculate Eq. (5.94) for each k in the first Brillion zone. In general, it turns out to be very challenging to solve Eq. (5.94) when the nonlocal nonlinear effects are present. For a first taste of the properties of the band structure, we now solve Eq. (5.94) in the linear regime where $C_{nl} \to 0$. The practical calculation is done by first truncating the infinite set of Eq. (5.94) to a certain reasonable limit, beyond which it can be neglected. Here we

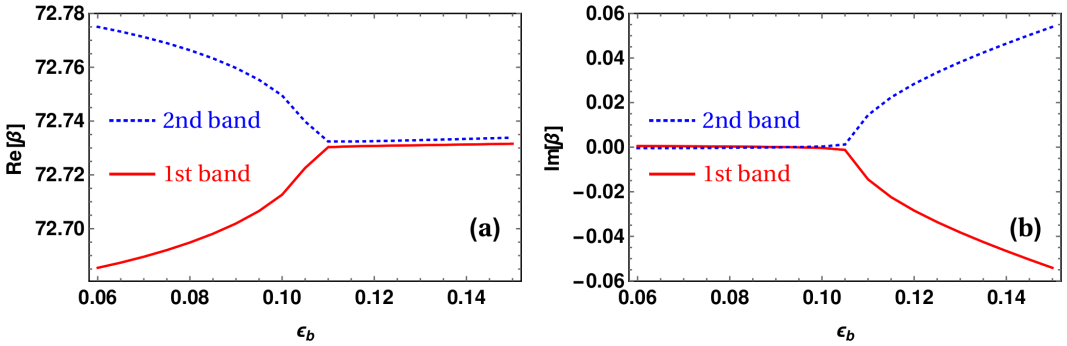

Figure 5.12: The eigenvalues of the Bloch wave number $k = 0.5G_0$ against ϵ_b for the linear potential. Here we only show the first two bands. Phase transition occurs at $\epsilon_b \simeq 0.11$. Below this threshold, the system remains in an unbroken PT-symmetric phase, otherwise it is related to a broken phase. Parameters are the same as in Fig. 5.9.

choose $n_{\max} = 2$ and the results are shown in Fig. 5.10 for the first two bands. Note that the results is further checked and compared to the ones obtained at a larger $n_{\max} = 3$, and they indeed give the same results. It can be seen that the band structure is purely real when a relatively small imaginary part of $V_{\rm L}(\xi)$ is chosen, i.e., $\epsilon_b = 0.06$. This refers to an unbroken PT-symmetry phase, and the resulting propagation dynamics of the system would be constant except for a linearly growing phase. However, for a larger $\epsilon_b = 0.15$, paired complex values appear firstly in the edge of the band structure, which means that the PT-symmetry of the system is broken at the edge states. The appearance of complex eigenvalues is associated to a phase transition of the system. For even larger ϵ_b, the band structure will be completely complex.

In contrast to the linear case, the calculation of the band structure turns out to be much more complicated since the central equation (5.94) involves the eigenfunction itself when the nonlocal nonlinear effects are presented. Usually, a self-consistent field theory is employed to solve Eq. (5.94) iteratively to obtain the eigenvalues and eigenfunctions. Specifically, the self-consistent calculation guarantees that the calculated eigenfunction $\psi_k(\xi)$ would satisfy the central equation Eq. (5.94) including the nonlocal nonlinear effects generated by $\psi_k(\xi)$ itself. We then apply the second Broyden method [194, 195] to perform the self-consistent calculation, the obtained band structure for $\epsilon_b = 0.06$ is shown in Fig. 5.11 for the first two bands. Compared to the band structure attained in the linear potential as shown in Fig. 5.10, it is evident that complex values emerge in both bands owing to the nonlocal nonlinear effects. In more detail, the real parts of the two bands seems to be repulsed from each other, meanwhile, the corresponding imaginary parts turn to be asymmetric. Consequently, it can be seen that the complex values are not paired any more as compared to the ones in linear potential.

5.2.4 Phase transition from unbroken to broken PT-symmetry

From the results obtained in the previous section, it is evident that phase transition occurs when either increasing the imaginary part of $V_L(\xi)$ or the nonlocal nonlinear effects to a critical value. In order to shown this in more detail, we then calculate the eigenvalues for a specific Bloch wave number $k = 0.5G_0$ at the first two bands against ϵ_b in the regime of $C_{nl} \simeq 0$. The reason why we chose $k = 0.5G_0$ in the edge is due to the observation that it is the first wave number whose associated eigenvalue evolves from real to complex as already indicated in both Fig. 5.10 and 5.11. The results are shown

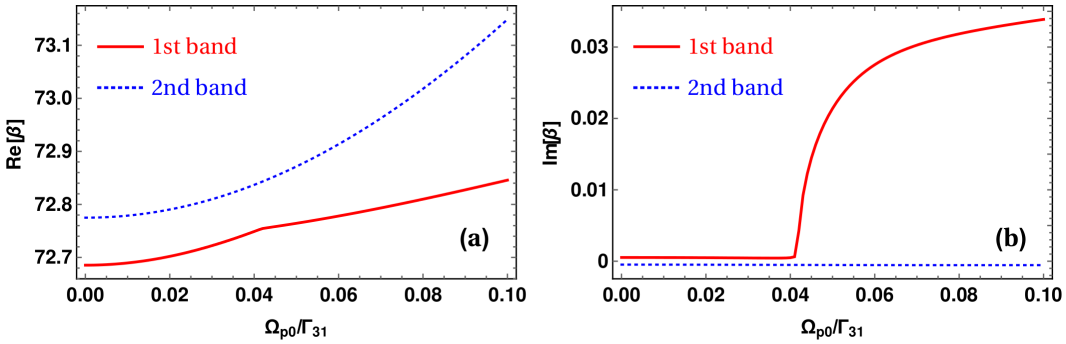

Figure 5.13: The eigenvalues of the Bloch wave number $k = 0.5G_0$ for the optical potential with the nonlocal nonlinear effects against Ω_{p0}. Phase transition can be also induced by the nonlocal nonlinear effects, and the critical value for the transition is of $\Omega_{p0} \simeq 0.042\Gamma_{31}$. Here we have chosen $\epsilon_b = 0.06$, and other parameters are the same as in Fig. 5.9.

in Fig. 5.12, in which complex eigenvalues start to appear approximately at $\epsilon_b \simeq 0.11$. At this critical point, the real part of the linear potential is equal to its imaginary part in magnitude. It also refers to an exceptional point [132, 167, 274–278]. When the nonlocal nonlinear effects are presented, we further calculate the eigenvalues for the same Bloch wave number $k = 0.5G_0$ in the first two bands against the initial amplitude of its eigenfunction, which is given in Fig. 5.13. It can bee found that complex eigenvalues start to arise approximately around $\Omega_{p0} \simeq 0.042\Gamma_{31}$, which is the critical value of Ω_{p0} for the phase transition. Below this point, the PT symmetry is preserved, otherwise it gives a broken PT symmetry. Furthermore, the phase transition behaves differently between the linear and nonlocal nonlinear cases. In the linear case, the complex eigenvalues appear always in pair after the transition, i.e., $\epsilon_b > 0.11$. However, in the nonlocal nonlinear case, only the first band has complex eigenvalues when $\Omega_{p0} > 0.042\Gamma_{31}$, meanwhile, the second band still remains in a preserved PT-symmetric phase. Note that there is a small deviation from zero for the imaginary parts of the eigenvalues below $\epsilon_b \simeq 0.11$ in Fig. 5.12(b) and below $\Omega_{p0} \simeq 0.042\Gamma_{31}$ in Fig. 5.13(b), this is due to higher-order effects of the applied standing-wave fields $\Omega_a(\mathbf{r})$ and $\Omega_R(\mathbf{r})$. For the same reason, the real parts of the eigenvalues in the two bands shown in Fig. 5.12(a) also differ from each other for a small value when $\epsilon_b > 0.11$.

5.2.5 Broken or unbroken PT-symmetric propagation dynamics

As we have already obtained the band structure in the previous section, now we move to investigate the propagation dynamics in the linear PT-symmetric periodic potential. For doing this, we numerically solve Eq. (5.82) by first excluding the nonlocal nonlinear effects ($C_{nl} \to 0$), however, all the higher-order effects in the linear potential are included. Our numerical results are given in Fig. 5.14. Fig. 5.14(a) depicts the eigenfunction in the first band with Bloch wave number $k = 0.5G_0$ propagating in the linear potential when $\epsilon_b = 0.15$. Owing to the associated complex eigenvalue, the PT-symmetry of the system is broken, and the eigenfunction is decaying with exponential rate determined by the imaginary part of the eigenvalue. For smaller $\epsilon_b = 0.06$, the eigenfunction in the same band with the same Bloch wave number propagates in a stationary state in the linear potential owing to the unbroken PT-symmetric phase of the system.

Next, we numerically calculate Eq. (5.82) in the presence of nonlocal nonlinear effects, the results are depicted in Fig. 5.15. As we can see, since the eigenvalue for Bloch wave

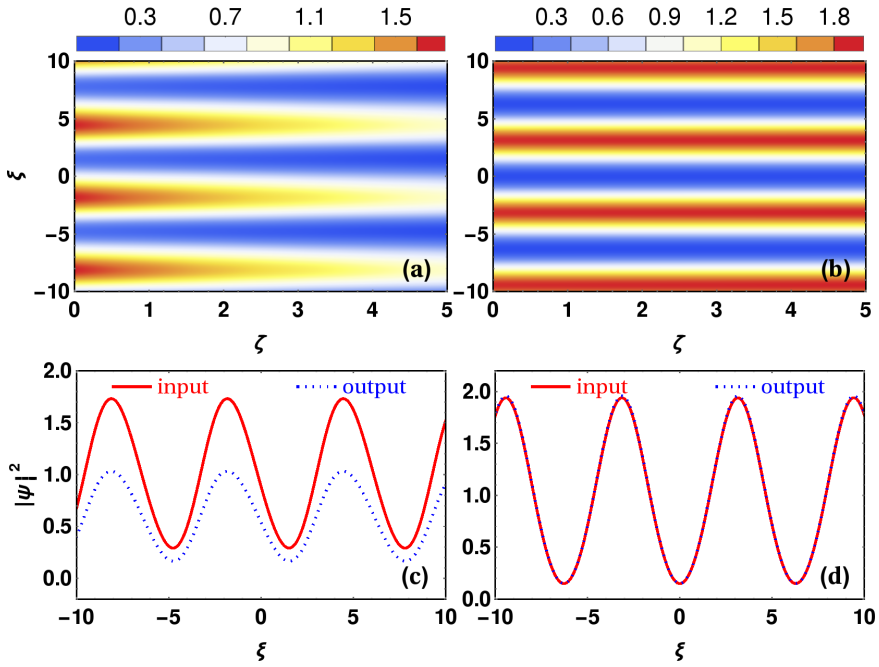

Figure 5.14: Propagation dynamics in the linear PT-symmetric periodic potential. (a) shows the probe propagation with a broken PT-symmetry phase when $\epsilon_b = 0.15$, and the output is given in (c). Probe propagation with a preserved PT-symmetry phase is illustrated in (b) for $\epsilon_b = 0.06$, and (d) gives the output of the probe field. The input profile of the probe is an eigenfunction in the first band with the Bloch wave number $k = 0.5G_0$ for both (a) and (b). Note that the eigenfunctions are in principle different from each other for different ϵ_b. Other parameters are the same as in Fig. 5.9.

number $k = 0.5G_0$ in the first band is now turned to be complex, the PT symmetry is broken in this case, and the associated eigenfunction cannot propagate constantly. Furthermore, it does not experience a simply exponentially growing or decaying behavior as in the linear case, instead, it propagates in an oscillating manner as shown in Fig. 5.15(a). This oscillation is attributed to the competition between the linear and nonlocal nonlinear effects. For comparison, we also calculated the propagation dynamics for the eigenfunction with the same Bloch wave number but in the second band, as shown in Fig. 5.15(b), in which it is evident to see the constant propagation because of the unbroken PT symmetry of the system. To understand better the oscillating behavior illustrated in Fig. 5.15(a), we employ the Fourier transform to analyze the propagation dynamics further. The coefficients of different wave components against the propagation distance are shown in Fig. 5.16. It is obvious to see that $|C_0|$ and $|C_{-1}|$ which have the largest amplitudes and thus contribute mostly to the propagation dynamics are mainly governed by the linear effects. Meanwhile, the other two weaker components $|C_{-1}|$ and $|C_{-2}|$ are mainly affected by the nonlocal nonlinear effects. Moreover, $|C_{-1}|$ exhibit an oscillating behavior in an almost linearly-growing background as shown in Fig. 5.16(c). The underlying physical mechanisim can be understood by first deriving the equations of motion for the coefficients

$$\begin{aligned} i\frac{dC_n(\zeta)}{d\zeta} =& (k+nG_0)^2 C_n(k,\zeta) + \sum_m V_m C_{n-m}(\zeta) \\ & - C_{nl} \sum_{p,q} C_{n-p+q}(\zeta) C_p(\zeta) C_q^*(\zeta) K_F[(p-q)G_0]\,, \end{aligned} \tag{5.96}$$

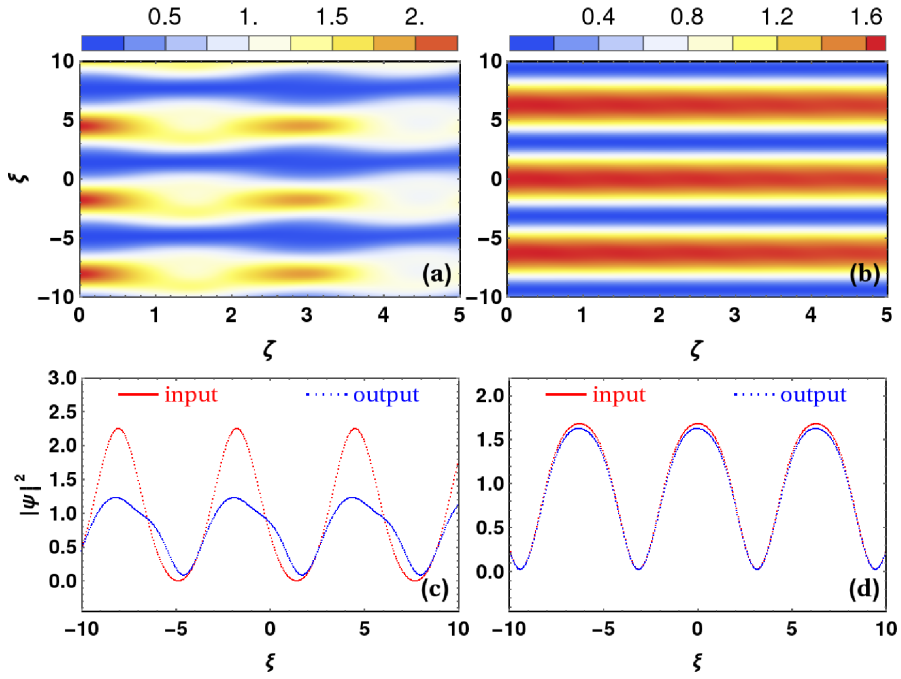

Figure 5.15: Propagation dynamics in the optical potential in the presence of nonlocal nonlinear effects. (a) shows the probe propagation with a broken PT-symmetry phase when the input is chosen to be the eigenfunction for Bloch wave number $k = 0.5G_0$ in the first band, and the output of the probe is given in (c). Probe propagation with an unbroken PT-symmetry phase is plotted in (b) when the input is chosen to be the eigenfunction for the same Bloch wave number in the second band, and (d) gives the output. Here we choose $\epsilon_b = 0.06$ and $\Omega_{p0} = 0.1\Gamma_{31}$, and other parameters are the same as in Fig. 5.9.

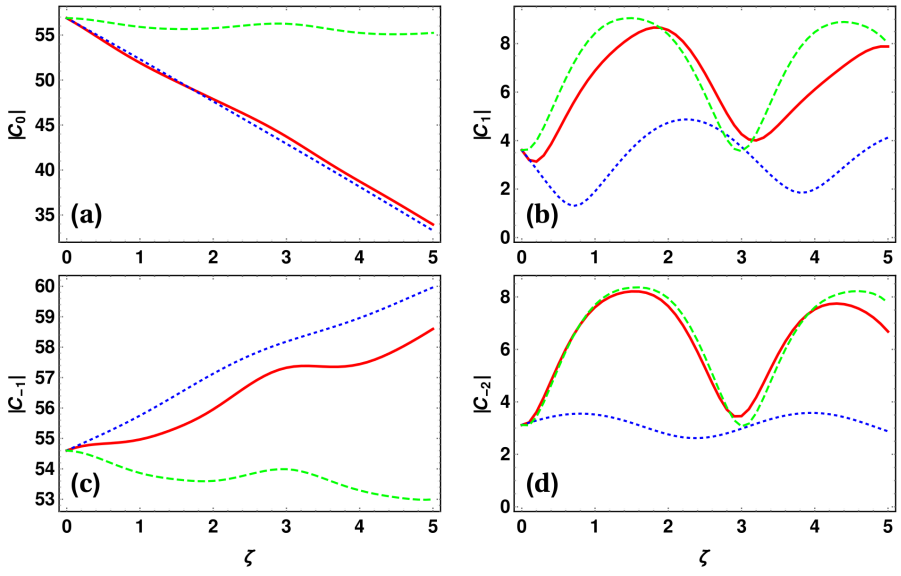

Figure 5.16: Fourier analysis of the propagation dynamics presented in Fig. 5.15(a). Here the red solid lines in (a)-(d) stand for the evolution of coefficient C_n against propagation distance, respectively, and the blue dotted lines represent C_n in the case when setting $C_{nl} = 0$ artificially in the numerical simulations, and the green dashed lines are C_n when manually setting $V_L(\xi) = 0$. Parameters are the same as in Fig. 5.15. Note that here we didn't plot C_2 since its value is much smaller than the other four coefficients and can be neglected.

where we have assumed $\psi(\xi,\zeta)=\sum_n C_n(\zeta)e^{i(nG_0+k)\xi}$. As we can find from Fig. 5.9, the zeroth Fourier component of $V(\xi)$, i.e., V_0 is much larger than the other components V_m ($m\neq 0$). Furthermore, $C_0(\zeta=0)$ and $C_{-1}(\zeta=0)$ are mostly important in the input eigenfunction as shown in Fig. 5.16. Thus, the linear term $V_0C_0(\zeta)$ dominates the evolution of $C_0(\zeta)$ which is described by Eq. (5.96), the nonlocal nonlinear effects are much weaker and can be neglected for the small value Ω_{p0} that we choose. For the same reason, $C_{-1}(\zeta)$ is mainly governed by the linear term $V_0C_{-1}(\zeta)$, however, the nonlocal nonlinearity starts to play a role. Finally, since $C_1(\zeta=0)$ and $C_{-2}(\zeta=0)$ are very small, the linear terms become much less important, consequently, $C_1(\zeta)$ and $C_{-2}(\zeta)$ are mainly determined by the nonlocal nonlinear effects.

5.2.6 Discussions

In this section, we have investigated in the cold interacting Rydberg atoms the light propagation dynamics involving PT symmetry, stimulated by the mathematical equivalence between the paraxial wave equation and the Schrödinger equation. By employing the ARG and EIT processes in two different atomic species, a linear periodical susceptibility respecting PT symmetry can be formed in the atomic system. This susceptibility acts approximately as the linear optical potential for the probe field. In the linear regime where the nonlocal nonlinear effects can be neglected, depending on the ratio between the real and imaginary parts of this linear potential, the associated band structure can be either completely real or partially complex, corresponding to an either unbroken or broken PT-symmetric phase of the system. The resulting propagation dynamics for the probe field which is chosen to be an specific eigenfunction appears to be stationary when the PT-symmetric phase of the system is unbroken, otherwise it grows or decays exponentially. This phase transition can be simply tuned by changing the amplitudes of the applied standing-wave fields. When the nonlocal nonlinear effects come into play and become important, it is found that the real and symmetric band structure in the linear case is turned to be partially complex and asymmetric, which means that the unbroken PT-symmetry of the system is destroyed. Consequently, the stationary propagation for the specific eigenfunction is changed to be oscillating due to the combination of the linear and nonlocal nonlinear effects.

As we can find from Sec. 5.2.2, the PT-symmetric periodic potential is not perfect since it is only the first-order approximation in the applied standing-wave fields. In principle, higher-order effects can play a role in the band structure and in the associated propagation dynamics. Fortunately, the involved parameters allow us to minimize the higher-order effects. Indeed, our numerical calculations have already included all higher-order effects, and the results indicate that the higher-order effects can be safely neglected for the parameters chosen in the main text.

Furthermore, we have implicitly assumed that the Rabi frequencies for the probe field in atoms A and B are the same. In general, they can be different from each other. Consequently, it will introduce an extra ratio coefficient between the two terms in the linear optical potential given Eq. (5.84b). Nevertheless, the main results still hold in the general case.

Our proposal is promising to be implemented in current experimental settings. In fact, we have chosen the parameters of ^{87}Rb and ^{85}Rb for atoms A and atoms B respectively. The choice of ^{87}Rb and ^{85}Rb is because that they are most widely used in most laboratories to study laser-atom interaction-related phenomena, of course, it can be further generalized to other atomic species to produce the desired PT-symmetric periodic potential and nonlocal nonlinearity.

5.3 Conclusions

In this chapter, we have studied light propagation dynamics in the presence of nonlocal nonlinear effects, which is induced by dipole-dipole interactions in Rydberg atoms. We first developed a model to describe the thermal Rydberg atoms interacting with laser fields in an EIT configuration. Under the crucial approximation that the time variation in the dipole-dipole interactions due to atomic motions can be neglected, we have found an analytical expression for the atomic response. In the near-resonant regime, it is shown that the nonlinear absorption for the probe field dominates the propagation dynamics and is weakened as the temperature increases. However, when the laser fields are chosen to be far-off resonant, the nonlocal nonlinear dispersion remains almost unchanged, meanwhile, the nonlocal nonlinear absorption is firstly enhanced and then weakened as the temperature grows, leading to an initially suppressed and then strengthened modulational instability. Counterintuitively, we find that each wave component will exhibit the MI effect in absorptive nonlinear media, which however simultaneously competes with the nonlocal nonlinear absorption, and eventually is suppressed.

In the followed section, we have investigate the PT-symmetric propagation dynamics in cold interacting Rydberg atoms. It is found that a linear periodical susceptibility respecting PT symmetry which acts as an optical potential for the probe field can be generated by invoking the ARG and EIT processes in two different atomic species. In the linear case where the nonlocal nonlinear effects can be neglected, the band structure can be completely real when the imaginary part of the linear potential is below a certain threshold, corresponding to an unbroken PT symmetry of the system. After exceeding this threshold, complex eigenvalues appear in the band structure, relating to a broken PT symmetry of the system. The resulting propagation dynamics is stationary for a specific eigenfunction which is in an unbroken PT-symmetric phase, otherwise it becomes exponentially growing or decaying. The phase transition from unbroken to broken PT symmetry can be simply tuned by changing the amplitude of the applied standing-wave fields. Moreover, when the nonlocal nonlinear effects become important, it is found that the unbroken PT-symmetry of the system can be destroyed. In other words, the completely real band structure is turned to be partially complex in the presence of strong nonlocal nonlinear effects, consequently, an otherwise constant propagation is modified to be oscillating owing to the competition between the linear and nonlocal nonlinear effects.

Chapter 6

Quantum nonlocality of a single photon in the x-ray regime

This chapter is devoted to the study of quantum nonlocality. In particular, we concern about the nonlocal nature of a single photon in the x-ray regime. We start by first presenting a general historic overview of quantum nonlocality of a single particle in Sec. 6.1. Based on the recent developed theory and followed experiments where the weak x-ray pulses with central frequency 14.4 keV interact with a transition of ^{57}Fe nuclei embedded in a thin cavity, we theoretically propose a scheme to test the nonlocality of a single photon in the x-ray regime. The x-ray pulses emitted from synchrotron radiation sources are so weak that they can be considered as single-photon sources [296]. We find that the x-ray pulses interacting with the cavity and the embedded ^{57}Fe nuclei can be treated as two modes of paths, leading to the entangled states between the two modes for the single x-ray photons as shown in Sec. 6.2. Analogous to a Mach-Zehnder interferometer with phase shifters inserted in the two arms [297], we then deduce a locality criterion for the x-ray photons in Sec. 6.3. Finally, in Sec. 6.4, we show that this locality criterion can be violated at specific incident angles and detunings of the x-ray pulses impinging on the cavity, and possible experimental procedures are discussed.

6.1 Introduction to quantum nonlocality of a single photon

As we have discussed in Sec. 2.2, the original manifestation given by Bell to show the divergence between local realism and quantum physics involves two or more correlated parties in the system. It has then been asked whether the nonlocality could be applied to a single particle, for example, a single photon. Unlike the nonlocality of correlated bipartite systems that have been widely accepted, there has been an intense debate on the nonlocality of a single photon. In 1991, Tan, Walls, and Collett (TWC) proposed at the first time an experiment to demonstrate the nonlocal properties of a single-photon field [100]. In their scheme, a single photon incident on a symmetric beam splitter was later detected in either of two homodyne detectors, each contains an additional local oscillator. It was found that the intensity correlation coefficient obtained from a quantum description of the system is greater than the bound value limited by local realism in the case that a weak local oscillator is assumed, thus violating the Bell-like inequality. However, Santos argued in a following comment that the scheme involved implicitly supplementary assumption related to the "no-enhancement hypothesis" and thus can only rule out a specific class of local models [101]. He also gave a local hidden-variable model which could reproduce the quantum prediction derived from Ref. [100], while it was criticized in Ref. [298] that the probability conservation is not preserved in this local model. Two years later, Hardy proposed a modified version of TWC's original scheme, in which the nonlocality of a single photon can be accomplished without using inequalities, thus avoiding the supplementary assumptions required in TWC's

scheme and ruling out the whole class of local hidden variable theories [102]. Disputes have also been aroused whether it is really nonlocality of a single photon since the proposals discussed above involves local oscillators and thus can be possibly modeled by a bipartite correlated system [103–105]. Furthermore, in the case that when there is indeed only one photon involved, van Enk clarified that the nonlocal nature of a single photon does not rise from the entanglement between the photon and the vacuum, but should be attributed to the entanglement between spatially separated modes of the photon [106]. An essentially distinct proposal to test the nonlocality of a single photon is to utilize the Mach-Zehnder interferometer [297, 299, 300] which does not involve extra local oscillators, while it may be vulnerable to the loophole of local communication since the measurements are in general not conducted in two spacelike separated locations. Until now, various proposals [301–305] to test the nonlocality of a single photon have been introduced in optical cavity and semiconductor systems, and a few experiments have been implemented on this subject in the optical regime [304, 306]. Besides, nonlocality of a single particle, e.g., neutrons, has already been verified experimentally [307].

6.2 Modeling weak x-ray pulses interacting with the thin cavity

In recent years, there have been increasingly striking progresses in the field of nuclear x-ray quantum optics. Classic quantum optical phenomena have been experimentally demonstrated in the x-ray regime, such as collective Lamb shift in single-photon superradiance [296], electromagnetically induced transparency [308]. In the mentioned cases, weak x-ray pulses interacting with resonant nuclei embedded in a planar x-ray cavity have been utilized. For those cavities, a full quantum-optical model which exactly describes the interaction between weak x-ray pulses and the nuclei has been developed [107]. Based on this model, spontaneously generated coherences can be experimentally examined and verified at the first time [108]. Those coherences were theoretically described four decades ago [309–311]. In the model, the weak x-ray pulse has been considered as only exciting one of the nuclei at a time and can thus be understood as a single resonant photon, later it was realized that the planar cavity can be interpreted as a combination of beam splitters [109]. It then naturally arises the question if we can test the nonlocality of a single photon in the x-ray regime using this setup.

Here we propose such an experiment to test the nonlocality of a single photon in the x-ray regime, which is experimentally accessible in current technology. The x-ray interacting with both the thin cavity and the embedded ^{57}Fe nuclei turns out to form an equivalent setup to the two paths in a Mach-Zehnder interferometer. Hence, a locality can be derived for the x-ray photons in the system similar as in Ref. [297]. Eventually, we find that this locality criterion can be violated at specific incident angles and detunings of the x-ray pulses impinging on the thin cavity, indicating the nonlocal nature of x-ray photons.

A schematic of the proposed experiment to examine the nonlocality of a single x-ray photon is shown in Fig. 6.1. The incoming x-ray pulses are emitted from a synchrotron radiation source with central frequency 14.4 keV at very low intensities. When impinging on the thin planar cavity with ^{57}Fe embedded in the central area, it will excite a cavity mode and also the first Mössbauer transition of the iron nuclei. The interaction between the weak incident x-ray pulses and the ^{57}Fe nuclei embedding thin cavity can be described using the quantum optical model, as developed in Ref. [107]. We then directly take from Ref. [107] the reflectance for the cavity and rewrite it as follows

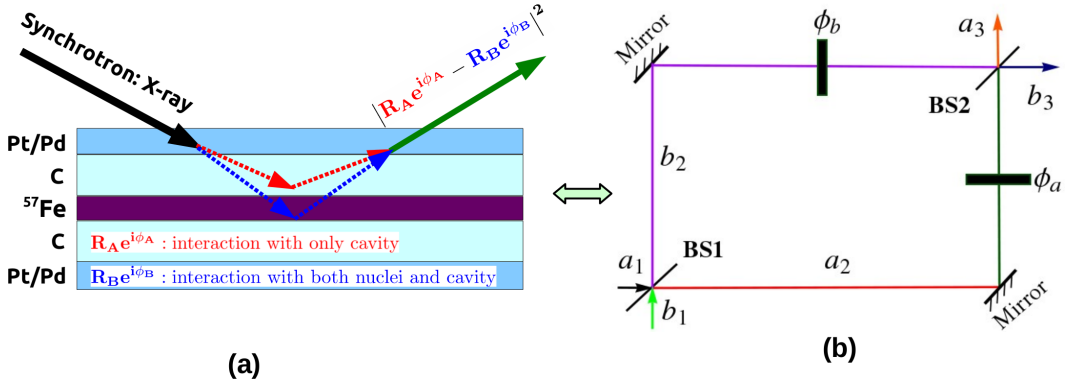

Figure 6.1: (a) The schematic diagram for the weak x-ray pulses interacting with the ^{57}Fe-embedded cavity. The thin planar cavity is made of several layers of Pt(Pd), C, ^{57}Fe with thickness within a few nanometers. The two different types of interaction for the x-ray pulses are represented by the red and blue dashed arrows respectively. They can be considered as two different paths; one is the path interacting with only the cavity, while the other one is the path with both the nuclei and the cavity. It is analogous to a Mach-Zehnder interferometer inserted by two phase shifters ϕ_a and ϕ_b in the two arms as shown in (b).

$$|R(\Delta\varphi,\Delta)|^2 = |R_A e^{i\phi_A} - R_B e^{i\phi_B}|^2\,, \tag{6.1a}$$

$$R_A = \sqrt{\sigma_0}, \qquad \phi_A = \mathrm{Arg}[q+i]\,, \tag{6.1b}$$

$$R_B = \frac{\gamma_{\mathrm{SR}}}{\Gamma}\frac{1}{\sqrt{\epsilon^2+1}}, \qquad \phi_B = \mathrm{Arg}[-\epsilon+i]\,, \tag{6.1c}$$

where $\sigma_0 = 1/(1+\frac{\kappa^2}{\Delta_C^2}), q = \kappa\gamma_{\mathrm{SR}}/(\Gamma\Delta_C)+i\gamma/\Gamma, \Gamma = \gamma+\gamma_{\mathrm{SR}}, \epsilon = (\Delta-\Delta_{\mathrm{LS}})/(\Gamma/2), \Delta_{\mathrm{LS}} = -2|g|^2N\Delta_C/3(\kappa^2+\Delta_C^2), \gamma_{\mathrm{SR}} = 4|g|^2N\kappa/3(\kappa^2+\Delta_C^2), \Delta_C = \delta_C\Delta\varphi$. Here $\Delta\varphi$ is the difference to the angle at which the guided mode is excited resonantly in the cavity, Δ is the detuning from the first Mössbauer transition, γ is the spontaneous decay rate of the excited state of this transition, and $\gamma_{\mathrm{SR}}, \Delta_{\mathrm{LS}}$ represent the superradiance and Lamb shift effects. g, N, κ denote the coupling constant between the x-ray pulse and the iron nuclei, the number of iron nuclei and the loss rate of the cavity, respectively. The reflectance for the x-ray pulses consists of two parts, one is contributed by the interaction only with the cavity, as given by $R_A e^{i\phi_A}$, the other one is due to the interaction with both the thin cavity and the embedded iron nuclei, as denoted by $R_B e^{i\phi_B}$. As an analogy to single photons incident on a Mach-Zehnder interferometer with phase shifters inserted in the two arms [297], the reflectance $|R|^2$can be considered as the probability of photons detected at one of the two output ports, depending on the relative phase shift between the two paths. From the reflectivity given in Eq. (6.1), we can redefine a scaled reflectivity

$$\begin{aligned} R_s(\phi_A,\phi_B) &= \frac{|R(\Delta\varphi,\Delta)|^2 - R_A^2(\Delta\varphi) - R_B^2(\Delta\varphi,\Delta)}{2R_A(\Delta\varphi)R_B(\Delta\varphi,\Delta)} \\ &= \cos[\phi_A(\Delta\varphi) - \phi_B(\Delta\varphi,\Delta)]\,. \end{aligned} \tag{6.2}$$

Later on we will construct a Bell's like inequality based on this scaled reflectivity.

6.2.1 The weak x-ray source

The x-ray pulses emitted from synchrotron light sources are weak in a sense that they contain less than one resonant photon in each pulse. In the Fock state representation, the state of the x-ray pulse can be written as

$$|\Psi\rangle \propto |0\rangle + \varepsilon|1\rangle + \varepsilon^2|2\rangle + \dots , \tag{6.3}$$

where we have $\varepsilon \ll 1$. It is reasonable for us to neglect the higher occupations in the Fock state, then the x-ray pulse can be well treated as a single photon source. In the following, we consider the single-photon case, i. e.,

$$|\Psi\rangle \simeq |0\rangle + \varepsilon|1\rangle . \tag{6.4}$$

6.2.2 The mode-entangled state of the x-ray photon

As has been briefly discussed above, the contributions to the reflectivity consist of two parts. One channel is due to the interaction between the x-ray photon and the thin cavity only, the other one is due to the interaction between the x-ray photon and both the cavity and the embedded iron nuclei. These two contributions can be considered as two effective paths where the x-ray photon could pass through. However, we have no information to distinguish which path the x-ray photon chooses to travel through. In other words, the x-ray photon could be either in the "cavity without nuclei (Path A)" or in the "cavity with nuclei (Path B)" path. This would lead to an entangled state of the x-ray photon between the two different modes of paths

$$|\Psi\rangle_E = c_A|1\rangle_A|0\rangle_B + c_B|0\rangle_A|1\rangle_B , \tag{6.5}$$

where E denotes "Entanglement", and c_i $(i = A, B)$ are the coefficients satisfying the normalization relation $|c_A|^2 + |c_B|^2 = 1$.

6.3 Derivation of the locality criterion in a Mach-Zehnder interferometer

From the discussions above, we can know that the weak x-ray pulses interacting with the thin cavity embedded with ^{57}Fe nuclei is closely connected to a single photon traveling in a Mach-Zehnder interferometer. With this analogy in mind, we will derive the locality criterion for the single x-ray photons here. First, let us have a look at the Mach-Zehnder interferometer as shown in Fig. 6.2. Two single-photon sources with different modes a_1 and b_1 arrive at the first lossless beam splitter (BS1) of the interferometer. The output after the beam splitter can be described as

$$\begin{bmatrix} a_2 \\ b_2 \end{bmatrix} = \begin{bmatrix} t_a & r_b \\ r_a & t_b \end{bmatrix} \begin{bmatrix} a_1 \\ b_1 \end{bmatrix} , \tag{6.6}$$

where a_2, b_2 are the intermediate modes after BS1, and t_i, r_i denote the amplitude reflection and transmission coefficients of mode i $(= a, b)$. We define the transformation

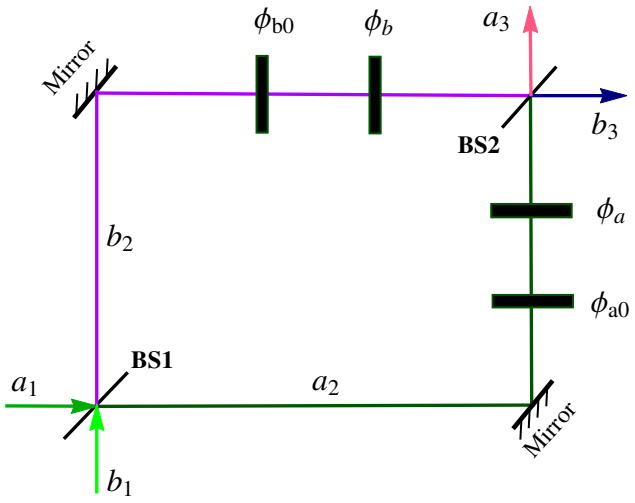

Figure 6.2: A schematic diagram for a Mach-Zehnder interferometer with inserted phase shifters ϕ_a and ϕ_b in the two arms. ϕ_{a0} and ϕ_{b0} account for the constant phase changes that the photon experiences in the two arms respectively. a_1, b_1 are the two modes of the input states, and a_2, b_2 are the two intermediate states, while a_3, b_3 represents the two output states. The two beam splitters are denoted by BS1 and BS2, and are assumed to be lossless and symmetric here.

matrix representing the beam splitter

$$M = \begin{bmatrix} t_a & r_b \\ r_a & t_b \end{bmatrix} . \tag{6.7}$$

We are considering the case of a lossless beam splitter, which means the conservation of probability should be satisfied, then the matrix M should be unitary. It results in $M^\dagger = M^{-1}$, i.e.,

$$\frac{1}{t_a t_b - r_a r_b} \begin{bmatrix} t_b & -r_b \\ -r_a & t_a \end{bmatrix} = \begin{bmatrix} t_a^* & r_a^* \\ r_b^* & t_b^* \end{bmatrix} , \tag{6.8}$$

where $t_i^*(r_i^*)$ is the complex conjugate of $t_i(r_i)$. For a unitary matrix, the determinant of M should be one, leading to $t_a t_b - r_a r_b = e^{i\varphi}$, which is only an overall factor and we can choose $\varphi = 0$ [312]. In this case, we find that

$$t_a^* = t_b \,, \tag{6.9a}$$
$$r_a = -r_b^* \,. \tag{6.9b}$$

These quantities can be rewritten as $|t_a|e^{i\varphi_{t_a}}$, $|r_a|e^{i\varphi_{r_a}}$, $|t_b|e^{i\varphi_{t_b}}$ and $|r_a|e^{i\varphi_{r_a}}$. Substituting these new forms into Eq. (6.9), it yields

$$|t_a| = |t_b| \,, \tag{6.10a}$$
$$|r_a| = |r_b| \,, \tag{6.10b}$$
$$\varphi_{r_a} - \varphi_{t_a} + \varphi_{r_b} - \varphi_{t_b} = \pi \,. \tag{6.10c}$$

Furthermore, the commutation relation $[i_2, i_2^\dagger] = 1$ $(i = a, b)$ and $[a_2, b_2^\dagger] = 0$ should be fulfilled for a lossless beam splitter [313]. This yields

$$t_a t_a^* + r_b r_b^* = 1\,, \tag{6.11a}$$
$$t_b t_b^* + r_a r_a^* = 1\,, \tag{6.11b}$$
$$t_a r_a^* + t_b^* r_b = 0\,. \tag{6.11c}$$

As the photon travels in the two arms, there might be constant phase changes ϕ_{a0}, ϕ_{b0} due to propagation effects. Furthermore, the two intermediate modes a_2, b_2 are modified by two phase shifters ϕ_a, ϕ_b independently, and then act as the input to the second BS2. The outputs at the two ports of the interferometer can be obtained

$$\begin{bmatrix} a_3 \\ b_3 \end{bmatrix} = \begin{bmatrix} t_a & r_b \\ r_a & t_b \end{bmatrix} \begin{bmatrix} e^{i(\phi_{a0}+\phi_a)} & 0 \\ 0 & e^{i(\phi_{b0}+\phi_b)} \end{bmatrix} \begin{bmatrix} a_2 \\ b_2 \end{bmatrix}, \tag{6.12}$$

here we have assumed two perfect mirrors and identical properties for the two beam splitters. When there is only one single photon in mode a incident onto the interferometer, we have

$$\begin{bmatrix} a_1 \\ b_1 \end{bmatrix} = \begin{bmatrix} 1 \\ 0 \end{bmatrix}, \tag{6.13}$$

and the outputs after the interferometer can be easily calculated from Eqs. (6.6) and (6.12)

$$\begin{bmatrix} a_3 \\ b_3 \end{bmatrix} = \begin{bmatrix} t_a^2 e^{i(\phi_{a0}+\phi_a)} + r_a r_b e^{i(\phi_{b0}+\phi_b)} \\ t_a r_a e^{i(\phi_{a0}+\phi_a)} + t_b r_a e^{i(\phi_{b0}+\phi_b)} \end{bmatrix}. \tag{6.14}$$

If we record N single photon measurements at a_3, b_3, then the photon number detected at the two ports are given as

$$N_a(\phi_a, \phi_b) = N\left|t_a^2 e^{i(\phi_{a0}+\phi_a)} + r_a r_b e^{i(\phi_{b0}+\phi_b)}\right|^2, \tag{6.15a}$$
$$N_b(\phi_a, \phi_b) = N\left|t_a r_a e^{i(\phi_{a0}+\phi_a)} + t_b r_a e^{i(\phi_{b0}+\phi_b)}\right|^2. \tag{6.15b}$$

In case the two phase shifters are set to zero, i.e., $\phi_a = \phi_b = 0$, then we have

$$N_{a0} = N\left|t_a^2 e^{i\phi_{a0}} + r_a r_b e^{i\phi_{b0}}\right|^2, \tag{6.16a}$$
$$N_{b0} = N\left|t_a r_a e^{i\phi_{a0}} + t_b r_a e^{i\phi_{b0}}\right|^2. \tag{6.16b}$$

Suppose now we only apply a phase shift ϕ_a in the first arm of the interferometer and set $\phi_b = 0$, then there will be $N_A = |N_a(\phi_{a0} + \phi_a, \phi_{b0} = 0) - N_{a0}|$ photons that change their paths, and $N - N_A$ photons that do not change their paths. Similarly, $N_B = |N_a(\phi_{a0} = 0, \phi_{b0} + \phi_b) - N_{a0}|$ photons change their paths and $N - N_B$ photons do not change their paths, if only ϕ_b is applied. When both phase shifters are applied simultaneously, the number of photons that change their paths is $N_{AB} = |N_a(\phi_{a0} + \phi_a, \phi_{b0} + \phi_b) - N_{a0}|$ and photons that do not change their paths are $N - N_{AB}$.

Assume now that those photons that do not change their paths, *both* when only ϕ_a is applied, *and* when only ϕ_b is applied, will still not change their paths when both ϕ_a and ϕ_b are applied. As discussed in Ref.[297], this assumption means that any cooperative

effects between ϕ_a and ϕ_b are not allowed. It may be considered as a single-photon version of the locality assumption. Let us introduce the sets S_N, S_A, S_B and S_{AB} as the total N photons, $N - N_A$ photons that do not change their path when only ϕ_a is used, $N - N_B$ photons that do not change their path when only ϕ_b is applied, and $N - N_{AB}$ photons that do not change their path when both ϕ_a and ϕ_b is applied, respectively. The locality assumption indicates that the set $S_A \cap S_B$ should be a subset of S_{AB}. Since the number of photons belonging to $S_A \cap S_B$ is equal to or greater than $N - N_A - N_B$. Then the locality assumption leads to the inequality

$$N - N_{AB} \geq N - N_A - N_B \,, \tag{6.17}$$

which is equivalent to

$$N_{AB} \leq N_A + N_B \,, \tag{6.18}$$

Substituting N_A, N_B and N_{AB} into Eq. (6.18), we have

$$|n_0 - n_{AB}| \leq |n_0 - n_A| + |n_0 - n_B| \,, \tag{6.19}$$

where n_i ($i \in \{0, A, B, AB\}$) is defined as

$$\begin{aligned} n_0 &= \left|t_a^2 e^{i\phi_{a0}} + r_a r_b e^{i\phi_{b0}}\right|^2 , \qquad n_A = \left|t_a^2 e^{i\phi_{a1}} + r_a r_b e^{i\phi_{b0}}\right|^2 , \\ n_B &= \left|t_a^2 e^{i\phi_{a0}} + r_a r_b e^{i\phi_{b1}}\right|^2 , \qquad n_{AB} = \left|t_a^2 e^{i\phi_{a1}} + r_a r_b e^{i\phi_{b1}}\right|^2 . \end{aligned} \tag{6.20}$$

In the upper expressions we have set $\phi_{a1} = \phi_{a0} + \phi_a$ and $\phi_{b1} = \phi_{b0} + \phi_b$. For a symmetric beam splitter, we can apply the Degiorgio's relation [312, 314, 315]

$$t_a = t_b = t \,, \tag{6.21a}$$

$$r_a = r_b = r \,, \tag{6.21b}$$

$$\varphi_r = \varphi_t + \frac{\pi}{2} \,, \tag{6.21c}$$

then the quantities n_i defined in Eq. (6.20) can be simplified to

$$\begin{aligned} n_0 &= \left|R_A e^{i\phi_{a0}} - R_B e^{i\phi_{b0}}\right|^2 , \qquad n_A = \left|R_A e^{i\phi_{a1}} - R_B e^{i\phi_{b0}}\right|^2 , \\ n_B &= \left|R_A e^{i\phi_{a0}} - R_B e^{i\phi_{b1}}\right|^2 , \qquad n_{AB} = \left|R_A e^{i\phi_{a1}} - R_B e^{i\phi_{b1}}\right|^2 , \\ R_A &= \left|t_a^2\right| , \qquad R_B = \left|r_a r_b\right| . \end{aligned} \tag{6.22}$$

Note that if the two beam splitters are symmetric, then we have $t_a = t_b = 1/\sqrt{2}$ and $r_a = r_b = i/\sqrt{2}$, which leads to $R_A = R_B = 1/2$. The inequality Eq. (6.19) then reads

$$\begin{aligned} &\left|\cos(\phi_{a0} - \phi_{b0}) - \cos(\phi_{a1} - \phi_{b1})\right| \\ &\leq \left|\cos(\phi_{a0} - \phi_{b0}) - \cos(\phi_{a1} - \phi_{b0})\right| + \left|\cos(\phi_{a0} - \phi_{b0}) - \cos(\phi_{a0} - \phi_{b1})\right| . \end{aligned} \tag{6.23}$$

For the specific case where $\phi_{a0} = 0, \phi_{b0} = 0$, this inequality can be reduced to

$$\sin^2\frac{\phi_a - \phi_b}{2} \leq \sin^2\frac{\phi_a}{2} + \sin^2\frac{\phi_b}{2}\,, \tag{6.24}$$

which is exactly the same result as in Ref. [297].

6.4 Quantum nonlocality of a single x-ray photon

6.4.1 Theoretical demonstration

For the x-ray case in the superradiant limit we have $\Gamma \simeq \gamma_{SR}$ [107, 108], the reflectance given in Eq. (6.1) can be simplified to

$$|R|^2 = |R_A e^{i\phi_A} - R_B e^{i\phi_B}|^2\,, \tag{6.25a}$$

$$R_A = \sqrt{\sigma_0}, \qquad \phi_A = \mathrm{Arg}[q + i]\,, \tag{6.25b}$$

$$R_B = \frac{1}{\sqrt{\epsilon^2 + 1}}, \quad \phi_B = \mathrm{Arg}[-\epsilon + i]\,. \tag{6.25c}$$

Taking the scaled reflectivity defined in Eq. (6.2), we then find the locality criterion for a single photon in the x-ray regime as following

$$\begin{aligned}&\left|R_s(\phi_{A0}, \phi_{B0}) - R_s(\phi_{A1}, \phi_{B1})\right| \\ &\leq \left|R_s(\phi_{A0}, \phi_{B0}) - R_s(\phi_{A1}, \phi_{B0})\right| + \left|R_s(\phi_{A0}, \phi_{B0}) - R_s(\phi_{A0}, \phi_{B1})\right|.\end{aligned} \tag{6.26}$$

In order to illustrate the nonlocality of a single x-ray photon, we need to show whether the inequality given in Eq. (6.26) can be violated or not. For this, we use the quantity $f(\Delta\varphi, \Delta)$

$$\begin{aligned}f(\Delta\varphi, \Delta) =&\left|R_s(\phi_{A0}, \phi_{B0}) - R_s(\phi_{A1}, \phi_{B1})\right| \\ &- \left|R_s(\phi_{A0}, \phi_{B0}) - R_s(\phi_{A1}, \phi_{B0})\right| - \left|R_s(\phi_{A0}, \phi_{B0}) - R_s(\phi_{A0}, \phi_{B1})\right|.\end{aligned} \tag{6.27}$$

A value $f(\Delta\varphi, \Delta) > 0$ indicates the violation of the locality at a specific incident angle $\Delta\varphi$ and detuning Δ. This quantity is shown for a broad range of parameters in Fig. 6.3. It is clearly visible that $f(\Delta\varphi, \Delta) > 0$ is satisfied in some regions where proper values for the incident angle $\Delta\phi$ and detuning Δ are chosen, suggesting that locality is violated.

6.4.2 Experimental implementations

We have theoretically discussed the violation of locality for the x-ray photons. In the context of experimentally testing nonlocality of the x-ray photons, we need to measure all the four quantities evolved in Eq. (6.27). Specifically, $R_s(\phi_{A0}, \phi_{B0})$ is the initial state of the system, $R_s(\phi_{A1}, \phi_{B0})$ and $R_s(\phi_{A0}, \phi_{B1})$ correspond to the two different cases where only the phase in Path A is shifted by $\Delta\phi_A = \phi_{A1} - \phi_{A0}$, or $\Delta\phi_B = \phi_{B1} - \phi_{B0}$ only in Path B, respectively, and $R_s(\phi_{A1}, \phi_{B1})$ denotes the case that the phase shifts $\Delta\phi_A$ and $\Delta\phi_B$ are applied in both paths. All these four quantities need to be determined independently from experimental measurements. Unfortunately, only the total reflection $|R|^2$ is directly measurable in current experimental facilities. Nevertheless, it is still possible to determine $R_s(\phi_A, \phi_B)$ via a series of measurements of $|R|^2$ at different incident

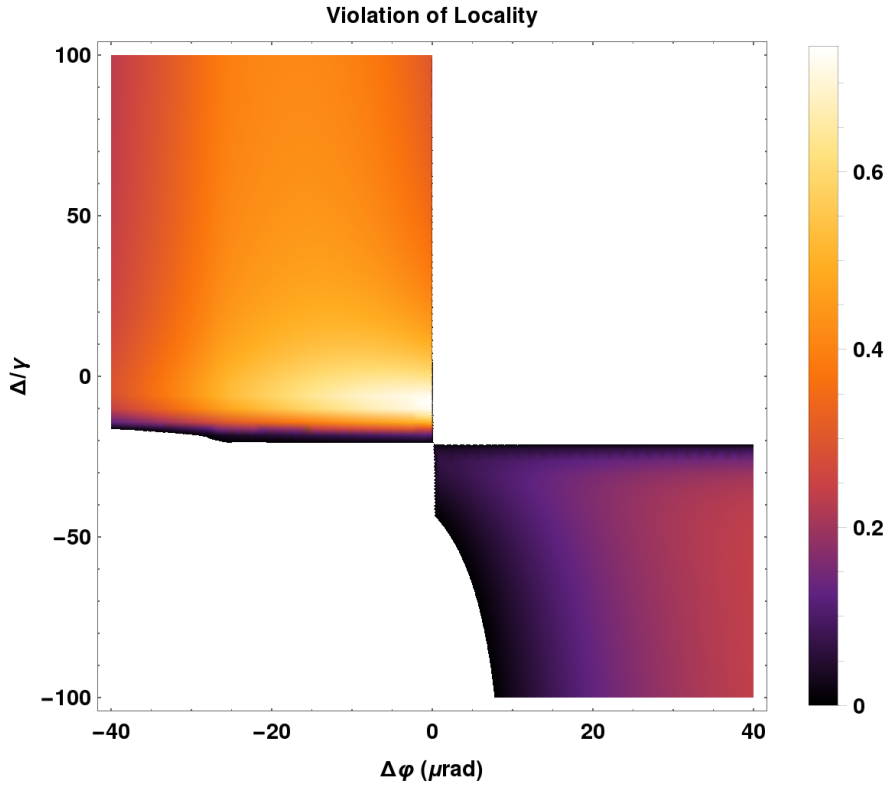

Figure 6.3: The violation-indicating quantity $f(\Delta\varphi, \Delta)$ as a function of $\Delta\varphi$ and Δ. Here we only plot the region where $f > 0$, indicating violation of locality defined in Eq. (6.26). The initial condition is chosen as $\Delta\varphi_0 = -\sqrt{3}\kappa, \Delta_0 = -\Gamma(\Delta\varphi_0)/2 + \Delta_{\mathrm{LS}}(\Delta\varphi_0)$, such that $\phi_{A0} = \pi/3, \phi_{B0} = \pi/4$. Parameters are: $\kappa = 45, \delta_C = -1, |g|^2 N = 2015, \gamma = 1$.

angles $\Delta\varphi$ and detunings Δ. For example, in order to determine $R_s(\phi_{A0}, \phi_{B0})$, we could perform the three following measurements

1. Measure the total reflection at $\{\Delta\varphi_0, \Delta_0\}$, which gives $\left|R(\Delta\varphi_0, \Delta_0)\right|^2$.

2. Measure the total reflection at $\{\Delta\varphi_0, \Delta \to \infty\}$, which yields $\left|R(\Delta\varphi_0, \Delta \to \infty)\right|^2$. From Eq.(6.1) we know that $R_B(\Delta\varphi_0, \Delta \to \infty) = 0$, so we have $|R_A(\Delta\varphi_0)|^2 = \left|R(\Delta\varphi_0, \Delta \to \infty)\right|^2$ at this step.

3. From Eq.(6.1), we solve $\epsilon(\Delta\varphi_0, \Delta_0) = \epsilon(\Delta\varphi = 0, \Delta_0^{'})$, which leads to

$$\Delta_0^{'} = \frac{\gamma_{\mathrm{SR}}(\Delta\varphi = 0)}{\gamma_{\mathrm{SR}}(\Delta\varphi_0)} \left[\Delta_0 - \Delta_{\mathrm{LS}}(\Delta\varphi_0)\right], \tag{6.28}$$

   we then measure the total reflectance at $\{\Delta\varphi = 0, \Delta_0^{'}\}$ which gives $\left|R(\Delta\varphi = 0, \Delta_0^{'})\right|^2$. Since $R_A(\Delta\varphi = 0) = 0$, we have $|R_B(\Delta\varphi = 0, \Delta_0^{'})|^2 = \left|R(\Delta\varphi = 0, \Delta_0^{'})\right|^2$. Furthermore, from Eq.(6.1) and (6.28) we find $R_B(\Delta\varphi = 0, \Delta_0^{'}) = R_B(\Delta\varphi_0, \Delta_0)$. Then we find that $|R_B(\Delta\varphi_0, \Delta_0)|^2 = \left|R(\Delta\varphi = 0, \Delta_0^{'})\right|^2$.

After these independent measurements, we have obtained the values for $\left|R(\Delta\varphi_0, \Delta_0)\right|^2$, $|R_A(\Delta\varphi_0)|^2$ and $|R_B(\Delta\varphi_0, \Delta_0)|^2$. These values are then substituted into the expression

for $R_s(\phi_{A0}, \phi_{B0})$ as given in Eq.(6.2). Finally, $R_s(\phi_{A0}, \phi_{B0})$ is determined

$$R_s(\phi_{A0}, \phi_{B0}) = \frac{|R(\Delta\varphi_0, \Delta_0)|^2 - |R(\Delta\varphi_0, \Delta \to \infty)|^2 - |R(\Delta\varphi_0 = 0, \Delta_0^{'})|^2}{2\sqrt{|R(\Delta\varphi_0, \Delta \to \infty)|^2 |R(\Delta\varphi_0 = 0, \Delta_0^{'})|^2}} . \tag{6.29}$$

Following the same procedure, the values for the other three quantities $R_s(\phi_{A1}, \phi_{B0})$, $R_s(\phi_{A0}, \phi_{B1})$ and $R_s(\phi_{A1}, \phi_{B1})$ can be also obtained. Consequently, the locality criterion can be tested experimentally.

6.5 Conclusions

We proposed a scheme to test the nonlocality of a single photon in the x-ray regime, based on the weak x-ray pulses emitted from synchrotron radiation sources interacting with ^{57}Fe nuclei which are embedded in a thin cavity. The x-ray pulse is so weak that it can be consdered as single photon sources around the first Mössbauer transition frequency in ^{57}Fe nuclei. In a full optical quantum model [107], the reflectance of the cavity for the x-ray photon can be derived, and it consists of two contributions from two different paths. One path is due to the x-ray photons interacting with the cavity only, while the other one results from the x-ray photons interacting with both the cavity and embedded nuclei. Analogous to a Mach-Zehnder interferometer with two phase shifters inserted into the two arms respectively, we then derived the locality criterion for the x-ray photon. Finally, we found the locality criterion can be violated at specific incident angles and detunings of the x-ray photon. Our scheme is feasible in current experiments, and a possible measurement scheme are also discussed.

For a proof-of-principle demonstration of nonlocality of a single photon that can be experimentally examined in the x-ray regime, we are left with one of the loopholes, which is local communication. In our scheme, the two effective paths for the single photon are intrinsically inseparable, this would imply that local communication between the two paths could in principle be possible. Apart from this loophole, one might argue that the absorption for the x-ray photon due to, for example, nuclei transition and cavity loss, would affect the actual experimental test. Fortunately, the effect due to absorption can be eliminated by performing the post-selection procedure, however, this may lead us to the second loophole of fair-sampling assumption [34].

On the other hand, our scheme would allow us to explore quantum nonlocality in a completely new energy regime for the first time, which is orders of magnitude obove currently existing setups. While we expect that the predictions of quantum theory hold in this domain, it is, as always, the experimental tests which decide if our understanding of nature is correct.

Chapter 7

Summary and outlook

Summary

The thesis is devoted to the study of coherent control and manipulation of classical or quantum light via nonlocal effects. It on the one hand sheds new light to the investigation of controlling classical light propagation in the presence of nonlolcal linear or nonlinear effects which may lead to promising applications in diverse fields, and on the other hand explores new aspects on the fundamental understanding of the physical properties of a single photon.

In the first and main part of the thesis, we focused on the coherent control and manipulation of classical light propagation via nonlocal linear or nonlinear effects in the paraxial regime. In Chapter 3, we first examined the validity of the paraxial approximation by studying beam propagation in an optically written waveguide structure induced in a five-level atomic system interacting with spatially dependent Gaussian control fields and an incoherent pump field. It has been shown that already in a single optically written waveguide, accurate results for the beam propagation cannot be obtained within the paraxial approximation when the width of the probe field is too small as compared to its wavelength. The correct propagation dynamics has been attained by numerically calculating the full Maxwell equations with FDTD method. Moreover, we have demonstrated that selective optical steering can be achieved in a controllable branched-waveguide structure which is formed inside the medium by applying a spatially dependent control field consisting of two parallel and one tilted Gaussian beams. The visibility of this selective steering can be easily controlled by the tilting angle of the tilted beam.

The recent theoretical and experimental developments in three-level lambda atomic systems under the EIT configuration have shown that the thermal motion and collisions can give rise to nonlocal linear effects in the Dicke narrowing regime. This specific type of nonlocal linear effects is in terms of linear susceptibility in which the linear dispersion is quadratic in $\mathbf{k}_\perp$ in momentum space and thus can be employed to exactly eliminate the paraxial diffraction of laser fields having arbitrary spatial profiles at certain circumstances. However, strong inevitable absorption involved in this physical mechanism owing to the required two-photon detuning leads to severe attenuation of the input laser beams, rendering it useless for practical application. Based on this physical mechanism, we then extended in Chapter 4 to study diffractionless and lossless light propagation, uniform phase modulation, and diffractionless image reproduction and frequency conversion. First, we applied an additional two-way incoherent pump to couple another transtion in a four-level double-lambda thermal atomic system interacting with both coherent probe and control fields. The effect of this incoherent field is to redistribute the populations among the four states. Subsequently, the coherent control field induces atomic coherences which leads to constant gain for the probe field. Depending on the intensity of the incoherent pump, the single-photon absorption can be completely compensated or even surpassed by the gain from the atomic coherences. Meanwhile, the

linear dispersion is still quadratic in $\mathbf{k}_\perp$ except for a different constant offset. As a result, the paraxial diffraction is exactly eliminated in the momentum space, and the probe field encoded with arbitrary images can propagate in the prepared thermal medium with neither diffraction nor absorption.

Next, we then found the constant offset in the linear dispersion can be utilized to apply an uniform π phase modulation to the probe beam while its other physical properties are exactly preserved. This uniform π phase modulation, which can be easily tuned by parameters such as the amplitude of the control field or the incoherent pump, has been accomplished at a low atomic density and in a rather short distance less than one Rayleigh length, and does not depend on the probe field intensity.

Furthermore, we proposed a novel scheme to realize diffractionless image reproduction and frequency conversion based on four-wave mixing (FWM) in a thermal five-level triple-lambda atomic vapor interacting with a probe laser beam encoded with arbitrary spatial profile, two coherent plane-wave control fields and an additional two-way incoherent pump. The generated FWM signal field has a different frequency but the same spatial distribution with respect to the probe field. At the time when the paraxial diffraction of both the probe and signal beams is eliminated by the nonlocal linear effects, the two-photon absorption is compensated by the gain from atomic coherences generated by the incoherent pump together with the two coherent laser fields. Furthermore, the conversion processes are tunable via changing the amplitude of the incoherent pump or the control fields.

In Chapter 5, we turned into studying light propagation dynamics in the presence of nonlocal nonlinear effects in interacting Rydberg atoms. We first developed a model to describe the thermal Rydberg atoms interacting with two coherent probe and control laser fields under the EIT configuration. Under the crucial approximation that the time variation in the dipole-dipole interactions due to atomic motion can be neglected, we have found an analytical form for the nonlocal nonlinear atomic response of the thermal Rydberg atoms. Based on this analytical form, we first studied the probe propagation in the regime where the single-photon transitions are near resonant, and it was found that the nonlinear absorption for the probe field is weakened as the temperature increases. Different from the dynamics in the near-resonant regime, it was shown that in the far-off regime the nonlocal nonlinear dispersion remains almost unchanged, meanwhile the nonlocal nonlinear absorption is firstly enhanced and then weakened as the temperature grows. Consequently, modulational instability (MI) is initially suppressed and then strengthened with increasing temperature. We then proposed a model to describe the MI effect in nonlocal nonlinear media with absorption. As compared to the purely dispersive media, counterintuitively, we have found that in absorptive nonlocal nonlinear media each wave component will exhibit the MI effect, which however simultaneously competes with the nonlocal nonlinear absorption, and eventually is suppressed.

Stimulated by the mathematical equivalence between the paraixal wave equation and the quantum Schrödinger equation, we proceeded to study the PT-symmetric propagation dynamics in cold interacting Rydberg atoms. By considering the ARG and EIT processes in two different atomic species, we were able to create a linear optical periodic potential respecting PT symmetry. It has been shown that this potential results in an either completely real or partially complex band structure, depending on the ratio between the real and imaginary parts of this potential. Below this threshold, the band structure is real, referring to an unbroken PT-symmetric phase. Otherwise complex conjugate eigenvalue pairs appear in band structure, corresponding to a broken PT symmetry of the system. This phase transition from unbroken to broken PT-symmetric phase can be

further induced by the presence of nonlinear nonlocal effects due to the Rydberg-Rydberg interactions. We then proceeded to investigate the related propagation dynamics. In the linear regime, it is stationary for the probe propagation in a PT-symmetric phase, otherwise, the probe experiences exponentially growing or decaying. However, in the nonlinear regime, oscillating behaviors appear in the probe propagation due to the combination of linear and nonlocal nonlinear effects.

In the second part of the thesis, quantum nonlocality of a single photon has been investigated in the x-ray regime in Chapter 6. Based on the recent developed theory and followed experiments where the weak x-ray pulses with central frequency at 14.4 keV interact with ^{57}Fe nuclei embedded in a thin cavity, we theoretically proposed a scheme to test the nonlocality of a single x-ray photon. The x-ray pulses emitted from the synchrotron radiation sources are so weak that they can only excite one of the nuclei at a time and can thus be considered as single-photon sources. We find that the x-ray pulses interacting with the cavity and the ^{57}Fe nuclei can be treated as a Mach-Zehnder interferometer, in which one mode of path is the empty cavity and the other one is the combination of the nuclei and the thin cavity, leading to an entangled state between the two modes for the single x-ray photons. Analogous to a Mach-Zehnder interferometer with phase shifters inserted in the two arms, we then deduce the locality criterion in terms of Bell-like inequality for the x-ray photons in the system. In the end, we find that this locality criterion can be violated at specific incident angles and detunings of the x-ray pulses impinging on the cavity, indicating the nonlocality of x-ray photons. We have also discussed the possible procedures to experimentally test the proposal.

Finally, we should emphasize that all the theoretical proposals demonstrated above are promising to be examined in current experimental settings.

Outlook

The results illustrated in this thesis certainly presents only a small and partial step toward the study on the coherent control of classical or quantum light via nonlocal effects, nevertheless, it may trigger further possible fresh ideas in these directions.

First, in the study of nonlocal linear effects in thermal atomic vapor, we mainly concern about the light propagation in the continuous-wave limit where the time evolution is ignored. In the theoretical calculations done in Chapter 4, we have already obtained the atomic susceptibility in the frequency and momentum space, which in return leads to a time and position-dependent atomic response by simply applying the Fourier transformation. Thus, an direct extension to study time evolution of the laser pulse propagation is obviously possible in our thermal atomic system. Considering the specific form of the nonlocal response for the thermal atoms obtained in Chapter 4, it is reasonable to argue that one can obtain a stationary pulse propagation, since the group velocity dispersion of the probe pulse can be in principle canceled by the atomic response.

Secondly, in the model developed to describe thermal interacting Rydberg atoms, we have to make the crucial approximation that the time variation in the dipole-dipole interactions due to atomic motion can be neglected, in order to obtain the analytical form of the atomic response. Owing to this crucial approximation, other physical consequences, such as time evolution, may not be covered from the proposed model. Improvements of the present model can be explored by further alleviating this approximation, for example, with input from statistical thermodynamics. One then may be able to understand better or interpret the time-dependent coherent phenomena found in these pioneer experiments which were conducted in thermal interacting Rydberg atoms.

Furthermore, with the input of physical concepts such as geometric phase or topological properties of the band structure [316, 317] developed in quantum theory, especially in solid state physics, it is possible to investigate the geometric phase or topological properties of the band structure in PT-symmetric systems. It would be reasonable to study the effect of phase transition on the topological properties of the energy bands. In particular, in the presence of nonlocal nonlinear effects, it would be hopeful to expect that interesting results can be possible found.

Lastly, in the quantum level, it is promising to explore the nonlocal realism of a single photon, apart from the quantum nonlocality. In fact, in the proposed scheme to test the quantum nonlocality of a single x-ray photon, the two intrinsically inseparable paths for the single photon may lead to one of the loopholes that local communication between the two paths could in principle be possible. However, this loophole is irrelevant in the study of nonlocal realism of entangled systems, which is directly linked to the concept of reality. Following the theoretical model to test nonlocal realism developed by Leggett [93], one may construct an inequality criterion to test the nonlocal realism of a single photon based on its quantum behaviors in the Mach-Zehnder interferometer, and may be further checked experimentally in the system of planar thin cavity interacting with x-ray photons emitted from synchrotron radiation sources.

Bibliography

[1] M. Born and E. Wolf, *Principles of optics*, 7th ed. (Cambridge University Press, New York, 1999).

[2] C. Cohen-Tannoudji, B. Diu, and F. Laloe, *Quantum Mechanics Vol. 1*, 1st ed. (WILEY-VCH, New York, 1991).

[3] P. J. Coles, J. Kaniewski, and S. Wehner, "Equivalence of wave–particle duality to entropic uncertainty," Nat Commun **5** (2014).

[4] J. D. Jackson, *Classical Electrodynamics*, 3rd ed. (John Wiley Sons, INC., Hoboken, 1999) chap. 1.

[5] Y. Aharonov and D. Bohm, "Significance of Electromagnetic Potentials in the Quantum Theory," Phys. Rev. **115**, 485 (1959).

[6] S. Popescu, "Dynamical quantum non-locality," Nat Phys **6**, 151 (2010).

[7] M. O. Scully and M. S. Zubairy, *Quantum Optics* (Cambridge University Press, New York, 1997).

[8] A. Einstein, B. Podolsky, and N. Rosen, "Can Quantum-Mechanical Description of Physical Reality Be Considered Complete?" Phys. Rev. **47**, 777 (1935).

[9] Y. R. Shen, *The Principles of Nonlinear Optics* (John Wiley and Sons, New York, 1984).

[10] R. W. Boyd, *Nonlinear Optics*, 3rd ed. (Academic Press, New York, 2008).

[11] G. P. Agrawal, *Nonlinear fiber optics*, 5th ed. (Academic Press, New York, 2012).

[12] S. T. Cundiff and J. Ye, "*Colloquium*: Femtosecond optical frequency combs," Rev. Mod. Phys. **75**, 325 (2003).

[13] F. Krausz and M. Ivanov, "Attosecond physics," Rev. Mod. Phys. **81**, 163 (2009).

[14] M. Fleischhauer, A. Imamoglu, and J. P. Marangos, "Electromagnetically induced transparency: Optics in coherent media," Rev. Mod. Phys. **77**, 633 (2005).

[15] I. Bloch, J. Dalibard, and W. Zwerger, "Many-body physics with ultracold gases," Rev. Mod. Phys. **80**, 885 (2008).

[16] K. Bongs and K. Sengstock, "Physics with coherent matter waves," Reports on Progress in Physics **67**, 907 (2004).

[17] J. M. Raimond, M. Brune, and S. Haroche, "Manipulating quantum entanglement with atoms and photons in a cavity," Rev. Mod. Phys. **73**, 565 (2001).

[18] J.-W. Pan, Z.-B. Chen, C.-Y. Lu, H. Weinfurter, A. Zeilinger, and M. Żukowski, "Multiphoton entanglement and interferometry," Rev. Mod. Phys. **84**, 777 (2012).

[19] M. Aspelmeyer, T. J. Kippenberg, and F. Marquardt, "Cavity optomechanics," Rev. Mod. Phys. **86**, 1391 (2014).

[20] O. Firstenberg, M. Shuker, A. Ben-Kish, D. R. Fredkin, N. Davidson, and A. Ron, "Theory of Dicke narrowing in coherent population trapping," Phys. Rev. A **76**, 013818 (2007).

[21] O. Firstenberg, M. Shuker, R. Pugatch, D. R. Fredkin, N. Davidson, and A. Ron, "Theory of thermal motion in electromagnetically induced transparency: Effects of diffusion, Doppler broadening, and Dicke and Ramsey narrowing," Phys. Rev. A **77**, 043830 (2008).

[22] O. Firstenberg, M. Shuker, N. Davidson, and A. Ron, "Elimination of the Diffraction of Arbitrary Images Imprinted on Slow Light," Phys. Rev. Lett. **102**, 043601 (2009).

[23] O. Firstenberg, P. London, M. Shuker, A. Ron, and N. Davidson, "Elimination, reversal and directional bias of optical diffraction," Nat. Phys. **5**, 665 (2009).

[24] O. Firstenberg, M. Shuker, A. Ron, and N. Davidson, "*Colloquium* : Coherent diffusion of polaritons in atomic media," Rev. Mod. Phys. **85**, 941 (2013).

[25] S. Sevinçli, N. Henkel, C. Ates, and T. Pohl, "Nonlocal Nonlinear Optics in Cold Rydberg Gases," Phys. Rev. Lett. **107**, 153001 (2011).

[26] D. E. Chang, V. Vuletic, and M. D. Lukin, "Quantum nonlinear optics –photon by photon," Nat Photon **8**, 685 (2014).

[27] N. Bohr, "Can Quantum-Mechanical Description of Physical Reality be Considered Complete?" Phys. Rev. **48**, 696 (1935).

[28] J. Bell, "On the Einstein-Podolsky-Rosen paradox," Physics **1**, 195 (1964).

[29] J. F. Clauser and A. Shimony, "Bell's theorem. Experimental tests and implications," Reports on Progress in Physics **41**, 1881 (1978).

[30] A. Aspect, P. Grangier, and G. Roger, "Experimental Tests of Realistic Local Theories via Bell's Theorem," Phys. Rev. Lett. **47**, 460 (1981).

[31] A. Aspect, P. Grangier, and G. Roger, "Experimental Realization of Einstein-Podolsky-Rosen-Bohm Gedankenexperiment: A New Violation of Bell's Inequalities," Phys. Rev. Lett. **49**, 91 (1982).

[32] A. Aspect, J. Dalibard, and G. Roger, "Experimental Test of Bell's Inequalities Using Time- Varying Analyzers," Phys. Rev. Lett. **49**, 1804 (1982).

[33] G. Weihs, T. Jennewein, C. Simon, H. Weinfurter, and A. Zeilinger, "Violation of Bell's Inequality under Strict Einstein Locality Conditions," Phys. Rev. Lett. **81**, 5039 (1998).

[34] M. Giustina, A. Mech, S. Ramelow, B. Wittmann, J. Kofler, J. Beyer, A. Lita, B. Calkins, T. Gerrits, S. W. Nam, R. Ursin, and A. Zeilinger, "Bell violation using entangled photons without the fair-sampling assumption," Nature **497**, 227 (2013).

[35] Z. Chen, M. Segev, and D. N. Christodoulides, "Optical spatial solitons: historical overview and recent advances," Reports on Progress in Physics **75**, 086401 (2012).

[36] W. Krolikowski, O. Bang, J. J. Rasmussen, and J. Wyller, "Modulational instability in nonlocal nonlinear Kerr media," Phys. Rev. E **64**, 016612 (2001).

[37] J. Wyller, W. Krolikowski, O. Bang, and J. J. Rasmussen, "Generic features of modulational instability in nonlocal Kerr media," Phys. Rev. E **66**, 066615 (2002).

[38] W. Królikowski, O. Bang, N. I. Nikolov, D. Neshev, J. Wyller, J. J. Rasmussen, and D. Edmundson, "Modulational instability, solitons and beam propagation in spatially nonlocal nonlinear media," Journal of Optics B: Quantum and Semiclassical Optics **6**, S288 (2004).

[39] B. K. Esbensen, A. Wlotzka, M. Bache, O. Bang, and W. Krolikowski, "Modulational instability and solitons in nonlocal media with competing nonlinearities," Phys. Rev. A **84**, 053854 (2011).

[40] P. W. Anderson, "Absence of Diffusion in Certain Random Lattices," Phys. Rev. **109**, 1492 (1958).

[41] H. De Raedt, A. Lagendijk, and P. de Vries, "Transverse Localization of Light," Phys. Rev. Lett. **62**, 47 (1989).

[42] D. S. Wiersma, P. Bartolini, A. Lagendijk, and R. Righini, "Localization of light in a disordered medium," Nature **390**, 671 (1997).

[43] T. Schwartz, G. Bartal, S. Fishman, and M. Segev, "Transport and Anderson localization in disordered two-dimensional photonic lattices," Nature **446**, 52 (2007).

[44] M. Segev, Y. Silberberg, and D. N. Christodoulides, "Anderson localization of light," Nat Photon **7**, 197 (2013).

[45] M. Leonetti, S. Karbasi, A. Mafi, and C. Conti, "Observation of Migrating Transverse Anderson Localizations of Light in Nonlocal Media," Phys. Rev. Lett. **112**, 193902 (2014).

[46] T. Kitagawa, M. A. Broome, A. Fedrizzi, M. S. Rudner, E. Berg, I. Kassal, A. Aspuru-Guzik, E. Demler, and A. G. White, "Observation of topologically protected bound states in photonic quantum walks," Nat Commun **3**, 882 (2012).

[47] M. C. Rechtsman, J. M. Zeuner, Y. Plotnik, Y. Lumer, D. Podolsky, F. Dreisow, S. Nolte, M. Segev, and A. Szameit, "Photonic Floquet topological insulators," Nature **496**, 196 (2013).

[48] Y. Lumer, Y. Plotnik, M. C. Rechtsman, and M. Segev, "Self-Localized States in Photonic Topological Insulators," Phys. Rev. Lett. **111**, 243905 (2013).

[49] G. Q. Liang and Y. D. Chong, "Optical Resonator Analog of a Two-Dimensional Topological Insulator," Phys. Rev. Lett. **110**, 203904 (2013).

[50] A. V. Poshakinskiy, A. N. Poddubny, L. Pilozzi, and E. L. Ivchenko, "Radiative Topological States in Resonant Photonic Crystals," Phys. Rev. Lett. **112**, 107403 (2014).

[51] P. Leboeuf and S. Moulieras, "Superfluid Motion of Light," Phys. Rev. Lett. **105**, 163904 (2010).

[52] I. Carusotto, "Superfluid light in bulk nonlinear media," Proceedings of the Royal Society A: Mathematical, Physical and Engineering Science **470** (2014).

[53] C. M. Bender and S. Boettcher, "Real Spectra in Non-Hermitian Hamiltonians Having $\mathcal{PT}$ Symmetry," Phys. Rev. Lett. **80**, 5243 (1998).

[54] C. M. Bender, S. Boettcher, and P. N. Meisinger, "PT-symmetric quantum mechanics," Journal of Mathematical Physics **40**, 2201 (1999).

[55] C. M. Bender, D. C. Brody, and H. F. Jones, "Complex Extension of Quantum Mechanics," Phys. Rev. Lett. **89**, 270401 (2002).

[56] C. M. Bender, D. C. Brody, and H. F. Jones, "Must a Hamiltonian be Hermitian?" American Journal of Physics **71**, 1095 (2003).

[57] C. Bender, D. Brody, and H. Jones, "Erratum: Complex Extension of Quantum Mechanics [Phys. Rev. Lett. 89, 270401 (2002)]," Phys. Rev. Lett. **92**, 119902 (2004).

[58] C. M. Bender, "Introduction to PT-symmetric quantum theory," Contemporary Physics **46**, 277 (2005).

[59] C. M. Bender, "Making sense of non-Hermitian Hamiltonians," Reports on Progress in Physics **70**, 947 (2007).

[60] A. Mostafazadeh, "Pseudo-Hermiticity versus PT symmetry: The necessary condition for the reality of the spectrum of a non-Hermitian Hamiltonian," Journal of Mathematical Physics **43**, 205 (2002).

[61] A. Mostafazadeh, "Pseudo-Hermiticity versus PT-symmetry. II. A complete characterization of non-Hermitian Hamiltonians with a real spectrum," Journal of Mathematical Physics **43**, 2814 (2002).

[62] A. Mostafazadeh, "Pseudo-Hermiticity versus PT-symmetry III: Equivalence of pseudo-Hermiticity and the presence of antilinear symmetries," Journal of Mathematical Physics **43**, 3944 (2002).

[63] P. Dorey, C. Dunning, and R. Tateo, "Spectral equivalences, Bethe ansatz equations, and reality properties in PT-symmetric quantum mechanics," Journal of Physics A: Mathematical and General **34**, 5679 (2001).

[64] K. Jones-Smith and H. Mathur, "Non-Hermitian quantum Hamiltonians with $\mathcal{PT}$ symmetry," Phys. Rev. A **82**, 042101 (2010).

[65] I. Friedler, D. Petrosyan, M. Fleischhauer, and G. Kurizki, "Long-range interactions and entanglement of slow single-photon pulses," Phys. Rev. A **72**, 043803 (2005).

[66] J. Pritchard, D. Maxwell, A. Gauguet, K. Weatherill, M. Jones, and C. Adams, "Cooperative Atom-Light Interaction in a Blockaded Rydberg Ensemble," Phys. Rev. Lett. **105**, 193603 (2010).

[67] D. Petrosyan, J. Otterbach, and M. Fleischhauer, "Electromagnetically Induced Transparency with Rydberg Atoms," Phys. Rev. Lett. **107**, 213601 (2011).

[68] T. Peyronel, O. Firstenberg, Q.-Y. Liang, S. Hofferberth, A. V. Gorshkov, T. Pohl, M. D. Lukin, and V. Vuletic, "Quantum nonlinear optics with single photons enabled by strongly interacting atoms," Nature **488**, 57 (2012).

[69] M. Gärttner and J. Evers, "Nonlinear absorption and density-dependent dephasing in Rydberg electromagnetically-induced-transparency media," Phys. Rev. A **88**, 033417 (2013).

[70] E. Urban, T. A. Johnson, T. Henage, L. Isenhower, D. D. Yavuz, T. G. Walker, and M. Saffman, "Observation of Rydberg blockade between two atoms," Nat Phys **5**, 110 (2009).

[71] Y. O. Dudin and A. Kuzmich, "Strongly Interacting Rydberg Excitations of a Cold Atomic Gas," Science **336**, 887 (2012).

[72] S. Baur, D. Tiarks, G. Rempe, and S. Dürr, "Single-Photon Switch Based on Rydberg Blockade," Phys. Rev. Lett. **112**, 073901 (2014).

[73] M. D. Lukin, M. Fleischhauer, R. Cote, L. M. Duan, D. Jaksch, J. I. Cirac, and P. Zoller, "Dipole Blockade and Quantum Information Processing in Mesoscopic Atomic Ensembles," Phys. Rev. Lett. **87**, 037901 (2001).

[74] M. Saffman, T. G. Walker, and K. Mølmer, "Quantum information with Rydberg atoms," Rev. Mod. Phys. **82**, 2313 (2010).

[75] D. Tong, S. M. Farooqi, J. Stanojevic, S. Krishnan, Y. P. Zhang, R. Côté, E. E. Eyler, and P. L. Gould, "Local Blockade of Rydberg Excitation in an Ultracold Gas," Phys. Rev. Lett. **93**, 063001 (2004).

[76] C. Ates, T. Pohl, T. Pattard, and J. M. Rost, "Strong interaction effects on the atom counting statistics of ultracold Rydberg gases," Journal of Physics B: Atomic, Molecular and Optical Physics **39**, L233 (2006).

[77] H. Weimer, R. Löw, T. Pfau, and H. P. Büchler, "Quantum Critical Behavior in Strongly Interacting Rydberg Gases," Phys. Rev. Lett. **101**, 250601 (2008).

[78] A. Chotia, M. Viteau, T. Vogt, D. Comparat, and P. Pillet, "Kinetic Monte Carlo modeling of dipole blockade in Rydberg excitation experiment," New Journal of Physics **10**, 045031 (2008).

[79] H. Schempp, G. Günter, C. S. Hofmann, C. Giese, S. D. Saliba, B. D. DePaola, T. Amthor, M. Weidemüller, S. Sevinçli, and T. Pohl, "Coherent Population Trapping with Controlled Interparticle Interactions," Phys. Rev. Lett. **104**, 173602 (2010).

[80] K. P. Heeg, *Models for correlated Rydberg gases*, Diploma thesis, University of Heidelberg, Heidelberg (2011).

[81] C. Ates, T. Pohl, T. Pattard, and J. M. Rost, "Many-body theory of excitation dynamics in an ultracold Rydberg gas," Phys. Rev. A **76**, 013413 (2007).

[82] C. Ates, S. Sevinçli, and T. Pohl, "Electromagnetically induced transparency in strongly interacting Rydberg gases," Phys. Rev. A **83**, 041802 (2011).

[83] K. Heeg, M. Gärttner, and J. Evers, "Hybrid model for Rydberg gases including exact two-body correlations," Phys. Rev. A **86**, 063421 (2012).

[84] M. Gärttner, *Many-Body Effects in Rydberg Gases: Coherent Dynamics of Strongly Interacting Two-Level Atoms and Nonlinear Optical Response of a Rydberg Gas in EIT Configuration*, Ph.D. thesis, University of Heidelberg, Heidelberg (2013).

[85] F. Shen, J. Gao, A. A. Senin, C. J. Zhu, J. R. Allen, Z. H. Lu, Y. Xiao, and J. G. Eden, "Many-Body Dipole-Dipole Interactions between Excited Rb Atoms Probed by Wave Packets and Parametric Four-Wave Mixing," Phys. Rev. Lett. **99**, 143201 (2007).

[86] H. Kubler, P. J. Shaffer, T. Baluktsian, R. Low, and T. Pfau, "Coherent excitation of Rydberg atoms in micrometre-sized atomic vapour cells," Nat. Photon. **4**, 112 (2010).

[87] B. Huber, T. Baluktsian, M. Schlagmüller, A. Kölle, H. Kübler, R. Löw, and T. Pfau, "GHz Rabi Flopping to Rydberg States in Hot Atomic Vapor Cells," Phys. Rev. Lett. **107**, 243001 (2011).

[88] A. Kölle, G. Epple, H. Kübler, R. Löw, and T. Pfau, "Four-wave mixing involving Rydberg states in thermal vapor," Phys. Rev. A **85**, 063821 (2012).

[89] J. A. Sedlacek, A. Schwettmann, H. Kubler, R. Low, T. Pfau, and J. P. Shaffer, "Microwave electrometry with Rydberg atoms in a vapour cell using bright atomic resonances," Nat. Phys. **8**, 819 (2012).

[90] T. Baluktsian, B. Huber, R. Löw, and T. Pfau, "Evidence for Strong van der Waals Type Rydberg-Rydberg Interaction in a Thermal Vapor," Phys. Rev. Lett. **110**, 123001 (2013).

[91] W. Li, C. Ates, and I. Lesanovsky, "Nonadiabatic Motional Effects and Dissipative Blockade for Rydberg Atoms Excited from Optical Lattices or Microtraps," Phys. Rev. Lett. **110**, 213005 (2013).

[92] D. Barredo, H. Kübler, R. Daschner, R. Löw, and T. Pfau, "Electrical Readout for Coherent Phenomena Involving Rydberg Atoms in Thermal Vapor Cells," Phys. Rev. Lett. **110**, 123002 (2013).

[93] A. Leggett, "Nonlocal Hidden-Variable Theories and Quantum Mechanics: An Incompatibility Theorem," Foundations of Physics **33**, 1469 (2003).

[94] S. Groblacher, T. Paterek, R. Kaltenbaek, C. Brukner, M. Zukowski, M. Aspelmeyer, and A. Zeilinger, "An experimental test of non-local realism," Nature **446**, 871 (2007).

[95] S. Popescu and D. Rohrlich, "Quantum nonlocality as an axiom," Foundations of Physics **24**, 379 (1994).

[96] S. Popescu, "Nonlocality beyond quantum mechanics," Nat Phys **10**, 264 (2014).

[97] M. Pawlowski, T. Paterek, D. Kaszlikowski, V. Scarani, A. Winter, and M. Zukowski, "Information causality as a physical principle," Nature **461**, 1101 (2009).

[98] L. Hardy, "Quantum Theory From Five Reasonable Axioms," (2001), arXiv:quant-ph/0101012 .

[99] L. Masanes and M. P. Müller, "A derivation of quantum theory from physical requirements," New Journal of Physics **13**, 063001 (2011).

[100] S. M. Tan, D. F. Walls, and M. J. Collett, "Nonlocality of a single photon," Phys. Rev. Lett. **66**, 252 (1991).

[101] E. Santos, "Comment on "Nonlocality of a single photon"," Phys. Rev. Lett. **68**, 894 (1992).

[102] L. Hardy, "Nonlocality of a Single Photon Revisited," Phys. Rev. Lett. **73**, 2279 (1994).

[103] D. M. Greenberger, M. A. Horne, and A. Zeilinger, "Nonlocality of a Single Photon?" Phys. Rev. Lett. **75**, 2064 (1995).

[104] L. Vaidman, "Nonlocality of a Single Photon Revisited Again," Phys. Rev. Lett. **75**, 2063 (1995).

[105] L. Hardy, "Hardy Replies:," Phys. Rev. Lett. **75**, 2065 (1995).

[106] S. J. van Enk, "Single-particle entanglement," Phys. Rev. A **72**, 064306 (2005).

[107] K. P. Heeg and J. Evers, "X-ray quantum optics with Mössbauer nuclei embedded in thin-film cavities," Phys. Rev. A **88**, 043828 (2013).

[108] K. P. Heeg, H.-C. Wille, K. Schlage, T. Guryeva, D. Schumacher, I. Uschmann, K. S. Schulze, B. Marx, T. Kämpfer, G. G. Paulus, R. Röhlsberger, and J. Evers, "Vacuum-Assisted Generation and Control of Atomic Coherences at X-Ray Energies," Phys. Rev. Lett. **111**, 073601 (2013).

[109] K. P. Heeg, C. Ott, D. Schumacher, H.-C. Wille, R. Röhlsberger, T. Pfeifer, and J. Evers, "Interferometric phase detection at x-ray energies via Fano resonance control," (2014), arXiv:1411.1545 .

[110] K. Makris, R. El-Ganainy, D. Christodoulides, and Z. Musslimani, "Beam Dynamics in $\mathcal{PT}$ Symmetric Optical Lattices," Phys. Rev. Lett. **100**, 103904 (2008).

[111] S. Longhi, "Bloch Oscillations in Complex Crystals with $\mathcal{PT}$ Symmetry," Phys. Rev. Lett. **103**, 123601 (2009).

[112] C. E. Ruter, K. G. Makris, R. El-Ganainy, D. N. Christodoulides, M. Segev, and D. Kip, "Observation of parity-time symmetry in optics," Nat Phys **6**, 192 (2010).

[113] L. Feng, M. Ayache, J. Huang, Y.-L. Xu, M.-H. Lu, Y.-F. Chen, Y. Fainman, and A. Scherer, "Nonreciprocal Light Propagation in a Silicon Photonic Circuit," Science **333**, 729 (2011).

[114] A. Regensburger, C. Bersch, M.-A. Miri, G. Onishchukov, D. N. Christodoulides, and U. Peschel, "Parity-time synthetic photonic lattices," Nature **488**, 167 (2012).

[115] Y. Sun, W. Tan, H.-q. Li, J. Li, and H. Chen, "Experimental Demonstration of a Coherent Perfect Absorber with PT Phase Transition," Phys. Rev. Lett. **112**, 143903 (2014).

[116] L. Feng, Z. J. Wong, R.-M. Ma, Y. Wang, and X. Zhang, "Single-mode laser by parity-time symmetry breaking," Science **346**, 972 (2014).

[117] H. Hodaei, M.-A. Miri, M. Heinrich, D. N. Christodoulides, and M. Khajavikhan, "Parity-time-symmetric microring lasers," Science **346**, 975 (2014).

[118] B. Peng, c. K. Özdemir, S. Rotter, H. Yilmaz, M. Liertzer, F. Monifi, C. M. Bender, F. Nori, and L. Yang, "Loss-induced suppression and revival of lasing," Science **346**, 328 (2014).

[119] H. G. L. Schwefel, "In optical pumping, less can be more," Science **346**, 304 (2014).

[120] L. Chang, X. Jiang, S. Hua, C. Yang, J. Wen, L. Jiang, G. Li, G. Wang, and M. Xiao, "Parity-time symmetry and variable optical isolation in active-passive-coupled microresonators," Nat Photon **8**, 524 (2014).

[121] P. J. Martin, B. G. Oldaker, A. H. Miklich, and D. E. Pritchard, "Bragg scattering of atoms from a standing light wave," Phys. Rev. Lett. **60**, 515 (1988).

[122] M. Ben Dahan, E. Peik, J. Reichel, Y. Castin, and C. Salomon, "Bloch Oscillations of Atoms in an Optical Potential," Phys. Rev. Lett. **76**, 4508 (1996).

[123] M. K. Oberthaler, R. Abfalterer, S. Bernet, J. Schmiedmayer, and A. Zeilinger, "Atom Waves in Crystals of Light," Phys. Rev. Lett. **77**, 4980 (1996).

[124] C. Lamprecht and M. A. M. Marte, "Comparing paraxial atom and light optics," Quantum and Semiclassical Optics: Journal of the European Optical Society Part B **10**, 501 (1998).

[125] T. Pertsch, P. Dannberg, W. Elflein, A. Bräuer, and F. Lederer, "Optical Bloch Oscillations in Temperature Tuned Waveguide Arrays," Phys. Rev. Lett. **83**, 4752 (1999).

[126] D. N. Christodoulides, F. Lederer, and Y. Silberberg, "Discretizing light behaviour in linear and nonlinear waveguide lattices," Nature **424**, 817 (2003).

[127] S. Longhi, "$\mathcal{PT}$-symmetric laser absorber," Phys. Rev. A **82**, 031801 (2010).

[128] Y. Chong, L. Ge, and A. Stone, "$\mathcal{PT}$-Symmetry Breaking and Laser-Absorber Modes in Optical Scattering Systems," Phys. Rev. Lett. **106**, 093902 (2011).

[129] Y. Chong, L. Ge, and A. Stone, "Publisher's Note: $\mathcal{PT}$-Symmetry Breaking and Laser-Absorber Modes in Optical Scattering Systems [Phys. Rev. Lett. 106, 093902 (2011)]," Phys. Rev. Lett. **108**, 269902 (2012).

[130] S. Fan, R. Baets, A. Petrov, Z. Yu, J. D. Joannopoulos, W. Freude, A. Melloni, M. Popović, M. Vanwolleghem, D. Jalas, M. Eich, M. Krause, H. Renner, E. Brinkmeyer, and C. R. Doerr, "Comment on "Nonreciprocal Light Propagation in a Silicon Photonic Circuit"," Science **335**, 38 (2012).

[131] L. Feng, M. Ayache, J. Huang, Y.-L. Xu, M.-H. Lu, Y.-F. Chen, Y. Fainman, and A. Scherer, "Response to Comment on "Nonreciprocal Light Propagation in a Silicon Photonic Circuit"," Science **335**, 38 (2012).

[132] X. Yin and X. Zhang, "Unidirectional light propagation at exceptional points," Nat. Mater. **12**, 175 (2013).

[133] Z. Lin, H. Ramezani, T. Eichelkraut, T. Kottos, H. Cao, and D. N. Christodoulides, "Unidirectional Invisibility Induced by $\mathcal{PT}$-Symmetric Periodic Structures," Phys. Rev. Lett. **106**, 213901 (2011).

[134] L. Feng, Y.-L. Xu, W. S. Fegadolli, M.-H. Lu, J. E. B. Oliveira, V. R. Almeida, Y.-F. Chen, and A. Scherer, "Experimental demonstration of a unidirectional reflectionless parity-time metamaterial at optical frequencies," Nat. Mater. **12**, 108 (2013).

[135] B. Midya, "Supersymmetry-generated one-way-invisible $\mathcal{PT}$-symmetric optical crystals," Phys. Rev. A **89**, 032116 (2014).

[136] S. Longhi, "A unidirectional invisible PT-symmetric complex crystal with arbitrary thickness," (2014), arXiv:1410.5278 .

[137] A. Sukhorukov, Z. Xu, and Y. Kivshar, "Nonlinear suppression of time reversals in $\mathcal{PT}$-symmetric optical couplers," Phys. Rev. A **82**, 043818 (2010).

[138] D. Jalas, A. Petrov, M. Eich, W. Freude, S. Fan, Z. Yu, R. Baets, M. Popovic, A. Melloni, J. D. Joannopoulos, M. Vanwolleghem, C. R. Doerr, and H. Renner, "What is - and what is not - an optical isolator," Nat Photon **7**, 579 (2013), commentary.

[139] B. Peng, S. K. Ozdemir, F. Lei, F. Monifi, M. Gianfreda, G. L. Long, S. Fan, F. Nori, C. M. Bender, and L. Yang, "Parity-time-symmetric whispering-gallery microcavities," Nat Phys **10**, 394 (2014).

[140] A. Guo, G. J. Salamo, D. Duchesne, R. Morandotti, M. Volatier-Ravat, V. Aimez, G. A. Siviloglou, and D. N. Christodoulides, "Observation of $\mathcal{PT}$-Symmetry Breaking in Complex Optical Potentials," Phys. Rev. Lett. **103**, 093902 (2009).

[141] S. Longhi, "Dynamic localization and transport in complex crystals," Phys. Rev. B **80**, 235102 (2009).

[142] S. Longhi, "Invisibility in $\mathcal{PT}$ -symmetric complex crystals," Journal of Physics A: Mathematical and Theoretical **44**, 485302 (2011).

[143] S. Longhi, "Talbot self-imaging in $\mathcal{PT}$-symmetric complex crystals," Phys. Rev. A **90**, 043827 (2014).

[144] R. Fleury, D. L. Sounas, and A. Alù, "Negative Refraction and Planar Focusing Based on Parity-Time Symmetric Metasurfaces," Phys. Rev. Lett. **113**, 023903 (2014).

[145] C. Hang, G. Huang, and V. V. Konotop, "$\mathcal{PT}$ Symmetry with a System of Three-Level Atoms," Phys. Rev. Lett. **110**, 083604 (2013).

[146] J. Sheng, M.-A. Miri, D. N. Christodoulides, and M. Xiao, "$\mathcal{PT}$-symmetric optical potentials in a coherent atomic medium," Phys. Rev. A **88**, 041803 (2013).

[147] P. Ginzburg, A. Hayat, N. Berkovitch, and M. Orenstein, "Nonlocal ponderomotive nonlinearity in plasmonics," Opt. Lett. **35**, 1551 (2010).

[148] M. Kauranen and A. V. Zayats, "Nonlinear plasmonics," Nat. Photon. **6**, 737 (2012).

[149] E. Brasselet, A. Lherbier, and L. J. Dubé, "Transverse nonlocal effects in optical reorientation of nematic liquidcrystals," J. Opt. Soc. Am. B **23**, 36 (2006).

[150] L. Lucchetti, L. Criante, F. Bracalente, F. Aieta, and F. Simoni, "Optical trapping induced by reorientational nonlocal effects in nematic liquid crystals," Phys. Rev. E **84**, 021702 (2011).

[151] D. Suter and T. Blasberg, "Stabilization of transverse solitary waves by a nonlocal response of the nonlinear medium," Phys. Rev. A **48**, 4583 (1993).

[152] J. P. Gordon, R. C. C. Leite, R. S. Moore, S. P. S. Porto, and J. R. Whinnery, "Long Transient Effects in Lasers with Inserted Liquid Samples," Journal of Applied Physics **36**, 3 (1965).

[153] K. S. Tikhonov, J. Sinova, and A. M. Finkel'stein, "Spectral non-uniform temperature and non-local heat transfer in the spin Seebeck effect," Nat Commun **4** (2013).

[154] S. Gatz and J. Herrmann, "Anisotropy, nonlocality, and space-charge field displacement in (2 + 1)-dimensional self-trapping in biased photorefractive crystals," Opt. Lett. **23**, 1176 (1998).

[155] F. Dalfovo, S. Giorgini, L. P. Pitaevskii, and S. Stringari, "Theory of Bose-Einstein condensation in trapped gases," Rev. Mod. Phys. **71**, 463 (1999).

[156] K. Góral, K. Rzążewski, and T. Pfau, "Bose-Einstein condensation with magnetic dipole-dipole forces," Phys. Rev. A **61**, 051601 (2000).

[157] V. M. Pérez-García, V. V. Konotop, and J. J. García-Ripoll, "Dynamics of quasicollapse in nonlinear Schrödinger systems with nonlocal interactions," Phys. Rev. E **62**, 4300 (2000).

[158] S. Sarkar and A. Bhattacharyay, "Non-local interactions in a BEC: an analogue gravity perspective," Journal of Physics A: Mathematical and Theoretical **47**, 092002 (2014).

[159] F. Maucher, S. Skupin, and W. Krolikowski, "Collapse in the nonlocal nonlinear Schrödinger equation," Nonlinearity **24**, 1987 (2011).

[160] O. Bang, W. Krolikowski, J. Wyller, and J. J. Rasmussen, "Collapse arrest and soliton stabilization in nonlocal nonlinear media," Phys. Rev. E **66**, 046619 (2002).

[161] C. Rotschild, T. Schwartz, O. Cohen, and M. Segev, "Incoherent spatial solitons in effectively instantaneous nonlinear media," Nat. Photon. **2**, 371 (2008).

[162] B. Alfassi, C. Rotschild, and M. Segev, "Incoherent surface solitons in effectively instantaneous nonlocal nonlinear media," Phys. Rev. A **80**, 041808 (2009).

[163] A. A. Minzoni, N. F. Smyth, A. L. Worthy, and Y. S. Kivshar, "Stabilization of vortex solitons in nonlocal nonlinear media," Phys. Rev. A **76**, 063803 (2007).

[164] F. Ye, Y. V. Kartashov, and L. Torner, "Stabilization of dipole solitons in nonlocal nonlinear media," Phys. Rev. A **77**, 043821 (2008).

[165] D. R. Solli, C. Ropers, P. Koonath, and B. Jalali, "Optical rogue waves," Nature **450**, 1054 (2007).

[166] J. M. Dudley, F. Dias, M. Erkintalo, and G. Genty, "Instabilities, breathers and rogue waves in optics," Nat. Photon. **8**, 755 (2014).

[167] W. D. Heiss, "The physics of exceptional points," Journal of Physics A: Mathematical and Theoretical **45**, 444016 (2012).

[168] D. Bohm, "A Suggested Interpretation of the Quantum Theory in Terms of "Hidden" Variables. I," Phys. Rev. **85**, 166 (1952).

[169] D. Bohm, "A Suggested Interpretation of the Quantum Theory in Terms of "Hidden" Variables. II," Phys. Rev. **85**, 180 (1952).

[170] R. Colbeck and R. Renner, "No extension of quantum theory can have improved predictive power," Nat Commun **2**, 411 (2011).

[171] M. F. Pusey, J. Barrett, and T. Rudolph, "On the reality of the quantum state," Nat. Phys. **8**, 475 (2012).

[172] R. Colbeck and R. Renner, "Is a System's Wave Function in One-to-One Correspondence with Its Elements of Reality?" Phys. Rev. Lett. **108**, 150402 (2012).

[173] J. F. Clauser, M. A. Horne, A. Shimony, and R. A. Holt, "Proposed Experiment to Test Local Hidden-Variable Theories," Phys. Rev. Lett. **23**, 880 (1969).

[174] D. M. Greenberger, M. A. Horne, A. Shimony, and A. Zeilinger, "Bell's theorem without inequalities," Am. J. Phys. **58**, 1131 (1990).

[175] C. Branciard, N. Brunner, N. Gisin, C. Kurtsiefer, A. Lamas-Linares, A. Ling, and V. Scarani, "Testing quantum correlations versus single-particle properties within Leggett's model and beyond," Nat Phys **4**, 681 (2008).

[176] J. S. Bell, *Speakable and unspeakable in quantum mechanics* (Cambridge University Press, Cambridge, 1987) p. 37.

[177] S. J. Freedman and J. F. Clauser, "Experimental Test of Local Hidden-Variable Theories," Phys. Rev. Lett. **28**, 938 (1972).

[178] J. F. Clauser and M. A. Horne, "Experimental consequences of objective local theories," Phys. Rev. D **10**, 526 (1974).

[179] B. Cirel'son, "Quantum generalizations of Bell's inequality," Letters in Mathematical Physics **4**, 93 (1980).

[180] C. Simon, V. Bužek, and N. Gisin, "No-Signaling Condition and Quantum Dynamics," Phys. Rev. Lett. **87**, 170405 (2001).

[181] C. Kittel, *Introduction to solid state physics*, 8th ed. (John Wiley & Sons, Inc, New York, 2005).

[182] P. Schlagheck and T. Paul, "Complex-scaling approach to the decay of Bose-Einstein condensates," Phys. Rev. A **73**, 023619 (2006).

[183] K. Rapedius and H. J. Korsch, "Resonance solutions of the nonlinear Schrödinger equation in an open double-well potential," Journal of Physics B: Atomic, Molecular and Optical Physics **42**, 044005 (2009).

[184] F. Jensen, *Introduction to Computational Chemistry*, 2nd ed. (John Wiley & Sons, Inc, West Sussex, 2007).

[185] P. Giannozzi, *Lecture Notes: Numerical Methods in Quantum Mechanics* (University of Udine, Udine, 2014).

[186] D. R. Hamann, "Semiconductor Charge Densities with Hard-Core and Soft-Core Pseudopotentials," Phys. Rev. Lett. **42**, 662 (1979).

[187] C. G. Broyden, "A class of methods for solving nonlinear simultaneous equations," Math. Comp. **19**, 577 (1965).

[188] D. Gay, "Some Convergence Properties of Broyden's Method," SIAM Journal on Numerical Analysis **16**, 623 (1979).

[189] E. Kvaalen, "A faster Broyden method," BIT Numerical Mathematics **31**, 369 (1991).

[190] C. T. Kelley, *Iterative Methods for Linear and Nonlinear Equations* (Society for industrial and Applied Mathematics, Philadelphia, 1995).

[191] G. P. Srivastava, "Broyden's method for self-consistent field convergence acceleration," Journal of Physics A: Mathematical and General **17**, L317 (1984).

[192] D. Vanderbilt and S. G. Louie, "Total energies of diamond (111) surface reconstructions by a linear combination of atomic orbitals method," Phys. Rev. B **30**, 6118 (1984).

[193] D. Singh, H. Krakauer, and C. S. Wang, "Accelerating the convergence of self-consistent linearized augmented-plane-wave calculations," Phys. Rev. B **34**, 8391 (1986).

[194] D. D. Johnson, "Modified Broyden's method for accelerating convergence in self-consistent calculations," Phys. Rev. B **38**, 12807 (1988).

[195] A. Baran, A. Bulgac, M. M. Forbes, G. Hagen, W. Nazarewicz, N. Schunck, and M. V. Stoitsov, "Broyden's method in nuclear structure calculations," Phys. Rev. C **78**, 014318 (2008).

[196] K. Ciesielski, "On Stefan Banach and some of his results." Banach Journal of Mathematical Analysis **1**, 1 (2007).

[197] C. O'Brien and O. Kocharovskaya, "Optically Controllable Photonic Structures with Zero Absorption," Phys. Rev. Lett. **107**, 137401 (2011).

[198] J. W. Goodman, *Introduction to Fourier Optics*, 2nd ed. (McGraw-Hill, New York, 1996) pp. 61–62.

[199] A. Taflove and S. C. Hagness, *Computational Electrodynamics: The Finite-Difference Time-Domain Method*, 3rd ed. (Artech House, London, 2005).

[200] A. F. Oskooi, D. Roundy, M. Ibanescu, P. Bermel, J. Joannopoulos, and S. G. Johnson, "Meep: A flexible free-software package for electromagnetic simulations by the FDTD method," Computer Physics Communications **181**, 687 (2010).

[201] G. Strang, "On the Construction and Comparison of Difference Schemes," SIAM Journal on Numerical Analysis **5**, 506 (1968).

[202] J. Durnin, "Exact solutions for nondiffracting beams. I. The scalar theory," J. Opt. Soc. Am. A **4**, 651 (1987).

[203] M. V. Berry and N. L. Balazs, "Nonspreading wave packets," American Journal of Physics **47**, 264 (1979).

[204] G. A. Siviloglou, J. Broky, A. Dogariu, and D. N. Christodoulides, "Observation of Accelerating Airy Beams," Phys. Rev. Lett. **99**, 213901 (2007).

[205] J. Durnin, J. J. Miceli, and J. H. Eberly, "Diffraction-free beams," Phys. Rev. Lett. **58**, 1499 (1987).

[206] V. Garces-Chavez, D. McGloin, H. Melville, W. Sibbett, and K. Dholakia, "Simultaneous micromanipulation in multiple planes using a self-reconstructing light beam," Nature **419**, 145 (2002).

[207] D. McGloin and K. Dholakia, "Bessel beams: Diffraction in a new light," Contemporary Physics **46**, 15 (2005).

[208] J. C. Gutiérrez-Vega, M. D. Iturbe-Castillo, and S. Chávez-Cerda, "Alternative formulation for invariant optical fields: Mathieu beams," Opt. Lett. **25**, 1493 (2000).

[209] P. Zhang, Y. Hu, T. Li, D. Cannan, X. Yin, R. Morandotti, Z. Chen, and X. Zhang, "Nonparaxial Mathieu and Weber Accelerating Beams," Phys. Rev. Lett. **109**, 193901 (2012).

[210] M. A. Bandres, J. C. Gutiérrez-Vega, and S. Chávez-Cerda, "Parabolic nondiffracting optical wave fields," Opt. Lett. **29**, 44 (2004).

[211] M. A. Bandres and B. M. Rodríguez-Lara, "Nondiffracting accelerating waves: Weber waves and parabolic momentum," New Journal of Physics **15**, 013054 (2013).

[212] A. G. Truscott, M. E. J. Friese, N. R. Heckenberg, and H. Rubinsztein-Dunlop, "Optically Written Waveguide in an Atomic Vapor," Phys. Rev. Lett. **82**, 1438 (1999).

[213] R. Kapoor and G. S. Agarwal, "Theory of electromagnetically induced waveguides," Phys. Rev. A **61**, 053818 (2000).

[214] P. K. Vudyasetu, D. J. Starling, and J. C. Howell, "All Optical Waveguiding in a Coherent Atomic Rubidium Vapor," Phys. Rev. Lett. **102**, 123602 (2009).

[215] T. N. Dey and G. S. Agarwal, "Subdiffraction propagation of images using saturated absorption of optical transition," Opt. Lett. **34**, 3199 (2009).

[216] T. N. Dey and J. Evers, "Nondiffracting optical beams in a three-level Raman system," Phys. Rev. A **84**, 043842 (2011).

[217] L. Zhang, T. N. Dey, and J. Evers, "Control of beam propagation in optically written waveguides beyond the paraxial approximation," Phys. Rev. A **87**, 043842 (2013).

[218] O. N. Verma, L. Zhang, J. Evers, and T. N. Dey, "Optical cloning of arbitrary images beyond the diffraction limits," Phys. Rev. A **88**, 013810 (2013).

[219] R. R. Moseley, S. Shepherd, D. J. Fulton, B. D. Sinclair, and M. H. Dunn, "Spatial Consequences of Electromagnetically Induced Transparency: Observation of Electromagnetically Induced Focusing," Phys. Rev. Lett. **74**, 670 (1995).

[220] D. Bortman-Arbiv, A. D. Wilson-Gordon, and H. Friedmann, "Induced optical spatial solitons," Phys. Rev. A **58**, R3403 (1998).

[221] M. Vengalattore and M. Prentiss, "Radial Confinement of Light in an Ultracold Anisotropic Medium," Phys. Rev. Lett. **95**, 243601 (2005).

[222] D. Tarhan, N. Postacioglu, and Özgür E. Müstecaplioğlu, "Ultraslow optical waveguiding in an atomic Bose-Einstein condensate," Opt. Lett. **32**, 1038 (2007).

[223] A. S. Zibrov, M. D. Lukin, L. Hollberg, D. E. Nikonov, M. O. Scully, H. G. Robinson, and V. L. Velichansky, "Experimental Demonstration of Enhanced Index of Refraction via Quantum Coherence in Rb," Phys. Rev. Lett. **76**, 3935 (1996).

[224] K. T. Kapale, M. O. Scully, S.-Y. Zhu, and M. S. Zubairy, "Quenching of spontaneous emission through interference of incoherent pump processes," Phys. Rev. A **67**, 023804 (2003).

[225] L.-G. Wang, S. Qamar, S.-Y. Zhu, and M. S. Zubairy, "Manipulation of the Raman process via incoherent pump, tunable intensity, and phase control," Phys. Rev. A **77**, 033833 (2008).

[226] J. Honer, H. Weimer, T. Pfau, and H. P. Büchler, "Collective Many-Body Interaction in Rydberg Dressed Atoms," Phys. Rev. Lett. **105**, 160404 (2010).

[227] R. Fleischhaker, T. N. Dey, and J. Evers, "Phase modulation induced by cooperative effects in electromagnetically induced transparency," Phys. Rev. A **82**, 013815 (2010).

[228] M. Macovei, J. Evers, and C. H. Keitel, "Coherent manipulation of collective three-level systems," Phys. Rev. A **71**, 033802 (2005).

[229] M. O. Scully, "Enhancement of the index of refraction via quantum coherence," Phys. Rev. Lett. **67**, 1855 (1991).

[230] M. Fleischhauer, C. H. Keitel, M. O. Scully, C. Su, B. T. Ulrich, and S.-Y. Zhu, "Resonantly enhanced refractive index without absorption via atomic coherence," Phys. Rev. A **46**, 1468 (1992).

[231] A. S. Zibrov, M. D. Lukin, L. Hollberg, D. E. Nikonov, M. O. Scully, H. G. Robinson, and V. L. Velichansky, "Experimental Demonstration of Enhanced Index of Refraction via Quantum Coherence in Rb," Phys. Rev. Lett. **76**, 3935 (1996).

[232] M. O. Oktel and O. E. Müstecaplıoğlu, "Electromagnetically induced left-handedness in a dense gas of three-level atoms," Phys. Rev. A **70**, 053806 (2004).

[233] Q. Thommen and P. Mandel, "Electromagnetically Induced Left Handedness in Optically Excited Four-Level Atomic Media," Phys. Rev. Lett. **96**, 053601 (2006).

[234] J. Kästel, M. Fleischhauer, S. F. Yelin, and R. L. Walsworth, "Tunable Negative Refraction without Absorption via Electromagnetically Induced Chirality," Phys. Rev. Lett. **99**, 073602 (2007).

[235] N. A. Proite, B. E. Unks, J. T. Green, and D. D. Yavuz, "Refractive Index Enhancement with Vanishing Absorption in an Atomic Vapor," Phys. Rev. Lett. **101**, 147401 (2008).

[236] Y. Yang, J. Xu, H. Chen, and S. Zhu, "Quantum Interference Enhancement with Left-Handed Materials," Phys. Rev. Lett. **100**, 043601 (2008).

[237] Z. J. Simmons, N. A. Proite, J. Miles, D. E. Sikes, and D. D. Yavuz, "Refractive index enhancement with vanishing absorption in short, high-density vapor cells," Phys. Rev. A **85**, 053810 (2012).

[238] P. P. Orth, R. Hennig, C. H. Keitel, and J. Evers, "Negative refraction with tunable absorption in an active dense gas of atoms," New Journal of Physics **15**, 013027 (2013).

[239] E. Kuznetsova, R. Rajapakse, and S. F. Yelin, "Enhanced index of refraction in four-wave-mixing media," Phys. Rev. A **88**, 033850 (2013).

[240] L. Zhang and J. Evers, "Diffractionless image propagation and frequency conversion via four-wave mixing exploiting the thermal motion of atoms," Phys. Rev. A **89**, 013817 (2014).

[241] J. Kong, F. Hudelist, Z. Y. Ou, and W. Zhang, "Cancellation of Internal Quantum Noise of an Amplifier by Quantum Correlation," Phys. Rev. Lett. **111**, 033608 (2013).

[242] S. Kocsis, G. Y. Xiang, T. C. Ralph, and G. J. Pryde, "Heralded noiseless amplification of a photon polarization qubit," Nat. Phys. **9**, 23 (2013).

[243] S. P. Tewari and G. S. Agarwal, "Control of Phase Matching and Nonlinear Generation in Dense Media by Resonant Fields," Phys. Rev. Lett. **56**, 1811 (1986).

[244] S. E. Harris, J. E. Field, and A. Imamoğlu, "Nonlinear optical processes using electromagnetically induced transparency," Phys. Rev. Lett. **64**, 1107 (1990).

[245] S. P. Tewari and G. S. Agarwal, "Vacuum-ultraviolet generation using electromagnetic-field-induced transparency," Phys. Rev. Lett. **66**, 1797 (1991).

[246] L. Deng and M. G. Payne, "Inhibiting the Onset of the Three-Photon Destructive Interference in Ultraslow Propagation-Enhanced Four-Wave Mixing with Dual Induced Transparency," Phys. Rev. Lett. **91**, 243902 (2003).

[247] Y. Wu, J. Saldana, and Y. Zhu, "Large enhancement of four-wave mixing by suppression of photon absorption from electromagnetically induced transparency," Phys. Rev. A **67**, 013811 (2003).

[248] P. Sorokin, J. Wynne, and J. Lankard, "Tunable coherent ir source based upon four-wave parametric conversion in alkali metal vapors," App. Phys. Lett. **22**, 342 (1973).

[249] A. G. Radnaev, Y. O. Dudin, R. Zhao, H. H. Jen, S. D. Jenkins, A. Kuzmich, and T. A. B. Kennedy, "A quantum memory with telecom-wavelength conversion," Nat Phys **6**, 894 (2010).

[250] D.-S. Ding, Z.-Y. Zhou, B.-S. Shi, X.-B. Zou, and G.-C. Guo, "Image transfer through two sequential four-wave-mixing processes in hot atomic vapor," Phys. Rev. A **85**, 053815 (2012).

[251] X. Liu, B. Kuyken, G. Roelkens, R. Baets, R. M. Osgood, and W. M. J. Green, "Bridging the mid-infrared-to-telecom gap with silicon nanophotonic spectral translation," Nat Photon **6**, 667 (2012).

[252] R. Fleischhaker and J. Evers, "Four-wave mixing enhanced white-light cavity," Phys. Rev. A **78**, 051802 (2008).

[253] I. Katzir, A. Ron, and O. Firstenberg, "Diffraction manipulation by four-wave mixing," (2014), arXiv:1401.3788 .

[254] L. J. Wang, A. Kuzmich, and A. Dogariu, "Gain-assisted superluminal light propagation," Nature **406**, 277 (2000).

[255] L. Deng and M. G. Payne, "Gain-Assisted Large and Rapidly Responding Kerr Effect using a Room-Temperature Active Raman Gain Medium," Phys. Rev. Lett. **98**, 253902 (2007).

[256] T. F. Gallagher, "Rydberg atoms," Reports on Progress in Physics **51**, 143 (1988).

[257] D. Jaksch, J. I. Cirac, P. Zoller, S. L. Rolston, R. Côté, and M. D. Lukin, "Fast Quantum Gates for Neutral Atoms," Phys. Rev. Lett. **85**, 2208 (2000).

[258] C. H. Greene, A. S. Dickinson, and H. R. Sadeghpour, "Creation of Polar and Nonpolar Ultra-Long-Range Rydberg Molecules," Phys. Rev. Lett. **85**, 2458 (2000).

[259] A. V. Gorshkov, J. Otterbach, M. Fleischhauer, T. Pohl, and M. D. Lukin, "Photon-Photon Interactions via Rydberg Blockade," Phys. Rev. Lett. **107**, 133602 (2011).

[260] O. Firstenberg, T. Peyronel, Q.-Y. Liang, A. V. Gorshkov, M. D. Lukin, and V. Vuletic, "Attractive photons in a quantum nonlinear medium," Nature **502**, 71 (2013).

[261] J. Otterbach, M. Moos, D. Muth, and M. Fleischhauer, "Wigner Crystallization of Single Photons in Cold Rydberg Ensembles," Phys. Rev. Lett. **111**, 113001 (2013).

[262] M. F. Maghrebi, N. Y. Yao, M. Hafezi, T. Pohl, O. Firstenberg, and A. V. Gorshkov, "Fractional Quantum Hall States of Rydberg Polaritons," (2014), arXiv:1411.6624 .

[263] D. Møller, L. Madsen, and K. Mølmer, "Quantum Gates and Multiparticle Entanglement by Rydberg Excitation Blockade and Adiabatic Passage," Phys. Rev. Lett. **100**, 170504 (2008).

[264] M. Müller, I. Lesanovsky, H. Weimer, H. Büchler, and P. Zoller, "Mesoscopic Rydberg Gate Based on Electromagnetically Induced Transparency," Phys. Rev. Lett. **102**, 170502 (2009).

[265] L. Isenhower, E. Urban, X. Zhang, A. Gill, T. Henage, T. Johnson, T. Walker, and M. Saffman, "Demonstration of a Neutral Atom Controlled-NOT Quantum Gate," Phys. Rev. Lett. **104**, 010503 (2010).

[266] H. Weimer, N. Yao, C. Laumann, and M. Lukin, "Long-Range Quantum Gates using Dipolar Crystals," Phys. Rev. Lett. **108**, 100501 (2012).

[267] H. Weimer, M. Muller, I. Lesanovsky, P. Zoller, and H. P. Buchler, "A Rydberg quantum simulator," Nat Phys **6**, 382 (2010).

[268] T. Keating, K. Goyal, Y.-Y. Jau, G. Biedermann, A. Landahl, and I. Deutsch, "Adiabatic quantum computation with Rydberg-dressed atoms," Phys. Rev. A **87**, 052314 (2013).

[269] R. Unanyan and M. Fleischhauer, "Efficient and robust entanglement generation in a many-particle system with resonant dipole-dipole interactions," Phys. Rev. A **66**, 032109 (2002).

[270] M. Saffman and K. Mølmer, "Efficient Multiparticle Entanglement via Asymmetric Rydberg Blockade," Phys. Rev. Lett. **102**, 240502 (2009).

[271] Z. Zuo and K. Nakagawa, "Multiparticle entanglement in a one-dimensional optical lattice using Rydberg-atom interactions," Phys. Rev. A **82**, 062328 (2010).

[272] C. S. Hofmann, G. Günter, H. Schempp, M. Robert-de Saint-Vincent, M. Gärttner, J. Evers, S. Whitlock, and M. Weidemüller, "Sub-Poissonian Statistics of Rydberg-Interacting Dark-State Polaritons," Phys. Rev. Lett. **110**, 203601 (2013).

[273] L.-D. Zhang, Y. Jiang, R.-G. Wan, S.-C. Tian, B. Zhang, X.-J. Zhang, J.-Y. Gao, Y.-P. Niu, and S.-Q. Gong, "Extremely narrowed and amplified gain spectrum induced by the Doppler effect," J. Phys. B **44**, 135505 (2011).

[274] S. Klaiman, U. Günther, and N. Moiseyev, "Visualization of Branch Points in $\mathcal{PT}$-Symmetric Waveguides," Phys. Rev. Lett. **101**, 080402 (2008).

[275] S. Longhi, "Spectral singularities and Bragg scattering in complex crystals," Phys. Rev. A **81**, 022102 (2010).

[276] E.-M. Graefe and H. Jones, "$\mathcal{PT}$-symmetric sinusoidal optical lattices at the symmetry-breaking threshold," Phys. Rev. A **84**, 013818 (2011).

[277] H. Ramezani, T. Kottos, V. Kovanis, and D. Christodoulides, "Exceptional-point dynamics in photonic honeycomb lattices with $\mathcal{PT}$ symmetry," Phys. Rev. A **85**, 013818 (2012).

[278] S. Longhi and G. Della Valle, "Optical lattices with exceptional points in the continuum," Phys. Rev. A **89**, 052132 (2014).

[279] J. Gong and Q.-h. Wang, "Geometric phase in $\mathcal{PT}$-symmetric quantum mechanics," Phys. Rev. A **82**, 012103 (2010).

[280] J. Gong and Q. hai Wang, "Time-dependent $\mathcal{P}\,\mathcal{T}$ -symmetric quantum mechanics," Journal of Physics A: Mathematical and Theoretical **46**, 485302 (2013).

[281] C. Bender, K. Milton, and V. Savage, "Solution of Schwinger-Dyson equations for PT-symmetric quantum field theory," Phys. Rev. D **62**, 085001 (2000).

[282] C. Bender, D. Brody, and H. Jones, "Scalar Quantum Field Theory with a Complex Cubic Interaction," Phys. Rev. Lett. **93**, 251601 (2004).

[283] C. Bender, D. Brody, and H. Jones, "Extension of $\mathcal{PT}$-symmetric quantum mechanics to quantum field theory with cubic interaction," Phys. Rev. D **70**, 025001 (2004).

[284] C. Bender, D. Brody, and H. Jones, "Erratum: Extension of $\mathcal{PT}$-symmetric quantum mechanics to quantum field theory with cubic interaction [Phys. Rev. D 70, 025001 (2004)]," Phys. Rev. D **71**, 049901 (2005).

[285] C. Bender, S. Brandt, J.-H. Chen, and Q. Wang, "Ghost busting: $\mathcal{PT}$-symmetric interpretation of the Lee model," Phys. Rev. D **71**, 025014 (2005).

[286] S. Longhi and G. Della Valle, "Photonic realization of $\mathcal{PT}$-symmetric quantum field theories," Phys. Rev. A **85**, 012112 (2012).

[287] C. Bender, V. Branchina, and E. Messina, "Ordinary versus $\mathcal{PT}$-symmetric ϕ^3 quantum field theory," Phys. Rev. D **85**, 085001 (2012).

[288] I. Goldsheid and B. Khoruzhenko, "Distribution of Eigenvalues in Non-Hermitian Anderson Models," Phys. Rev. Lett. **80**, 2897 (1998).

[289] C. Dembowski, B. Dietz, H.-D. Gräf, H. Harney, A. Heine, W. Heiss, and A. Richter, "Observation of a Chiral State in a Microwave Cavity," Phys. Rev. Lett. **90**, 034101 (2003).

[290] I. Rotter, "A non-Hermitian Hamilton operator and the physics of open quantum systems," Journal of Physics A: Mathematical and Theoretical **42**, 153001 (2009).

[291] Y.-C. Lee, M.-H. Hsieh, S. T. Flammia, and R.-K. Lee, "Local $\mathcal{PT}$ Symmetry Violates the No-Signaling Principle," Phys. Rev. Lett. **112**, 130404 (2014).

[292] F. Cannata, G. Junker, and J. Trost, "Schrödinger operators with complex potential but real spectrum," Physics Letters A **246**, 219 (1998).

[293] A. Mostafazadeh, "Two-component formulation of the Wheeler-DeWitt equation," Journal of Mathematical Physics **39**, 4499 (1998).

[294] A. Mostafazadeh, "Conceptual aspects of $\mathcal{PT}$ -symmetry and pseudo-Hermiticity: a status report," Physica Scripta **82**, 038110 (2010).

[295] A. Mostafazadeh, "Pseudo-Hermitian Representation of Quantum Mechanics," International Journal of Geometric Methods in Modern Physics **07**, 1191 (2010).

[296] R. Röhlsberger, K. Schlage, B. Sahoo, S. Couet, and R. Rüffer, "Collective Lamb Shift in Single-Photon Superradiance," Science **328**, 1248 (2010).

[297] H.-W. Lee and J. Kim, "Quantum teleportation and Bell's inequality using single-particle entanglement," Phys. Rev. A **63**, 012305 (2000).

[298] S. M. Tan, D. F. Walls, and M. J. Collett, "Tan, Walls, and Collett reply," Phys. Rev. Lett. **68**, 895 (1992).

[299] M. Czachor, "Bell theorem without inequalities: A single-particle formulation," Phys. Rev. A **49**, 2231 (1994).

[300] D. Home and G. S. Agarwal, "Quantum nonlocality of single photon states," Physics Letters A **209**, 1 (1995).

[301] M. Revzen and A. Mann, "Bell's inequality for a single particle," Foundations of Physics **26**, 847 (1996).

[302] G. Björk, P. Jonsson, and L. L. Sánchez-Soto, "Single-particle nonlocality and entanglement with the vacuum," Phys. Rev. A **64**, 042106 (2001).

[303] C. C. Gerry, "Nonlocality of a single photon in cavity QED," Phys. Rev. A **53**, 4583 (1996).

[304] D. Fattal, K. Inoue, J. Vučković, C. Santori, G. S. Solomon, and Y. Yamamoto, "Entanglement Formation and Violation of Bell's Inequality with a Semiconductor Single Photon Source," Phys. Rev. Lett. **92**, 037903 (2004).

[305] L. Heaney, A. Cabello, M. F. Santos, and V. Vedral, "Extreme nonlocality with one photon," New Journal of Physics **13**, 053054 (2011).

[306] B. Hessmo, P. Usachev, H. Heydari, and G. Björk, "Experimental Demonstration of Single Photon Nonlocality," Phys. Rev. Lett. **92**, 180401 (2004).

[307] Y. Hasegawa, R. Loidl, G. Badurek, M. Baron, and H. Rauch, "Violation of a Bell-like inequality in single-neutron interferometry," Nature **425**, 45 (2003).

[308] R. Röhlsberger, H.-C. Wille, K. Schlage, and B. Sahoo, "Electromagnetically induced transparency with resonant nuclei in a cavity," Nature **482**, 199 (2012).

[309] G. S. Agarwal, *in Quantum Optics, Springer Tracts in Modern Physics Vol. 70* (Springer, Berlin, 1974) pp. 1–128.

[310] Z. Ficek and S. Swain, *Quantum Interference and Coherence: Theory and Experiments* (Springer Science, New York, 2005).

[311] M. Kiffner, M. Macovei, J. Evers, and C. Keitel, *in Progress in Optics*, Vol. 55 (Elsevier Science, Burlington, 2010) pp. 85–197.

[312] C. H. Holbrow, E. Galvez, and M. E. Parks, "Photon quantum mechanics and beam splitters," Am. J. Phys. **70**, 260 (2002).

[313] R. A. Campos, B. E. A. Saleh, and M. C. Teich, "Quantum-mechanical lossless beam splitter: SU(2) symmetry and photon statistics," Phys. Rev. A **40**, 1371 (1989).

[314] V. Degiorgio, "Phase shift between the transmitted and the reflected optical fields of a semireflecting lossless mirror is $\pi/2$," Am. J. Phys. **48**, 81 (1980).

[315] A. Zeilinger, "General properties of lossless beam splitters in interferometry," Am. J. Phys. **49**, 882 (1981).

[316] J. Zak, "Berry's phase for energy bands in solids," Phys. Rev. Lett. **62**, 2747 (1989).

[317] D. Xiao, M.-C. Chang, and Q. Niu, "Berry phase effects on electronic properties," Rev. Mod. Phys. **82**, 1959 (2010).

Acknowledgements

I would like to express my deepest gratitude to my supervisor PD. Dr. Jörg Evers. It is impossible to finish this thesis without his great guidance and enlightenment. I am always recharged and stimulated from his inspiring suggestions after every discussions of physics, and I will always memorize the exciting moments when we finally solved the problems which seems to be tricky at the first place. His scientific insights and his powerful way of doing sciences has impressed me and is the most important source stimulating me all the time. It may need to take much more time for me to fully understand how important this means to me. I have learned so much from not only his scientific skills but also his noble personalities. His patience and encouragement is still vivid to me in our first discussion when I start to speak in my poor English, and lasts in the following time. He has been an exceptional example keeping me promoting and improving myself further.

I would like to express my sincere gratitude to Honorarprof. Christoph H. Keitel not only for offering the friendly and active atmosphere in this outstanding group, but also for the financial support in the last stages of my PhD study.

I am deeply graceful to Prof. Dr. Jürgen Berges for reading my thesis and writing the second reference report and the further members of my examination committee Prof. Dr. Matthias Weidemüller and Prof. Dr. Markus Oberthaler for their interest in my research topic.

I would like to take this chance to deeply thank Prof. Shangqing Gong (龚尚庆) and Prof. Yueping Niu (钮月萍) who encouraged and recommended me to apply for a PhD position in the great Max Planck Institute for Nuclear Physics. I have also had a wonderful time when I was in Prof. Gong's excellent group.

I am deeply indebted to my Proof Readers Enderalp Yakaboylu, Kilian Heeg, Polo lango and Jonas Gunst whose contributions have been one of the most significant resources to polish my thesis. I am also deeply graceful to Kilian Heeg and Patrick Reiser for their great help in translating the abstract of the thesis into German language. I will always remember this in my heart.

I should also thank Dr. Frank Köck and Mr. Carsten Pinnow for computer-related supports, and Ms Sibel Babacan for her kind help in administrative affairs.

I feel really lucky that I have so many kind and smart colleagues: Martin Gärttner, Kilian Heeg, Andreas Reichegger, Patrick Reiser, Paolo Lango, Jonas Gunst, Andreas Fisher, Enderalp Yakaboylu, Sebastian Meuren .... During the last three years, they have answered many of my stupid questions about Germany and Europe, and of course, we have also shared a lot of our opinions in other interesting topics. Their kindness and friendship is part of the reasons that I start to love Heidelberg immediately after I came here, and is unforgettable in my lifetime. I would like to specially thank Martin Gärttner and Kilian Heeg for their thoughtful help in my living here in the beginning when I came to Heidelberg.

I am indebted to my other friends, Chunpu Liu (刘呈普), Ni Cui (崔妮), Luling Jin (金璐玲), Meng Wen (温猛), Jianxing Li (栗建兴), Wen-Te Liao (廖文德), Xiangjin Kong (孔祥进), Yanwei Li (李延伟), Ruoyu Liu (柳若愚), Zuoye Liu (刘作业),Yonghao Mi (米永浩), Difa Ye (叶地发), Xueguang Ren (任雪光), Shaofeng Zhang (张少锋), Suli

Han (韩素立), Helen Poon (潘海琳). I have enjoyed the many times when we talked about physics and other interesting things in the last three years. The uncountable joyful moments, which have always washed away all the tiredness I sometimes felt from work, are unerasable memories to me forever. It is because of them that I feel like at home with my brothers and sisters when I live here at Heidelberg. I owe special thanks to Difa Ye (叶地发) and Jianxing Li (栗建兴) for their help in temporary accommodation for short transition periods.

This thesis is devoted to my beloved parents Xiewu Zhang (张协武) and Xihua Xu (徐细华). They may not fully understand what I am doing and will do, but their unlimited support and endless love is the last shelter where I can refresh and warm up myself. When I look back at the past, they have been always there ready to enjoy my happy moments and to help me getting through tough times, and I know that they will continue to do so in the future. I wish that this thesis could be a small present to deliver my great love and thankfulness to them.